

AURORAL EFFECTS ON METEORIC
METALS IN THE UPPER ATMOSPHERE

A DISSERTATION
SUBMITTED TO THE DEPARTMENT OF ELECTRICAL ENGINEERING
AND THE COMMITTEE ON GRADUATE STUDIES
OF STANFORD UNIVERSITY
IN PARTIAL FULFILLMENT OF THE REQUIREMENTS
FOR THE DEGREE OF
DOCTOR OF PHILOSOPHY

By
Craig James Heinselman
June 1999

© Copyright 1999 by Craig James Heinselman
All Rights Reserved

I certify that I have read this dissertation and that in my opinion it is fully adequate, in scope and quality, as a dissertation for the degree of Doctor of Philosophy.

Umran S. Inan
(Principal Adviser)

I certify that I have read this dissertation and that in my opinion it is fully adequate, in scope and quality, as a dissertation for the degree of Doctor of Philosophy.

John D. Kelly

I certify that I have read this dissertation and that in my opinion it is fully adequate, in scope and quality, as a dissertation for the degree of Doctor of Philosophy.

Lambertus Hesselink

Approved for the University Committee on Graduate Studies:

Abstract

Meteors deposit many tons of material into Earth's upper atmosphere each day. The physics and chemistry of meteoric metals in the atmosphere have long been active topics of study, but sophisticated models have emerged just recently of the gas-phase chemical reactions that affect the evolution of the state of these metals. At high latitudes, this portion of the upper atmosphere is also shared by the aurora borealis, or northern lights, which dramatically alter the properties of the background plasma.

This thesis concerns coupled chemical models and one-dimensional dynamical models that were developed to investigate the effects of auroral ionization on the time evolution of meteoric iron and sodium elements and compounds in the upper atmosphere. These models are used to show that aurorae can result in rapid ionization of recently deposited iron and sodium, with time constants on the order of 15 minutes. The models are also used to investigate the influences of aurorae on the background iron and sodium layers. Because of the nominal altitude of the neutral iron layer, aurorae will not normally have a measurable impact on that constituent. For sodium, on the other hand, the impact is more significant but highly dependent on the chemical makeup of the aurorally produced ions. For either case, sporadic neutral atom layers at auroral altitudes are significantly affected.

A case study of radar and lidar measurements from the Sondrestrom Facility in Greenland is used to test the sodium model. Results are presented which are consistent with the model predictions of the effects of the aurorally enhanced ionization. For this specific case, evidence is also presented to support a gas-phase chemical mechanism for the formation of a thin sporadic sodium layer.

Acknowledgements

I begin by thanking my wife, Denise, and daughters, Karen and Susan, without whose incredible patience this thesis would never have been completed. The many evenings and weekends of thesis-related absence would not have been bearable without their support and understanding.

I thank John Kelly for his constant mentorship and encouragement over the past 17 years. Without his support this thesis would never even have been started.

Jim Vickrey was also instrumental in my pursuit of this degree. Our many stimulating discussions laid a firm foundation for my progress in understanding some of the intricacies of this field.

Thanks to my principal advisor, Umran Inan, who was willing to take me on as a student in spite of the fact that my areas of interest were somewhat different from his own. I also thank him for giving me a chance to come back to Stanford after a long absence and *finally* take him up on an offer to work toward a degree under his tutelage.

I have enjoyed opportunities for discussions with a wide variety of researchers in this field over the years. Contrary to popular belief, science and engineering are not solitary endeavours carried out by isolated individuals; the people and personalities make the pursuit of research both enjoyable and productive. To mention but a few, I thank Jeff Thayer, Brent Watkins, and Dave Bedey for many educational and fruitful discussions. Jeff and Brent were especially generous in allowing me to ‘skim the cream’ of early sodium lidar measurements.

I also thank the faculty and students at Stanford for providing a stimulating environment in which to learn the foundations of much of this work.

Tusind tak to John Jørgensen and the rest of the Sondrestrom site crew members over the past decade and a half for their dedication and comraderie. They truly make Sondrestom a wonderful place to visit and live!

Thanks to Mary McCready for her attention to *hyphenated* detail in reading and correcting the grammar in an early version of this work.

I owe debts of gratitude to Rolando Garcia for making his model output available to me, Miguel Larsen for providing the TMA trail photograph, and Rachel Cox for pointing me toward important references in the chemistry literature (of which I was sadly ignorant).

Finally, I thank my parents, Jim and Shirley, for teaching me that learning is a life-long endeavour. They also instilled in me the belief that it is important to find a job that you enjoy; advice that I have been fortunate enough to be able to follow.

Portions of this work were supported by NSF Cooperative Agreements ATM-9317167 and ATM-9813556.

Contents

Abstract	iv
Acknowledgements	v
1 Introduction	1
1.1 Thesis Organization	3
1.2 Thesis Contributions	3
2 Meteoric Material	5
2.1 Deposition	6
2.2 Composition and Material State	11
2.3 Diffusive Mixing	16
2.4 Altitude Profiles	19
2.5 Chapter Summary	25
3 Chemistry	26
3.1 Iron Model	28
3.2 Sodium Model	42
3.3 Auroral Effects	50
3.3.1 Auroral Effects on Iron Chemistry	57
3.3.2 Auroral Effects on Sodium Chemistry	61
3.4 Chapter Summary	70

4	Dynamics	71
4.1	Ion Layer Formation	72
4.2	Neutral Layer Formation and Diffusion	89
4.3	Chapter Summary	92
5	Case Study	93
5.1	Chapter Summary	107
6	Conclusions	108
A	Diffusion in the Upper Atmosphere	111
A.1	Molecular Diffusion	111
A.2	Eddy Diffusion	115
B	Incoherent Scatter Radar	122
B.1	Incoherent Scatter Theory	123
B.2	Radar Techniques	131
B.3	The Sondrestrom Radar	138
C	Sodium Density Lidar	143
C.1	Sodium Cross-section	144
C.2	Sodium Lidar Technique	150
C.3	The Sondrestrom Lidar	151
D	Ion Flux	155
D.1	Simplified Form of Ion Velocity	155
D.2	Ion Flux Derivation	157
D.3	Collision Frequencies	161
E	Modeling Issues	166
E.1	Chemical Model Example	166
E.2	Ion Dynamics Model	169

List of Tables

2.1	CI Carbonaceous Chondrite Elemental Abundances	11
2.2	Meteor Ionization Coefficients	13
3.1	Iron Chemistry	29
3.2	Models Used for Chemical Reactants	31
3.3	Sodium Chemistry	43
3.4	<i>E</i> -Region Oxygen and Nitrogen Chemistry	56
A.1	Eddy Diffusion	116
B.1	Sondrestrom Radar Parameters	138
C.1	Sodium Absorption Oscillator Strengths	145
C.2	Sodium D_2 Hyperfine Lines	146
C.3	Equations for q_n Correction Factors	147
C.4	Sondrestrom Lidar Parameters	153
D.1	Neutral Gas Polarizabilities	162
E.1	Iron Chemistry Example	167

List of Figures

2.1	Meteoric Material Deposition Profile	9
2.2	Meteor Ionization Coefficients	14
2.3	Eddy and Molecular Diffusion Coefficients	21
2.4	Total Iron Number Density Profile with a Perfect Sink at 90 km	22
2.5	Total Iron Number Density Profile and Residence Time	23
2.6	Total Sodium Number Density Profile	24
3.1	Schematic of the Iron Chemistry Reactions.	30
3.2	Iron Chemistry Reactants, Winter, Night, 67° N	33
3.3	Iron Chemistry Steady-State Profiles	34
3.4	Iron Profile Comparison with Data	36
3.5	Iron Reaction Rate, Winter, Night	38
3.6	Iron Reaction Rate, Winter, Day	39
3.7	Iron Reaction Rate, Summer, Day	40
3.8	Iron Reaction Rate, Winter, Night, 75-85 km	41
3.9	Schematic of the Sodium Chemistry Reactions.	45
3.10	Sodium Chemistry Reactants, Winter, Night, 67° N	46
3.11	Sodium Chemistry Steady-State Profiles	47
3.12	Sodium Profile Comparison with Data	49
3.13	Sodium Reaction Rate, Winter, Night	51
3.14	Sodium Reaction Rate, Summer, Day	52
3.15	Sodium Reaction Rate, Winter, Night, 75-90 km	53
3.16	Auroral Electron Density Example	55
3.17	Iron Reaction Rate, Auroral Effect on Recently Deposited Fe	58

3.18	Example of Auroral Ionization of Meteoric Material?	60
3.19	Iron Reaction Rate, Auroral Effect on Background Fe Profile	62
3.20	Sodium Reaction Rate, NO ⁺ Auroral Effect on Recently Deposited Na	63
3.21	Sodium Reaction Rate, O ₂ ⁺ Auroral Effect on Recently Deposited Na	64
3.22	Sodium Charge Exchange Time Constant versus O ₂ ⁺ Fractional Concentration	66
3.23	Sodium Reaction Rate, NO ⁺ Auroral Effect on Background Na Profile	67
3.24	Sodium Reaction Rate, O ₂ ⁺ Auroral Effect on Background Na Profile	68
3.25	Schematic of a Subset of the Sodium Chemistry Reactions from <i>Cox and Plane</i> (1998).	69
4.1	Diffusion Perpendicular to B	78
4.2	Electric-Field Driven Formation of Sporadic- <i>E</i> Layers	82
4.3	Electric Field Estimates from the Sondrestrom ISR on 30 July 1998	86
4.4	Neutral Wind Estimates from the Sondrestrom ISR on 30 July 1998	87
4.5	Model of Sporadic- <i>E</i> Dynamics on 30 July 1998	88
4.6	Model of Sporadic Sodium Layer Formation	91
5.1	ISR and Lidar Measurements, 11 December 1997	94
5.2	ISR and Lidar Measurements, 0:00 to 3:30 UT, 11 December 1997	96
5.3	All-sky Images at 427.8 nm, 1:20 to 1:58 UT, 11 December 1997	97
5.4	All-sky Images at 427.8 nm, 2:00 to 2:37 UT, 11 December 1997	98
5.5	All-sky Images at 427.8 nm, 2:39 to 3:16 UT, 11 December 1997	99
5.6	Model Auroral Electron Density Profiles	101
5.7	Model of 11 December 1997 Measurements	102
5.8	Model of 11 December 1997 Measurements, No Eddy Diffusion	104
5.9	Sodium Column Contents, 11 December 1997, Measurements and Model	105
5.10	High Altitude Sporadic Sodium Layer, 6 February 1998	106
A.1	Diffusion Scale Heights	113
A.2	Molecular Diffusion Coefficients	114
A.3	TMA Measurement of Winds and Diffusion	118

B.1	Incoherent Scatter Spectra	128
B.2	Incoherent Scatter Autocorrelation Functions	129
B.3	Range-Time Diagrams for Incoherent Scatter	136
B.4	Incoherent Scatter Autocorrelation Function Contours	139
B.5	Sondrestrom Radar Data Example	141
C.1	Sodium D_2 Line Shape	148
C.2	Sodium D_2 Line Effective Cross-section	149
C.3	Lidar Data Example	152
D.1	Gyro and Collision Frequencies	164
E.1	Schematic of the Example Iron Chemistry Reactions.	167
E.2	Lax-Wendroff	170
E.3	Modified Lax-Wendroff	172

Chapter 1

Introduction

...and thus ever, behind the coarse effect, is a fine cause, which, being narrowly seen, is itself the effect of a finer cause.

Ralph Waldo Emerson

Seven decades ago observations were reported by *Slipher*(1929) of strong emissions near the 589 nm sodium lines in Earth's night sky. *Slipher*(1929) did not comment specifically on the cause of these emissions and it was almost a decade later that *Bernard*(1938) correctly identified the airglow line as being due to a layer of neutral sodium atoms high in the atmosphere. Over the years, steady progress was made toward understanding the characteristics of these layers with the help of sounding rocket campaigns and new ground-based measurement techniques such as resonance lidar. Nonetheless, the relative inaccessibility of the region hindered the development of a comprehensive understanding of the chemical and physical interactions of this sodium layer with the upper atmosphere. Even the question of the source of the sodium led to considerable lively debate, with one camp claiming that sodium transported upward from sea salt is the most likely source [e.g. *Franck and Rieke*(1939), *Bernard*(1939)] while the other explained it as coming from outside the atmosphere via meteoroid ablation [e.g. *Cabannes et al.*(1938), *Gadsden*(1968)]. The consensus has settled quite firmly on a meteoric origin for the material, but it is only in the last few years that steady-state chemical models have been developed which can explain many of the measured characteristics of the metal layers in Earth's upper atmosphere [e.g. *Plane*

et al.(1998), *Helmer et al.*(1998), *McNeil et al.*(1996), *Plane and Helmer*(1995)]. The next obvious step, and one being pursued now by a number of groups, is the extension of these models toward making predictions of the temporal variations of the metallic layers.

The practical applications of the sodium layer include the generation of artificial guide stars to compensate telescope optics for the effects of atmospheric turbulence [e.g. *Foy and Labeyrie*(1985), *Fugate et al.*(1991)]. Perhaps more importantly, however, the presence of a sodium layer makes possible the routine monitoring of physical characteristics of this largely inaccessible atmospheric region. The altitudes at which significant concentrations of metal atoms reside also happen to be near the interface between the turbulent homosphere and the chemically stratified heterosphere. This region also often encompasses the mesopause, the coldest region in Earth's atmosphere. Regular monitoring of these interface altitudes thus has important implications in terms of estimating the transport of energy and material and assessing the state of each region.

The aforementioned lidar techniques make it possible to more or less continuously measure altitude profiles of neutral metal atom layers. These measurements allow both the probing of the layers themselves and the measurement of the dynamics of the atmosphere in which the metal atoms are entrained. To be an effective tracer of neutral constituent dynamics, it is critical that the chemistry of the metals be well understood in a time-varying sense because that chemistry may be a source of variability in the observed metal atom concentrations. At high latitudes the metal atom layers share their atmospheric region with a highly dynamic phenomenon: the aurora borealis. Proper interpretation of lidar measurements thus requires a good understanding of the influences of aurorae on the metallic layers. The work presented in this thesis has two overall goals. Firstly, we develop numerical models of the chemistry and physics of sodium and of iron to make specific predictions about the expected interaction of aurorae with these metals, and apply these predictions to interpret high latitude measurements. The second goal entails the validation of the models via a case study of measurements of select characteristics.

1.1 Thesis Organization

This thesis is organized into several related topical areas. Chapter 2 begins by describing the process of meteor ablation that deposits metal atoms in the upper atmosphere. We then discuss the composition of the meteoroids (which determines what is deposited) and describe the diffusive mixing which leads to an altitude profile of the meteoric material. This altitude profile, which represents a long time-integration of the deposition, is needed as a seed for the chemical processes for both iron and sodium discussed in Chapter 3. Chapter 3 includes a description of the models used in this thesis, which are based on the chemical reactions recently reported in the literature, and describes the manner in which the models can explain measurements of the layering of sodium. Chapter 3 also includes predictions of the influence that auroral ionization can have on the state of sodium and iron, in a time-resolved sense. A mechanism other than chemistry that also leads to the layering of metallic atoms in the upper atmosphere is discussed in Chapter 4. This electric-field driven mechanism has been well established by other researchers, but its importance in terms of the layering of neutral atoms is presently an active area of research. Chapter 5 includes a case study of a set of measurements made at the high latitude upper atmospheric research station in Sondrestrom, Greenland [*Kelly(1983)*, *Kelly et al.(1995)*]. An understanding of these measurements requires proper incorporation of the effects discussed in Chapters 3 and 4. Chapter 6 concludes this thesis with a summary of the important results and scientific contributions.

1.2 Thesis Contributions

The major contributions of this thesis are as follows.

1. The influences of auroral ionization on the gas-phase chemistries of iron and sodium in the upper atmosphere are assessed in a time-resolved sense via the use of numerical models of the pertinent reactions. Auroral ionization is found to have a significant influence on the chemistries of recently deposited iron and sodium and on the chemistry of the background sodium layer, but generally not

on the chemistry of the background iron layer.

2. Experimental evidence is presented of the formation of a sporadic ion layer by the combined effects of Lorentz forcing and ion-neutral collisions. The experimental results are compared with a dynamical model of the process, including the influences of electric fields, diffusion, and the bulk motion of the neutral atmosphere.
3. Models are developed and described which couple the chemistries of iron and sodium with dynamical variations due to diffusion, magnetospheric electric fields, and auroral ionization. The resulting sodium model is shown to provide a mechanism by which altitudinally thin neutral sodium layers can be formed, in accordance with previously published results.
4. Measurements are presented which show the combined effects of ion layer formation and transport, neutral sodium layer formation and diffusion, and the chemical influence of auroral ionization on sodium chemistry. These measurements are shown to be consistent with the models of the relevant physical and chemical processes.

Chapter 2

Meteoric Material

METEOR...
 METEOr...
 METEOr...
 METeor...
 MEteor...
 Meteor...
 meteor...
 meteorite

Edward Bryant

Virtually everyone who has spent time gazing into the night sky has been treated to the spectacle of a shooting star. Strangely, most people know very little about these startling phenomena, though this situation has changed somewhat in recent years due to the Hollywood spectacles of ‘killer’ meteors. Partly because of this, most people would doubtless be surprised to learn that the typical visible meteor is caused by a pea-sized grain with a mass of only a tenth of a gram [*Bone(1993)*]. A 0.1-g meteoroid results in a 6th visual magnitude meteor [*Vedder(1961)*] and the streak of light lasts only about a second. For historical reasons, the term *meteor* actually refers to the phenomenon that causes the streak of light and not to the incoming rock. Prior to impacting Earth’s atmosphere, the rock grains are termed *meteoroids* and the meteoroids that survive their interaction with the atmosphere and reach the ground are called *meteorites*.

We begin this chapter by describing the process by which meteoric material is deposited in the upper atmosphere. This process describes the heating of the incoming object and its subsequent loss of mass to the atmospheric gas (the mass loss is termed *ablation*). Next, the composition of the meteoroids and the state of the ablated material are discussed in terms of several sets of measurements presented in the literature. The influence of diffusion on the meteor trails is then considered and this diffusion is used to make estimates of the steady-state profiles of meteoric metals in the atmosphere. These profiles are precisely what is needed for various aspects of the chemistry discussion in Chapter 3.

2.1 Deposition

Even a simplified physical theory of the meteor phenomenon is more complex than it might be thought to be at first glance. This complexity is largely due to the fact that the ablation process changes the mass, and possibly the shape, of the infalling meteoroid as it decelerates in Earth's atmosphere. Chapter 1 of *Bronshten(1983)* presents a theory for meteors with a large number of simplifying approximations and parameterized effects. That theory, largely based on information found in *Öptik(1958)*, nonetheless does a satisfactory job of explaining many aspects of meteor measurements. While not central to the work in this thesis, it is instructive to consider here the salient points of the *Bronshten(1983)* theory. The first fundamental relation of the theory gives the deceleration of the meteoroid body as being due simply to atmospheric drag, given by

$$M \frac{dv}{dt} = -\Gamma S \rho(z) v^2 \quad (2.1)$$

where M is the meteoroid mass, v is its velocity, Γ is the drag coefficient, S is the cross-sectional area of the meteoroid, and $\rho(z)$ is the density of the air at altitude z . Neither Γ nor S can be easily quantified with any accuracy even for a 'typical' meteoroid. In fact, both parameters can realistically be expected to change during the ablation process. For the simple theory considered here, however, the meteoroid is assumed to be self-similar during ablation and, as a result, Γ is assumed constant (though this is a

questionable assumption even with self-similarity). The second fundamental equation of the theory asserts that a certain portion of the kinetic energy of the meteoroid is expended during the ablation of meteoroid material, as described by

$$\frac{dM}{dt} = -\Lambda \frac{S\rho v^3}{2Q} \quad (2.2)$$

where Λ is the heat-transfer coefficient (≤ 1) and Q is the latent heat of vaporization of the meteoroid material, including the energy required to bring the temperature of the meteoroid to its evaporation temperature. Combining equations (2.1) and (2.2), the following equation can be derived:

$$\frac{dM}{M} = \frac{\Lambda}{2Q\Gamma} v dv = \sigma v dv \quad (2.3)$$

where we once again invoke self-similarity and assume that σ is constant. Equation (2.3) has a simple solution:

$$M = M_0 \exp \left[\frac{\sigma}{2} (v^2 - v_0^2) \right]. \quad (2.4)$$

We then make the assumption that the meteoroid has a more or less uniform density, leading to a relation between its cross-section S and mass M :

$$\frac{S}{S_0} = \left(\frac{M}{M_0} \right)^\mu. \quad (2.5)$$

If the meteoroid remains self-similar, the shape variation parameter, μ , is $2/3$. In any event, equations (2.4) and (2.5) can be used with (2.1) to yield the following:

$$\exp \left[\frac{1-\mu}{2} \sigma (v^2 - v_0^2) \right] \frac{dv}{v} = -\frac{\Gamma S_0}{M_0} \rho(z) v dt. \quad (2.6)$$

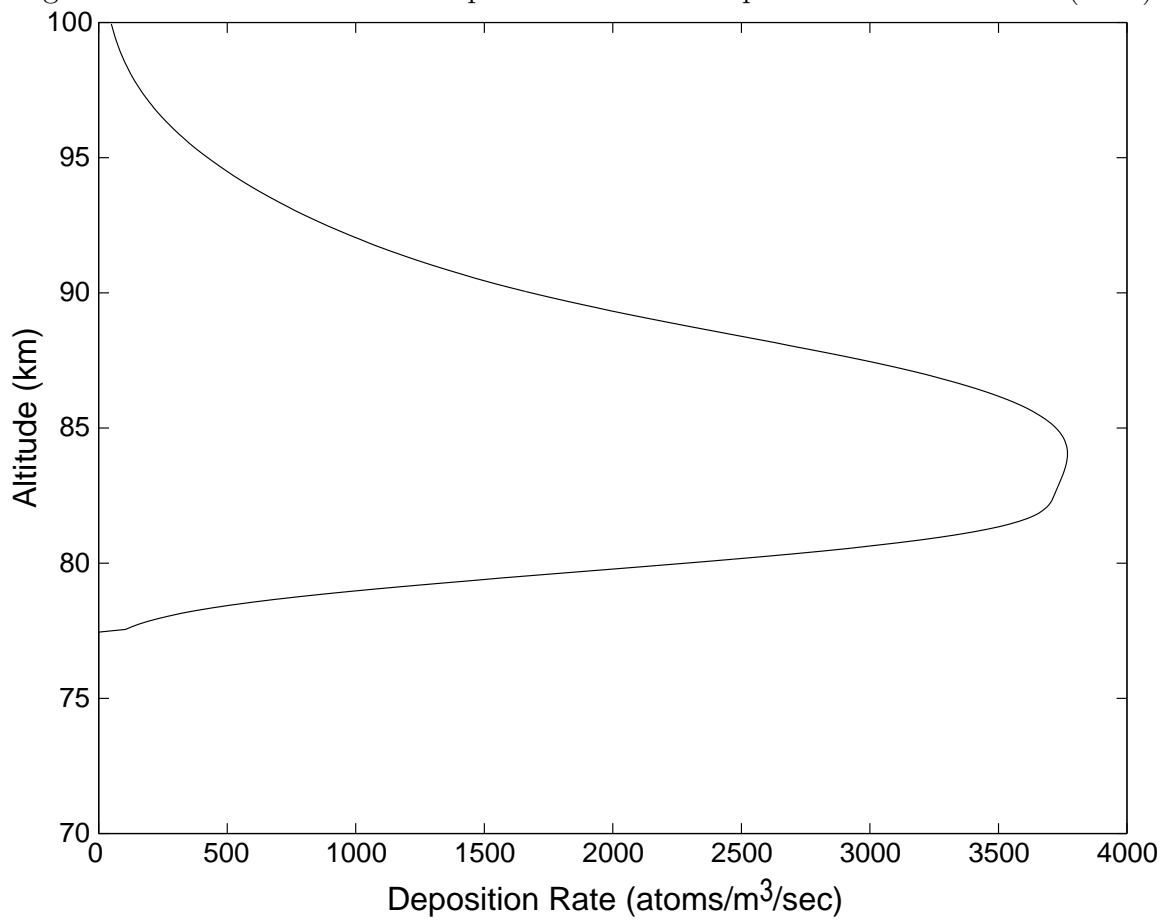
The further assumptions of a linear path for the meteoroid (which is not a bad assumption for the velocities involved) and a horizontally stratified ionosphere yields equation (2.7), which is equation (3.14) of *Bronshten*(1983), except that Bronshten's

equation contains a pair of typographical errors (M and S instead of M_0 and S_0):

$$\exp\left[\frac{1-\mu}{2}\sigma(v^2-v_0^2)\right]\frac{dv}{v} = -\frac{\Gamma S_0}{M_0}\sec(\chi)\rho(z)dz \quad (2.7)$$

where χ is the zenith angle of the incoming meteoroid's path. Unfortunately, equation (2.7) does not have a simple solution. The left hand side can be integrated in terms of the exponential integral, Ei , but this integral must be evaluated numerically [Abramowitz and Stegun(1965)]. Similarly, the right side can be integrated analytically if a functional form for the atmospheric density is known. In any event, equation (2.7) yields a relationship between the meteoroid's velocity and its altitude. When combined with equation (2.2) it thus describes the altitude range over which the material is deposited during ablation. A slightly more sophisticated approach was used by *Hunten et al.*(1980) to describe an altitude profile for the deposited meteoric material. In their analysis, they assumed a distribution of meteoroid sizes and velocities to calculate the ablation rate as a function of altitude. The basic calculations were derived from the work by *Gadsden*(1968). Figure 2.1 shows the *Hunten et al.*(1980) profile scaled for a total altitude-integrated deposition rate of 4×10^7 atoms/m²/s.

The ablation profile derived by *Hunten et al.*(1980) describes how meteoric material is deposited with altitude. There still remains, however, the question of how much total material is deposited into the upper atmosphere. *Hunten et al.*(1980) used a value given by *Hughes*(1975), based primarily on visual observations of meteor flux combined with satellite measurements of micrometeoroid impacts. *Hughes*(1975) also attempted to utilize meteor radar measurements of fluxes but found that those estimates conflicted significantly with the trends of the other measurements. The explanation for this discrepancy is that meteor radars are only sensitive to the ionization produced by the meteoroids and, as such, there is a significant bias (underestimation) in those measurements. In any event, *Hughes*(1975) estimated that the total influx of material to Earth's upper atmosphere is on the order of 44 tons/day! Though this quantity appears to be an enormous amount of material, it must be kept in mind that the material is distributed over the entire upper atmosphere of the Earth and, as such, the local deposition rate is much more reasonable. *Hughes*(1975) also estimated a size

Figure 2.1: Meteoric Material Deposition Profile Adapted from *Hunten et al.*(1980)

(mass) distribution for the meteoric material, which peaks at masses of 10^{-5} grams per meteoroid — quite a small value. From *Vedder(1961)*, this value corresponds to a visual magnitude of 16 which is far from being visible with the unaided eye [*Muirden(1983)*]. Other techniques have also been used to estimate the total material influx from meteoroids. For example, measurements of the accumulation of iridium in sedimentary rocks, combined with estimates of the fractional composition of iridium in meteoroids, allowed *Wasson and Kyte(1987)* to estimate that the total flux could be over 200 tons/day. More direct estimates have also been made from measurements at satellite altitudes with the Long Duration Exposure Facility (LDEF). With LDEF, impact craters were collected on the 5.6 m^2 of thermal control panel surfaces over the course of a 5.77 year exposure at altitudes ranging from 331 to 480 km. An analysis of the crater sizes and numbers by *Love and Brownlee(1993)* suggested a cumulative flux value of approximately 110 tons/day. *Love and Brownlee(1993)* also showed a strong peak in the mass distribution of micrometeors around 1.5×10^{-5} grams, which corresponds to a meteoroid diameter of $220 \mu\text{m}$.

So far, the estimates discussed have been of average daily material influxes over the course of the year. Another related question is the relative impact of meteor showers compared to the more steady influx from sporadic meteoroids. It turns out that, while much more impressive visually, meteor showers do not account for nearly as much material as the sporadic flux. Estimates of material deposition by meteor showers are in the range of several tons per day. *Rosinski and Snow(1961)* reported 6.6 tons/day for 2 days of Quadrantids and 4.8 tons/day for 6 days of Geminids (*Hughes(1978)* gave somewhat lower numbers), but they also estimated the influx for sporadic meteors at less than one ton/day. Even if this ratio is maintained, this relatively modest value for the amount of additional material deposited by meteor showers can perhaps help explain why showers do not have a larger impact on the total amount of metal in the upper atmosphere. In particular, it helps explain the lack of correlation between showers and sporadic-*E* events, as reported by *Whitehead(1989)*. A recent report by *Grebowsky et al.(1998)* argues that there is some correlation with measurements from sounding rocket campaigns, but the effect is far from overwhelming.

Table 2.1: CI Carbonaceous Chondrite Elemental Abundances

Element	Symbol	Weight (%)	Number (mol/g)
Oxygen	O	44.80	0.028000
Iron	Fe	18.20	0.003260
Silicon	Si	10.30	0.003670
Magnesium	Mg	9.26	0.003810
Sulfur	S	5.50	0.001720
Carbon	C	3.40	0.002830
Nickel	Ni	1.08	0.000184
Calcium	Ca	0.95	0.000237
Aluminum	Al	0.86	0.000319
Sodium	Na	0.50	0.000217

2.2 Composition and Material State

The most common types of meteoroids in space are thought to be the carbonaceous chondrites [*Baldwin and Sheaffer(1971)*]. These meteoroids have elemental compositions that most closely resemble that of the sun and they show practically no thermal metamorphism [*Norton(1998)*]. Due to their internal structure, which usually consists of mm-size spherical chondrules embedded in a fine grained matrix, these chondrites are prone to break-up in the atmosphere and, as a result, they are less likely than other types of meteoroids to survive ablation and reach the ground as meteorites, which explains why of the ~ 2750 known meteorites only 60 are carbonaceous chondrites. The elemental composition of the volatile-rich type I carbonaceous chondrites (also known as CI chondrites) have been extensively studied and reported by a number of authors [*Mason(1971)*, *Wasson and Kallemeyn(1988)*, *Heide and Wlotzka(1995)*]. Table 2.1 summarizes the measurements reported in *Heide and Wlotzka(1995)* for the 10 most abundant elements by weight. As that table shows, the bulk of the metallic portion of the material consists of iron and magnesium. While sodium only makes up 0.5% of the meteoroids by weight, it is an important tracer for ablated meteoric material because of its large resonant cross-section at wavelengths near 589 nm (see Appendix C), which makes atomic sodium relatively easy to monitor from the ground.

Strangely enough, simultaneous measurements of neutral atmospheric sodium and

iron do not reflect this expected abundance ratio. From resonant lidar measurements, *Kane and Gardner*(1993b) reported column integrated *neutral* iron-to-sodium abundance ratios of approximately 2.5 to 1 and not the 15 to 1 ratio from Table 2.1 — a factor of 6 difference. Though the lidar technique is only sensitive to neutral atomic sodium and iron and not to compounds of those metals, chemistry alone cannot explain this large difference in the ratios. Part of the explanation comes from the fact that meteoroids do not fully ablate. *Hunten et al.*(1980) suggested that only 2/3 of the meteoric material enters the gas phase, leaving the remaining 1/3 as residual dust. Data from a more recent theoretical analysis by *Love and Brownlee*(1991) can be used (with a little effort) to predict that 73% of the material enters the vapor stage, primarily between 85 and 90 km altitude. However, the material originally in the meteoroids does not boil off evenly. Due to thermodynamic considerations, sodium ablates well before iron, magnesium, or silicon [*Fegley and Cameron*(1987)]. This fractionation mechanism was also used by *Kopp*(1997) to explain the number density ratio measurements from five sounding rocket flights instrumented with mass spectrometers. On the other hand, *Kopp*(1997) also showed that the average (over all the flights) ratio of iron to sodium *ions* followed very closely that of CI chondrites. It would appear, therefore, that several questions remain as to the proper explanation of the material ratios. Perhaps some as yet uncovered mechanisms act to preferentially remove additional material from the gas phase. *Rosinski and Snow*(1961) and *Hunten et al.*(1980), for example, calculated the rate of re-coagulation of material to form additional atmospheric dust particles. Evidence that this coagulation may occur was presented by *Kelley et al.*(1998). The extent to which material is lost from the gas phase due to this process is as yet unclear. What is known, however, is that some portion of the material does remain gaseous and thus detectable by a number of different ground- and rocket-based measurement techniques.

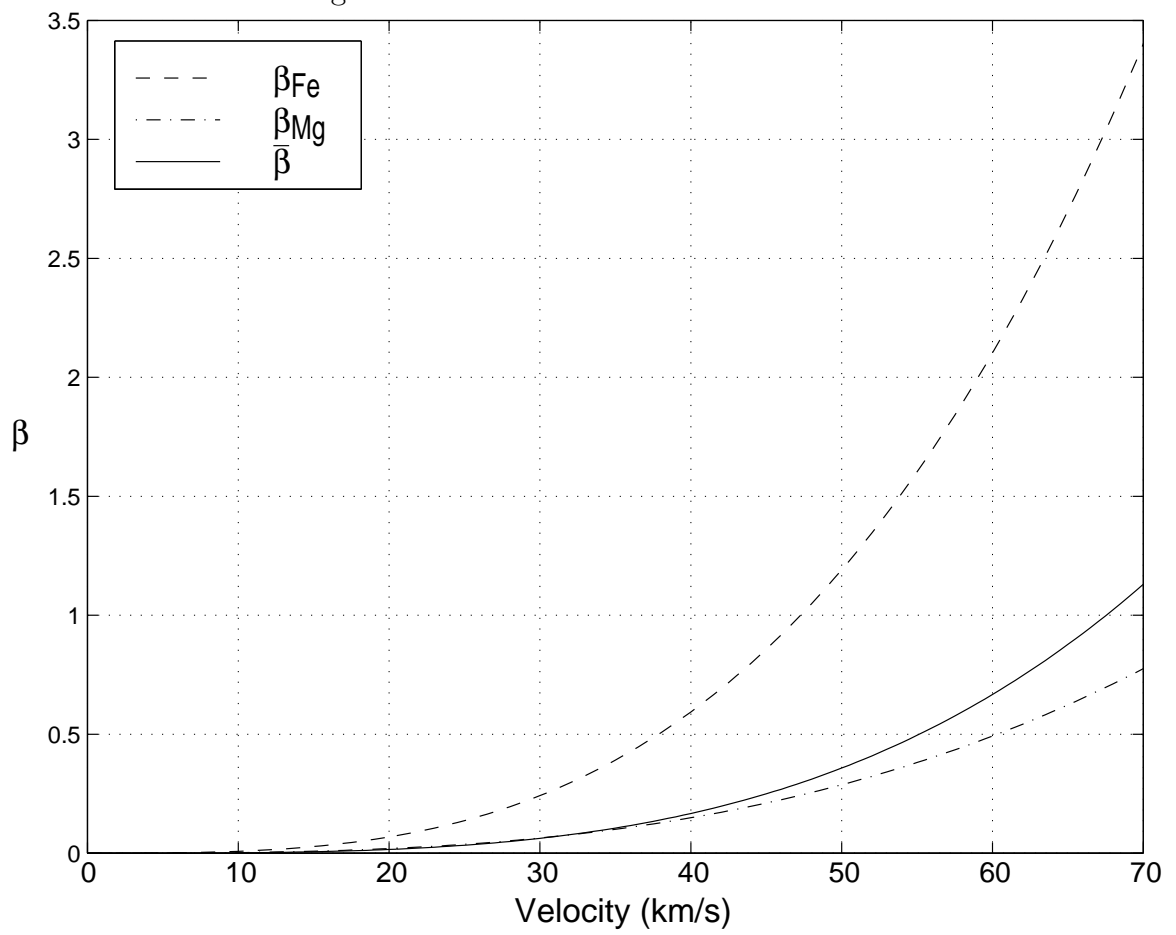
As has just been suggested, an important question to be answered concerns the ionized state of the recently ablated material. Using a laser radar (lidar) system tuned to measure neutral atomic sodium (see Appendix C for a description of the technique), *Kane and Gardner*(1993a) presented evidence of the deposition of thin trails of neutral sodium atoms into the upper atmosphere by meteor ablation. This

Table 2.2: Meteor Ionization Coefficients. Velocity, v , is in m/s.

Element	Coefficient
Fe	$\beta_{\text{Fe}} = 2.60 \times 10^{-15} v^{3.12}$
Mg	$\beta_{\text{Mg}} = 3.95 \times 10^{-15} v^{2.95}$
	$\bar{\beta} = 3.04 \times 10^{-17} v^{3.42}$

result indicates that at least a portion of the material ends up in a neutral state, but it reveals nothing about the fraction of the material that starts there. Laboratory measurements made by *Slattery and Frichtenicht*(1967) addressed this question for iron, quantifying the number of ion/electron pairs created for each iron atom as a function of the initial meteoroid velocity. In *Bronshten*(1983) and elsewhere this parameter is called β , though it is sometimes wrongly interpreted as an ionization *probability*, an incorrect terminology because β can be larger than 1 if multiple air molecules are also ionized. Chapter 5 of *Bronshten*(1983) summarized the results from a number of such experiments for the elements O, Fe, Mg, Ca, and Si. He also presented a composite parameterization which he labeled $\bar{\beta}$. Table 2.2 summarizes the relations for Fe, Mg, and the composite coefficient. The three functions in Table 2.2 are plotted in Figure 2.2 for the whole range of typical meteoroid velocities, showing that for the majority of meteoroids, which have velocities on the order of 15 km/s [*Hunten et al.*(1980), *Erickson*(1968)], only a very small number of the ablating atoms result in an electron/ion pair being produced. On the other hand, for high velocity meteoroids like those found in the Leonids meteor shower with velocities around 60 to 70 km/s, on average nearly every atom produces at least one free electron and, in fact, the iron atoms each produce several. In addition to describing the initial state of the ablated material, β is also relevant to meteor radar applications. An important parameter for describing the scattering of radio waves from meteor ionization trails is the electron line density, q , which is the number of electron/ion pairs formed per meter of trail length. The relationship between q and β as presented by *Bronshten*(1983)

Figure 2.2: Meteor Ionization Coefficients



(and also *McKinley*(1961)) is given in the following equation:

$$q = -\frac{\beta}{m_a v} \left(\frac{dM}{dt} \right) \quad (2.8)$$

where the parameter m_a is the average mass of a meteor atom and M is the meteoroid mass.

As was mentioned earlier, measurements of the *neutral* concentrations of iron and sodium do not correspond well to the expected relative abundances while the *ionized* concentrations do. One possible approach to explaining the difference between these ratios is the existence of different populations of meteoroids. *McNeil et al.*(1998) used differential ablation to explain the ratio of sodium to calcium in the upper atmosphere. Using CI chondrite composition they showed that low velocity meteoroids (12 km/s) deposit the bulk of their sodium near 89 km, an altitude at which neutral atomic sodium is a chemically stable state, while calcium is deposited near 76 km and thus is quickly tied up in molecular sink compounds. In addition, while essentially all of the sodium is deposited, almost 1/3 of the calcium remains in a solid state (constituting the remaining dust). With proper adjustment of the particle sizes and velocities, *McNeil et al.*(1998) were able to reproduce the measured abundance ratios for the neutral species. They found the best agreement at a velocity of only 11 km/s (somewhat smaller than usually reported), leaving the abundances of the atomic ions to be accounted for. *McNeil et al.*(1998) postulated a high velocity component to the sporadic flux consisting of meteoroids which deposit their material in an ionized state and at higher altitudes. The deposition altitude is high enough that the steady-state chemical equilibrium condition is singly ionized atoms. One possible problem with the *McNeil et al.*(1998) approach is that it appears to be quite sensitive to the assumed distributions. Though actual measurements do show a good deal of variability, it remains to be seen whether this mechanism is robust enough to explain future measurements on its own or if recoagulation also plays an important role.

2.3 Diffusive Mixing

Immediately after ablation the meteoric material begins to diffuse. The diffusion processes are in fact quite complex because, at these altitudes, they involve mixing due to turbulent eddies in the background atmosphere as well as simpler molecular diffusion due to thermally-induced Brownian motion. A more involved discussion of diffusion is presented in Appendix A, but for the work presented here a simple Fick's law approach is used. First consider a single, vertically oriented cylinder of meteoric material in the gas state. Ignoring the effects of chemistry and recoagulation, the continuity equation for that material is

$$\frac{dn}{dt} = -\nabla \cdot (n\vec{v}) = -\frac{1}{r} \frac{\partial}{\partial r} (rnv_r) \quad (2.9)$$

where n is the material concentration, \vec{v} is the vector velocity, r is the radial distance from the center of the cylinder, and v_r is the radial component of \vec{v} . For approximately the first half minute, the mixing is dominated by molecular diffusion [e.g. *Blamont(1963)*, *Rees et al.(1972)*]. The horizontal diffusive flux during this time is given simply by the following equation (for the radial component) [*Banks and Kockarts(1973b)*]:

$$nv_r = -D \left(\frac{\partial n}{\partial r} \right) \quad (2.10)$$

where D is the molecular diffusion coefficient with units m^2/s . Combining equations (2.9) and (2.10) yields

$$\frac{\partial n}{\partial t} = D \frac{1}{r} \left(-\frac{1}{r^2} \frac{\partial n}{\partial r} + r \frac{\partial^2 n}{\partial r^2} \right). \quad (2.11)$$

For times longer than one minute, the diffusion can be dominated by turbulent eddy motion (if those eddies are present). In this case, the molecular diffusion coefficient, D , in equations (2.10) and (2.11) can simply be replaced by the sum of the eddy and molecular diffusion coefficients, $K + D$. A number of assumptions go into this approximation, of course, such as eddies which are isotropic and purely horizontal diffusion, but this approach is clearly a reasonable one at least for discussing vertical trails. The solution to equation (2.11) is given by the following for an initially

Gaussian density distribution [McKinley(1961)]:

$$n(r, t) = \frac{q}{\pi (4(K + D)t + r_0^2)} \exp \left[-\frac{r^2}{4(K + D)t + r_0^2} \right] \quad (2.12)$$

where q is the initial total number of molecules at the altitude of interest and r_0 is the initial trail radius. From Appendix A, the numerical value of K is on average of the order of 100–200 m²/s in the meteor ablation region. On the other hand, it is also highly variable both spatially and temporally and it may sometimes be an order of magnitude larger than the average value. Using 100 m²/s, the trail is on the order of a kilometer in diameter after two minutes. Combining this value with estimates of meteoroid fluxes, it can be shown that meteor trails begin to overlap, on average, after just a few minutes.

Possibly because only the most intense meteors are visible as shooting stars, the influx of meteoric material is often thought of as discrete events. Strictly speaking this is true, but as the previous paragraph indicates it is also possible to consider a constant flux of material, horizontally homogeneous (fully diffused/mixed) but with vertical variations. For this thesis we assume that the vertical profile of meteoric flux has the shape given by *Hunten et al.*(1980) and shown in Figure 2.1, while the total flux for any given constituent is scaled to yield column contents predicted by measurements. The metal-specific profiles that result from a differential ablation model like that of *McNeil et al.*(1998) are not considered. This approximation does not have a significant impact on the final results because the intent here is simply to generate a realistic profile (one which matches measurements). This basic approach follows that presented in *Helmer et al.*(1998) and *Plane et al.*(1999). The material deposition profile of *Hunten et al.*(1980) is assumed to be balanced by eventual downward motion of all the material. This assumption boils down to the recognition that the meteoroid material loses most of its kinetic energy during the ablation process and, as a result, it cannot escape Earth's gravity. The assumption can be written mathematically as follows:

$$\Phi(z) = \int_z^\infty \phi(z') dz' = -nv_z \quad (2.13)$$

where the symbol $\phi(z)$ is the deposition rate at altitude z and $\Phi(z)$ is the height-integrated deposition rate above altitude z . From *Banks and Kockarts(1973b)* and assuming that the material motion is driven solely by diffusion, the vertical velocity is given by the following:

$$v_z = -K \left[\frac{1}{n} \frac{\partial n}{\partial z} - \frac{1}{n_n} \frac{\partial n_n}{\partial z} \right] - D \left[\frac{1}{n} \frac{\partial n}{\partial z} + (1 + \alpha_T) \frac{1}{T} \frac{\partial T}{\partial z} + \frac{mg}{k_B T} \right] \quad (2.14)$$

where α_T is the thermal diffusion factor (which is assumed to be small), n_n is the background neutral number density, m is the mass of a molecule of the deposited species, g is gravitational acceleration, and k_B is Boltzmann's constant. Using the assumption of hydrostatic equilibrium, the following relation can be used:

$$\frac{mg}{k_B T} = -\frac{1}{n} \frac{\partial n}{\partial z} - \frac{1}{T} \frac{\partial T}{\partial z}. \quad (2.15)$$

Combining equations (2.14) and (2.15), and with the assumption that α_T can be neglected, yields the following approximate relation:

$$v_z \simeq -(K + D) \left(\frac{1}{n} \frac{\partial n}{\partial z} - \frac{1}{n_n} \frac{\partial n_n}{\partial z} \right) - D \frac{(m - m_n) g}{k_B T} \quad (2.16)$$

where m_n is the mean mass of the neutral atmosphere. Equations (2.13) and (2.16) can be combined to yield the following ordinary differential equation:

$$\frac{\partial n}{\partial z} = \left[\frac{1}{n_n} \frac{\partial n_n}{\partial z} - \frac{D}{K + D} \frac{(m - m_n) g}{k_B T} \right] n + \left(\frac{\Phi}{K + D} \right). \quad (2.17)$$

A final further simplifying approximation can be made by comparing the sizes of the first two terms of equation (2.17). For altitudes at least up through 130 km, the first term dominates and the following ODE results. (It should be noted that equation (2.18) is equivalent to the equation solved by *Helmer et al.(1998)* and *Plane et al.(1999)*.)

$$\frac{\partial n}{\partial z} = \left(\frac{1}{n_n} \frac{\partial n_n}{\partial z} \right) n + \left(\frac{\Phi}{K + D} \right) \quad (2.18)$$

The coefficients of this ODE are functions of altitude, z , but equation (2.18) can

nonetheless be readily solved with ‘canned’ numerical techniques. One important missing item, however, is a boundary condition. We follow the lead of *Helmer et al.*(1998) and choose the boundary condition on a case-by-case basis to match measurements. The total material flux for the metallic constituent of interest is also specified to properly scale the integrated flux, $\Phi(z)$.

2.4 Altitude Profiles

The solutions to equation (2.18) give steady-state altitude profiles of metallic atom number densities. It is interesting to look at those solutions for various conditions and to consider the implications of the sensitivity of the resulting profiles to input parameters. First, however, it is worth reiterating some of the assumptions that go along with equation (2.18). It was mentioned earlier rather briefly that the constituent motion is assumed to be due solely to diffusion. This assumption specifically ignores any vertical motion of the background atmosphere driven, for example, by atmospheric gravity waves [*Hines*(1974), *Beer*(1974)]. The background motion can, of course, be accounted for via a simple superposition of an additional velocity component. More troublesome, however, is the neglected Lorentz force term for the ionized portion of the metallic material. As a first approximation, equation (2.18) can be used but under a number of conditions the Lorentz term dominates. In this case, it is often easier to resort to dynamic descriptions, as discussed in Chapter 4. In cases where the electric fields and wind shears are small, however, equation (2.18) does a satisfactory job of describing the relevant physics [*Helmer et al.*(1998)]. Another assumption implicit in the application of this ODE is that all species of interest are in a gas phase. For the solid phase or coagulated fraction of the meteoric material, the dynamics can not be simply described by the diffusion equation (2.16) because gravitational and viscous effects become important. Additionally, the recoagulation of material violates a continuity equation where the ‘tracked particles’ combine to form fewer total numbers. For the purposes of this section, the number densities are assumed to be gas-phase material densities that remain in that phase. Furthermore, each chemical compound containing, for example, iron is assumed to have only a single iron atom

and the iron-containing molecules or atoms are tracked without regard to their specific chemical composition. This approach is the same one used by *Thomas(1974)* in his mathematical description of *total mixing ratios*.

We first consider the altitude profile of iron. To do this, a choice must be made concerning the assumed rate of influx of meteoric material. Through comparisons with published measurements [*Alpers et al.(1990)*] we can estimate that a reasonable starting point for iron is $\sim 10^8$ atoms/m²/s, corresponding to just less than 500 kg of iron per day over the surface of the earth. If all of the meteoroid material were to end up in the gas phase, the fractional abundance of iron from Table 2.1 would put the the total material influx at only about 2.5 tons per day instead of the approximately 100 tons per day discussed earlier. Such estimates lend support to the premise that only a fraction of the material does end up as a gas (or at least that only a fraction stays in that state for an extended length of time). A similar conclusion was drawn by *Helmer et al.(1998)* from midlatitude measurements. In any event, the rate of $\sim 10^8$ atoms/m²/s is used to scale the *Hunten et al.(1980)* deposition profile shown earlier in Figure 2.1. The eddy and molecular diffusion profiles from *Danilov and Kalgin(1992)* for a high latitude location (80° N), as shown in Figure 2.3, are also needed to solve equation (2.18). We see from Figure 2.3 that for the altitudes of primary interest (80 to 110 km) the dominant diffusion mechanism is expected to be eddy diffusion during the winter and that the lower portion (up to 100 km altitude) is eddy-diffusion dominated during the summer. Another necessary profile of parameters is the neutral number density of the background atmosphere. For this purpose we use the MSISE-90 model [*Hedin(1991)*] for the location of the Sondrestrom Radar [*Kelly(1983)*, *Kelly et al.(1995)*] and nominal solar conditions. The final parameter needed is the boundary condition which is to be adjusted to yield the proper (measurement-matching) material profile. For this work the choice was made to specify the total iron density at 70 km altitude as that boundary. To assess the sensitivity of the results to the choice of this parameter, equation (2.18) was first solved for a 70 km density of only 1 atom/m³, corresponding to a near perfect sink for the gas-phase material, perhaps via recoagulation or polymerization [*Plane et al.(1999)*]. The results of that calculation are shown in Figure 2.4, which also shows the corresponding average time for an atom

Figure 2.3: Eddy and Molecular Diffusion Coefficients from *Danilov and Kalgin(1992)*.

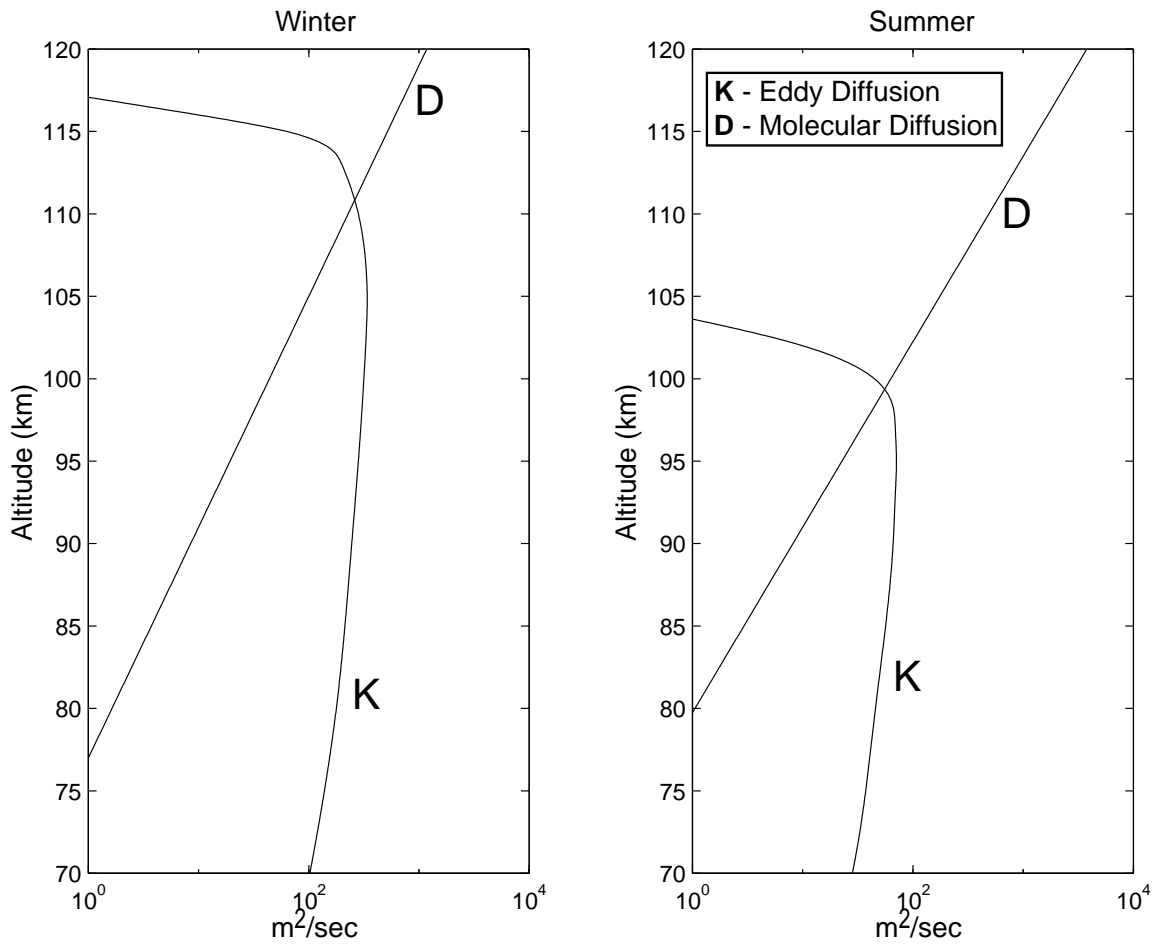
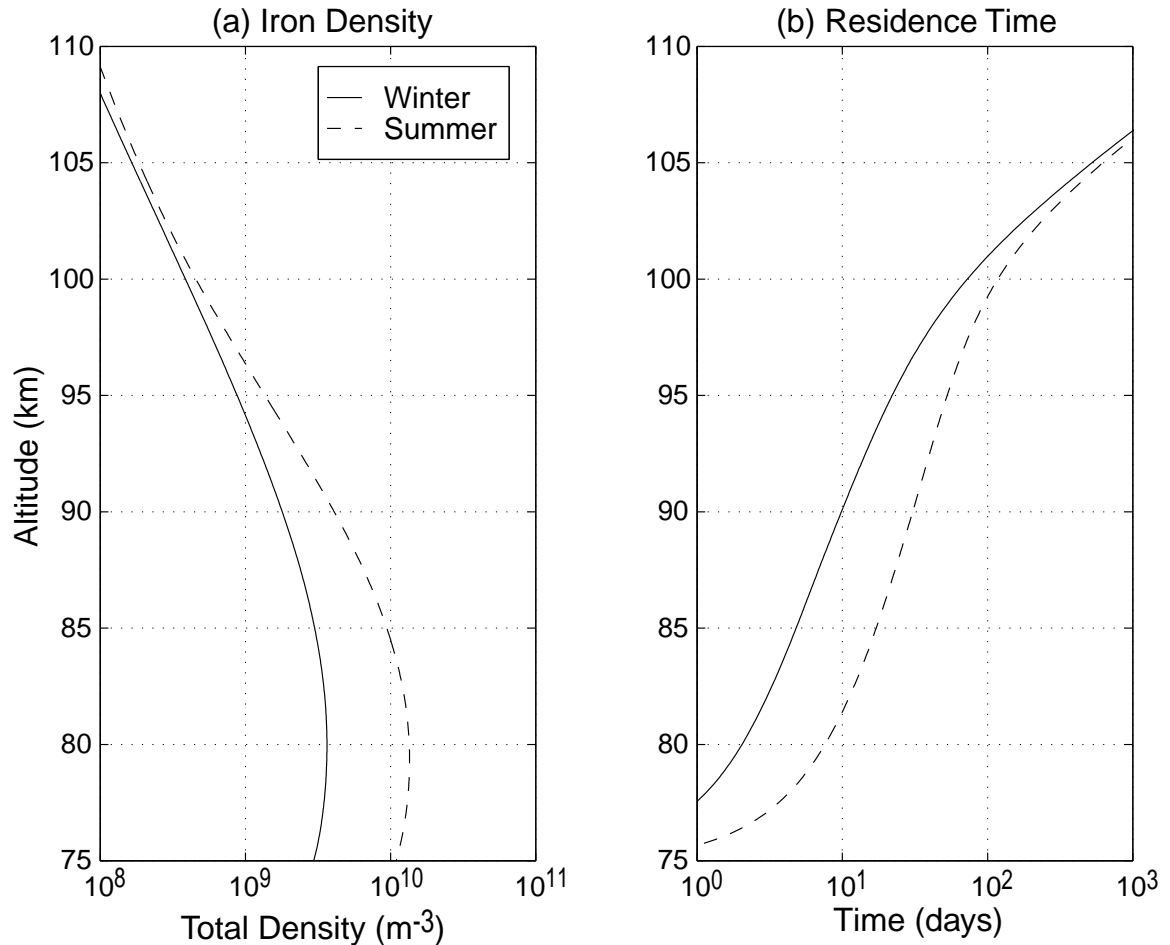
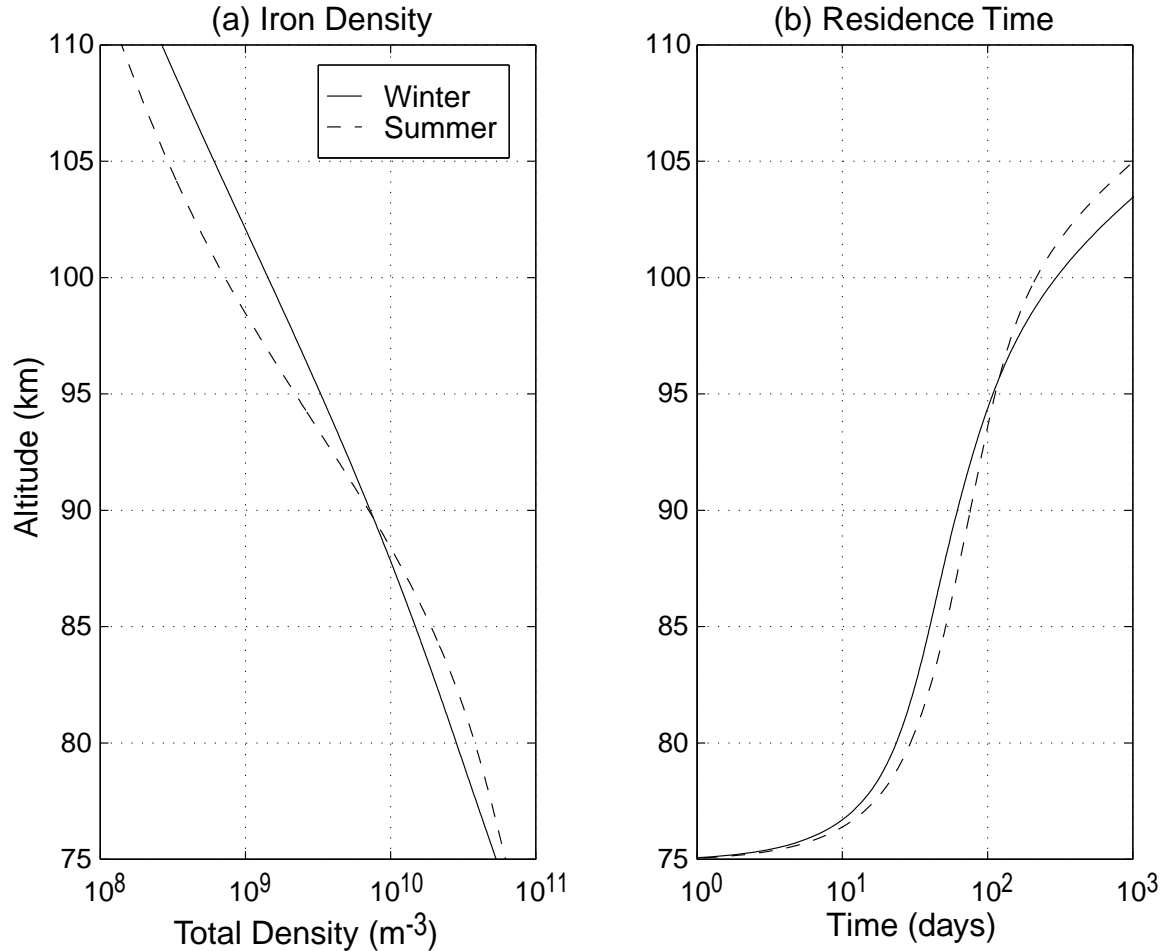


Figure 2.4: Iron Profile Estimate. (a) Total iron number density profile with a perfect sink at 90 km altitude. (b) Time for iron to diffuse from deposition altitude to 70 km.



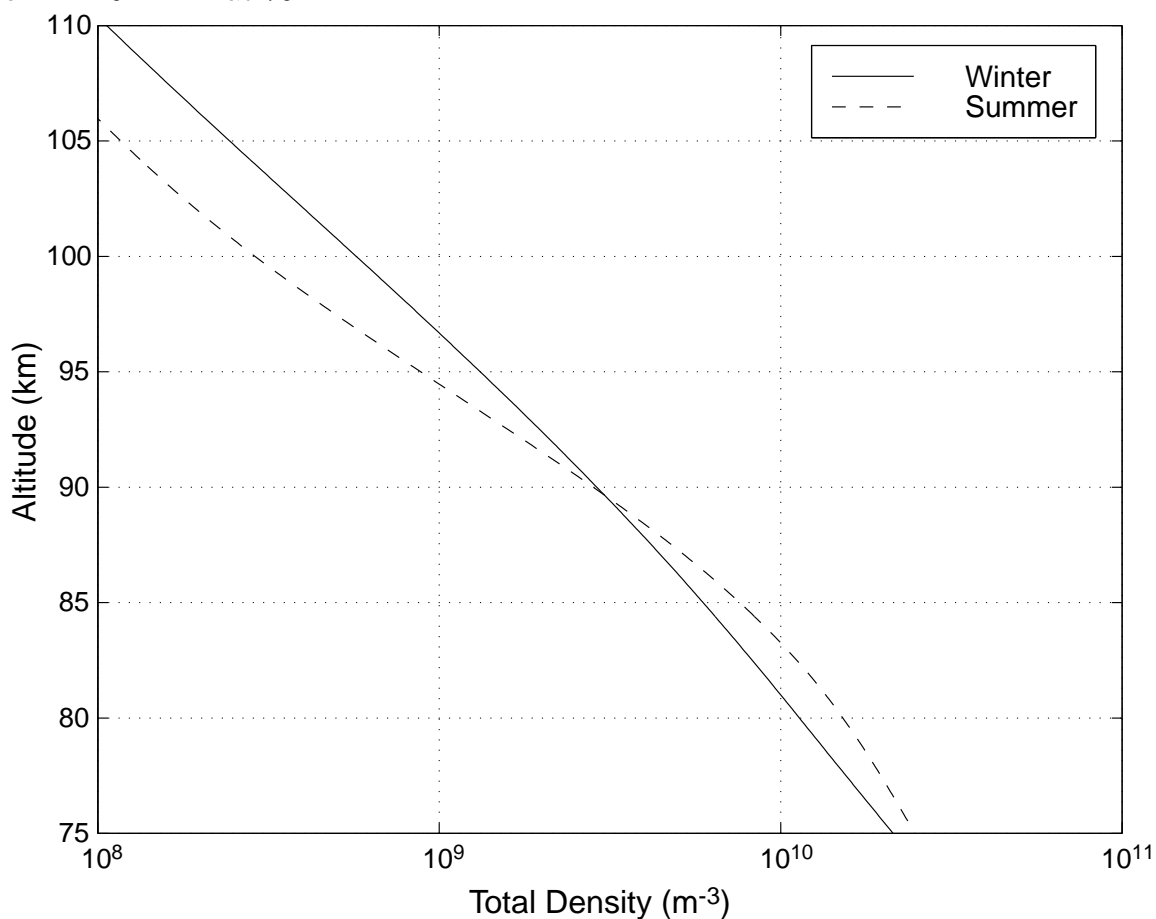
at each altitude to diffuse downward to 70 km, as computed from the velocities given by equation (2.16). Even with a near-perfect sink, this calculation indicates that the average residence time for iron atoms is between tens and hundreds of days, depending on altitude. It thus appears that the atmosphere acts like a substantial low-pass filter for meteoric material concentrations, consistent with the lack of correlation between meteor showers and metal ion-rich sporadic- E layers [Whitehead(1989)]. On the other hand, the long residence time of iron atoms is somewhat at odds with measurements of significant day-to-day variability in metal atom layer measurements (see Chapter 3 for examples). Explanations of this variability must therefore presumably

Figure 2.5: Iron Profile Estimate. (a) Total iron number density profile with a boundary condition of 10^{11} m^{-3} at 70 km. (b) Time for iron to diffuse from deposition altitude to 70 km.



entail other forcing mechanisms such as Lorentz forcing of ions or atmospheric gravity wave forcing of neutrals. Horizontal inhomogeneities and nonsteady-state or heterogeneous chemistry may also play roles in the dynamical behavior of the metals. It is apparent from Figure 2.4 that the boundary condition is of limited utility for the purpose of adjusting the profile densities. This fact is further demonstrated in Figure 2.5 which shows results of the same calculation repeated with an iron density of 10^{11} m^{-3} at 70 km. As is shown in Chapter 3, when combined with chemistry considerations this total profile provides a reasonable replication of the characteristics of lidar

Figure 2.6: Sodium Profile Estimate. Total sodium profile with a boundary condition of $4 \times 10^{10} \text{ m}^{-3}$ at 70 km.



measurements of neutral atomic iron.

The formation of the altitude profile for sodium is very similar to that for iron. As mentioned earlier, the neutral atomic iron to sodium ratio reported by *Kane and Gardner*(1993b) is approximately 2.5 to 1, quite different from the 15 to 1 ratio in Table 2.1. When both the total material flux and boundary condition are adjusted by this ratio, equation (2.18) yields the profile shown in Figure 2.6. This profile, when combined with the chemistry described in Chapter 3, leads to a neutral atomic sodium profile that agrees quite well with measurements. In both the case of sodium and that of iron it should be noted that the lidar measurements used to validate this approach are not sensitive in much of the altitude range for which predictions

are made. Lidars measure only the neutral atomic iron and sodium while totally ignoring other metal containing compounds such as NaHCO_3 and Na^+ . In practice, this means that nearly all of the sodium measurements used for validation come from altitudes between 80 and 100 km. As will be seen in Chapter 3, this limitation is not a significant one for the purposes of predicting the influence of auroral ionization on the sodium and iron layers, due to the fact that the primary influence is on the neutral atomic sodium, which *is* measured. As a result, the only significant aspect of the total profile determination is that the resulting neutral atom layers (as opposed to compounds or ions) have characteristics that match the measurements.

2.5 Chapter Summary

In this chapter we review the processes which lead to altitude profiles of metallic atoms and compounds in the upper atmosphere. Material is deposited into the atmosphere in a gas phase by meteoroid ablation and, under the influence of diffusion, quasi steady-state altitude profiles of that material are derived from an assumed total material deposition rate and a lower altitude boundary condition. The resulting profiles for iron and sodium are shown in Figures 2.5 and 2.6, respectively. In accordance with published measurements, we confirm that the relative abundances of iron and sodium do not agree with the expected abundances based on meteorite composition data and we briefly discuss some possible causes for this disagreement. In this chapter we also review the issue of the ionization of the material during ablation, as parameterized by the ionization coefficients shown in Figure 2.2, and point out that the velocity dependencies of the coefficients have important implications in terms of interpreting observational data.

Chapter 3

Chemistry

I came to my professor, Clive, whom I admired very much, and I said “I have a new theory of electrical conductivity as a cause of chemical reactions.” He said, “This is very interesting,” and then he said “Good-bye.” He explained to me later that he knew very well that there are so many different theories formed, and that they are almost certain to be wrong, for after a short time they disappear; and therefore by using the statistical manner of forming his ideas, he concluded that my theory would not exist long.

Svante Arrhenius

In Chapter 2 we described the processes of meteor ablation and diffusion that were used to deduce altitude profiles of the various metallic species without considering the chemical states of the metals. In this chapter the role of chemistry is discussed with regard to a number of recent developments in this area. In particular, we begin the chapter with descriptions of models that were developed for iron and then sodium, as a prelude to the discussion of our main topic: the impact of auroral ionization on the chemical dynamics of metals in the upper atmosphere. The investigation of auroral influence is a new topic and is thus considered in some detail.

According to a review by *Hunten*(1967), the basic gas phase chemistry for sodium in the upper atmosphere was discussed in the literature as early as 1939 and then elaborated upon during the 1940's, 50's and 60's. Numerous other review papers have tracked the advances made in understanding this chemistry over the years [e.g. *Ferguson*(1972), *Brown*(1973), *Murad*(1978), *Plane*(1991), *Plane and Helmer*(1994)]. The

apparent slow progress in this field has been due, in large part, to the fact that the relevant upper atmospheric region is largely inaccessible. Occasional instrumented rocket flights have made spot measurements of the chemical states of some of the constituents, but these measurements can, at best, be used to bound various postulated sets of chemical reactions [e.g. *Clemesha et al.*(1995)]. The advent of resonant lidar techniques (see Appendix C) have allowed nearly continuous monitoring of some chemical species, but they are not yet capable of measuring more than a few different neutral and ionized metal atoms [e.g. *Megie et al.*(1978), *Tilgner and von Zahn*(1988), *Bills and Gardner*(1990), *Alpers et al.*(1990), *Plane*(1991) and references therein]. The lidar measurements have provided increasingly stricter bounds on the required behavior of the chemical models, but they do not definitively allow measurements of specific chemical reactions (or even of all the constituents of any one reaction). As a result, progress in this field has relied heavily on laboratory measurements of the rates of various postulated reactions along with *ab initio* theoretical estimates of molecular characteristics and reaction rates [*Plane and Helmer*(1994)]. This approach, of including as many potentially viable reactions as possible, tends to result in quite complicated models of atmospheric chemistry. From an engineering standpoint, the number of internal degrees of freedom greatly exceeds what can be determined from any given set of observations. Nonetheless, the use of such models shows a good deal of promise in terms of reproducing measurements of long term averages of many parameters and, more importantly, might be expected to result in models from which extrapolations can be made well beyond the conditions of the existing measurements. A central focus of this thesis is the testing of one such extrapolation.

In addition to describing the characteristics of the ‘background’ layers of metals such as iron and sodium, chemical models are also being developed to explain a number of transient phenomena. Among the most surprising of these phenomena, and one which is presently being pursued vigorously by a number of groups, is the occurrence of sporadic neutral atom layers. The first observation of thin neutral layers of sodium is typically attributed to *Clemesha et al.*(1978). There is some evidence of an earlier detection of a layer in observations by *Sandford and Gibson*(1970), but those authors did not comment on the significance of the observation. More recently,

sporadic layers of iron and calcium have also been reported [*Bills and Gardner*(1990), *Alpers et al.*(1990), *Granier et al.*(1985)]. As indicated in recent papers by *Gardner et al.*(1995) and *Clemesha*(1995), the cause of these layers is still very much in question. One quantitative chemical theory for sporadic sodium layer formation has been proposed by *Cox and Plane*(1998), which we examine more closely in Chapter 4. Some other potentially viable theories do not rely on simple gas-phase chemistry but, rather, consider the absorption of metal atoms onto the surfaces of dust particles followed by their forced release [e.g. *von Zahn et al.*(1987), *von Zahn and Hansen*(1988), *Beatty et al.*(1989), *Hansen and von Zahn*(1990), *Kirkwood and von Zahn*(1991)]. In this chapter we focus our attention on discussions of the chemistry of gas-phase reactions only and do not consider heterogeneous processes, which are in any event much more speculative. We therefore leave open the question of the influence of dust on the chemical state of the system. The case study in Chapter 5 shows an instance where gas-phase chemistry alone provides results consistent with a set of measurements.

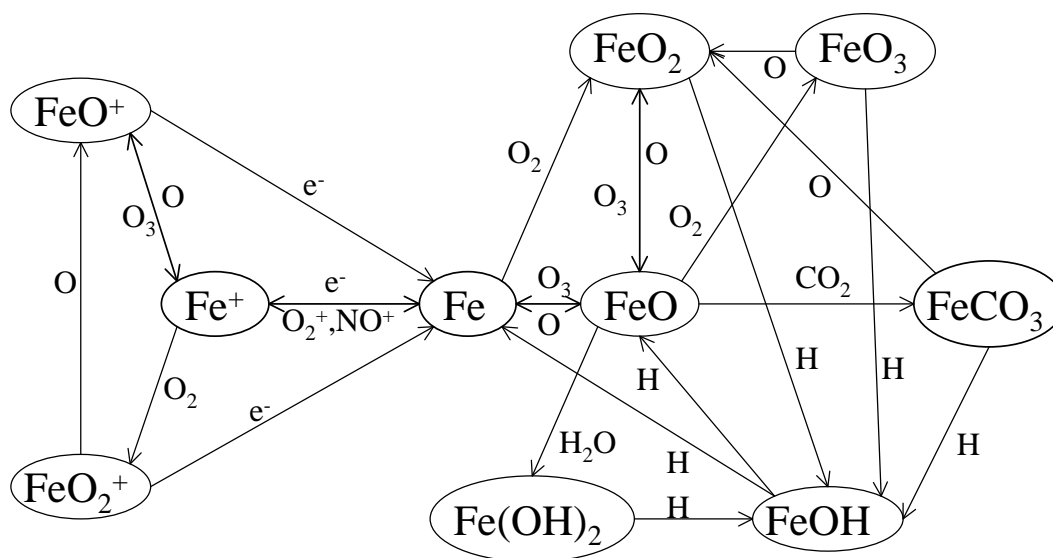
3.1 Iron Model

The model of upper atmospheric iron described in this thesis is based on the chemical reactions presented in *Helmer et al.*(1998). This set of reactions, while excluding some of the reactions speculated by *Brown*(1973) and including a number that earlier studies had not considered, is in any event on much firmer experimental footing. Many of the critical reaction rates (including temperature dependencies) were measured by *Helmer et al.*(1998) in a laboratory setting, however, there do remain several reactions that have not been precisely measured and estimates have been used via analogy to reactions of other metal species. The model presented by *Helmer et al.*(1998) was aimed at reproducing extensive measurements at a midlatitude station, 40° N, where the data were taken from an earlier paper by *Kane and Gardner*(1993b). The extension of the concepts to high latitudes as required for our work was quite straightforward. The specific chemical reactions for the iron model are contained in Table 3.1 and illustrated schematically in Figure 3.1. Note that Table 3.1 breaks with tradition in the chemistry community by presenting all reaction rates in *SI* units.

Table 3.1: Iron Chemistry

Reaction	Rate Coefficient
$\text{Fe} + \text{O}_3 \rightarrow \text{FeO} + \text{O}_2$	$k_1 = 3.44 \times 10^{-16} \exp(-1.21/RT) \text{ m}^3/\text{s}$
$\text{Fe} + \text{O}_2 + \text{X} \rightarrow \text{FeO}_2 + \text{X}$	$k_2 = 3.25 \times 10^{-42} \exp(-15.3/RT) \text{ m}^6/\text{s}$
$\text{FeO} + \text{O} \rightarrow \text{Fe} + \text{O}_2$	$k_3 = 1.8 \times 10^{-16} (T/200)^{1/2} \text{ m}^3/\text{s}$
$\text{FeO} + \text{O}_3 \rightarrow \text{FeO}_2 + \text{O}_2$	$k_4 = 2.2 \times 10^{-16} \exp(-4.6/RT) \text{ m}^3/\text{s}$
$\text{FeO} + \text{O}_2 + \text{X} \rightarrow \text{FeO}_3 + \text{X}$	$k_5 = 6.5 \times 10^{-42} (200/T)^{1.5} \text{ m}^6/\text{s}$
$\text{FeO} + \text{H}_2\text{O} + \text{X} \rightarrow \text{Fe}(\text{OH})_2 + \text{X}$	$k_6 = 8.0 \times 10^{-41} (200/T)^{1.5} \text{ m}^6/\text{s}$
$\text{FeO} + \text{CO}_2 + \text{X} \rightarrow \text{FeCO}_3 + \text{X}$	$k_7 = 2.0 \times 10^{-40} (200/T)^{1.5} \text{ m}^6/\text{s}$
$\text{FeO}_2 + \text{O} \rightarrow \text{FeO} + \text{O}_2$	$k_8 = 5.0 \times 10^{-16} \exp(-8.3/RT) \text{ m}^3/\text{s}$
$\text{FeO}_2 + \text{H} \rightarrow \text{FeOH} + \text{O}$	$k_9 = 1.0 \times 10^{-15} \exp(-8.3/RT) \text{ m}^3/\text{s}$
$\text{FeO}_3 + \text{O} \rightarrow \text{FeO}_2 + \text{O}_2$	$k_{10} = 2.5 \times 10^{-16} (T/200)^{1/2} \text{ m}^3/\text{s}$
$\text{FeO}_3 + \text{H} \rightarrow \text{FeOH} + \text{O}_2$	$k_{11} = 5.0 \times 10^{-16} (T/200)^{1/2} \text{ m}^3/\text{s}$
$\text{FeOH} + \text{H} \rightarrow \text{FeO} + \text{H}_2$	$k_{12} = 5.0 \times 10^{-17} \exp(-6.7/RT) \text{ m}^3/\text{s}$
$\text{FeOH} + \text{H} \rightarrow \text{Fe} + \text{H}_2\text{O}$	$k_{13} = 2.0 \times 10^{-18} \exp(-5.0/RT) \text{ m}^3/\text{s}$
$\text{Fe}(\text{OH})_2 + \text{H} \rightarrow \text{FeOH} + \text{H}_2\text{O}$	$k_{14} = 1.1 \times 10^{-16} \exp(-2.5/RT) \text{ m}^3/\text{s}$
$\text{FeCO}_3 + \text{O} \rightarrow \text{FeO}_2 + \text{CO}_2$	$k_{15} = 2.0 \times 10^{-16} \exp(-27.0/RT) \text{ m}^3/\text{s}$
$\text{FeCO}_3 + \text{H} \rightarrow \text{FeOH} + \text{CO}_2$	$k_{16} = 2.0 \times 10^{-16} \exp(-12.5/RT) \text{ m}^3/\text{s}$
$\text{Fe} + \text{O}_2^+ \rightarrow \text{Fe}^+ + \text{O}_2$	$k_{17} = 1.1 \times 10^{-15} \text{ m}^3/\text{s}$
$\text{Fe} + \text{NO}^+ \rightarrow \text{Fe}^+ + \text{NO}$	$k_{18} = 9.2 \times 10^{-16} \text{ m}^3/\text{s}$
$\text{Fe}^+ + \text{e}^- \rightarrow \text{Fe} + h\nu$	$k_{19} = 1.0 \times 10^{-18} \text{ m}^3/\text{s}$
$\text{Fe}^+ + \text{O}_3 \rightarrow \text{FeO}^+ + \text{O}_2$	$k_{20} = 7.0 \times 10^{-16} \text{ m}^3/\text{s}$
$\text{Fe}^+ + \text{O}_2 + \text{X} \rightarrow \text{FeO}_2^+ + \text{X}$	$k_{21} = 1.0 \times 10^{-42} (200/T) \text{ m}^6/\text{s}$
$\text{FeO}^+ + \text{O} \rightarrow \text{Fe}^+ + \text{O}_2$	$k_{22} = 1.0 \times 10^{-16} \text{ m}^3/\text{s}$
$\text{FeO}^+ + \text{e}^- \rightarrow \text{Fe} + \text{O}$	$k_{23} = 1.0 \times 10^{-13} (200/T)^{1/2} \text{ m}^3/\text{s}$
$\text{FeO}_2^+ + \text{O} \rightarrow \text{FeO}^+ + \text{O}_2$	$k_{24} = 1.0 \times 10^{-16} \text{ m}^3/\text{s}$
$\text{FeO}_2^+ + \text{e}^- \rightarrow \text{Fe} + \text{O}_2$	$k_{25} = 3.0 \times 10^{-13} (200/T)^{1/2} \text{ m}^3/\text{s}$

Figure 3.1: Schematic of the Iron Chemistry Reactions. For each reaction, the reactants are on the left side of the line in the direction of the arrow.



One significant departure of the present work from the model described in *Helmer et al.*(1998) is that the model developed here does include time dependencies while the *Helmer et al.*(1998) model was steady-state and, as such, was used to predict the state of iron in chemical equilibrium. In particular, the model in *Helmer et al.*(1998) was used to simulate average nighttime profiles under the assumption that dynamical fluctuations would average out. However, to the extent that the rate coefficients and chemical reactions of Table 3.1 are valid, the development of a time-dependent model is conceptually straightforward (though numerically more complex).

The chemical model for iron basically partitions the available Fe (from Chapter 2) among 10 separate species: Fe^+ , FeO^+ , FeO_2^+ , Fe , FeO , FeO_2 , FeO_3 , FeOH , Fe(OH)_2 , and FeCO_3 . This partitioning is facilitated by the presence of a number of other reactants: O , O_2 , O_3 , H , H_2O , CO_2 , N_2 , O_2^+ , NO^+ , a third body X which is taken to be either N_2 or O_2 , and free electrons, e^- , whose number density is the sum of all ion number densities. The concentrations of these reactants must be determined by some external means as it is well beyond the scope of the present work to model the chemistry and transport associated with them. External models are thus used to

Table 3.2: Models Used for Chemical Reactants

Reactant	Model
O	MSISE-90
O ₂	MSISE-90
O ₃	<i>Garcia and Solomon(1994)</i>
H	MSISE-90
H ₂	<i>Garcia and Solomon(1994)</i>
H ₂ O	<i>Garcia and Solomon(1994)</i>
CO ₂	<i>Garcia and Solomon(1994)</i>
N ₂	MSISE-90
Temperature, T	MSISE-90
Background N _e (e ⁻)	IRI-95
Background NO ⁺	0.822×N _e
Background O ₂ ⁺	0.178×N _e

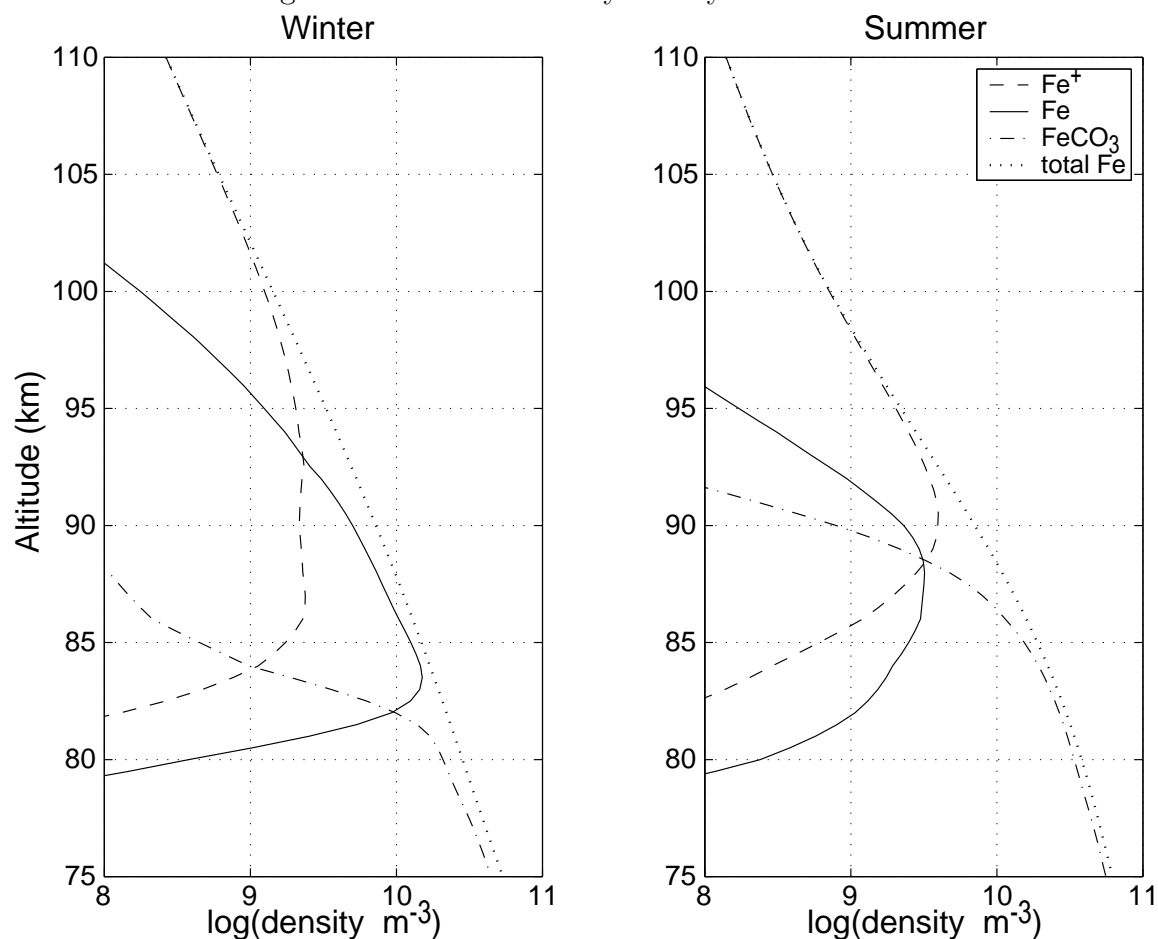
estimate these parameters; the Mass Spectrometer and Incoherent Scatter (MSISE-90) model [*Hedin(1991)*] and the model by *Garcia and Solomon(1994)* are used for the neutral species concentrations and temperatures and the International Reference Ionosphere (IRI-95) model [*Rawer et al.(1978)*, *Bilitza(1990)*, *Bilitza(1998)*] is used for background electron densities. IRI-95 also provides individual concentrations of NO⁺ and O₂⁺, but that model contains a discontinuity in those profiles at 100 km altitude, so a fixed relative concentration is used for those constituents instead. In particular, the NO⁺ concentration is taken as 82.2% of the total background electron density and the remaining 17.8% was assigned to O₂⁺, corresponding to the low altitude limit for IRI-95 under the conditions of the case study in Chapter 5. Note that earlier measurements and theoretical calculations have shown that the relative concentrations of NO⁺ and O₂⁺ are in fact highly variable [e.g. *Danilov(1994)*, *Roble et al.(1987)*] but the charge transfer reactions that they are used with in Table 3.1 have almost identical rate coefficients so the specific partitioning is not critical for this study. It should also be noted that IRI-95, even at high latitudes, does not include the effects of auroral ionization, which is added externally in a later section. Table 3.2 specifies the model used for each reactant.

In the absence of transport, a model such as the one developed here can be written as a vector ordinary differential equation (see Appendix E). The ‘state vector’ must,

however, contain all constituents that are expected to vary during the course of the simulation. This requirement places some constraints on the use of external models. In particular, if the reactions being simulated might have a significant impact on the externally supplied parameters a decision must be made as to how to proceed. For example, the external variables could be used as an ‘initial’ condition for additional parameters in the state vector. Another alternative would be to use those external concentrations as ‘final’ conditions with no additional parameters. The case of the iron model used here turns out to be less complicated. Figure 3.2 shows altitude profiles for all of the neutral reactants as well as for the total iron density from Figure 2.5, indicating that the total iron density is orders of magnitude below that of the other reactants for the entire range of interest. The only reactant whose density approaches that of iron is H, and that only occurs below approximately 75 km altitude. Thus, these reactants can be safely assumed to be unaffected by the chemical processes being modeled. The case of the ions is a bit more complicated because at night the electron densities are typically not much greater than the iron densities at some altitudes. In fact, though IRI-95 maintains that the ions are still a combination of NO^+ and O_2^+ , it is reasonable to ask what portion of the night-time ionization is in fact associated with long-lived metallic atoms. According to measurements analyzed by *Danilov*(1994), NO^+ does indeed dominate the composition when compared to metallic ions above an altitude of approximately 98 km. In this thesis we demonstrate that these are the altitudes above which the charge exchange reactions are significant, so the choice was made to hold these densities to the IRI-95 values and not allow the charge transfer reactions to eat away at the molecular ion densities. This assumption is not an unreasonable approximation because even at night sources of ionization are present, such as galactic EUV, cosmic radiation, and scattered EUV [*Wallis and Budzinski*(1981)], which work to replace molecular ions lost by the charge transfer reactions. In the end, an evaluation of the validity of this assumption must rest on the ability of the resulting model to reproduce measured profiles of the various constituents. This assumption was also employed by *Helmer et al.*(1998) in their successful modeling effort using a model very similar to that presented here.

As an initial test, the model is used to study the steady-state behavior of iron

Figure 3.3: Iron Chemistry Steady-State Profiles

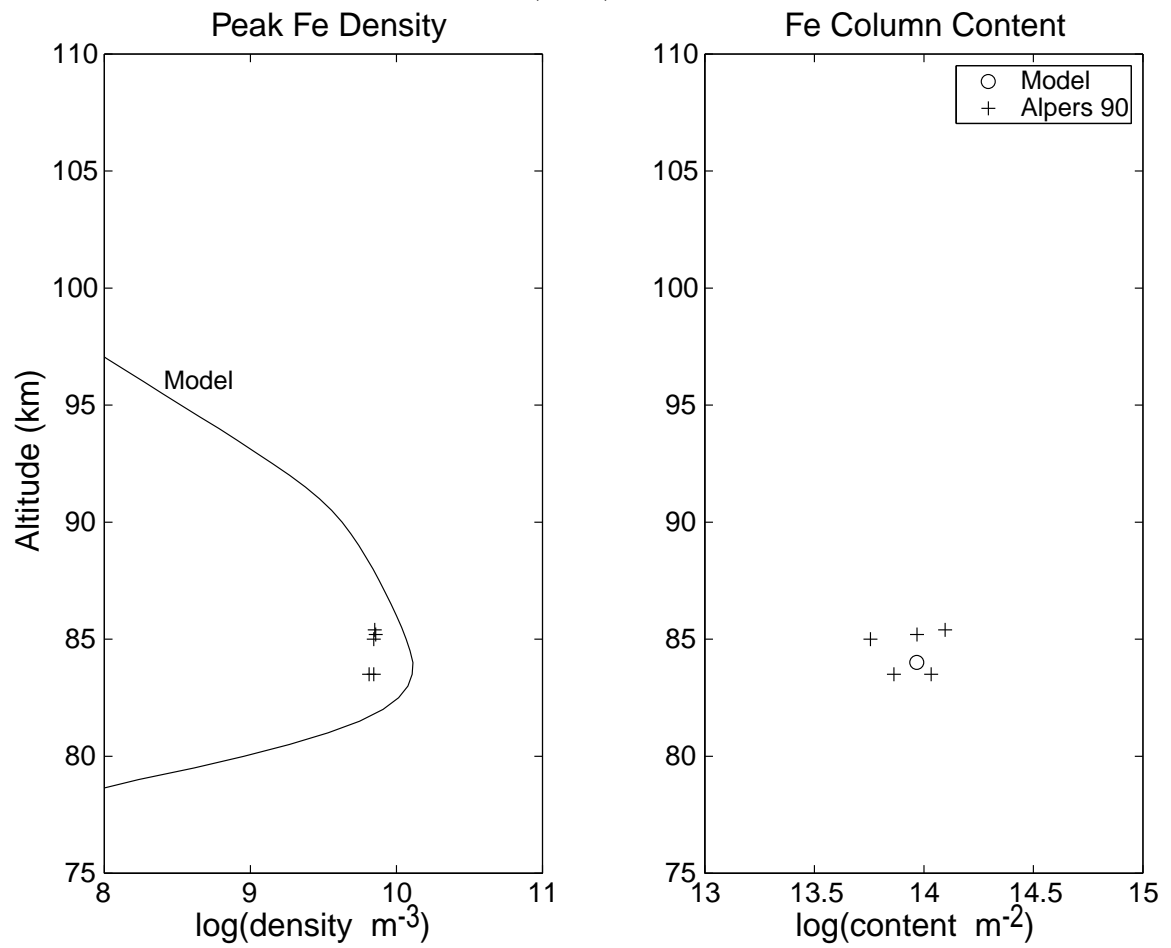


under a number of conditions, by setting the initial condition for the model to a profile of the total amount of iron in a given state (e.g. neutral atomic Fe) and allowing the model to run for a time much greater than the time constants of any of the reactions. Experimentation indicated that 10^6 seconds is sufficient for this purpose. Model runs were completed for the Sondrestrom Radar Facility location [Kelly(1983)] and for both summer and winter conditions. The results of the model runs are shown in Figure 3.3, in which only the three dominant constituents are plotted: Fe, Fe⁺, and FeCO₃. Curves with the total iron profiles are also included, indicating that these three chemicals do indeed dominate the total concentrations. Figure 3.3 also shows the cause of the ‘layering’ of neutral atomic Fe in the upper

atmosphere. In the context of this model, the top side of the Fe layer is limited by the charge exchange reactions with NO^+ and O_2^+ which drive the state of the iron toward an ionized condition, Fe^+ , combined with the general decrease in the total iron with increasing altitude. This limitation results in a top-side profile that is not especially steep but which does fall off faster than the background atmosphere (the Fe mixing ratio decreases with increasing altitude). On the bottom side of the layer the equilibrium chemical condition changes, favoring FeCO_3 , occurring very rapidly with altitude in winter and less so in summer. The only constituent that can be compared with lidar measurements is of course Fe. *Helmer et al.*(1998) had a large number of measurements available to validate their results. The case in hand is much more limited, though, in a sense, the model results presented here simply represent a minor extrapolation of the well-validated *Helmer et al.*(1998) results. Many of the important constituents in the chemical equations of Table 3.1 do have significant latitudinal dependencies, so a simple comparison with *Kane and Gardner*(1993b) is not appropriate. Instead, the results are compared with the modest data set presented in *Alpers et al.*(1990), which was collected from Andøya, Norway, at a geographic latitude of 69° N during five nights in the spring of 1990. This site is approximately 2° further north geographically than the Sondrestrom facility. *Alpers et al.*(1990) listed nightly averages of the peak Fe density, the altitude of the peak, and the total column content for each of those nights. The chemical model is run for a date near the center of the set of observations and the results are compared in Figure 3.4. The left hand panel of Figure 3.4 shows that the model model results agree with the altitude of the layer peak but that they represent a slight overestimation of the peak density, which could easily be a result of the very simple total content estimates developed in Chapter 2. The right hand panel shows that the model estimates of the total height-integrated Fe content lie basically in the middle of the 5 measurements by *Alpers et al.*(1990). It thus appears, at least from this limited data set, that the iron chemical model sufficiently reproduces this steady-state behavior.

The iron model is now used to investigate the transient behavior of this chemical system. The goal is to gain some insight into the expected chemical evolution of iron that has been deposited in the upper atmosphere. As was mentioned in Chapter 2, the

Figure 3.4: Iron Profile Comparison with Data. Peak density, altitude of the peak, and column content from *Alpers et al.*(1990).



majority of meteoroids have velocities on the order of 15 km/s. According to Figure 2.2, the vast majority of the iron deposited at that velocity is in a neutral state. As a result, the following figures contain model results with an initial condition of neutral atomic Fe at a constant density of 10^{10} Fe atoms/m³ at all altitudes. These figures should be interpreted not as the time evolution of a single meteor trail, however, but rather as the evolution of material at each altitude in the absence of any diffusion. All the figures have Sondrestrom as the location and they show, as a gray scale, the number densities of various iron-containing compounds. Figure 3.5 shows the evolution of Fe and Fe⁺ over the course of 8 hours for winter night-time conditions, clearly illustrating the ionization of Fe by the charge transfer process, which appears to be extremely slow; after 8 hours only 5% of the iron atoms are ionized. The obvious explanation for this result is that the *E*-region electron densities at night are simply so low that there isn't sufficient NO⁺ and O₂⁺ in the background ionosphere to efficiently ionize Fe. Figure 3.6 displays the same parameters except that the ionospheric densities correspond to winter day-time conditions, showing the charge transfer to be more efficient than with night-time ion densities, but after 8 hours still only about 20% of the Fe is ionized at 110 km altitude. Summer day-time conditions are shown in Figure 3.7, indicating that there should be a significant difference between the summer and winter ionization rates. The higher background densities in the summer *E* region combined with different chemical conditions in general will almost completely ionize the Fe at 110 km over the course of 8 hours. However, it still takes approximately 2 hours to ionize half the iron. In either case, however, Figure 3.3 shows that the steady-state condition for Fe at 110 km is as Fe⁺. Figures 3.5 through 3.7 all show an apparently very rapid reaction at low altitudes (below ~80 km). Within one pixel width the Fe almost completely vanishes into some other compound. Figure 3.3 suggests that this compound might be FeCO₃, but Figure 3.8 suggests a somewhat different and more complicated process, indicating that Fe is initially removed to FeO. In fact, after only five seconds most of the Fe at 75 km is tied up in other compounds. As time progresses, however, the FeO concentration diminishes and FeO₂ begins to grow. After 30 seconds, the FeCO₃ concentration is only to 4% of the initial Fe concentration. Thus, there is an interplay between the

Figure 3.5: Iron Reaction Rate, Winter, Night. Initial condition is neutral Fe at all altitudes.

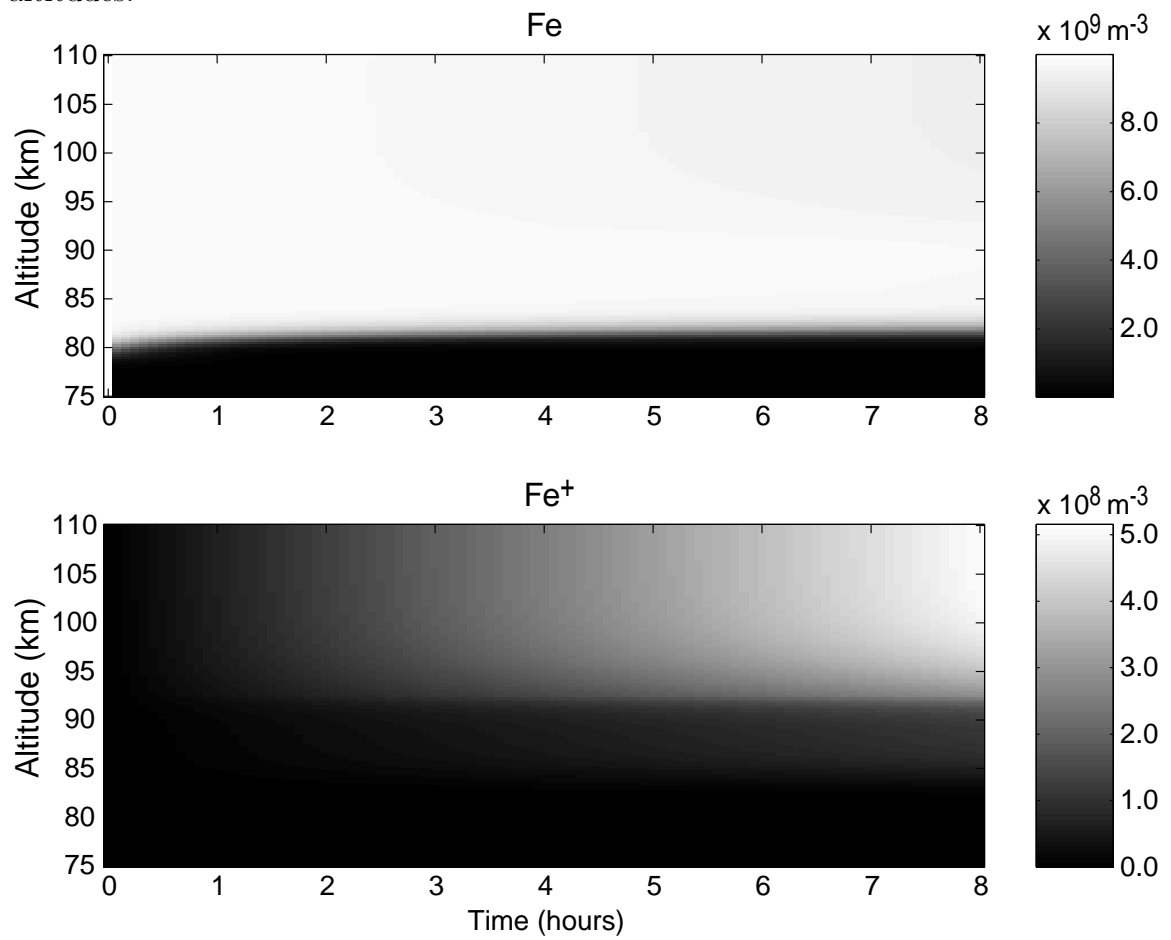


Figure 3.6: Iron Reaction Rate, Winter, Day

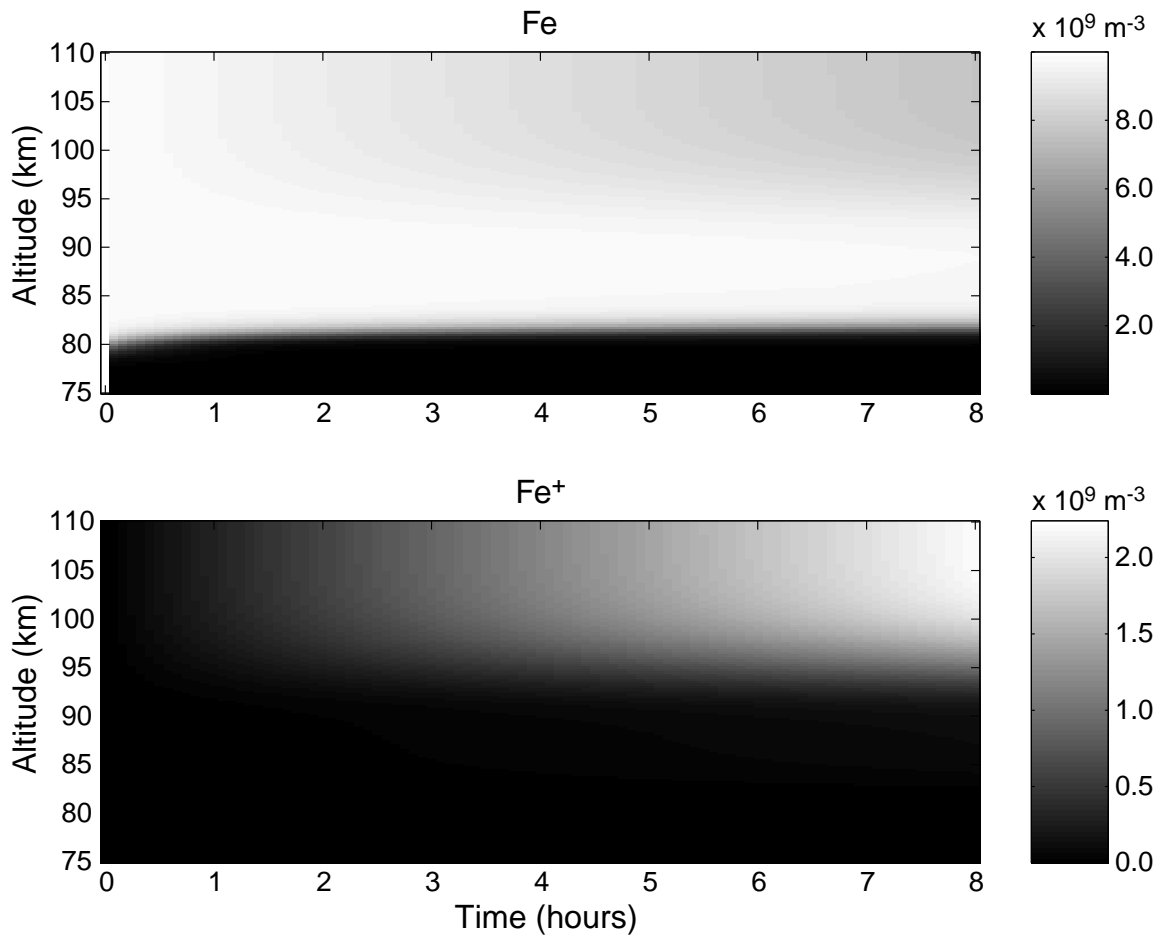


Figure 3.7: Iron Reaction Rate, Summer, Day

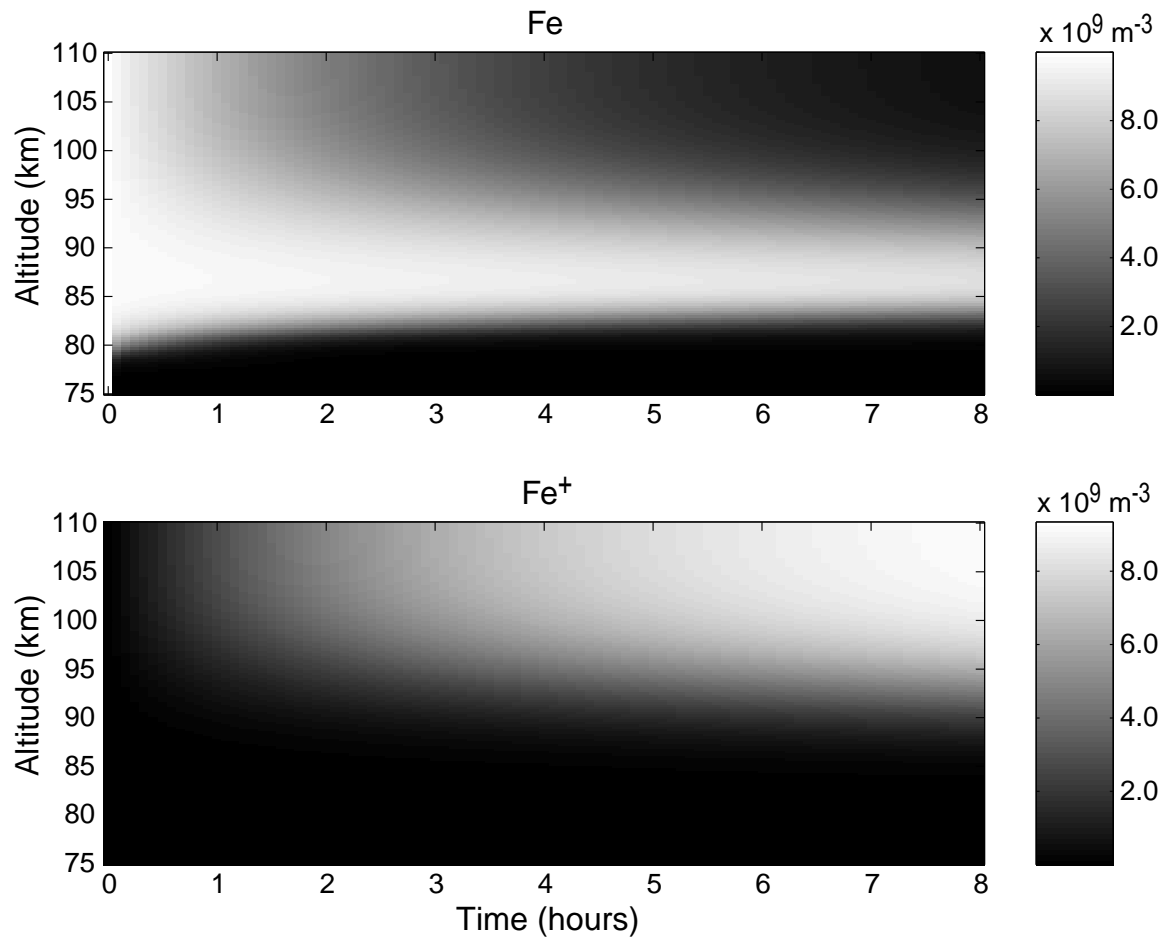
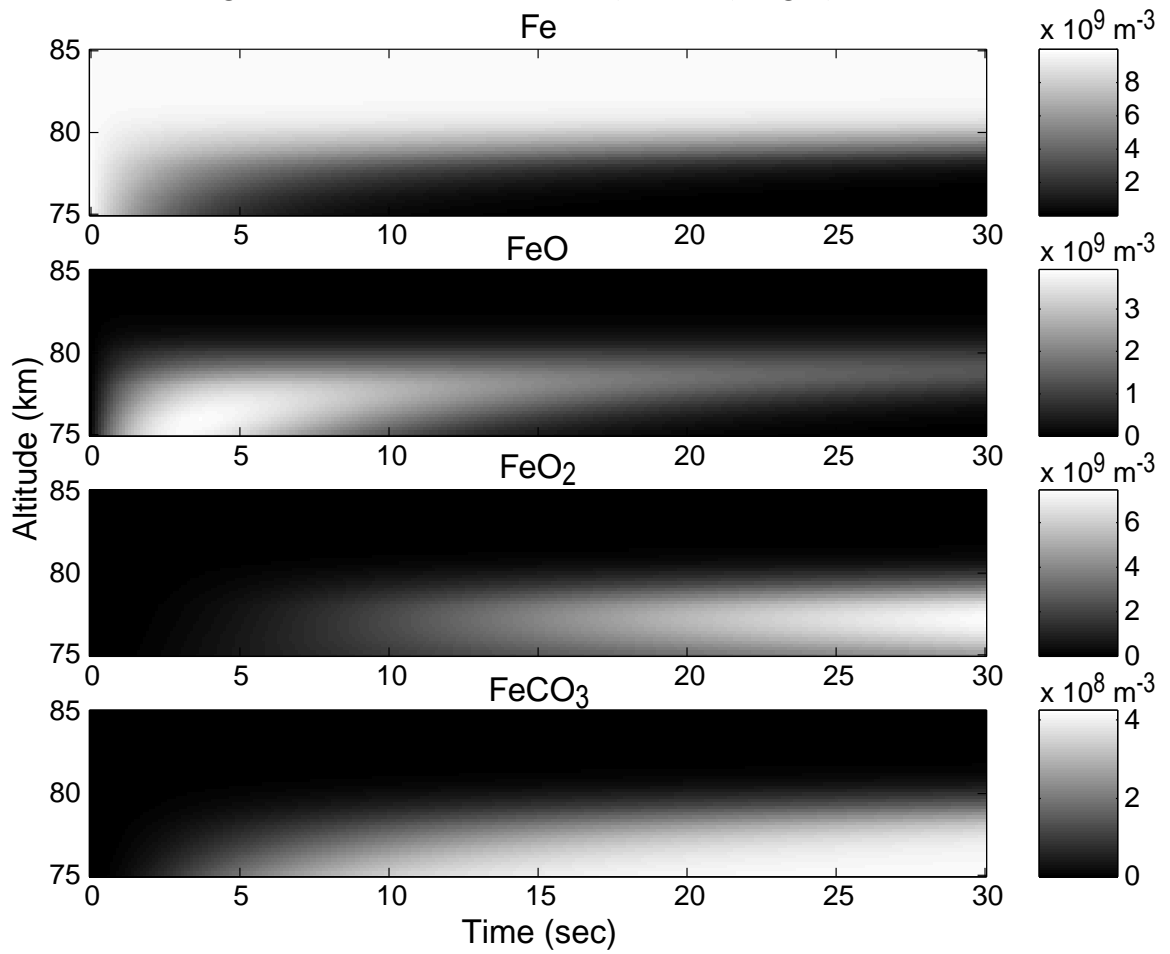


Figure 3.8: Iron Reaction Rate, Winter, Night, 75-85 km



various reaction rates that results in a more complicated behavior than one might think at first. Whether or not this actually occurs in the upper atmosphere is very difficult to determine. Perhaps a sufficient number of instrumented rocket flights could be used, but as mentioned earlier it is probably more realistic to consider recreating these kinds of conditions in a laboratory setting. It is important to note here that all of the effects studied so far have assumed quiet high-latitude conditions. The effects of auroral ionization are addressed in future sections.

3.2 Sodium Model

Study of the chemistry of upper atmospheric sodium has a much longer history than that of the chemistry of iron, largely due to the very large resonant scattering cross-section of sodium atoms, making them easily observable from the ground. Soon after the discovery of a sodium layer by *Bernard*(1938), the issue of the chemical state was taken up by various researchers, including *Chapman*(1939). The central importance of oxygen atoms and molecules (O, O₂, and O₃) to the chemistry of the region was recognized from the start, though many of the controlling reaction rates were determined much later. The reactions considered in this thesis are based primarily on the recent work by *Plane et al.*(1998) and *Cox and Plane*(1998). The set of reactions used in our model, shown in Table 3.3, are basically a composite of the reactions in those two publications with two rate coefficients updated based on the work of *Levandier et al.*(1997). It should be noted that other groups have modeled sodium [e.g. *McNeil et al.*(1995)], and that the similarities between the various models are much greater than their differences.

The *Plane et al.*(1998) model was based on their earlier work in *Plane*(1991), *Helmer and Plane*(1993), and *Plane and Helmer*(1994) but updated with new rate coefficients and modified for high latitude conditions to reproduce the average background Na layer characteristics from resonant lidar measurements made in the Canadian arctic and at the Amundsen-Scott South Pole Station. As with the *Helmer et al.*(1998) model, *Plane et al.*(1998) reported estimates of the steady-state profiles of Na-containing species. The addition of the chemistry from *Cox and Plane*(1998)

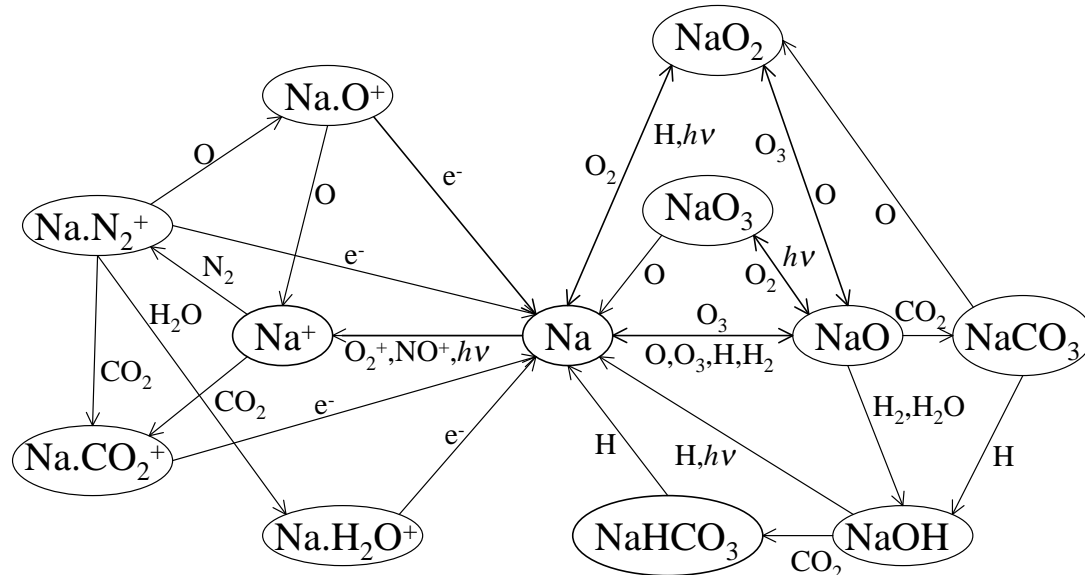
Table 3.3: Sodium Chemistry

Reaction	Rate Coefficient
$\text{Na} + \text{O}_3 \rightarrow \text{NaO} + \text{O}_2$	$k_1 = 1.1 \times 10^{-15} \exp(-116/T) \text{ m}^3/\text{s}$
$\text{NaO} + \text{O} \rightarrow \text{Na} + \text{O}_2$	$k_2 = 2.2 \times 10^{-16} (T/200)^{1/2} \text{ m}^3/\text{s}$
$\text{Na} + \text{O}_2 + \text{X} \rightarrow \text{NaO}_2 + \text{X}$	$k_3 = 5.0 \times 10^{-42} (T/200)^{-1.22} \text{ m}^6/\text{s}$
$\text{NaO} + \text{O}_3 \rightarrow \text{NaO}_2 + \text{O}_2$	$k_4 = 1.1 \times 10^{-15} \exp(-568/T) \text{ m}^3/\text{s}$
$\text{NaO} + \text{O}_3 \rightarrow \text{Na} + 2\text{O}_2$	$k_5 = 3.2 \times 10^{-16} \exp(-550/T) \text{ m}^3/\text{s}$
$\text{NaO} + \text{O}_2 + \text{X} \rightarrow \text{NaO}_3 + \text{X}$	$k_6 = 5.3 \times 10^{-42} (T/200)^{-1} \text{ m}^6/\text{s}$
$\text{NaO}_2 + \text{O} \rightarrow \text{NaO} + \text{O}_2$	$k_7 = 5.0 \times 10^{-16} \exp(-940/T) \text{ m}^3/\text{s}$
$\text{NaO}_3 + \text{O} \rightarrow \text{Na} + 2\text{O}_2$	$k_8 = 2.5 \times 10^{-16} (T/200)^{1/2} \text{ m}^3/\text{s}$
$\text{NaO} + \text{H}_2\text{O} \rightarrow \text{NaOH} + \text{OH}$	$k_9 = 4.4 \times 10^{-16} \exp(-507/T) \text{ m}^3/\text{s}$
$\text{NaO} + \text{H}_2 \rightarrow \text{NaOH} + \text{H}$	$k_{10} = 1.1 \times 10^{-15} \exp(-1100/T) \text{ m}^3/\text{s}$
$\text{NaO} + \text{H}_2 \rightarrow \text{Na} + \text{H}_2\text{O}$	$k_{11} = 1.1 \times 10^{-15} \exp(-1400/T) \text{ m}^3/\text{s}$
$\text{NaO} + \text{H} \rightarrow \text{Na} + \text{OH}$	$k_{12} = 3.0 \times 10^{-16} \exp(-668/T) \text{ m}^3/\text{s}$
$\text{NaO}_2 + \text{H} \rightarrow \text{Na} + \text{HO}_2$	$k_{13} = 1.0 \times 10^{-15} \exp(-1000/T) \text{ m}^3/\text{s}$
$\text{NaOH} + \text{H} \rightarrow \text{Na} + \text{H}_2\text{O}$	$k_{14} = 4.0 \times 10^{-17} \exp(-550/T) \text{ m}^3/\text{s}$
$\text{NaO} + \text{CO}_2 + \text{X} \rightarrow \text{NaCO}_3 + \text{X}$	$k_{15} = 1.3 \times 10^{-39} (T/200)^{-1} \text{ m}^6/\text{s}$
$\text{NaCO}_3 + \text{O} \rightarrow \text{NaO}_2 + \text{CO}_2$	$k_{16} = 5.0 \times 10^{-16} \exp(-1200/T) \text{ m}^3/\text{s}$
$\text{NaCO}_3 + \text{H} \rightarrow \text{NaOH} + \text{CO}_2$	$k_{17} = 1.0 \times 10^{-15} \exp(-1400/T) \text{ m}^3/\text{s}$
$\text{NaOH} + \text{CO}_2 + \text{X} \rightarrow \text{NaHCO}_3 + \text{X}$	$k_{18} = 1.9 \times 10^{-40} (T/200)^{-1} \text{ m}^6/\text{s}$
$\text{NaHCO}_3 + \text{H} \rightarrow \text{Na} + \text{H}_2\text{O} + \text{CO}_2$	$k_{19} = 1.1 \times 10^{-17} \exp(-910/T) \text{ m}^3/\text{s}$
$\text{Na} + \text{O}_2^+ \rightarrow \text{Na}^+ + \text{O}_2$	$k_{20} = 2.7 \times 10^{-15} \text{ m}^3/\text{s}$
$\text{Na} + \text{NO}^+ \rightarrow \text{Na}^+ + \text{NO}$	$k_{21} = 3.0 \times 10^{-16} \text{ m}^3/\text{s}$
$\text{Na}^+ + \text{N}_2 + \text{X} \rightarrow \text{Na.N}_2^+ + \text{X}$	$k_{22} = 4.8 \times 10^{-42} (T/200)^{-2.2} \text{ m}^6/\text{s}$
$\text{Na.N}_2^+ + \text{CO}_2 \rightarrow \text{Na.CO}_2^+ + \text{N}_2$	$k_{23} = 8.0 \times 10^{-16} \text{ m}^3/\text{s}$
$\text{Na.N}_2^+ + \text{H}_2\text{O} \rightarrow \text{Na.H}_2\text{O}^+ + \text{N}_2$	$k_{24} = 8.0 \times 10^{-16} \text{ m}^3/\text{s}$
$\text{Na.N}_2^+ + \text{O} \rightarrow \text{Na.O}^+ + \text{N}_2$	$k_{25} = 6.0 \times 10^{-16} \text{ m}^3/\text{s}$
$\text{Na.O}^+ + \text{O} \rightarrow \text{Na}^+ + \text{O}_2$	$k_{26} = 8.0 \times 10^{-16} \text{ m}^3/\text{s}$
$\text{Na.N}_2^+ + \text{e}^- \rightarrow \text{Na} + \text{N}_2$	$k_{27} = 1.0 \times 10^{-12} (T/200)^{-1/2} \text{ m}^3/\text{s}$
$\text{Na.CO}_2^+ + \text{e}^- \rightarrow \text{Na} + \text{CO}_2$	$k_{28} = 1.0 \times 10^{-12} (T/200)^{-1/2} \text{ m}^3/\text{s}$
$\text{Na.H}_2\text{O}^+ + \text{e}^- \rightarrow \text{Na} + \text{H}_2\text{O}$	$k_{29} = 1.0 \times 10^{-12} (T/200)^{-1/2} \text{ m}^3/\text{s}$
$\text{Na.O}^+ + \text{e}^- \rightarrow \text{Na} + \text{O}$	$k_{30} = 1.0 \times 10^{-12} (T/200)^{-1/2} \text{ m}^3/\text{s}$
$\text{Na}^+ + \text{CO}_2 + \text{X} \rightarrow \text{Na.CO}_2^+ + \text{X}$	$k_{31} = 3.7 \times 10^{-41} (T/200)^{-2.9} \text{ m}^6/\text{s}$
$\text{NaO}_2 + h\nu \rightarrow \text{Na} + \text{O}_2$	$k_{32} = 4.0 \times 10^{-9} \text{ s}^{-1}$
$\text{NaOH} + h\nu \rightarrow \text{Na} + \text{OH}$	$k_{33} = 1.0 \times 10^{-9} \text{ s}^{-1}$
$\text{NaO}_3 + h\nu \rightarrow \text{NaO} + \text{O}_2$	$k_{34} = 1.0 \times 10^{-10} \text{ s}^{-1}$
$\text{Na} + h\nu \rightarrow \text{Na}^+ + \text{e}^-$	$k_{35} = 2.0 \times 10^{-11} \text{ s}^{-1}$

extends the model explicitly to estimates of time-varying conditions, describing a mechanism whereby Na^+ in sporadic-*E* layers can be quickly neutralized to form a sporadic sodium layer, and representing the only presently available quantitative theory for sporadic atom layer formation. The specifics of this mechanism will be discussed in greater detail in Chapters 4 and 5. The two reaction rate estimates updated by *Levandier et al.*(1997) are the charge transfer reactions with NO^+ and O_2^+ and are critical to understanding the impact of auroral ionization, as is discussed in Section 3.3. It should also be noted that very recently the results of *Plane et al.*(1998), *Cox and Plane*(1998), and *Levandier et al.*(1997) were combined into a steady-state model by *Plane et al.*(1999) for investigating the sodium layer at 40° N latitude, where they showed that this combination of chemical reactions reproduced a large set of measurements from that latitude.

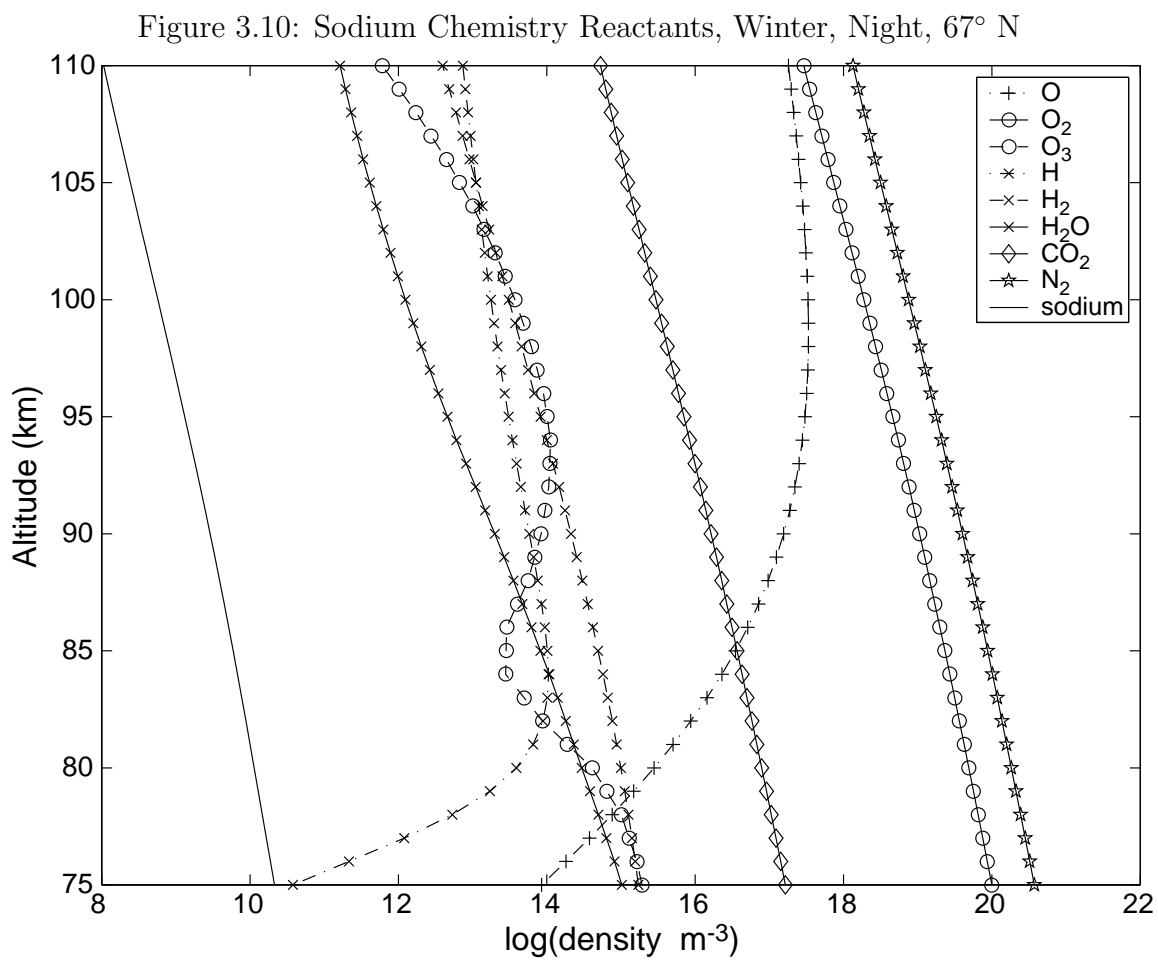
A schematic representation of the chemical reactions for the sodium model is contained in Figure 3.9, showing that sodium is partitioned among 12 different species: Na^+ , Na.O^+ , Na.N_2^+ , Na.CO_2^+ , $\text{Na.H}_2\text{O}^+$, Na , NaO , NaO_2 , NaO_3 , NaOH , NaCO_3 , and NaHCO_3 . Note that Na.O^+ , Na.N_2^+ , Na.CO_2^+ , and $\text{Na.H}_2\text{O}^+$ are all cluster ions and, as such, they are written with a period separating the sodium and ligands. As with the iron model, a number of reactants are involved in this chemistry: O , O_2 , O_3 , H , H_2 , H_2O , CO_2 , N_2 , O_2^+ , NO^+ , a third body X which is taken to be either N_2 or O_2 , free electrons, e^- , whose number density is the sum of all ion densities, and solar photons, $h\nu$. An example altitude profile of the reactants and the total sodium content is shown in Figure 3.10. The various reactant concentrations are taken from the models discussed in Section 3.1 and the specific sources are shown in Table 3.2. Solar photons are included in this sodium model but were excluded from the iron model for several reasons. First, the rate at which sodium is ionized in the absence of atmospheric attenuation has been estimated to be approximately $2 \times 10^{-11} \text{ s}^{-1}$ while the rate for iron is only $5 \times 10^{-13} \text{ s}^{-1}$ [*Swider*(1969)]. Furthermore, the atmospheric attenuation at the ionizing wavelengths for iron and sodium are also very different. For iron the unit optical depth occurs above ~ 110 km while for sodium this depth is down to ~ 40 km [e.g. *Swider*(1969), *Rees*(1989)]. Thus the incident light for ionizing iron is much more attenuated (below the $1/e$ level) when compared to sodium. When the sodium

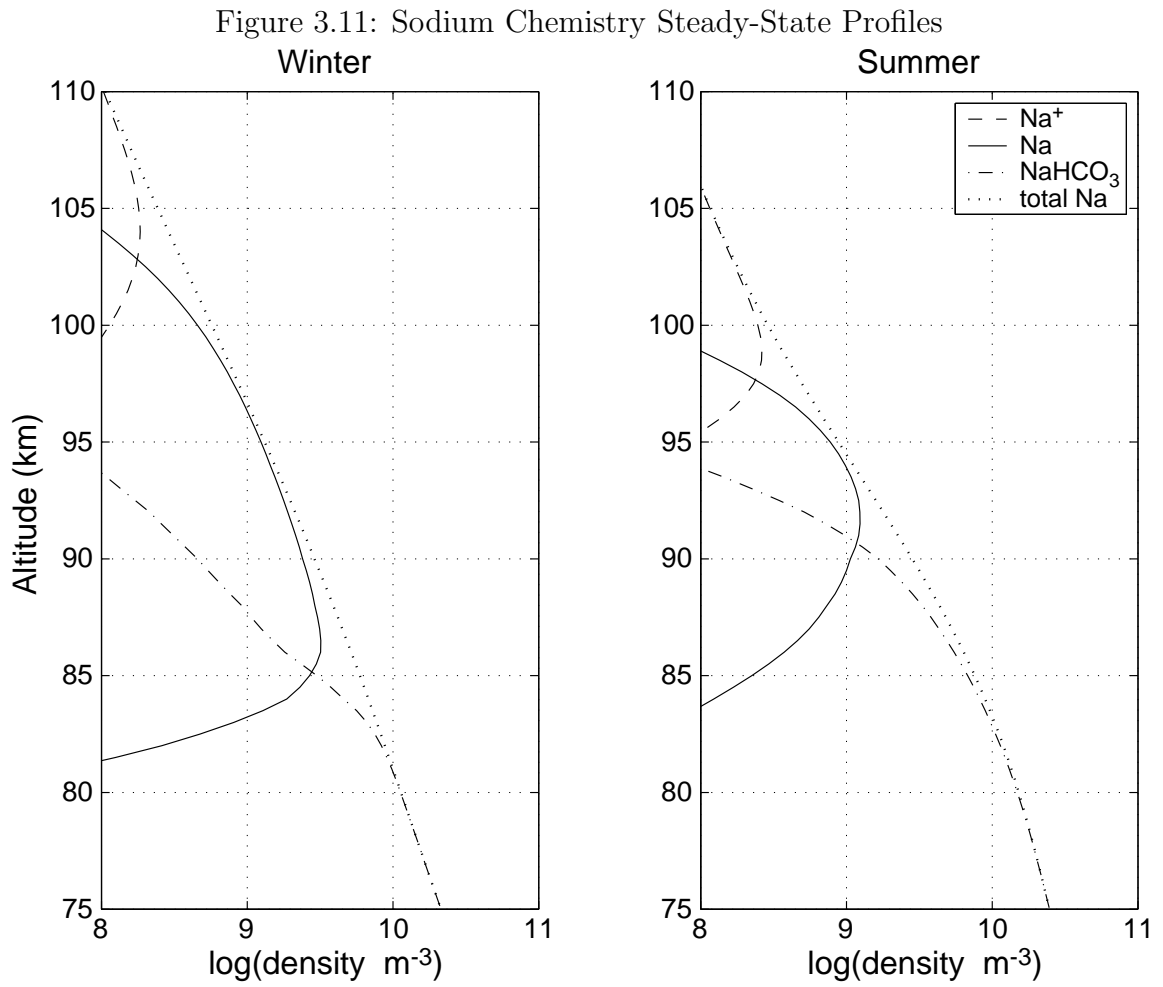
Figure 3.9: Schematic of the Sodium Chemistry Reactions. For each reaction, the reactants are on the left side of the line in the direction of the arrow. The dots in the chemical compounds indicate cluster ions.



model was run with the solar flux terms artificially turned on and off, no significant change in the steady-state chemical makeup of the system was noted. Thus, it can be concluded that solar ionization does not have a significant direct impact on the metal atoms — though it does have a significant indirect impact via the production of NO⁺ and O₂⁺. The exclusion of this effect for iron is thus well supported and, in fact, it can be argued that it could be excluded from the sodium model as well.

In Figure 3.11 the sodium model is used to calculate steady-state profiles of the dominant constituents, Na, Na⁺, and NaHCO₃. This figure is completely analogous to Figure 3.3 for iron with the same set of conditions for both. For sodium, as for iron, the top side of the profile is dominated by the singly ionized atomic state, driven by the ionospheric concentrations of NO⁺ and O₂⁺ which drive reactions k_{20} and k_{21} in Table 3.3. As mentioned earlier, these are the reactions for which rates were determined by *Levandier et al.*(1997) via laboratory experiments. For temperatures typically seen in the ionosphere, even under auroral precipitation conditions, the rate coefficients are nearly constant and not strong functions of temperature. It should be noted that

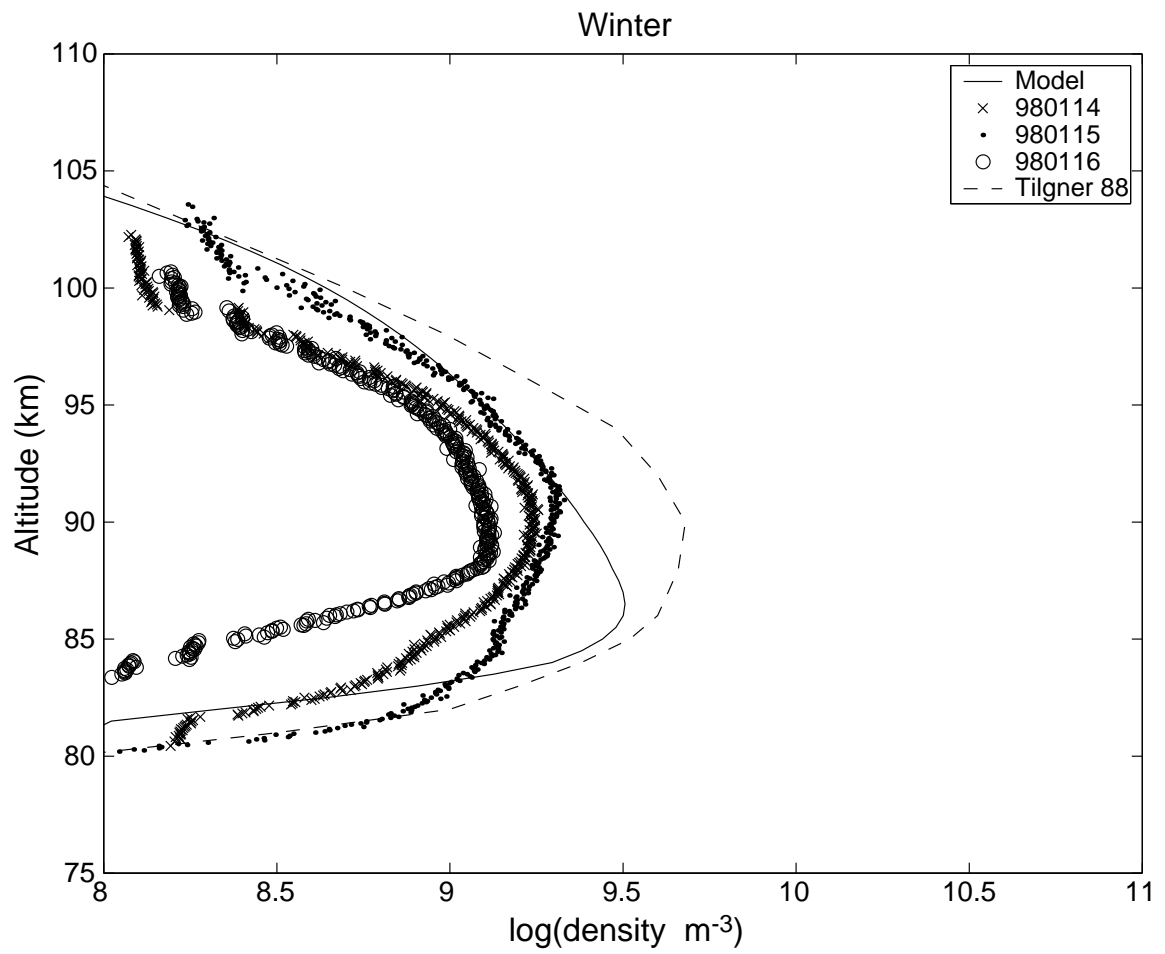




Levandier et al.(1997) were forced to make a number of theoretical corrections to their data, so there is some uncertainty associated with the values. It is also useful to note that the two reaction coefficients, for NO^+ and O_2^+ , differ by nearly an order of magnitude with the reaction for O_2^+ being much faster. This fact, combined with the uncertainty in the relative concentrations of these two ions [*Danilov*(1994)] has at most a subtle effect on the steady-state concentrations of sodium-containing species. However, the case of auroral ionization considered in a time varying sense is more interesting, as we shall see in Section 3.3. The bottom sides of the steady-state profiles in Figure 3.11 are dominated by sodium bicarbonate, NaHCO_3 . This molecule has been shown by *Rajasekhar and Plane*(1993) to be very thermodynamically stable and represents the principle sodium sink in this model. Once tied up in this compound, it is difficult to release the sodium again under normal conditions, though the release of sodium via dissociative electron attachment has been proposed as a source of sporadic sodium layers [*von Zahn and Murad*(1990)]. *Cox et al.*(1993), however, argued that the total density of NaHCO_3 is insufficient to explain sporadic layer densities. Note also that in Figure 3.11 the column content of Na varies greatly with season, a result supported by measurements in *Plane et al.*(1999).

Plane et al.(1998) provided experimental support for the chemistry used in our model. Nonetheless it is instructive to compare the model output with other high latitude measurements. Figure 3.12 presents such a comparison, showing the model output for winter conditions along with measurements of the median Na density profiles from three consecutive nights over Sondrestrom (see Appendix C) and a set of measurements from *Tilgner and von Zahn*(1988). The data from *Tilgner and von Zahn*(1988) in Figure 3.12 were obtained from a 19 night average of the density profiles collected at Andøya, Norway, during the winter of 1985/86. By taking median values from the Sondrestrom system it was possible to remove a number of effects such as atmospheric gravity waves and short duration cloud cover. On the other hand, the altitude profiles in Figure 3.12 also show the signal quantization present in the on-line data integrations (steps in the signals at low densities). Figure 3.12 also illustrates that there is significant night-to-night variability in the median density profiles. Even greater variability is seen when individual 1-minute profiles are inspected. In any

Figure 3.12: Sodium Profile Comparison with Data. Data from three consecutive nights over Sondrestrom and from *Tilgner and von Zahn*(1988).



event, the model output presented in Figure 3.12 is consistent with many of the characteristics of the measured layers. This comparison suggests that at steady-state the model results are consistent with the measurements.

As was done for iron, the sodium model is now used to investigate the transient behavior of the system. Each of the following figures has, as its initial condition, neutral atomic Na with a density of 10^{10} m^{-3} at all altitudes. Figure 3.13 shows the chemical evolution of Na and Na^+ for eight hours under winter night-time conditions for Sondrestrom. Note the very similar behavior of sodium to that of iron in Figure 3.5. Again, the charge transfer reactions which tend to ionize Na above 100 km altitude are very slow due to the low background ion densities at night. After eight hours approximately 4% of the sodium is ionized at 110 km altitude. Next, summer day-time conditions are considered in Figure 3.14. Again analogous to iron, eight hours is sufficient time during the summer day for the ionization of nearly all the sodium at 110 km. The half-life of neutral sodium at 110 km is also on the order of two hours. Note that a prominent Na layer forms between about 87 and 96 km altitude — approximately 5 km higher than for iron in Figure 3.7. Figures 3.13 and 3.14 both show that Na disappears very rapidly below about 85 km. Figure 3.11 showed that the dominant steady-state constituent at those altitudes is NaHCO_3 . Figure 3.15 shows the evolution of several important Na compounds for the first 30 seconds after ‘deposition’. As with iron, the loss of neutral atomic Na is not a simple transfer to NaHCO_3 . Intermediate species such as NaO and NaO_2 hold the sodium for some time before eventually transferring it to the sink. It can be shown, in fact, that the reactant that determines the steepness of the bottom of the Na layer is O, though comparisons of instantaneous O profiles and Na profiles must be done with the various system time constants in mind.

3.3 Auroral Effects

Prior to discussing the effects of aurorae on the chemistry of upper atmospheric metals, we now provide some background about the nature of auroral phenomena.

Figure 3.13: Sodium Reaction Rate, Winter, Night. Initial condition is neutral Na at all altitudes.

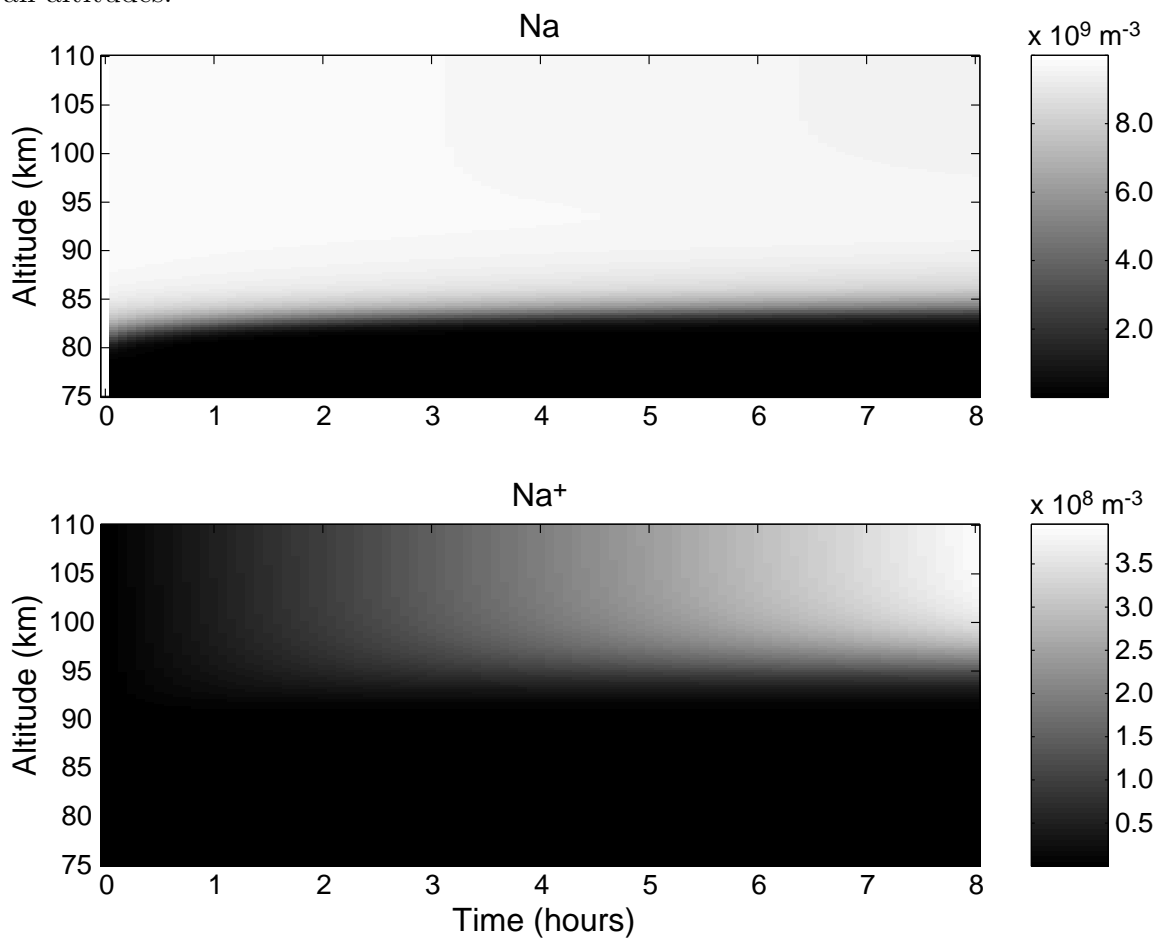


Figure 3.14: Sodium Reaction Rate, Summer, Day

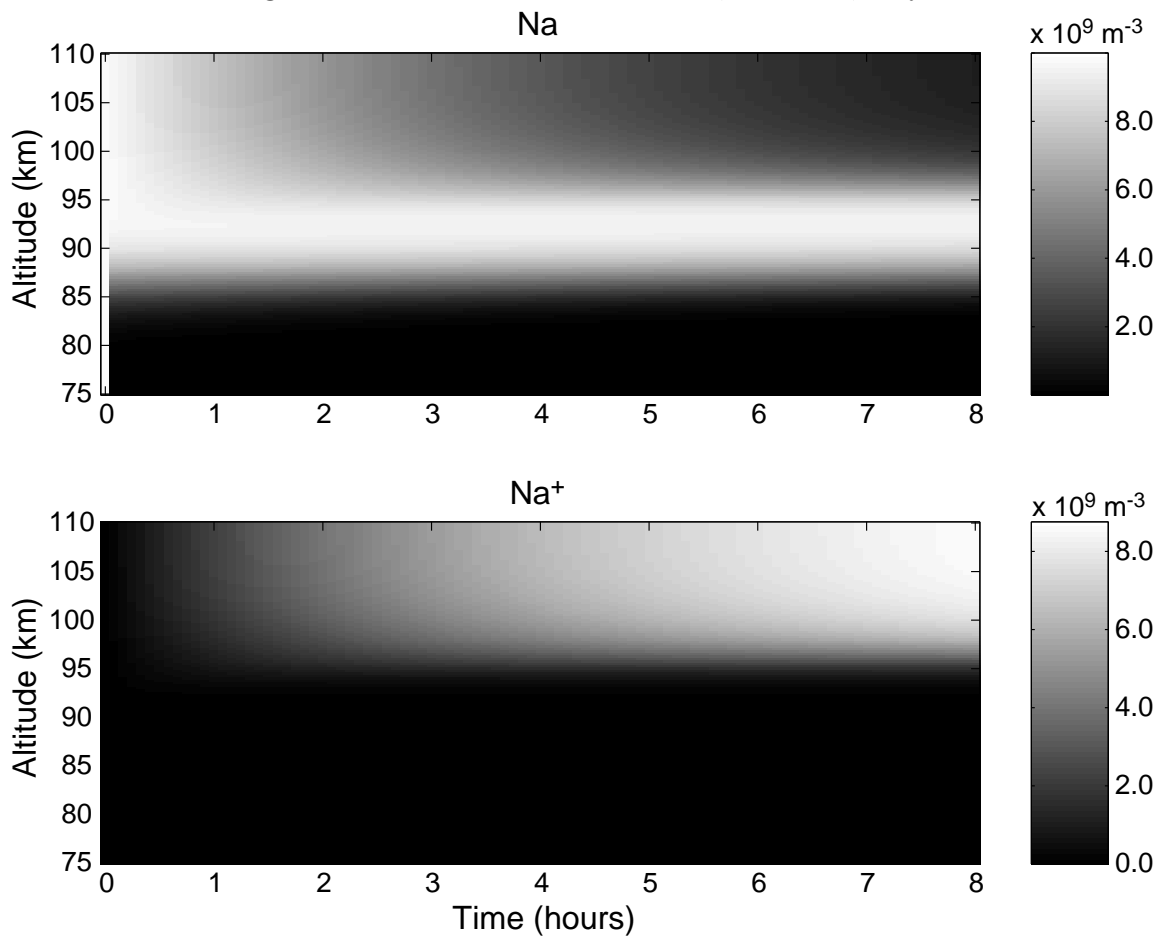
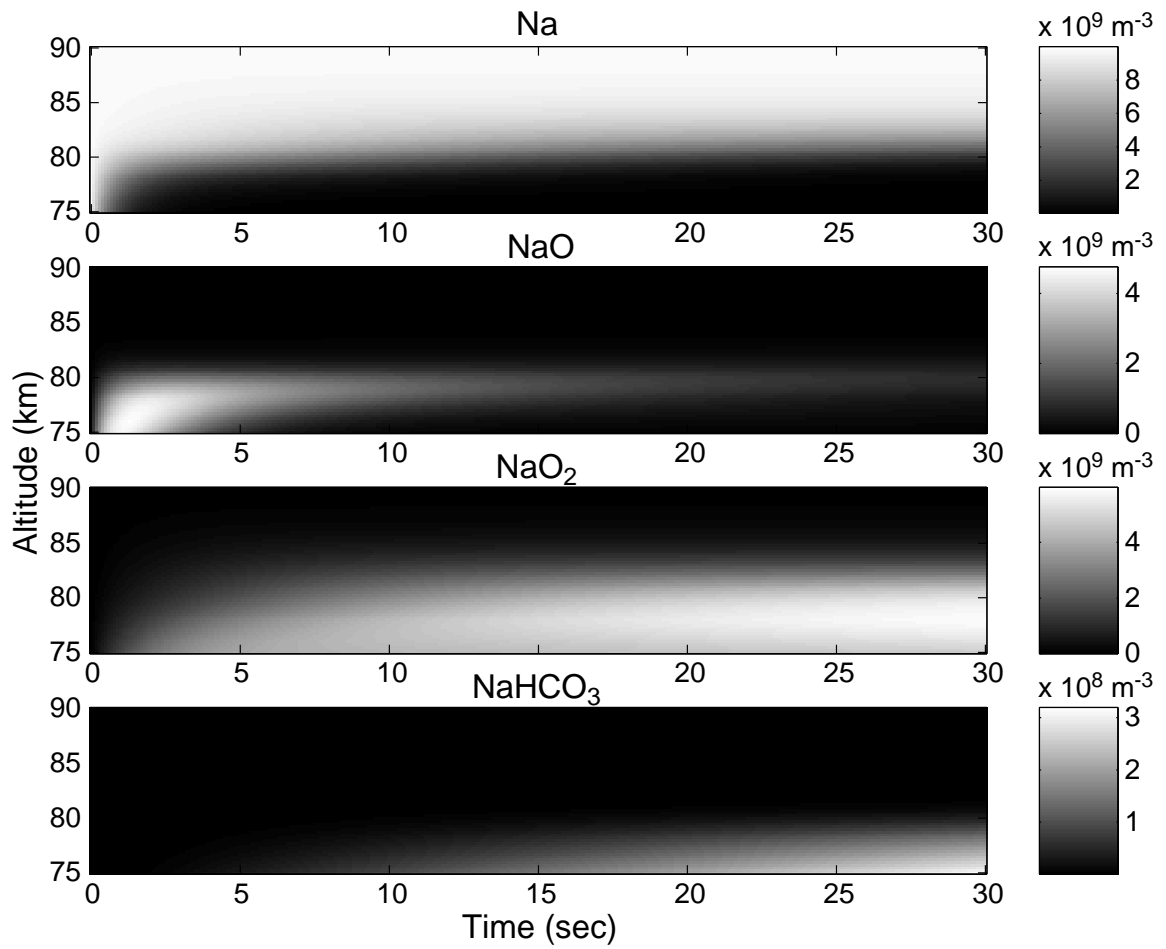


Figure 3.15: Sodium Reaction Rate, Winter, Night, 75-90 km



Aurorae have been the topic of scientific investigation for several centuries and a surprising amount was deduced from ground-based observations prior to the advent of rocket flight. It has long been recognized that auroral arcs are produced by energetic electrons (and to a lesser extent protons) which penetrate the polar atmosphere from above [e.g. *Chamberlain(1995)*, *Brekke(1997)*]. These electrons typically have energies on the order of keV to tens of keV and the phenomena known as aurorae arise when this energy is deposited in the atmosphere, producing light in the form of atomic and molecular emissions, heat, and ionization. The altitudes at which this energy is deposited is dependent upon the energies and pitch-angle distributions of the precipitating particles as well as on the atmospheric density profile [*Rees(1963)*, *Rees(1982)*, *Rees(1989)*]. The peak deposition altitude for 1 keV electrons is approximately 170 km while 40 keV electrons deposit most of their energy at around 90 km. Thus, the aurorae of greatest interest here must have significant fluxes of electrons with energies greater than about 10 keV. Electrons with such high energies are commonly present in aurorae and aurorally produced electron densities on the order of 10^{12} m^{-3} are regularly seen at high latitudes down to altitudes of 100 km and lower. Such high electron densities below 90 km altitude, on the other hand, are quite rare. Figure 3.16 shows an example of electron density profiles as a function of time for an intense auroral display measured with the Sondrestrom Radar.

For both solar illumination and auroral particle produced ionization, the direct products of the ionizing processes are primarily N_2^+ and O_2^+ . Rocket-borne mass spectrometer measurements of the *E* region show very little N_2^+ , however, because rapid chemical reactions quickly reduce the concentrations of that species in favor of NO^+ . A summary of some of the relevant reactions is given in Table 3.4, which also includes estimates of the reaction rates through the inclusion of estimates of reactant concentrations. The value for NO was estimated from *Siskind et al.(1998)*, the electron density was taken as 10^{12} m^{-3} , and the other reactants are given in Figure 3.2. Note that this estimate indicates that the highest reaction rates are $k_5[\text{O}]$ and $k_6[\text{O}_2]$ by several orders of magnitude and that both of the corresponding fast reactions remove N_2^+ . The lifetime of N_2^+ is thus extremely short and the dominant ions in the *E* region are NO^+ and O_2^+ . The ratio of these two reaction products is not easily

Figure 3.16: Auroral Electron Density Example. Measurements are from the Sondrestrom Incoherent Scatter Radar and have been integrated in time. The density gray scale has been allowed to saturate at 10^{12} m^{-3} , but some densities reached twice that value.

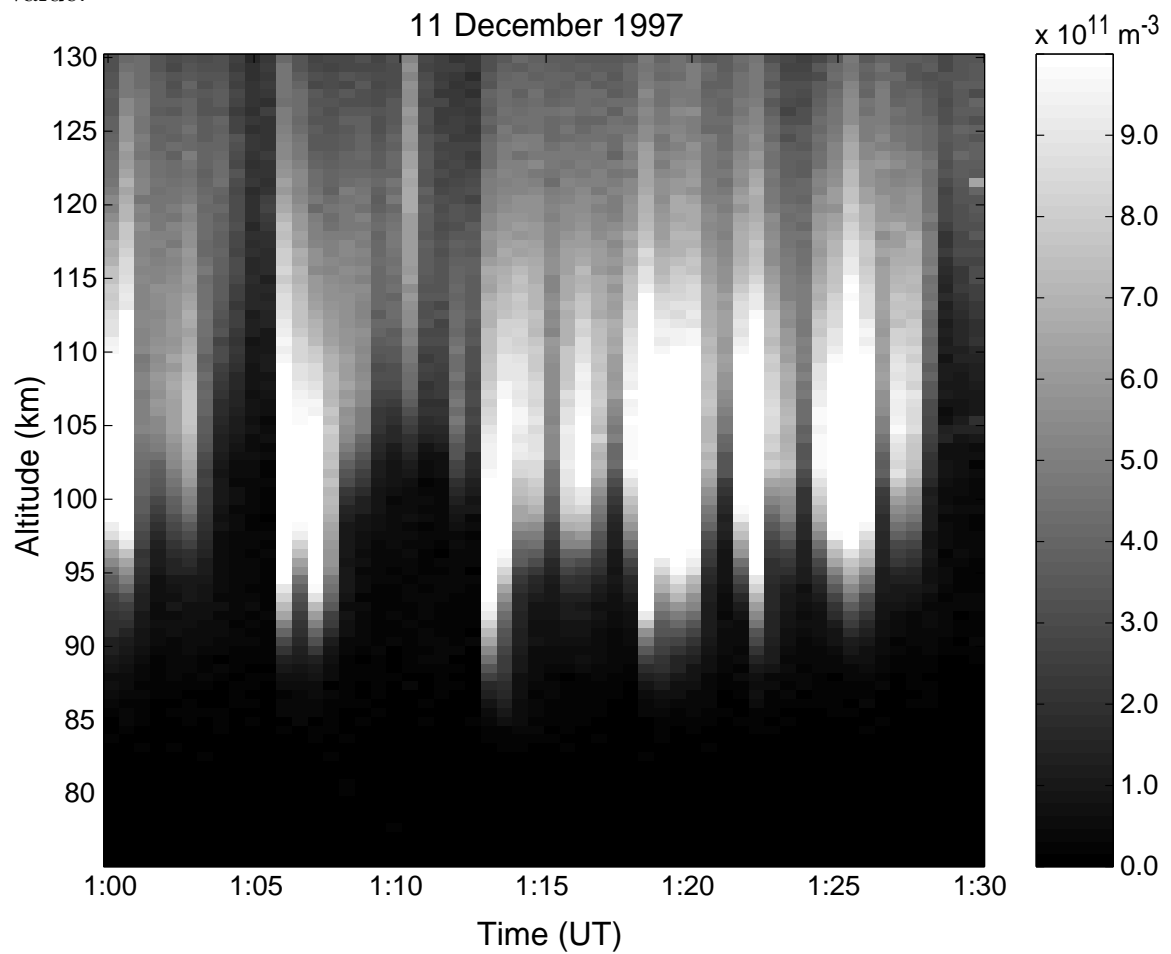


Table 3.4: *E*-Region Oxygen and Nitrogen Chemistry [Brekke(1997)]. Rate estimates use $[e^-] \approx 10^{12} \text{ m}^{-3}$, $[\text{NO}] \approx 5 \times 10^{13} \text{ m}^{-3}$, $[\text{N}_2] \approx 8 \times 10^{18} \text{ m}^{-3}$, $[\text{O}_2] \approx 2 \times 10^{18} \text{ m}^{-3}$, $[\text{O}] \approx 3 \times 10^{17} \text{ m}^{-3}$, $T = 300 \text{ K}$.

Reaction	Rate Coefficient (m^3/s)	Rate Estimate (s^{-1})
$\text{O}_2^+ + e^- \rightarrow \text{O} + \text{O}$	$k_1 = 1.9 \times 10^{-13} (\text{Te}/300)^{-0.5}$	$k_1[e^-] \approx 0.2$
$\text{O}_2^+ + \text{NO} \rightarrow \text{NO}^+ + \text{O}_2$	$k_2 = 4.4 \times 10^{-16}$	$k_2[\text{NO}] \approx 0.02$
$\text{O}_2^+ + \text{N}_2 \rightarrow \text{NO}^+ + \text{NO}$	$k_3 = 5.0 \times 10^{-22}$	$k_3[\text{N}_2] \approx 0.004$
$\text{N}_2^+ + e^- \rightarrow \text{N} + \text{N}$	$k_4 = 1.8 \times 10^{-13} (\text{Te}/300)^{-0.39}$	$k_4[e^-] \approx 0.1$
$\text{N}_2^+ + \text{O} \rightarrow \text{NO}^+ + \text{N}$	$k_5 = 1.4 \times 10^{-16} (\text{T}/300)^{-0.44}$	$k_5[\text{O}] \approx 40$
$\text{N}_2^+ + \text{O}_2 \rightarrow \text{N}_2 + \text{O}_2^+$	$k_6 = 5.0 \times 10^{-17} (\text{T}/300)^{-0.8}$	$k_6[\text{O}_2] \approx 100$
$\text{NO}^+ + e^- \rightarrow \text{N} + \text{O}$	$k_7 = 2.1 \times 10^{-13} (\text{Te}/300)^{-0.85}$	$k_7[e^-] \approx 0.2$

estimated here, however, because of the role of O and NO in the reactions. The density of NO is significantly affected by auroral precipitation [Swider and Narcisi(1977), Siskind et al.(1998)] and theoretical studies have shown that the resulting balance between NO^+ and O_2^+ depends on the length of time the aurora remains present [Jones and Rees(1973), Rees and Jones(1973)]. It was seen in Section 3.1 that this variability does not have a significant impact on the iron chemistry. For sodium, however, this uncertainty needs to be addressed.

The influence of auroral ionization on the chemistries of metallic atoms was discussed briefly by Nygrén et al.(1990) in the context of a source of metal ions for sporadic-*E* layer formation. In their analysis, Nygrén et al.(1990) postulated a source of neutral metal atoms and estimated the ionization effects from direct auroral electron impact versus charge exchange from aurorally produced ionization enhancements. Their argument basically considered that the probability of ionizing a metal atom by electron impact must be approximately equal (within an order of magnitude) to the mixing ratio of the metal atoms in the background atmosphere. As is shown in Figure 3.2, this mixing ratio is only approximately one part in 10^{10} . Even considering the fact that the effect is integrated (because the lifetime of metal ions tends to be long due to slow recombination rates), the probability of ionization due to electron impact is much lower than that due to charge exchange. However, Nygrén et al.(1990) did not take into consideration the natural steady-state chemical makeup of the metals and simply assumed a source of neutral metal atoms — the availability of which we

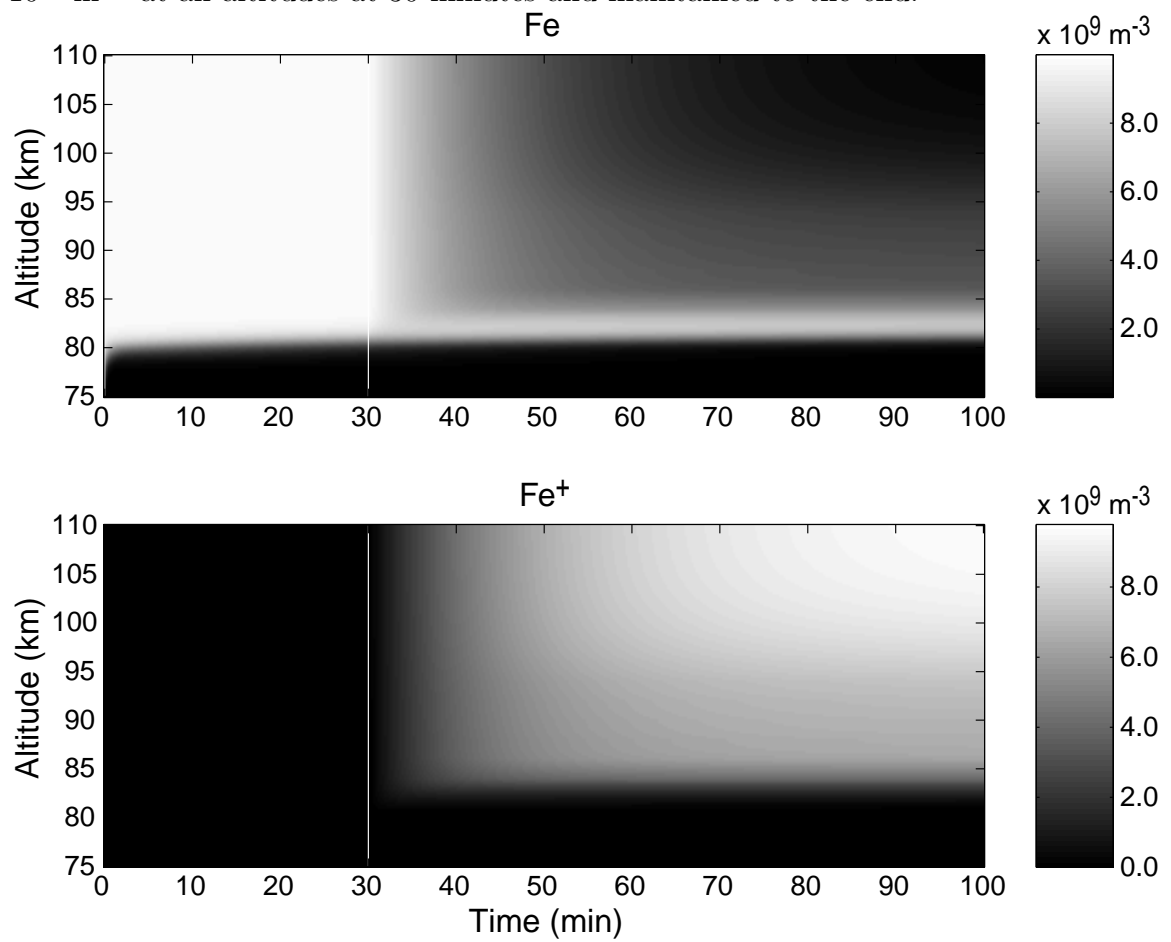
saw to be highly altitude dependent in the previous sections. They also used a very simple model to represent the chemistry of the region, calculating only the ionization arising from an assumed charge transfer rate coefficient of $5 \times 10^{-16} \text{ m}^3/\text{s}$. In our work we consider the chemistry in greater detail with the help of the models described in the previous sections.

3.3.1 Auroral Effects on Iron Chemistry

We first examine the influence of auroral electron density enhancements on iron in the context of recently deposited neutral Fe, similar to the case investigated in Figures 3.5, 3.6, and 3.7. In this case, a fixed amount of Fe is introduced at all altitudes and the simulation is allowed to run for 30 minutes, after which time an enhancement in electron density of 10^{12} m^{-3} is added at all altitudes. Although the resulting electron density profile is not a realistic representation of that produced by an auroral arc, we note that our intent here is to investigate the influence of enhanced ionization at each altitude without having to sort out the altitude dependencies of the ionization from those imposed by the chemistry. Figure 3.17 contains the result of the model run. As anticipated, we see that this sudden enhancement in electron density (also in NO^+ and O_2^+) has an immediate impact on the rate of ionization of Fe. At altitudes above 90 km half the available Fe is ionized in just over 10 minutes, exactly as predicted on the basis of the rate coefficients for charge transfer. From Table 3.1, both k_{17} and k_{18} are approximately $10^{-15} \text{ m}^3/\text{s}$, which means that the effective rate with a 10^{12} m^{-3} electron density should be 10^{-3} s^{-1} , corresponding to an e-folding time (ignoring all other reactions) of 1000 seconds, or 16.7 minutes. Note that just above 80 km there is a region where the ionization reaction is not effective, leading to the formation of a narrow Fe layer. Thus it appears that even very energetic auroral particles have an effective lower altitude limit, based on this chemistry.

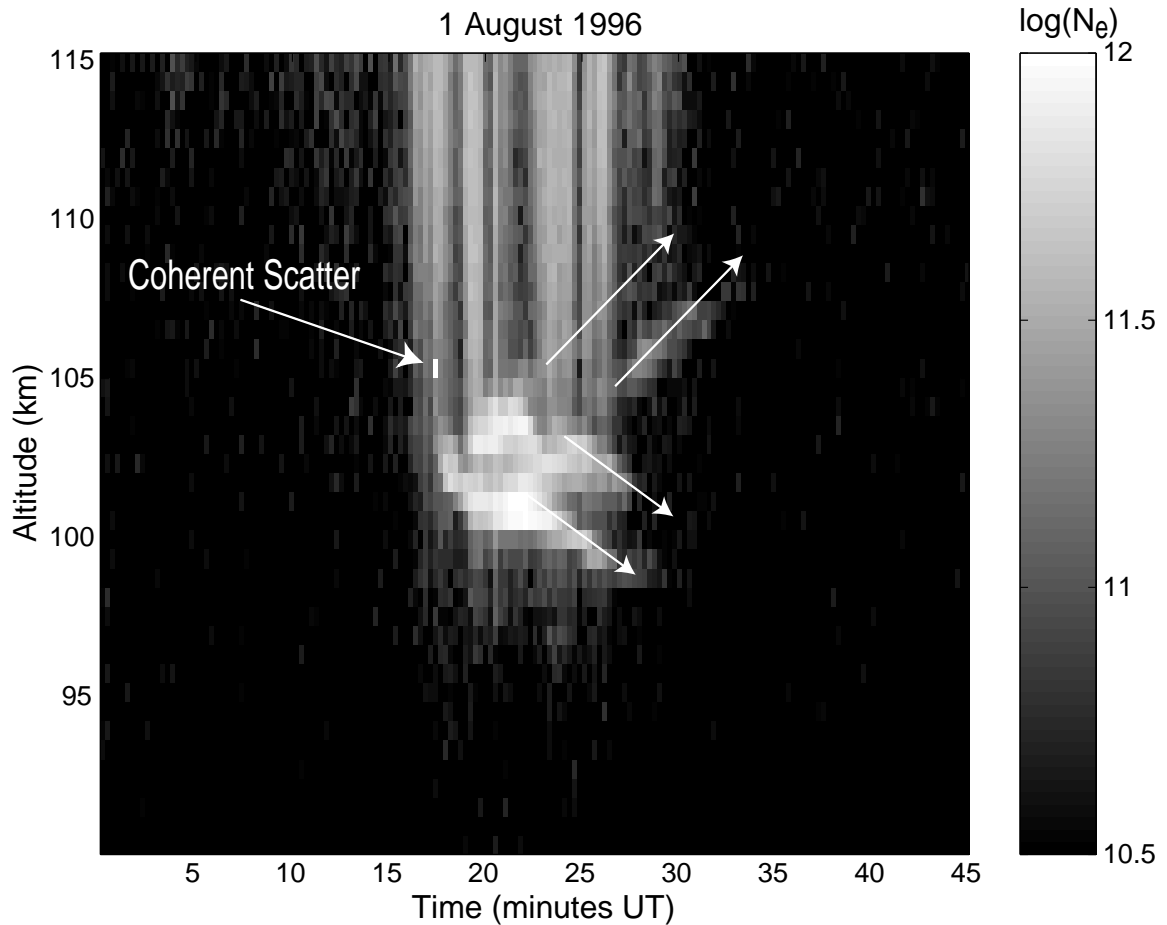
The dramatic increase in ionization rate due to auroral particle precipitation can have significant implications for recently deposited meteoric material. In particular, a neutral meteor trail which is normally not detectable by radiowave techniques will diffuse into the background before a significant portion of that material has time to

Figure 3.17: Iron Reaction Rate, Auroral Effect on Recently Deposited Fe, Winter Night. Initial condition is neutral Fe at all altitudes. Electron density is enhanced by 10^{12} m^{-3} at all altitudes at 30 minutes and maintained to the end.



ionize. On the other hand, a meteoroid ablating in an auroral arc can potentially ionize prior to diffusion and leave a detectable ion trail behind. In terms of the incoherent-scatter radar measurements described in Appendix B, the *detection* of such an ion trail is, however, not likely to be a frequent occurrence for a number of reasons. First, the amount of meteoric material deposited must be quite large for it to exceed the detection threshold of, for example, $\sim 10^{10} \text{ m}^{-3}$ for the incoherent scatter radar at Sondrestrom. Simple calculations indicate that a meteoroid on the order of 0.1 grams or more in mass must ablate completely to yield a measurable amount of material in a fully ionized trail, i.e., the size of a meteoroid that makes up a typical shooting star. The problem of measuring this effect is that the volume probed by the Sondrestrom Radar is quite small during any single measurement — on the order of 1 km across at *E*-region altitudes (note that the overall coverage of the radar can be quite large with the aid of antenna motion). The chances of a large meteoroid and aurora entering the radar volume simultaneously is similarly small. This low probability of *detection* can be contrasted with the probability of *occurrence* of this effect. The total volume of the auroral oval is quite large and meteoroids very likely ablate in that region frequently. In any event, at least one candidate for this effect was discovered in the incoherent scatter radar data from Sondrestrom, as displayed in Figure 3.18. What makes this a possible candidate are, first, the coherent return from a hard target immediately prior to the formation of the sporadic layers and, second, the divergent behavior of the layers. The hard target may be an ablating meteoroid (though it may also be a range-aliased return from an orbiting satellite). Note that this coherent return appears near the start of the local auroral ionization enhancement, which shows up as enhancements extending downward from above the top of the figure. One reasonable explanation for the time series in Figure 3.18 is that a nearly vertically-oriented meteor trail was advected into the radar's antenna beam by neutral winds. Shears in the winds are known to distort such trails and the time sequence in the figure may well be such a distorted trail. In this scenario, the apparent divergence of four thin ionization layers are simply different parts of the trail drifting into the beam as time progresses. It might be argued that the coherent return measurement and thin layer formation are simply coincidental, but the problem still

Figure 3.18: Example of Auroral Ionization of Meteoric Material? Spectral analysis confirmed that the indicated pixel is a coherently scattered return (narrow spectral width). Auroral ionization extends downward from above and the four arrows indicate four thin sporadic ionization layers (incoherently scattered). Time is in minutes after UT midnight.



remains to explain the divergent behavior of multiple thin layers. This behavior is not easily described by the presently accepted sporadic- E formation theories discussed in Chapter 4.

Next, the influence of auroral ionization on the state of the *background* Fe layer is investigated by initializing the model with the winter profile of Figure 3.3. Electron densities are enhanced by 10^{12} m^{-3} at all altitudes for 10 minutes starting 5 minutes into the model run (so the background level is visible) and the evolution of Fe and Fe^+ are displayed for these conditions in Figure 3.19. Note that 10 minutes of enhanced ionization has a dramatic effect on the state of Fe and that the conversion back to the steady-state condition is very slow. This slow return to a neutral state has implications for the portion of meteoric material that is deposited in an ionized state at these altitudes and it suggests that the ionized material will not reach equilibrium quickly. On the other hand, Figure 3.19 also shows that the steady-state densities are not greatly affected for altitudes above about 90 km, due, of course, to the fact that the steady-state condition for iron above 90 km is already ionized! With the majority of auroral ionization occurring above this altitude (e.g. Figure 3.16), the implication here is that auroral precipitation will typically *not* affect the background Fe layer. As mentioned earlier, however, it may affect recently deposited material or material that has formed sporadic atom layers of iron at higher altitudes.

3.3.2 Auroral Effects on Sodium Chemistry

As was done with iron, the effects of auroral ionization enhancements on sodium are first considered with regard to recently deposited neutral Na. The model is initialized with a fixed amount (10^{10} m^{-3}) of Na at all altitudes and then advanced in time. After 30 minutes the ion density is increased at all altitudes by 10^{12} m^{-3} . Unlike the case for iron, the charge exchange reactions which ionize sodium have very different rate constants. This fact has long been recognized, having been reported from laboratory measurements at least as early as *Farragher et al.*(1969). The updated rate constants from *Levandier et al.*(1997) put the rate coefficient for charge transfer with NO^+ at $3.0 \times 10^{-16} \text{ m}^3/\text{s}$ and with O_2^+ at $2.7 \times 10^{-15} \text{ m}^3/\text{s}$ (see Table 3.3). As a result of the

Figure 3.19: Iron Reaction Rate, Auroral Effect on Background Fe Profile, Winter Night. Initial condition is steady-state profile for Fe and its compounds. Electron density is enhanced by 10^{12} m^{-3} at all altitudes between 5 minutes and 15 minutes, as indicated by the white rectangles.

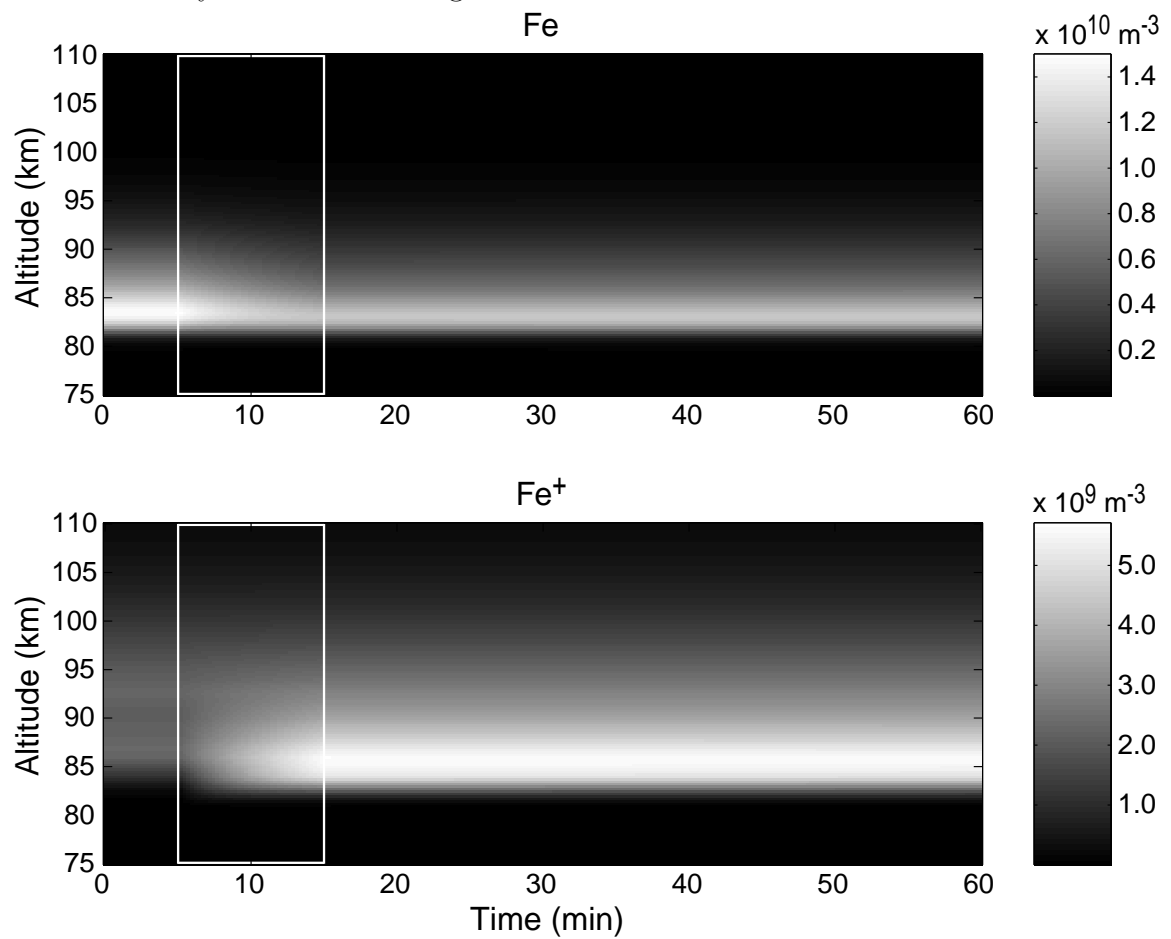
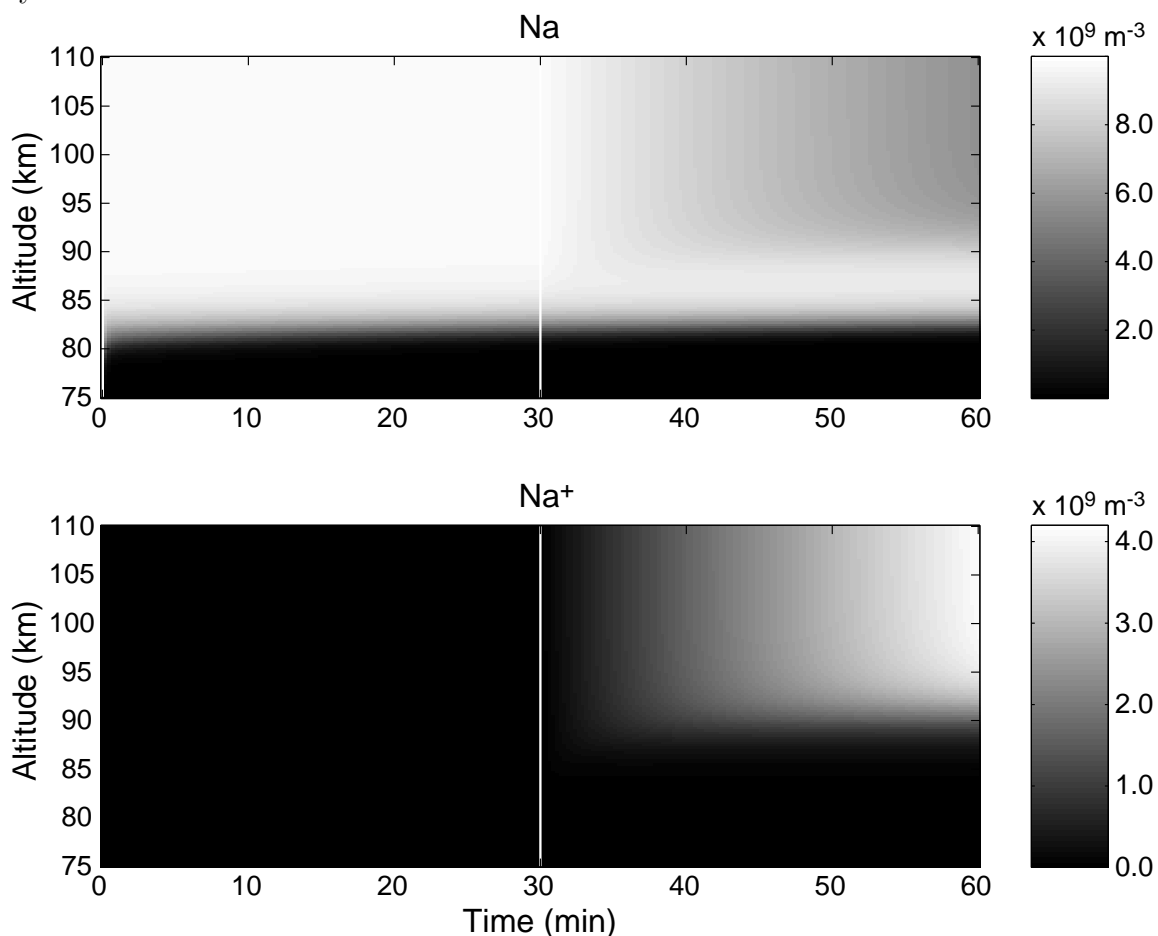
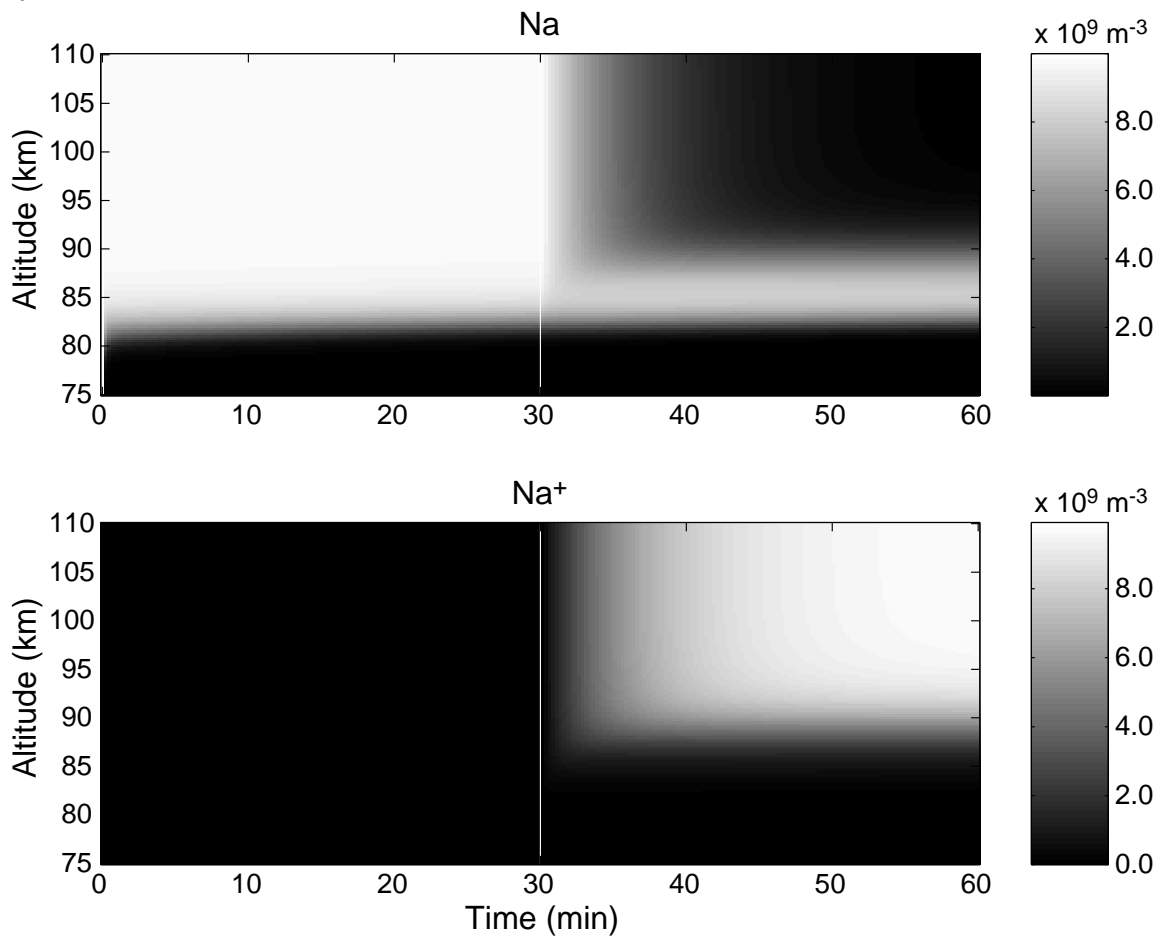


Figure 3.20: Sodium Reaction Rate, NO^+ Auroral Effect on Recently Deposited Na, Winter Night. Initial condition is neutral Na at all altitudes. NO^+ density is enhanced by 10^{12} m^{-3} at all altitudes at 30 minutes and maintained to the end.



previously mentioned variability in the $[\text{O}_2^+]/[\text{NO}^+]$ ratio, the model is run twice, with the assumption that the entire auroral ionization enhancement is associated with each of these ions, yielding an estimate of bounds on the behavior that can be expected. The first sodium example is shown in Figure 3.20 for NO^+ . This figure shows the appreciable enhancement in charge transfer rate that arises from this level of added ionization. After 30 minutes of auroral ionization approximately 40% of the Na at altitudes above 95 km is converted to Na^+ . Figure 3.21 contains a similar plot for O_2^+ . The much greater charge transfer rate is clearly visible and essentially all of the

Figure 3.21: Sodium Reaction Rate, O_2^+ Auroral Effect on Recently Deposited Na, Winter Night. Initial condition is neutral Na at all altitudes. O_2^+ density is enhanced by 10^{12} m^{-3} at all altitudes at 30 minutes and maintained to the end.



Na has been ionized in only 10 to 15 minutes. As with iron, there remains a layer of neutral Na from approximately 82 to 90 km altitude which is unaffected by the added ionization. The e-folding time constants for the charge exchange reactions with each of these ions can readily be calculated from the reaction rates. For the reaction with NO^+ this time constant is 55 minutes; for the O_2^+ reaction it is 6.2 minutes. For a realistic ionosphere the e-folding time is expected to be somewhere between these values. *Swider and Narcisi(1977)* showed that there is often, though not always, more NO^+ than O_2^+ in the auroral E region so it might be expected that the appropriate time constant favors the slower reaction. Figure 3.22 shows the variation of this time constant with changes in the NO^+ and O_2^+ composition, assuming a 10^{12} m^{-3} total increase, indicating that the most significant changes in the time constant occur for very low O_2^+ levels, which is where *Swider and Narcisi(1977)* indicates the relative concentrations might be. Thus, unless a measurement of the relative concentrations of O_2^+ and NO^+ can be made for the specific situation of interest, the resulting estimate of the influence of auroral ionization on neutral Na will have large errors associated with it. However, Figures 3.20 and 3.21 put bounds on the influence.

We now address the possible influence of auroral ionization on the steady-state sodium layer. The conditions for the following figures are identical to those for the similar analysis of iron chemistry in Figure 3.19. The only exception is that the additional ionization is assumed to be associated with just one background ion at a time. Figure 3.23 shows the auroral influence for NO^+ , indicating that the slow charge transfer rate with NO^+ yields only a subtle change in the neutral Na layer with a 10 minute auroral enhancement. Figure 3.24 shows results for the case of pure O_2^+ . In this case, the change in the Na layer is significant, especially from approximately 90 km altitude and upward. Unlike the case for iron, the model prediction of the steady-state sodium layer does have significant neutral Na densities at these higher altitudes and, as a result, it should be possible to see this effect under some circumstances. It must be recognized, of course, that 10^{12} m^{-3} at 90 km represents a fairly intense and relatively rare auroral form, the observation of which may require some patience. On the other hand, many sporadic sodium layers, with significantly enhanced column contents, do occur well above this altitude so such measurements should be possible, and indeed we

Figure 3.22: Sodium Charge Exchange Time Constant versus O_2^+ Fractional Concentration. Total ion concentration is 10^{12} m^{-3} .

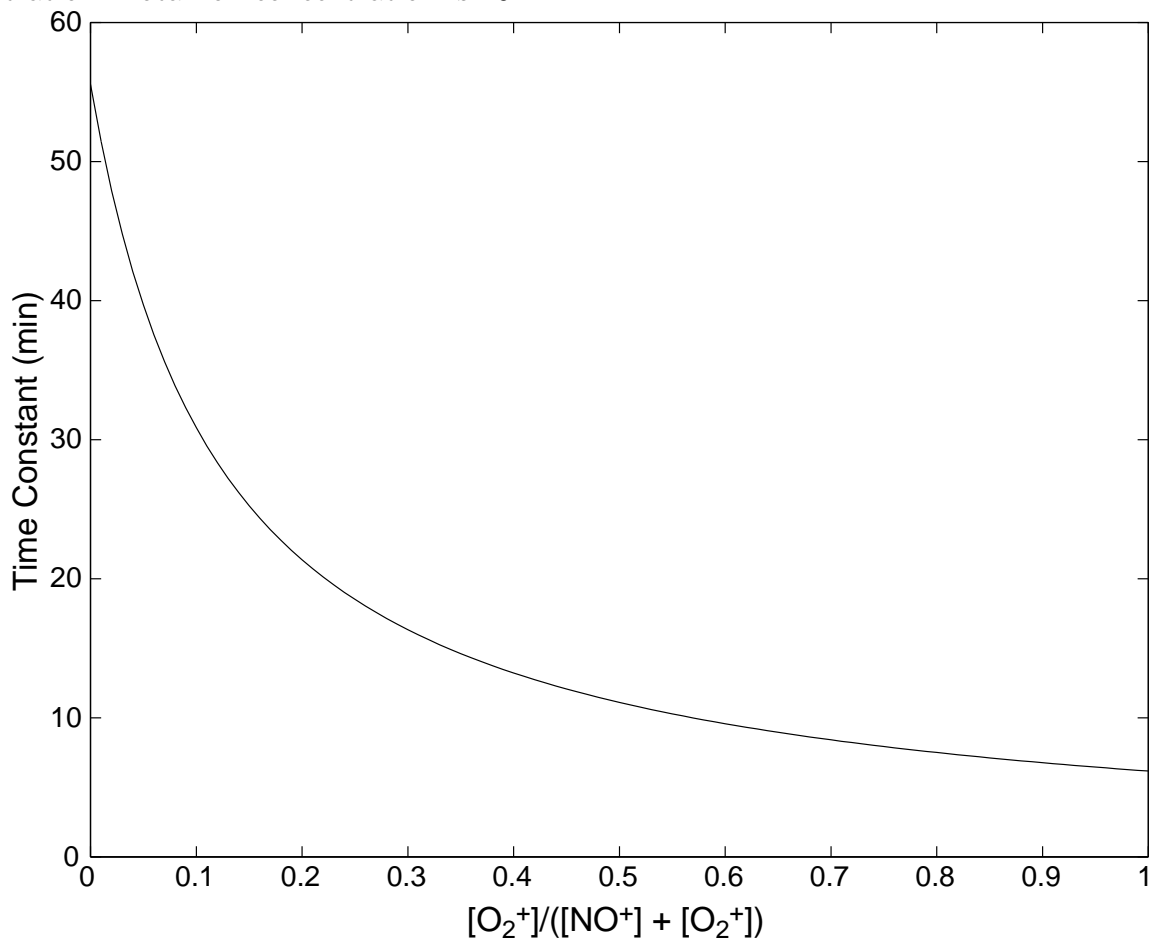


Figure 3.23: Sodium Reaction Rate, NO^+ Auroral Effect on Background Na Profile, Winter Night. Initial condition is steady-state profile for Na and its compounds. Electron density is enhanced by 10^{12} m^{-3} at all altitudes between 5 minutes and 15 minutes, as indicated by the white rectangles.

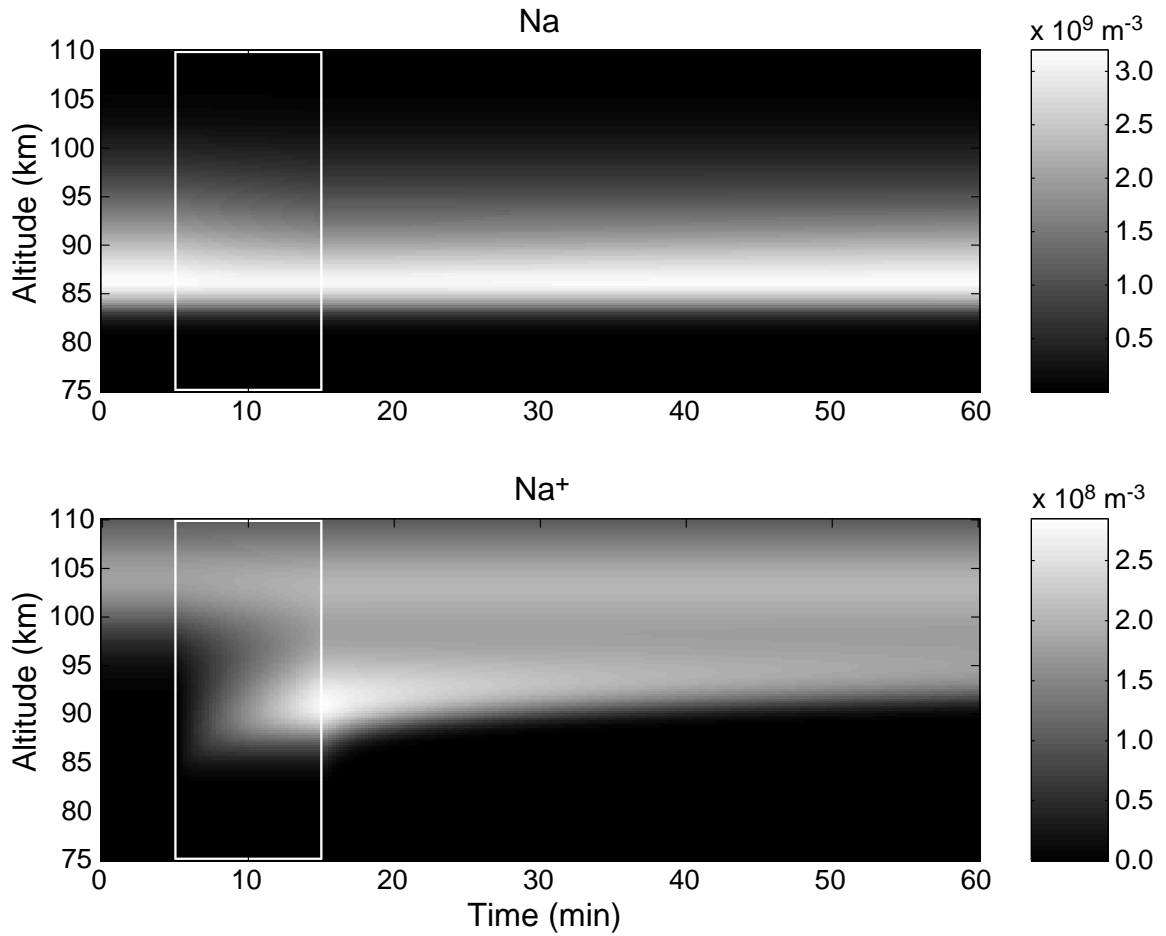


Figure 3.24: Sodium Reaction Rate, O_2^+ Auroral Effect on Background Na Profile, Winter Night. Initial condition is steady-state profile for Na and its compounds. Electron density is enhanced by 10^{12} m^{-3} at all altitudes between 5 minutes and 15 minutes, as indicated by the white rectangles.

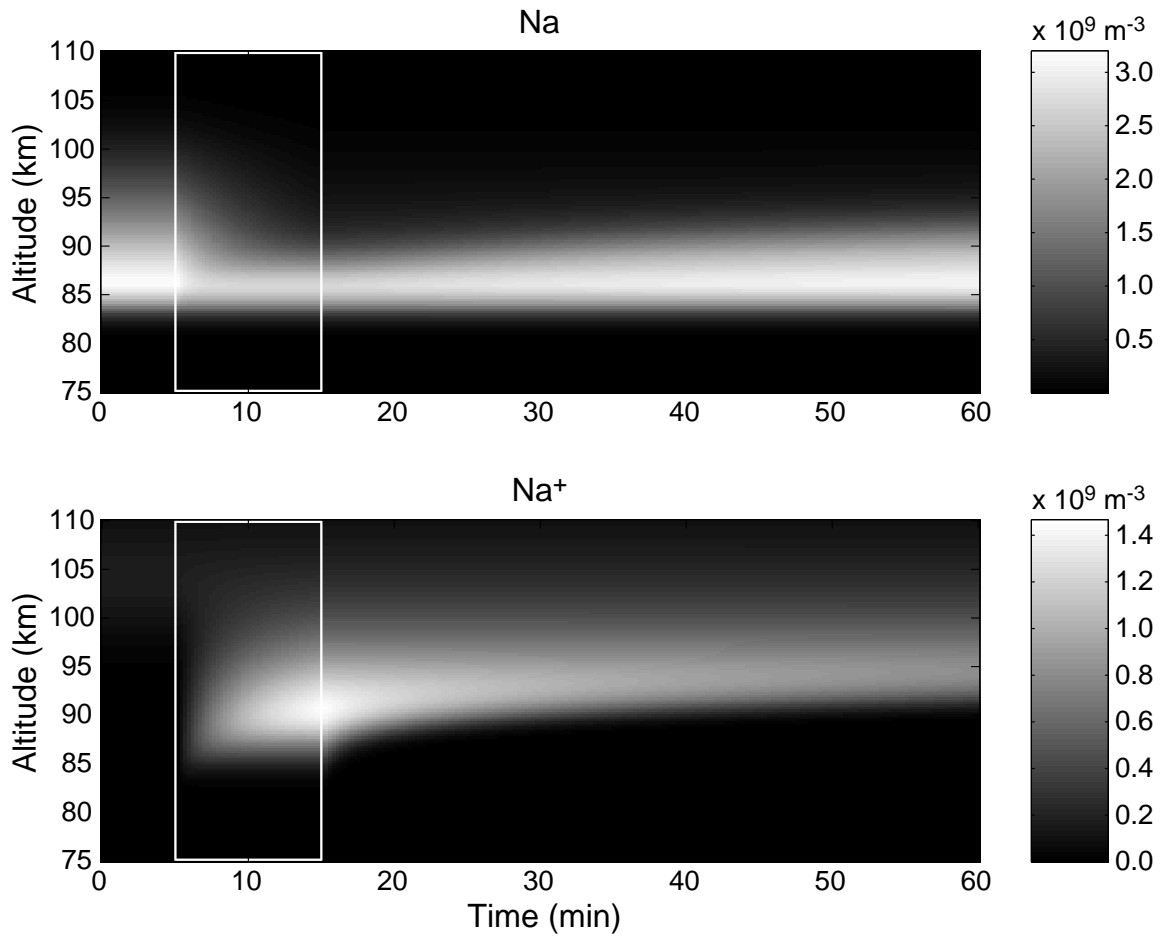
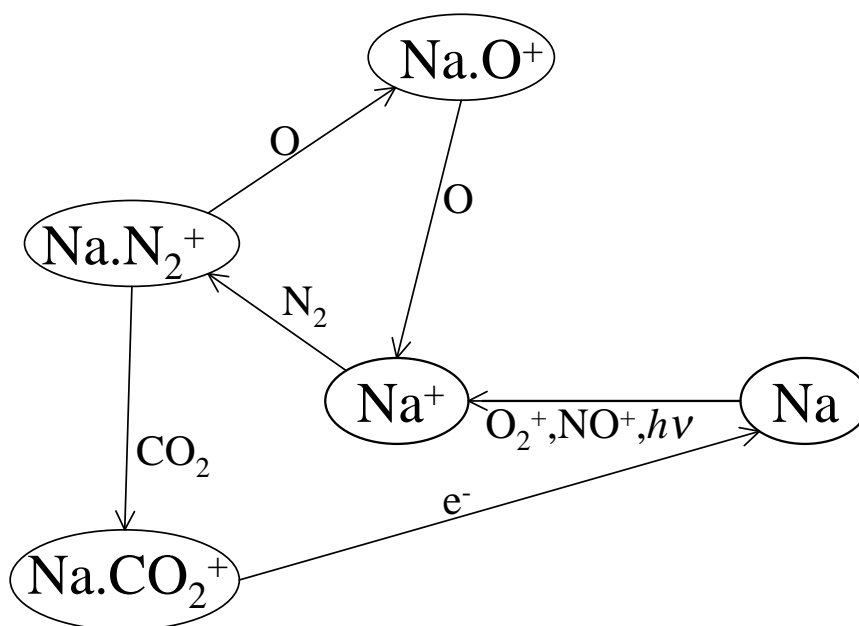


Figure 3.25: Schematic of a Subset of the Sodium Chemistry Reactions from *Cox and Plane*(1998). The dots in the chemical compounds indicate cluster ions.



illustrate such an example in Chapter 5. A significant qualitative difference between the sodium chemistry of Figures 3.23 and 3.24 and the iron chemistry of Figure 3.19 is in the response of the layers to the removal of the enhanced ionization. For the case of iron the response was extremely slow, with no noticeable recombination over the course of the 45 minutes of the model run. Sodium, on the other hand, at lower altitudes is seen to recombine much more rapidly, due, essentially, to the chemical pathways investigated by *Cox and Plane*(1998). Referring to Figure 3.25, *Cox and Plane*(1998) discussed the cluster-ion reactions involving Na^+ , Na.N_2^+ , Na.O^+ , and Na.CO_2^+ . According to their model, under normal circumstances at high altitudes the reactions cycle Na quickly from Na^+ to Na.N_2^+ to Na.O^+ and then back to Na^+ again. If, however, the Na^+ is by some means transported to a lower altitude where the concentration of CO_2 increases relative to that of O , a portion of the Na^+ is diverted to Na.CO_2^+ , from which it can be efficiently neutralized by dissociative recombination to Na . This process is, in a nut shell, the *Cox and Plane*(1998) mechanism for sporadic sodium layer formation with sporadic- E forcing as the driver for moving the Na^+ to a

lower altitude. This same chemistry can also neutralize the recently ionized Na from the auroral effects.

3.4 Chapter Summary

In this chapter we describe time-dependent models that we developed of the gas-phase chemistries of upper atmospheric iron and sodium. These models are based on sets of chemical reactions and reaction rates that have recently been used to explain time-averaged measurements of steady-state altitude profiles of iron and sodium, and the outputs from our models are shown to compare favorably with time-averaged sets of measurements of both of these constituents.

The chemical models that we developed are used to investigate the potential influence of auroral ionization on the chemical states of iron and sodium compounds. For both iron and sodium we find that recently ablated meteoric material can be significantly affected by aurorae, as can sporadic neutral atom layers at altitudes of 90 km and higher. For the steady-state material profiles, we find that iron would be susceptible to auroral ionization if it weren't for the fact that the natural state for iron is ionized at the altitudes at which auroral energy is normally deposited. Neutral sodium, on the other hand, is normally present at somewhat higher altitudes and, as such, it can be affected by the presence of aurorae. Whether or not the state of sodium is significantly altered depends largely on both the ion densities in the aurorae and on the ion composition, with the presence of significant densities of O_2^+ yielding the greatest effects.

Chapter 4

Dynamics

Jack be nimble, Jack be quick, Jack jump over the candlestick,
But figure out β and also time T , “ a ” due to gravity, velocity V ,
And don’t forget $y = VT \sin \beta$ minus $1/2aT^2$, or you’ll regret later.
Figure trajectory right to the inch, Or it might be a “singe” instead of a cinch!

L. A. Graham

In Chapter 3 the chemistries of the ionized and neutral compounds of iron and sodium were considered. The model developed thereof did not consider the effects of transport of the various species — different altitudes were considered completely separately with no interaction. In developing their steady-state models, researchers such as *McNeil et al.*(1995), *Plane et al.*(1998), and *Helmer et al.*(1998) have explicitly or implicitly assumed that the chemical redistribution of atoms among the various constituents occurs rapidly compared to the time scales of vertical transport. *Plane et al.*(1998) compared the cycling time of neutral sodium to the other reservoir species with the expected residence time of total sodium in a given altitude bin based on eddy diffusion and deposition rates (calculations similar to those shown in Figures 2.4 and 2.5). They found, based on this analysis, that the sodium chemistry should have ample time to come to equilibrium. An analysis of the effects of atmospheric gravity wave motion (which is much faster than diffusion) was performed by *Hickey and Plane*(1995) using a perturbation analysis of the full sodium chemistry. They showed that gravity wave effects on the chemistry are probably not important above ~ 85 km but that they can play a role at 80 km and below. They argued, however,

that 80 km is below the altitude at which lidar systems typically measure Na, so the usual assumption that sodium is a simple tracer for wave motion in lidar data is a reasonably good one.

Each of the analyses previously mentioned has ignored one important point: that the motions of the ionized portions of the gases experience Lorentz forcing in addition to simple momentum transfer via collisions with the background atmosphere. This additional forcing can, under rather normal conditions, have a significant impact on the vertical distribution of the ion species. This fact was considered by *McNeil et al.*(1996) to explain high altitude observations of magnesium made from space shuttle flights. (Magnesium must be measured from above the stratosphere because the magnesium atomic resonances are effectively masked by ozone absorption bands.) In their model, *McNeil et al.*(1996) used a very simple set of chemical reactions including only Mg and Mg^+ , but they were able to reproduce many aspects of the measurements. The recent sporadic sodium layer formation mechanism of *Cox and Plane*(1998) is another example of the importance of Lorentz forcing. In that mechanism, a sporadic- E layer (consisting of, in part, Na^+) is driven by electric fields and/or wind shears to altitudes where the chemical balance shifts, clearly requiring a departure from the chemical equilibrium assumption. Due to the importance of these effects on the interpretation of measurements of atmospheric metals, we discuss in the following the role of the Lorentz force in forming and driving sporadic- E layers at high latitudes. We then discuss in Section 4.2 the simultaneous modeling of dynamics and chemistry for demonstrating this neutral layer formation mechanism. These discussions provide important foundations for understanding the measurements discussed in Chapter 5.

4.1 Ion Layer Formation

The term sporadic- E (E_s) has long been used to describe the intermittent occurrence of layers of ionization in the Earth's upper atmosphere. Originally the definition of sporadic- E was tied to the scattering of radio waves (primarily at HF frequencies) and was characterized by the following International Geophysical Year definition [*Thomas*

and Smith(1959)]:

...we consider as an E_s reflection any abnormal E -region reflection which is characterized by one of more of the following:

1. Random time of occurrence;
2. Partial transparency;
3. Variation of penetration frequency with transmitter power as deduced from F -region reflections;
4. Uniform apparent reflection height, regardless of frequency.

Unfortunately, this definition encompasses a wide variety of ionized phenomena, including auroral arcs and possibly even meteor echoes. The working definition of sporadic- E somewhat evolved as progress was made in understanding the physical processes responsible for some of the measurements. Review articles over the years traced this progress from a simple phenomenological descriptions to several quite sophisticated theories for the formation of different structures [e.g. *Thomas and Smith(1959)*, *Whitehead(1970)*, *Whitehead(1989)*, *Nygrén(1990)*, *Mathews(1998)*], though there remain problems with explaining all the characteristics of the very large number of available observations. For the purposes of this thesis, sporadic- E is defined with regard to an increase in the ion number densities in an altitudinally thin layer (on the order of one to a few kilometers thick) in or near the background (steady-state) E region.

A major breakthrough was realized in understanding the formation of midlatitude sporadic- E when *Whitehead(1961)* recognized that vertical shears in the zonal horizontal neutral winds, when combined with the anisotropic behavior of a plasma in a magnetic field, could lead to the vertical compression of a collisional plasma. One major difficulty with this theory was the lifetime of known E -region ions, NO^+ and O_2^+ , under the electron density conditions known to exist in sporadic- E layers. The rapid recombination of the molecular ions would simply not support the measured high densities. This problem was solved with the recognition of the relatively long lifetimes of meteoric metal ions. Subsequent measurements of metallic ions comprising sporadic- E layers by rocket-borne mass spectrometers [e.g. *Young et al.(1967)*] and

incoherent scatter radars [e.g. *Behnke and Vickrey(1975)*, *Turunen et al.(1988)*] supported this wind shear mechanism at midlatitudes. However, at high latitudes these shears in the zonal horizontal winds are much less effective than at midlatitudes, due to the fact that the magnetic field lines at high latitudes are nearly vertical and, as such, horizontal winds, regardless of orientation, tend to drive ions in horizontal directions with very little vertical component (which results in ineffective compression into layers).

The importance of electric fields in high latitude sporadic- E formation was recognized by *Nath et al.(1980)*, who chose to consider only NO^+ and O_2^+ based on the false assumption that the metallic ions are confined to lower altitudes (below 110 km). In addition, *Nath et al.(1980)* did not pay any particular attention to the importance of the direction of the neutral wind or electric field. As a result, the recognition of the importance of electric fields must be attributed to *Nygrén et al.(1984b)*. In a different paper, *Nygrén et al.(1984a)* recognized that the ion mass also plays a role in determining the specific altitude of formation for layers and that this can lead to multiple ionized layers. This claim was disputed by *Jones(1989)*, but measurements presented by *Huuskonen et al.(1988)* appear to support the *Nygrén et al.(1984a)* theory. Further theoretical progress for high latitude sporadic- E formation was made nearly simultaneously by *Bristow and Watkins(1991)* and *Kirkwood and von Zahn(1991)*. Both groups recognized the importance of an increasing ion-neutral collision frequency with decreasing altitude and the role that this can play in generating a transient layer. These various results are addressed in the following paragraphs.

Essentially all of the sporadic- E formation theories consider the solution of the continuity equation by estimating the ion flux with the help of the ion momentum equation and several simplifying assumptions. The continuity equation for each ion species can be stated as follows:

$$\frac{\partial n_j}{\partial t} = -\nabla \cdot (n_j \vec{v}_j) + (P_j - L_j) \quad (4.1)$$

where n_j is the number density of ion j , \vec{v}_j is the ion velocity, P_j is the production rate, and L_j is the loss rate. Similarly, for electrons we have

$$\frac{\partial n_e}{\partial t} = -\nabla \cdot (n_e \vec{v}_e) + (P_e - L_e). \quad (4.2)$$

For an ionospheric plasma consisting solely of singly positively ionized species, it can also be stated that to a good approximation

$$\sum_j n_j \approx n_e \quad (4.3)$$

and

$$\sum_j (P_j - L_j) = (P_e - L_e). \quad (4.4)$$

Implicit in equations (4.3) and (4.4) are several assumptions which may not always be applicable. For equation (4.3), for instance, the bulk charge neutrality cannot be assumed when considering the effects of polarization electric fields leading to ambipolar diffusion. The first simplification made for our derivation is that the production and loss rates are much less than the divergence of the flux and, as such, that they can be neglected. This assumption may not strictly be valid when chemical processes are considered, but it is a simple matter to add production and loss back into the model later. Another simplification is that only vertical variations in the ion densities are considered — the resulting model is 1-dimensional and we assume horizontal homogeneity. Again, this assumption is not always justified but measurements have generally shown that sporadic- E layers tend to have much smaller altitude extent than horizontal extent. With these approximations, Equation 4.1 becomes

$$\frac{\partial n_j}{\partial t} = -\frac{\partial}{\partial z} (n_j v_z). \quad (4.5)$$

This equation can be numerically integrated as an initial value problem if a suitable relation for the vertical flux, $n_j v_z$, can be found.

The ion momentum equation can be used to yield the flux needed in Equation 4.5 [e.g. *Nygrén et al.*(1984a), *Bristow and Watkins*(1991)]. One addition that is made in

the context of this thesis, however, is the inclusion of terms to describe the influence of eddy motion of the background atmosphere. Eddy diffusion was also included in the formulation by *Carter*(1995), though his approach was somewhat different and did not distinguish between eddy and molecular diffusion except in magnitude. In particular, Carter's derivation did not account for the fact that eddy diffusion tends to force minor constituent scale heights toward the background atmospheric scale height (see Appendix A). Recognizing the fact that the momentum transferred from the eddy motion to the ions is a transfer from a neutral species to an ionized one, the eddy term should be included in the ion momentum equation as an addition to the effective neutral wind. This approach maintains the anisotropic behavior of the plasma due to Lorentz forces. Thus, the resulting steady-state ion momentum equation can be written as follows:

$$0 = -\nabla p_j + n_j m_j \vec{g} + n_j q_e \left(\vec{E} + \vec{v}_j \times \vec{B} \right) - n_j m_j \nu_{jn} \left[\vec{v}_j - \vec{u} + K \left(\frac{\nabla n_j}{n_j} - \frac{\nabla n_n}{n_n} \right) \right] \quad (4.6)$$

where $p_j = n_j k_B T_j$ is the pressure due to random thermal motion, k_B is Boltzmann's constant, T_j is the temperature of ion j , m_j is the mass of ion j , \vec{g} is gravity, q_e is the magnitude of an electron's charge, \vec{E} is the electric field, \vec{B} is the magnetic flux density, ν_{jn} is the momentum transfer collision frequency between ion j and the background neutral atmosphere (see Appendix D for more details concerning this term), \vec{u} is the neutral atmosphere bulk velocity, K is the eddy diffusion coefficient, and n_n is the neutral atmosphere number density. A similar equation can be written for electrons, though the gravity term is, of course, negligible:

$$0 \approx -\nabla p_e - n_e q_e \left(\vec{E} + \vec{v}_e \times \vec{B} \right) - n_e m_e \nu_{en} \left[\vec{v}_e - \vec{u} + K \left(\frac{\nabla n_e}{n_e} - \frac{\nabla n_n}{n_n} \right) \right]. \quad (4.7)$$

To a good approximation for this analysis the magnetic flux density \vec{B} is due solely to the Earth's field and is not significantly affected by currents flowing in the plasma.

The same assumption does not necessarily hold for the electric field \vec{E} because extremely small displacements of the electrons with respect to the ions can result in significant polarization electric fields. In particular, internal electric fields, \vec{E}_{int} , can be set up which must satisfy Gauss's law locally:

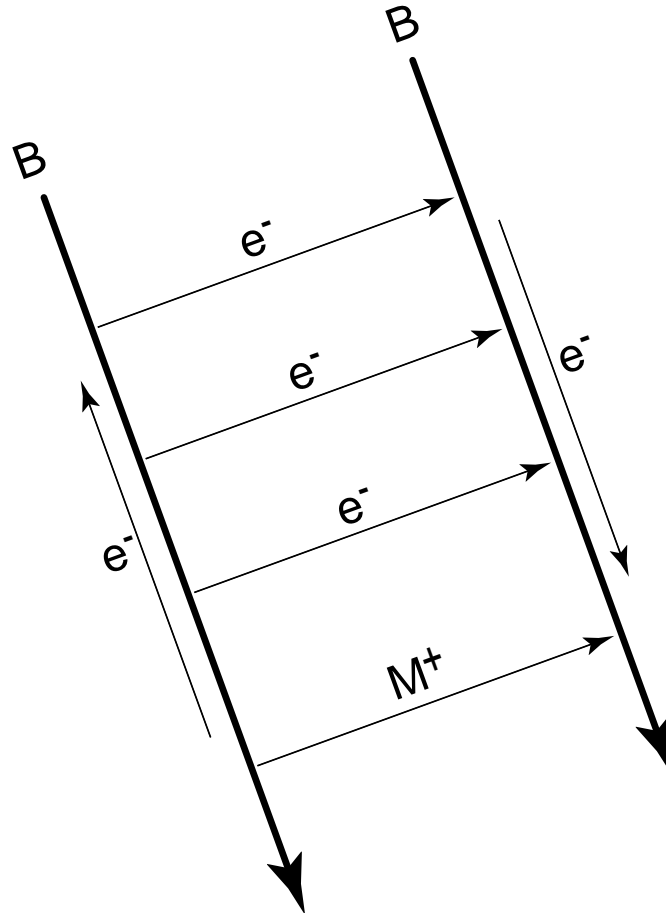
$$\nabla \cdot \vec{E}_{int} = \frac{q_e \left(\sum_j n_j - n_e \right)}{\epsilon_0}. \quad (4.8)$$

This relation, which couples equations (4.6) and (4.7), is not especially useful for simulating ion motion because its solution requires integration over all space. A further simplification can be made to equation (4.7) by recognizing that over the altitude range of interest the product of the electron mass and the electron-neutral collision frequency is small. Adopting this approximation and rearranging equation (4.7) yields the following:

$$\vec{E} = -\frac{1}{n_e q_e} \nabla (n_e k_B T_e) - \vec{v}_e \times \vec{B} \quad (4.9)$$

where T_e is the electron temperature. In the direction parallel to \vec{B} , equation (4.9) basically states that the electric field is that field required to exactly cancel the electron pressure gradient, which is another way of stating the assumptions typically used to describe ambipolar diffusion in the absence of or parallel to a magnetic field [e.g. *Chen(1984)*, *Brekke(1997)*]. Such a statement embodies the fact that the ions diffuse approximately twice as fast as they normally would due solely to the ion pressure gradient because they are 'dragged along' by the electrons. The electrons, on the other hand, are significantly inhibited from diffusing by their electro-static coupling to the more massive ions. The case of ambipolar diffusion perpendicular to \vec{B} is somewhat more complicated. The problem arises from the fact that throughout the E region the electron-neutral collision frequency is quite low and that the electrons do not readily diffuse perpendicular to field lines. As a result, as ions diffuse across field lines due to collisions it is often easier for electrons to neutralize the additional charge via motion along \vec{B} locally [e.g. *Chen(1984)*, *Goldston and Rutherford(1995)*] and across \vec{B} elsewhere (via integrated Pedersen conductivity or, possibly, in the

Figure 4.1: Diffusion perpendicular to \vec{B} . As ions (M^+) diffuse due to collisions with neutrals in a sporadic- E layer, the electrons (e^-) move more easily parallel to \vec{B} locally and diffuse perpendicular to \vec{B} over a much larger volume of space.



magnetosphere). This type of ambipolar diffusion is illustrated schematically in Figure 4.1, an effect similar to which was studied by *Farley(1959)* and *Farley(1960)* in terms of the shielding of small scale electric fields. In Farley’s words, “...the ‘internal impedance’ of the thin source layer is greater than the ‘load impedance’ presented by the rest of the ionosphere.” Thus the locally generated electric fields are effectively shorted out by the integrated effect of the rest of the ionosphere — as long as this along- \vec{B} neutralization occurs more quickly than the ions diffuse there will effectively be no internal electric field supported. *Vickrey and Kelley(1982)* also considered a

similar effect except that they were looking at the impact of a conducting E layer on the F region diffusion. One of their conclusions was that the integrated Pedersen conductivity of the E region would result in F region perpendicular ion diffusion at the unimpeded ion diffusion velocity. Based on these arguments, it is a reasonable approximation to assume that the diffusion-generated internal electric fields are due solely to pressure gradients parallel to the \vec{B} -field. This approximation can be expressed as follows:

$$\vec{E}_{int} = -\frac{1}{n_e q_e} \nabla_{\parallel} (n_e k_B T_e) \quad (4.10)$$

where the notation ∇_{\parallel} signifies the vector component of the gradient in the direction parallel to \vec{B} . There clearly are circumstances for which this approximation does not hold up, but at high latitudes other effects tend to dominate the perpendicular electric fields. In particular, large scale and intense magnetospherically-generated electric fields perpendicular to \vec{B} map quite efficiently along magnetic field lines and dominate this component of the local \vec{E} -field vector. Denoting this mapped electric field as \vec{E}_{ext} and using the result in equation (4.10), equation (4.6) can now be written as follows:

$$\begin{aligned} 0 = & -\nabla (n_j k_B T_j) \\ & -\frac{n_j}{n_e} \nabla_{\parallel} (n_e k_B T_e) \\ & + n_j m_j \vec{g} \\ & + n_j q_e \left(\vec{E}_{ext} + \vec{v}_j \times \vec{B} \right) \\ & - n_j m_j \nu_{jn} \left[\vec{v}_j - \vec{u} + K \left(\frac{\nabla n_j}{n_j} - \frac{\nabla n_n}{n_n} \right) \right]. \end{aligned} \quad (4.11)$$

We now need to solve equation (4.11) for the ion flux $n_j \vec{v}_j$ (or, more specifically, for the z -component of the flux, $n_j v_z$) for inclusion in equation (4.5). *Brekke(1997)* solves a similar equation by redefining several parameters and making use of various vector identities (see chapter 7 of that reference). Another approach, more amenable to computer assisted derivation, is outlined in Appendix D. This approach uses matrix notation for the vector relations and relies on matrix inversion to solve some of the

more involved mathematics. The result of this derivation is given in the following rather complicated expression.

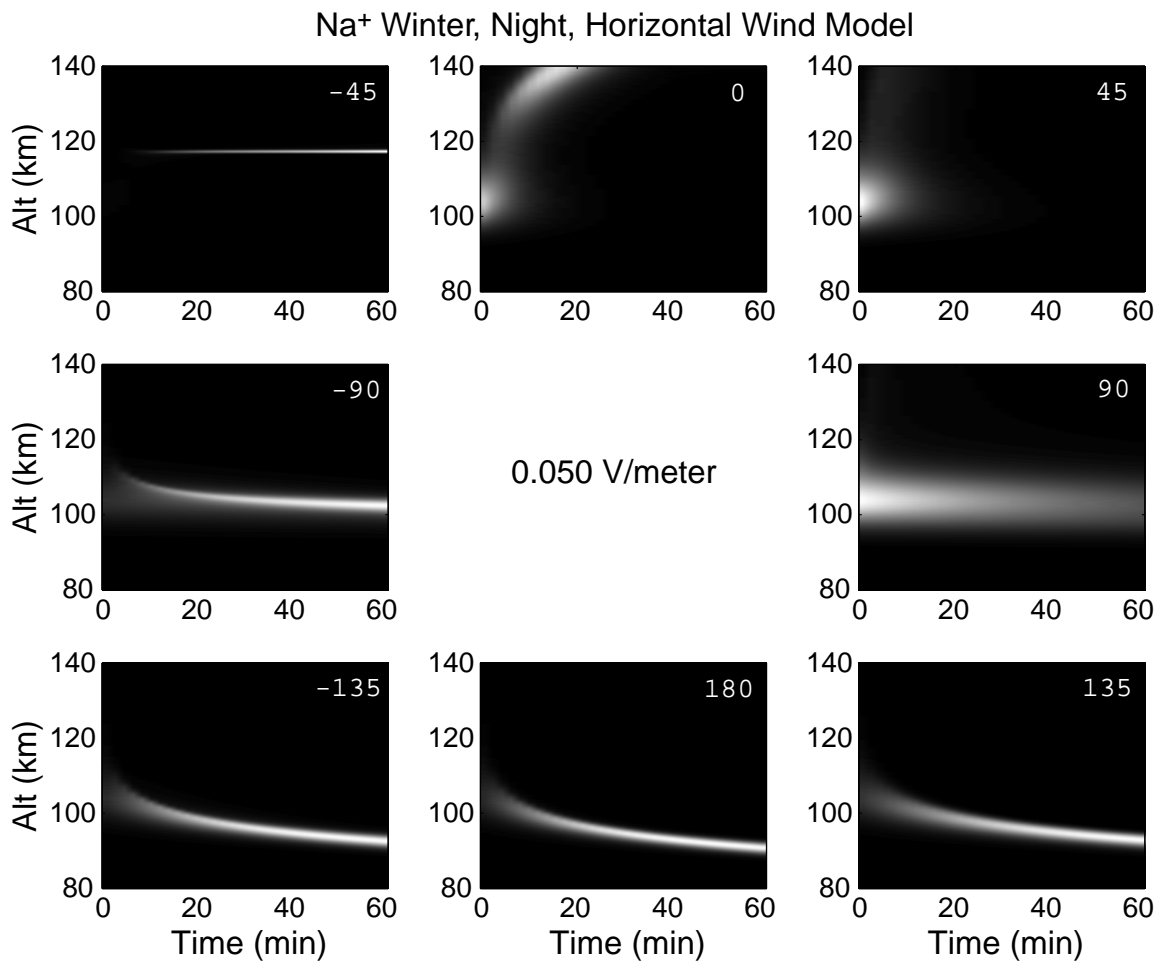
$$\begin{aligned}
n_j v_z = & - \left[\left(\frac{k_B T_j}{m_j \nu_{jn}} + K \right) \frac{m_j^2 \nu_{jn}^2 + q_e^2 B_z^2}{m_j^2 \nu_{jn}^2 + q_e^2 B^2} \right] \frac{\partial n_j}{\partial z} \\
& - \left[\frac{k_B T_e}{m_j \nu_{jn}} \frac{B_z^2}{B^2} \frac{n_j}{n_j + n_{eo}} \right] \frac{\partial n_j}{\partial z} \\
& - \left[\frac{k_B}{m_j \nu_{jn}} \left(\frac{\partial T_i}{\partial z} \frac{m_j^2 \nu_{jn}^2 + q_e^2 B_z^2}{m_j^2 \nu_{jn}^2 + q_e^2 B^2} + \frac{\partial T_e}{\partial z} \frac{B_z^2}{B^2} \right) \right] n_j \\
& + \left[K \frac{1}{n_n} \frac{\partial n_n}{\partial z} \frac{m_j^2 \nu_{jn}^2 + q_e^2 B_z^2}{m_j^2 \nu_{jn}^2 + q_e^2 B^2} \right] n_j \\
& - \left[\frac{g}{\nu_{jn}} \frac{m_j^2 \nu_{jn}^2 + q_e^2 B_z^2}{m_j^2 \nu_{jn}^2 + q_e^2 B^2} \right] n_j \\
& + \left[\frac{q_e B_y m_j \nu_{jn} + q_e^2 B_x B_z}{m_j^2 \nu_{jn}^2 + q_e^2 B^2} u_x \right] n_j \\
& - \left[\frac{q_e B_x m_j \nu_{jn} - q_e^2 B_y B_z}{m_j^2 \nu_{jn}^2 + q_e^2 B^2} u_y \right] n_j \\
& + \left[\frac{m_j^2 \nu_{jn}^2 + q_e^2 B_z^2}{m_j^2 \nu_{jn}^2 + q_e^2 B^2} u_z \right] n_j \\
& + \left[\frac{q_e^2 B_y E_{\perp x} - q_e^2 B_x E_{\perp y} + m_j \nu_{jn} q_e E_{\perp z}}{m_j^2 \nu_{jn}^2 + q_e^2 B^2} \right] n_j \\
& - \left[\frac{k_B T_e}{m_j \nu_{jn}} \frac{B_z^2}{B^2} \frac{\partial n_{eo}}{\partial z} \right] \frac{n_j}{n_j + n_{eo}}.
\end{aligned} \tag{4.12}$$

In this equation, the x -, y -, and z -components of \vec{B} are given by B_x , B_y , and B_z respectively. Similarly, the three components of \vec{E}_{ext} are $E_{\perp x}$, $E_{\perp y}$, and $E_{\perp z}$ where the \perp has been added to emphasize the fact that this vector is orthogonal to \vec{B} . The neutral wind \vec{u} has components u_x , u_y , and u_z . The electron number density in equation (4.12) has also been split up into a pair of components corresponding to the modeled ions and the ‘other’ electrons (e.g. aurorally-produced or background), $n_e = n_j + n_{eo}$. For each term of equation (4.12) the last portion (outside of the []) contains the variables that will vary continuously during a model run. All of the other components are more or less constant.

Solving equation (4.5) with equation (4.12) as an initial value problem is somewhat more involved than the model used in Chapter 3 for chemistry. The chemical models were ODE's, for which a number of very robust numerical techniques exist. The present problem, however, is a partial differential equation (PDE) and greater care is required to both formulate the problem and to ensure numerical stability. Appendix E describes the numerical formulation of the problem. This set of equations, along with appropriate input conditions for the neutral wind fields and electric fields, includes the formation mechanisms described in previous studies by *Whitehead(1961)*, *Nygrén et al.(1984b)*, *Bristow and Watkins(1991)*, and *Kirkwood and von Zahn(1991)* as well as the dynamics of *Carter(1995)*. The resulting one-dimensional model is initially used to investigate the ability of high-latitude electric fields to form thin ionization layers.

The ion studied is Na^+ because of its importance to the measurements in this thesis. As an initial condition, the steady-state winter Na^+ profile from Figure 3.11 is used. The neutral number densities are taken from the Mass Spectrometer and Incoherent Scatter model (MSISE-90) [*Hedin(1991)*] as are the neutral temperatures. The electron and ion temperatures are assumed to be in thermal equilibrium with the neutrals and are both taken from the MSISE-90 temperatures. The background electron densities, n_{eo} , are taken from the International Reference Ionosphere model (IRI-95) [*Rawer et al.(1978)*, *Bilitza(1990)*, *Bilitza(1998)*]. The ion-neutral collision frequency model is as discussed in Appendix D. The magnetic field model used is the International Geomagnetic Reference Field (IGRF-95). The eddy diffusion profile is taken from *Danilov and Kalgin(1992)* and is shown in Figure 2.3, though the molecular diffusion coefficient cannot be taken from that source (it is built into the momentum equations). Finally, the neutral winds must also be supplied and for this set of model runs they are taken from the Horizontal Wind Model (HWM-93) [*Hedin et al.(1996)*]. Using these conditions, the model was run with a 50 mV/meter electric field (not unusual at high latitudes) for 8 different electric field orientations. The results of those model runs are shown in Figure 4.2 which shows the formation of distinct layers for all electric field directions except north, north-east, and east. The layers which are quickly formed in the north-west quadrant are those discussed

Figure 4.2: Electric Field Driven Formation of Sporadic- E Layers. A 50 mV/m electric field drives the formation of sporadic- E for some field orientations. The angles indicated in the upper right corner of each plot are relative to magnetic north.



by *Nygrén et al.*(1984b). Those with a southerly component of the electric field correspond to formation by the mechanism discussed by *Bristow and Watkins*(1991) and *Kirkwood and von Zahn*(1991). It is useful to look at a simplified version of the ion velocity under the influence of electric fields to understand the basic idea behind the formation of layers in these various directions. Extracting only that term from equation (4.12) results in the following equation:

$$v_z = \frac{q_e^2 B_y E_{\perp x} - q_e^2 B_x E_{\perp y} + m_j \nu_{jn} q_e E_{\perp z}}{m_j^2 \nu_{jn}^2 + q_e^2 B^2}. \quad (4.13)$$

We now impose a coordinate system that places the x -direction toward magnetic east, the y -direction toward magnetic north, and the z -direction upward (with x and y in the horizontal plane). With this rotated coordinates $B_x = 0$ and in the northern hemisphere $B_y > 0$ so equation 4.13 reduces to

$$v_z = \frac{q_e^2 B_y E_{\perp x} + m_j \nu_{jn} q_e E_{\perp z}}{m_j^2 \nu_{jn}^2 + q_e^2 B^2} \quad (4.14)$$

where $E_{\perp z} > 0$ for a northward directed electric field and $E_{\perp x} > 0$ for an eastward directed field. *Nygrén et al.*(1984b) essentially recognized that the ion-neutral collision frequency, ν_{jn} , is a strong function of altitude with higher collision frequencies at lower altitudes. If the electric field is oriented in the magnetic north-west direction then $E_{\perp z}$ is positive and $E_{\perp x}$ is negative. At higher altitudes, then, $E_{\perp x}$ dominates v_z because ν_{jn} is small and the sign of v_z is negative or downward. At lower altitudes, on the other hand, $E_{\perp z}$ dominates, resulting in a positive or upward ion velocity, v_z . At some intermediate altitude the ions thus tend to be compressed into thin layers, precisely as seen in the upper left panel of Figure 4.2. Ions congregate at the point where the $E_{\perp x}$ and $E_{\perp z}$ terms cancel to give $v_z = 0$. This point is, of course, modified by the other terms in equation (4.12). *Bristow and Watkins*(1991) and *Kirkwood and von Zahn*(1991) recognized that $v_z = 0$ is not a necessary condition for layer formation. At lower altitudes, where the ion-neutral collisions dominate ion motion, the

vertical velocity can be approximated as follows:

$$v_z \simeq \frac{q_e E_{\perp z}}{m_j \nu_{jn}}. \quad (4.15)$$

At lower altitudes the vertical ion velocity is thus smaller. For a downward flux, then, the ions at higher altitudes tend to overtake those at lower altitudes and a ‘pile-up’ condition can exist, as shown in the lower three panels of Figure 4.2.

The sporadic- E layer formation mechanisms just described are supported by a number of experimental results [e.g. *Kirkwood and von Zahn(1991)*, *Kirkwood and von Zahn(1993)* *Bristow and Watkins(1993)*, *Kirkwood(1997)*, *Parkinson et al.(1998)*]. The incomplete measurement of some parameters, however, has led some to question aspects of the theory [e.g. *Jones(1989)*, *Bedey(1996)*]. *Bedey(1996)*, in particular, questioned the generally accepted ion-neutral collision frequency model (see Appendix D) based on an analysis of the altitude of formation of layers with electric fields directed toward the north-west quadrant. However, his analysis neglected the influence of the neutral wind on the altitude of the convergent null. Experiments were conducted with the Sondrestrom Incoherent Scatter Radar (see Appendix B for system details) to more precisely test this theory. In these experiments the radar antenna was set to probe a variety of different directions, describing a cone with a half-angle of 20° about the zenith direction. By scanning in this manner, several different line-of-sight directions were probed sequentially. An incoherent scatter radar (ISR) measures ion velocity from the Doppler shift of the return signal. As a result, any given measurement reveals just a single component of that velocity vector. By measuring different components, simple matrix techniques can be used to extract the total vector. Crucial assumptions underlying this approach are that the velocity vectors are time stationary over the time of a full scan and also that the vectors are horizontally uniform over the volume probed throughout the scan. These assumptions are not always strictly valid and the ISR user must constantly watch for indications of their violation. As has been discussed in previous paragraphs, the important driving parameters for the formation and dynamics of sporadic- E layers are the electric field and the neutral wind. The electric field can be estimated by making Doppler measurements of the

plasma in the F region (above ~ 200 km altitude). At those altitudes the ion-neutral collisions can reasonably be ignored. The effects of gravity on the ions can similarly be neglected as can the horizontal pressure gradients because those gradients do not significantly add to the ion velocities at these altitudes. The steady-state momentum equation can thus be simplified as:

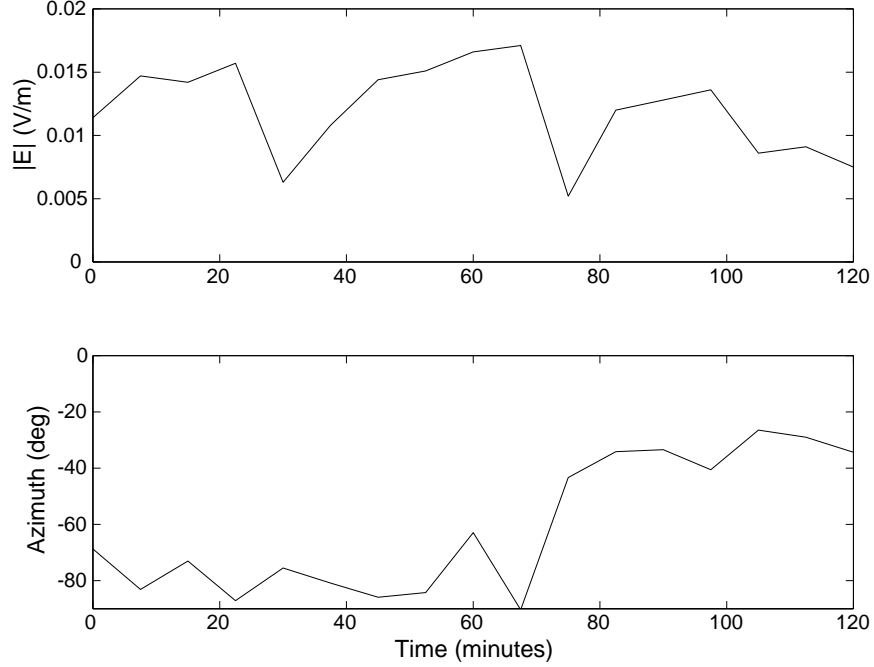
$$0 = n_j q_e \left(\vec{E} + \vec{v}_j \times \vec{B} \right) \quad (4.16)$$

which can be simply rearranged to yield:

$$\vec{E} = -\vec{v}_j \times \vec{B}. \quad (4.17)$$

So an estimate of the vector ion velocity in the F region can be used with a magnetic field model to yield an estimate of the electric field vector. E region velocity measurements are more difficult precisely because of the steep gradients in the ion-neutral collision frequency. These gradients make it important to measure velocities with good range resolution, but this requirement is in some ways counter to making good velocity measurements (where estimates of longer autocorrelation function lags are desired). However, in the specific case investigated here the night-time densities in the absence of aurorally-enhanced electron densities were quite low — except when a sporadic- E layer was present. Thus, even though a longer transmitter pulse was used (which smears over a larger range extent for any given sample), essentially all of the power in the return comes from only the sporadic- E layer. In this way, such a layer can be used as a sampling function which selects out a narrow range of altitudes. This feature allowed the use of a longer transmitter pulse which then yielded more accurate Doppler velocity measurements (see Appendix B for a brief discussion of ISR techniques). An implicit assumption here is that the neutral wind and ion-neutral collision frequency are nearly constant over the thickness of the sporadic- E . This assumption should be valid for narrow layers but must be examined more closely for the thicker ones. Under this condition, considering only horizontal motion for the neutrals (so the pressure gradient terms can reasonably be neglected), and neglecting the usually small horizontal motion due to eddy diffusion, the approximate ion

Figure 4.3: Electric Field Estimates from the Sondrestrom ISR on 30 July 1998



momentum equation is as follows:

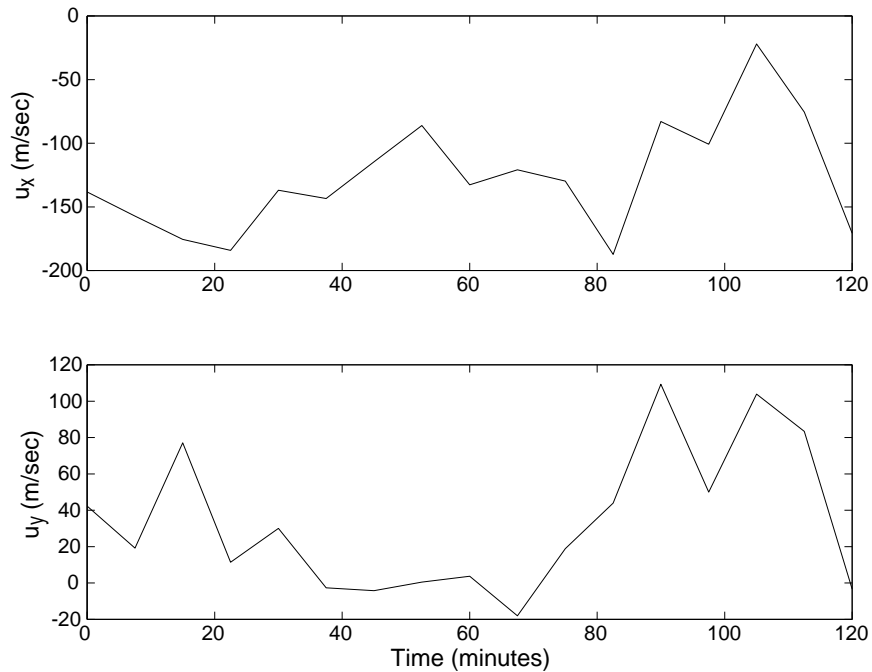
$$0 = n_j q_e \left(\vec{E} + \vec{v}_j \times \vec{B} \right) - n_j m_j \nu_{jn} (\vec{v}_j - \vec{u}). \quad (4.18)$$

Once again, simple manipulation yields

$$\vec{u} = \vec{v}_j - \frac{q_e}{m_j \nu_{jn}} \left(\vec{E} + \vec{v}_j \times \vec{B} \right). \quad (4.19)$$

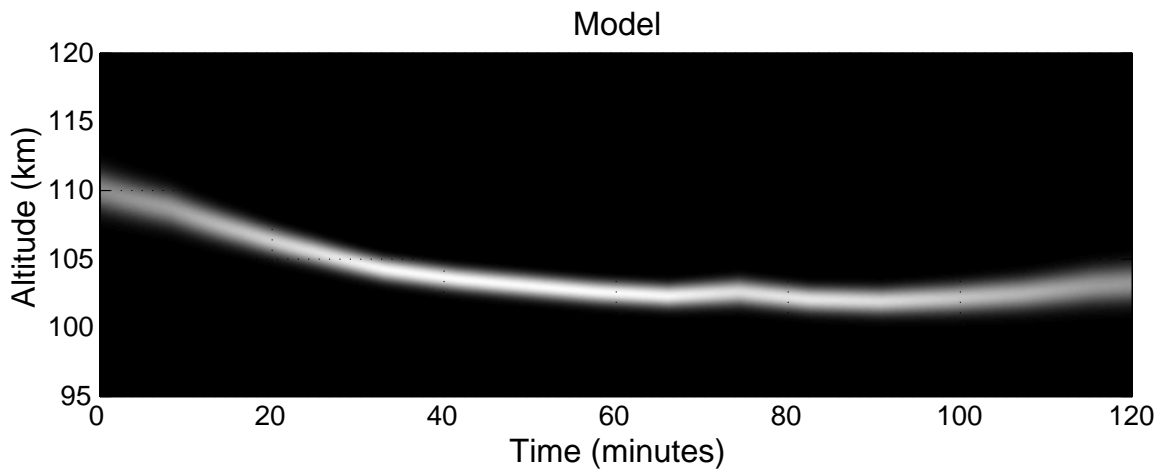
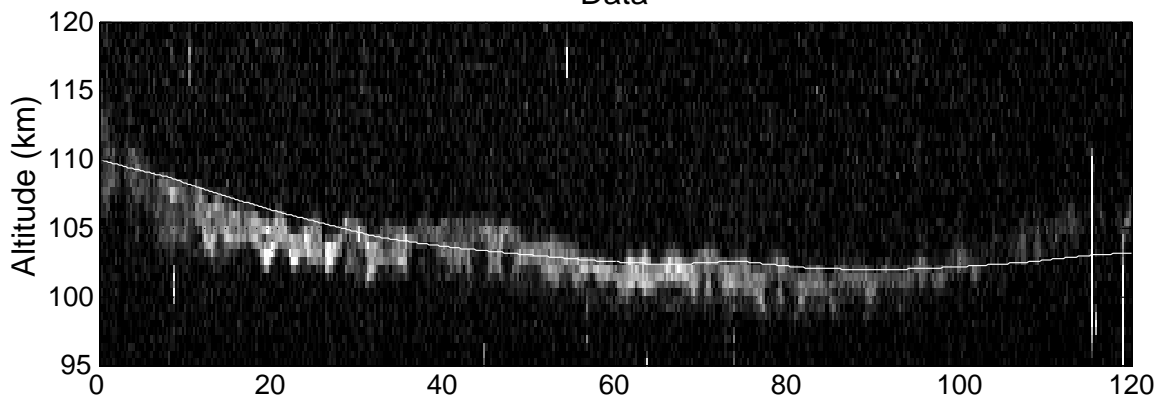
So, with the help of the electric field estimates from F region measurements, measurements of ion velocities in the E region can be used to generate neutral wind estimates. Putting this idea into practice, Figure 4.3 contains estimates of the electric field strength and direction from the Sondrestrom ISR on the morning of 30 July 1998. These measurements were collected starting just after 0:40 UT on that day but the data were shifted to start at 0:00 for the simulation. Note that in Figure 4.3 there is an abrupt change in direction at around 70 minutes into the experiment. This change in direction was accompanied by a dip in the electric field strength. Keeping

Figure 4.4: Neutral Wind Estimates from the Sondrestrom ISR on 30 July 1998



in mind the requirement for time stationarity in combining the measurements to yield an ion velocity, the results around this time must be regarded as questionable. Figure 4.4 shows the horizontal neutral wind estimates for the same time period. Note that these estimates are quite variable, but their impact on the ion dynamics model is an integrated one so that the effect of these variations on the final result is relatively small. The magnitude of the neutral winds has a similarly small impact. With proper choice of an initial condition, the data are now available to try and model the measured sporadic- E layer dynamics. Figure 4.5 shows the results of that modeling effort. The upper panel shows the ISR measurements of electron density as functions of altitude and time. Note that there is evidence for some horizontal inhomogeneity in the sporadic layer in that the azimuthal scanning of the antenna can be seen as an altitude modulation of the layer with time. The lower panel shows the result of the model run, assuming Fe^+ as the main constituent of the layer. The altitude of the peak of the model layer is also included in the upper panel as a white line. This comparison shows good agreement between the data and model and does not indicate

Figure 4.5: Model of Sporadic-*E* Dynamics on 30 July 1998
Data



any significant bias due to the collision frequency estimate. After approximately 100 minutes it should be noted that the data and model appear to diverge, most probably due to the fact that the sporadic- E layer fades in intensity and, as a result, the ISR measurements are also degraded. Note that the model results show a slight increase in the altitude of the layer around 70 minutes, which is the time that the electric field changed in direction. All in all, this data set appears to validate the model presented here, at least in a general sense. It does *not* support the contention of *Bedey*(1996) that the standard ion-neutral collision frequency formulation needs serious revision.

4.2 Neutral Layer Formation and Diffusion

There currently is significant research activity on the topic of the formation of sporadic neutral atom layers. One significant aspect of many of the observations of these thin layers is their correlation with the occurrence of sporadic- E [e.g. *Clemesha et al.*(1980), *von Zahn and Hansen*(1988), *Beatty et al.*(1989), *Hansen and von Zahn*(1990), *Mathews et al.*(1993), *Kane et al.*(1993), *Heinselman et al.*(1998)]. The only quantitative theory for the formation of sporadic sodium in the presence of sporadic- E is that presented by *Cox and Plane*(1998), though a number of qualitative explanations have been presented by other authors [e.g. *Hansen and von Zahn*(1990)]. As was indicated in Chapter 3, the *Cox and Plane*(1998) mechanism is embedded in the sodium chemistry model of this thesis. One aspect that is missing from that model, however, is the dynamics of the Na layer after its formation. Recall that a basic premise of the chemical models was that material redistribution is not significant because the chemical reactions are more rapid than diffusion. This condition does not hold for the case of sporadic atom layers. The number densities routinely measured in these layers greatly exceed the number densities expected in all gas states from the steady-state diffusive equilibrium considerations. The *Cox and Plane*(1998) formation mechanism postulates that the additional Na is transported and layered in the form of Na^+ . We considered this Na^+ transport and layering in the previous section but did not consider any production or loss mechanisms as it was assumed that $P_j = L_j = 0$. To properly model the formation and evolution of sporadic Na layers with the *Cox*

and Plane(1998) mechanism, a coupled ion dynamics and chemistry model is needed along with the addition of a neutral dynamics model.

Modelling of the neutral dynamics can be done in a manner similar to that for the ionized gas. The one dimensional continuity equation, in the absence of production and loss, is simply Equation 4.5 for neutral atoms:

$$\frac{\partial n}{\partial t} = -\frac{\partial}{\partial z}(nv_z). \quad (4.20)$$

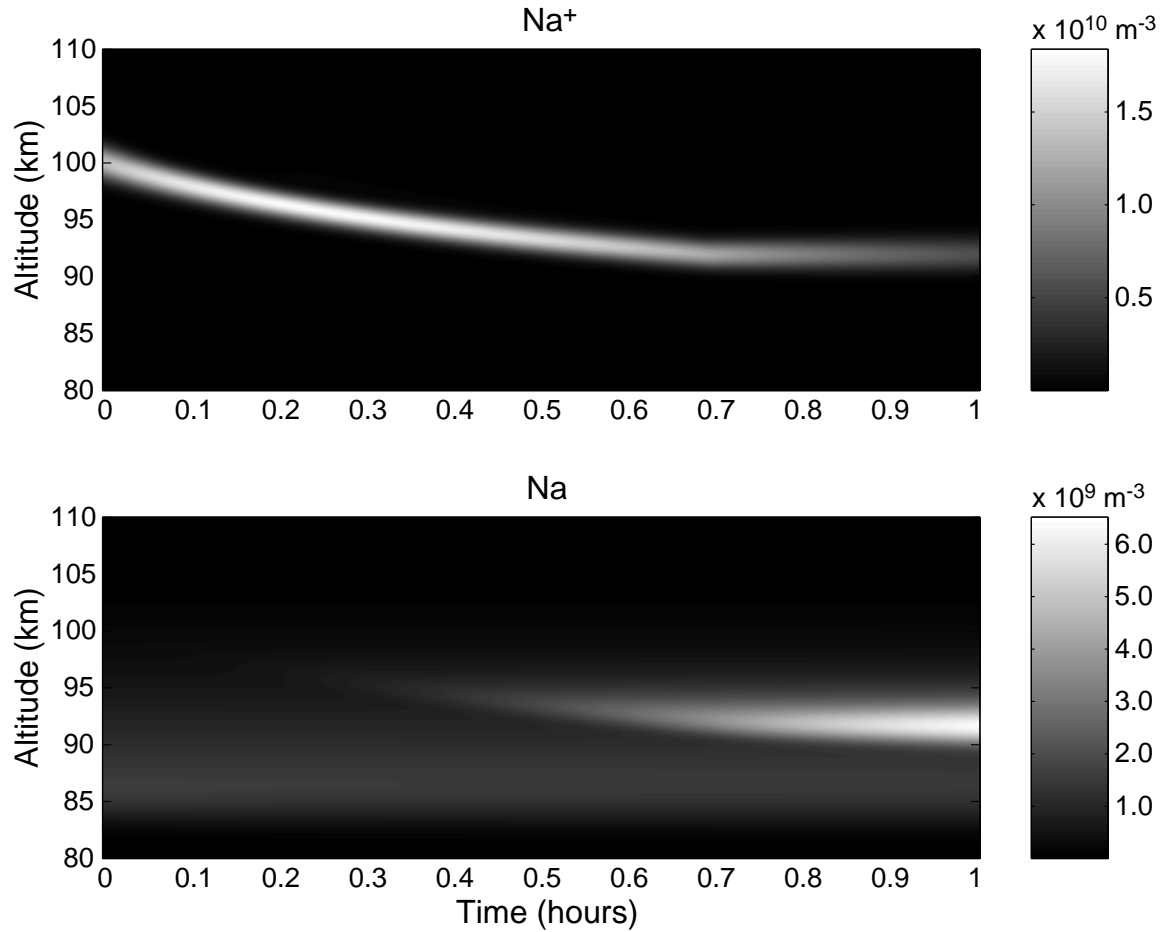
The vertical flux is given by the sum of the diffusive flux [Banks and Kockarts(1973b)] and the bulk atmospheric flux. Using the approximations that were invoked in Section 2.3, this sum can be expressed as:

$$nv_z = \left[u_z + (K + D) \frac{1}{n_n} \frac{\partial n_n}{\partial z} \right] n - [K + D] \frac{\partial n}{\partial z}. \quad (4.21)$$

As with the ions, the flux for the minor neutral species is a function of both the number density n and the spatial derivative of that density. The modified *Lax-Wendroff* scheme of Appendix E can thus be used to model the partial differential equation (4.20). One important thing to note here is that, unlike for the ion flux case, there are no mechanisms in this pair of equations which would easily support the formation of layers of neutral constituents. Vertical profiles of u_z could be imposed which would modify the concentrations somewhat (due, for example, to atmospheric gravity waves), but realistic profiles in this vertical wind alone would not create the narrow structures regularly observed in lidar profiles.

As was mentioned earlier, the ion and neutral dynamics models must be combined with the chemical models if the neutral layer formation mechanism of Cox and Plane(1998) is to be properly modeled. This process is somewhat tricky and quite literally books have been written which treat the modeling of both dynamics and chemistry of atmospheric constituents [e.g. Seinfeld and Pandis(1998), Jacobson(1999)]. One popular and quite powerful technique is known as operator splitting [Seinfeld and Pandis(1998)]. With this technique the dynamical perturbations and chemical perturbations are treated sequentially for each major time step. As was

Figure 4.6: Model of Sporadic Sodium Layer Formation



pointed out by *Mendillo et al.*(1993), the rates of change due to dynamical effects versus those due to chemical effects are quite different. As a result, a simple time step for all processes is not appropriate. This problem is handled in the coupling of the chemical and dynamical models, each of which has its own independent internal time step. In the case of the chemical solver the time step varies as conditions warrant (to maintain accuracy). The resulting model was used to investigate the dynamical behavior of the *Cox and Plane*(1998) sporadic layer formation mechanism. Figure 4.6 shows an example of such a model run, in which the model is initialized with an already-formed sporadic-*E* layer at 100 km altitude. A southward electric field of 50 mV/m is imposed to drive the layer downward in altitude and the neutral wind is set

to zero. After 0.7 hours the electric field intensity is reduced to 5 mV/m to maintain the altitude and relative shape of the sporadic- E and allow the neutralizing chemical reactions to occur. Note how the chemical reactions do transfer Na^+ to Na over the course of 15 minutes or so, thus forming an intense and reasonably narrow Na layer. The diffusion of that layer is also clearly seen in the time sequence, even though the time of the model run is not excessively long. The model results clearly indicate that if there is a sufficient amount of Na^+ present, a sporadic neutral sodium layer can be produced in a reasonable amount of time via gas phase chemical reactions.

The implications of this result are quite significant, as the case in hand is one where the sodium content is *not* a simple tracer for the background atmospheric motion. A case where the total sodium content in the upper atmosphere increases by more than a factor of two over the course of a half an hour is shown in Chapter 5. This Lorentz forcing of the ions is thus shown to be a viable mechanism by which ion layer formation can be followed by chemical processes to form thin neutral layers.

4.3 Chapter Summary

In this chapter we review the theories that describe the formation of thin layers of enhanced ionization in the E region of the ionosphere (sporadic- E layers). These layers of predominantly metal ions are shown to be formed by the combined influences of ion-neutral coupling and Lorentz forcing by magnetospheric electric fields. A set of measurements is presented which supports the described theory. The generally accepted theories are also extended to include the effects of turbulent eddies in the neutral atmosphere and additional ionization such as that due to auroral particles.

We develop a model which combines the effects of this ion forcing with the diffusion of Chapter 2 and the chemistry of Chapter 3. This model is shown to be capable of explaining the formation of sporadic neutral sodium layers between 90 and 95 km altitude.

Chapter 5

Case Study

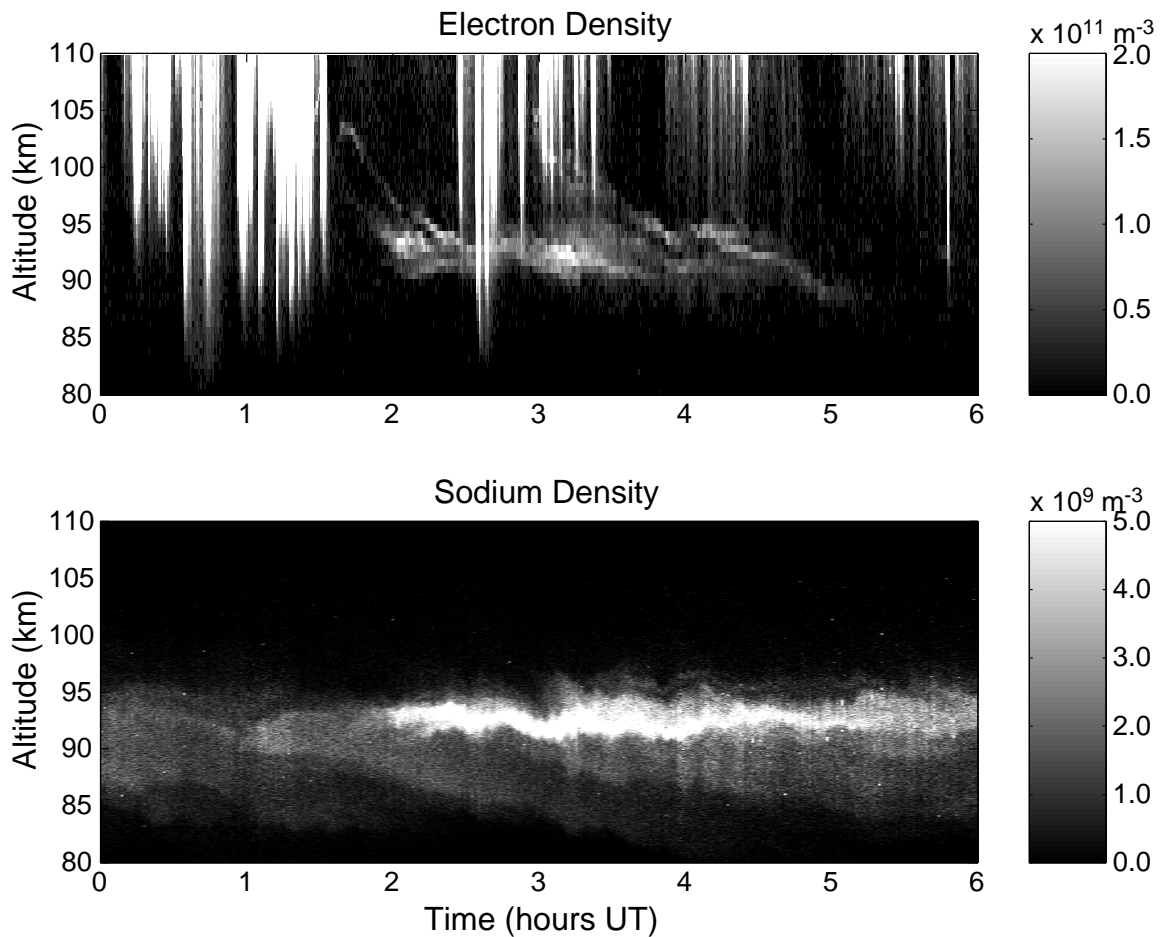
Knowing how hard it is to collect a fact, you understand why most people want to have some fun analyzing it.

Jesse L. Greenstein

One difficulty inherent to upper atmospheric experimental research is the lack of control of the measurement conditions. Experimentalists are stuck in the role of waiting for conditions amenable to testing the various applicable theories. One indication of this circumstance was hinted at in Chapter 3 where only a single case of an ablating meteoroid in the presence of intense aurora was identified. This fact notwithstanding, a data set was collected at the Sondrestrom Facility on the night of 10-11 December 1997 with atmospheric conditions which allow the testing of many critical aspects of the theoretical work presented in this thesis. These data were published by *Heinselman et al.*(1998) in the context of a test of the *Cox and Plane*(1998) sporadic sodium layer generation mechanism, without any model results for comparison.

Figure 5.1 shows the lidar and radar measurements for 6 hours of the experiment on 11 December 1997, illustrating a number of interesting features contained in the data set from that evening. The upper panel contains electron densities from the ISR as functions of altitude and time. The ISR antenna was fixed in a vertical direction for the duration of this experiment to ensure that overlapping volumes were probed by it and by the sodium resonance lidar. Unfortunately, this arrangement did not allow the extraction of any electrodynamic information for this data set. The electron density

Figure 5.1: ISR and Lidar Measurements, 11 December 1997. The upper panel shows ISR measurements of electron number density vs. altitude and time above Sondrestrom. The ISR antenna was oriented vertically to provide an overlapping volume with the lidar. The lower panel shows neutral Na density as a function of time and altitude from the sodium resonance lidar.



data shows that aurorae of varying intensity and varying particle energies (deposited to varying altitudes) was present during the night. The aurorae are characterized in Figure 5.1 by density enhancements extending downward from higher altitudes. The auroral densities were allowed to saturate the gray scale so other features could be seen, but they did reach as high as $2 \times 10^{12} \text{ m}^{-3}$ at times. In addition, thin sporadic- E layers are also apparent in the electron density data. These altitudinally thin layers begin to appear around 1:30 UT (though they may be buried in the auroral densities earlier) and remain until around 5 UT. When they appear at 1:30 they are at approximately 105 km altitude and over the course of a half hour they descend to ~ 93 km. Note that this occurs during an apparent break in the auroral activity. Shortly after the sporadic ion layer reaches ~ 93 km a sporadic sodium layer is seen to form near that same altitude. This sodium layer shows some altitude modulation but gradually dissipates during the course of several hours (it has also been allowed to saturate the scale to make the background sodium layer visible).

One problem with comparing measurements like the ones presented here with one-dimensional model results is that of accounting for advection. In essence, advection represents horizontal transport of material into the measurement volume and the local changes that result due to horizontal inhomogeneities. The main goal here is to evaluate the influence that auroral ionization has on the measured sodium densities, so the presence and absence of aurora in the sodium layer is of primary importance. The focus of this discussion is therefore centered on the earlier portions of the measurements in Figure 5.1 and in particular on the first 3.5 hours of that data set. That time segment is therefore reproduced in Figure 5.2 with the gray scale for sodium adjusted to accentuate the sporadic sodium layer. The issue, then, is how to interpret the absence of aurora in the ISR measurements. Recognizing that auroral forms can have quite dramatic horizontal structure, the absence of aurora in the 0.5° antenna beam does not automatically correspond to absence of aurora just beside the beam. Fortunately, other measurements were also collected along with the ISR and lidar measurements during the same period. In particular, the image intensified all-sky imager at the facility was operated with one optical filter centered at 427.8 nm (see *Mende et al.*(1988) and *Doolittle et al.*(1990) for brief descriptions of and

Figure 5.2: ISR and Lidar Measurements, 0:00 to 3:30 UT, 11 December 1997. The upper panel shows ISR measurements of electron number density vs. altitude and time above Sondrestrom. The lower panel shows neutral Na density as a function of time and altitude from the sodium resonance lidar.

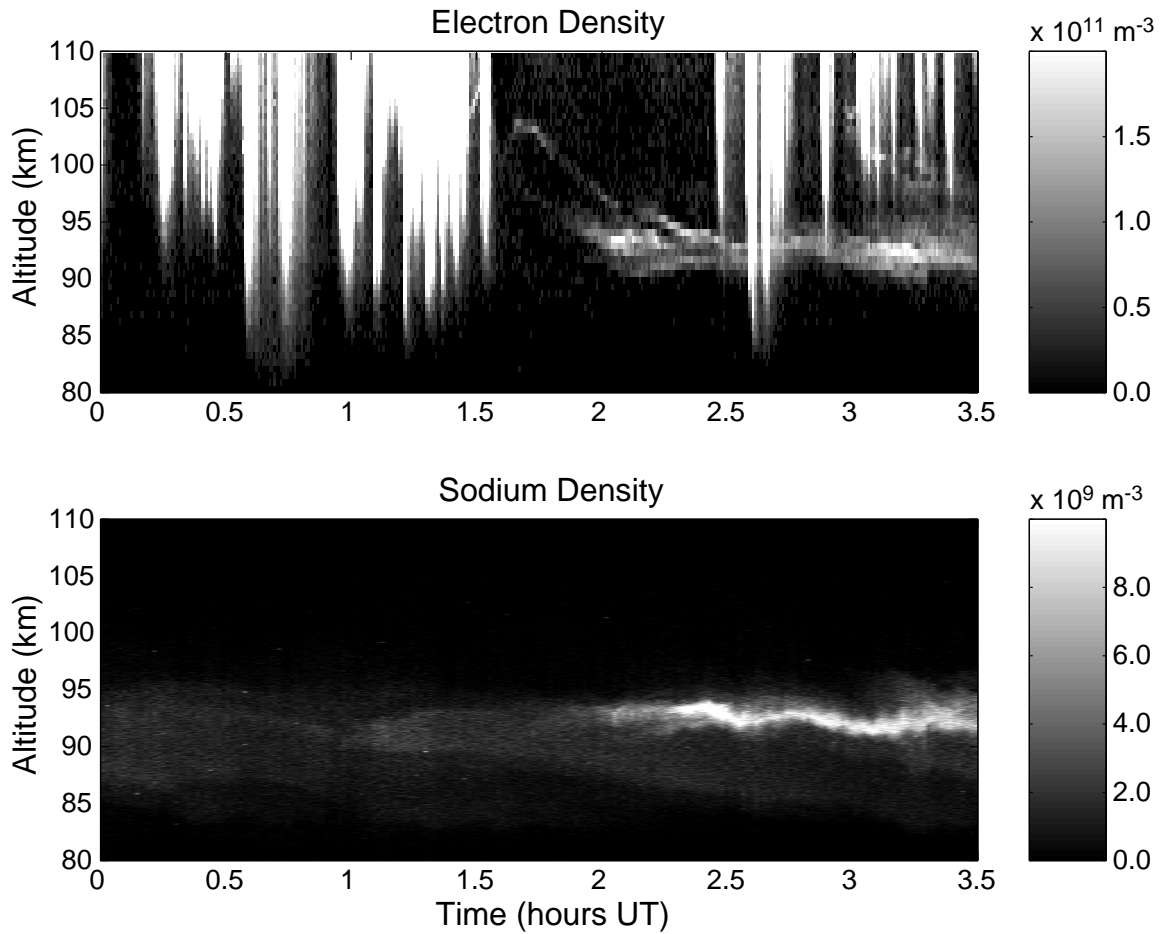
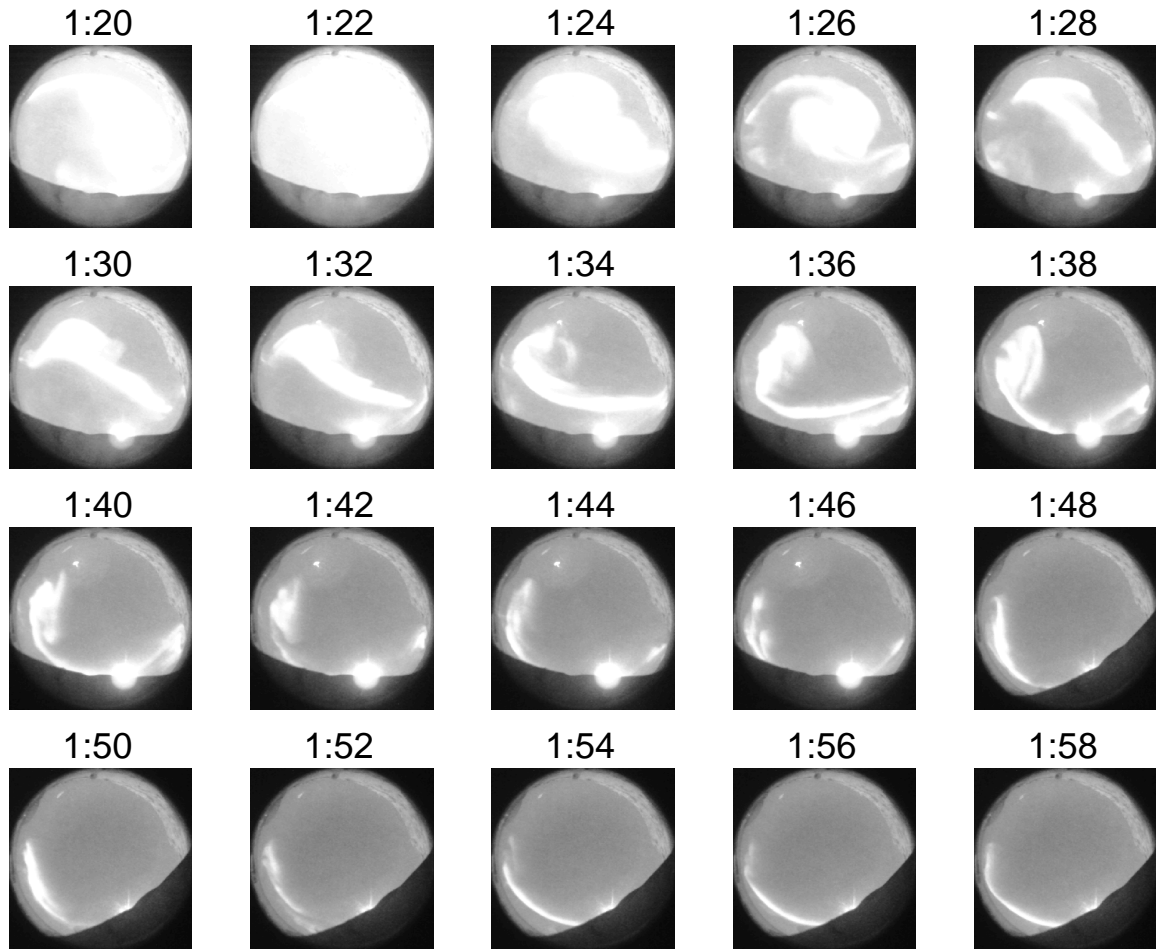


Figure 5.3: All-sky Images at 427.8 nm, 1:20 to 1:58 UT, 11 December 1997



data from this imager). The emission at 427.8 nm is from N_2^+ 1 negative, a direct product of the precipitating auroral electrons and one which has a lifetime of only 70 ns [Brekke(1997)]. Measurements of the emissions from this short-lived ion are also good indicators of the location of E -region auroral ionization and can thus be used to determine when the aurorae are present in the vicinity of the measurement volume. Figures 5.3, 5.4, and 5.5 show a time sequence of the collected images. In each of the panels of these figures, geographic north is up and east is to the left (the imager looks upward at the aurorae). Each image represents a horizon-to-horizon view of the sky, though it should be noted that the Sondrestrom facility resides in a shallow

Figure 5.4: All-sky Images at 427.8 nm, 2:00 to 2:37 UT, 11 December 1997

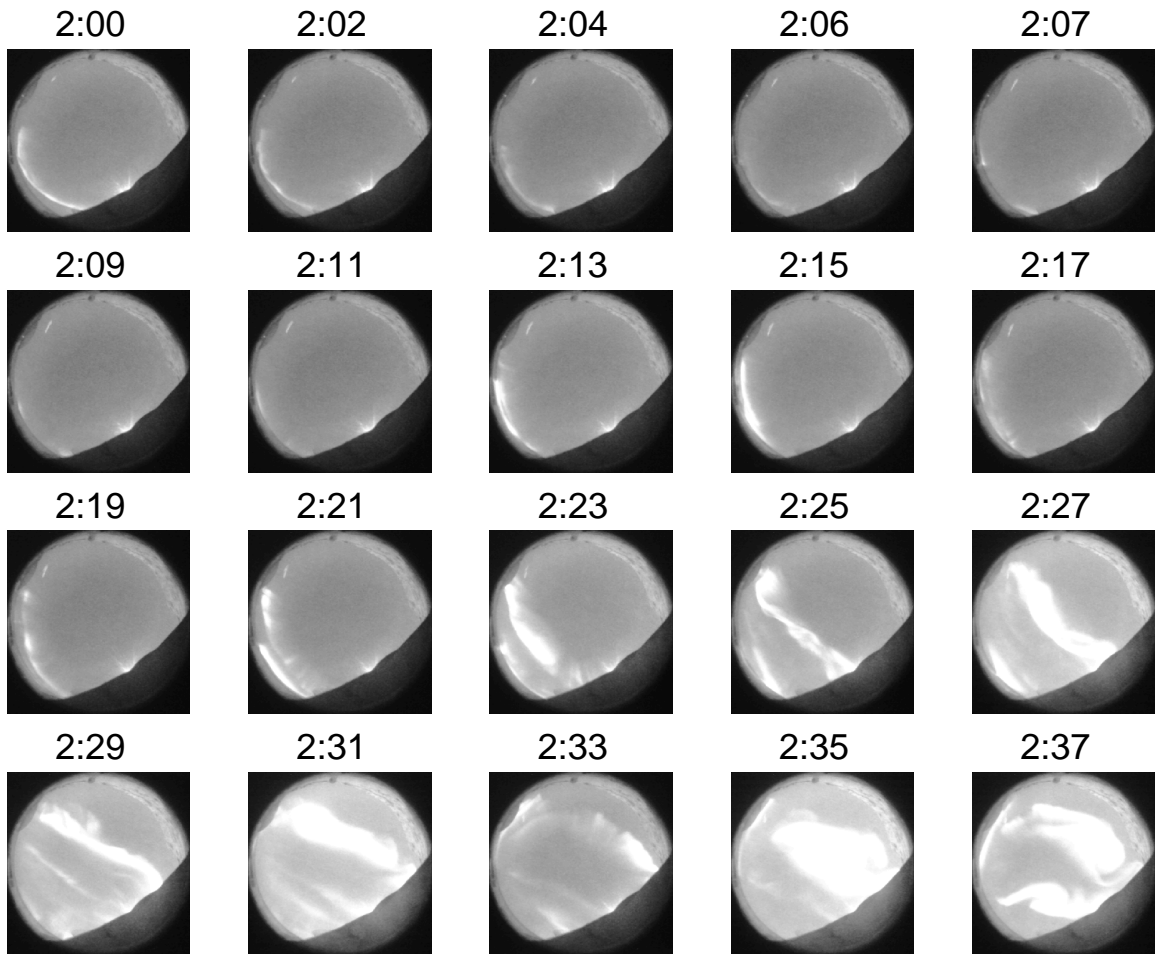
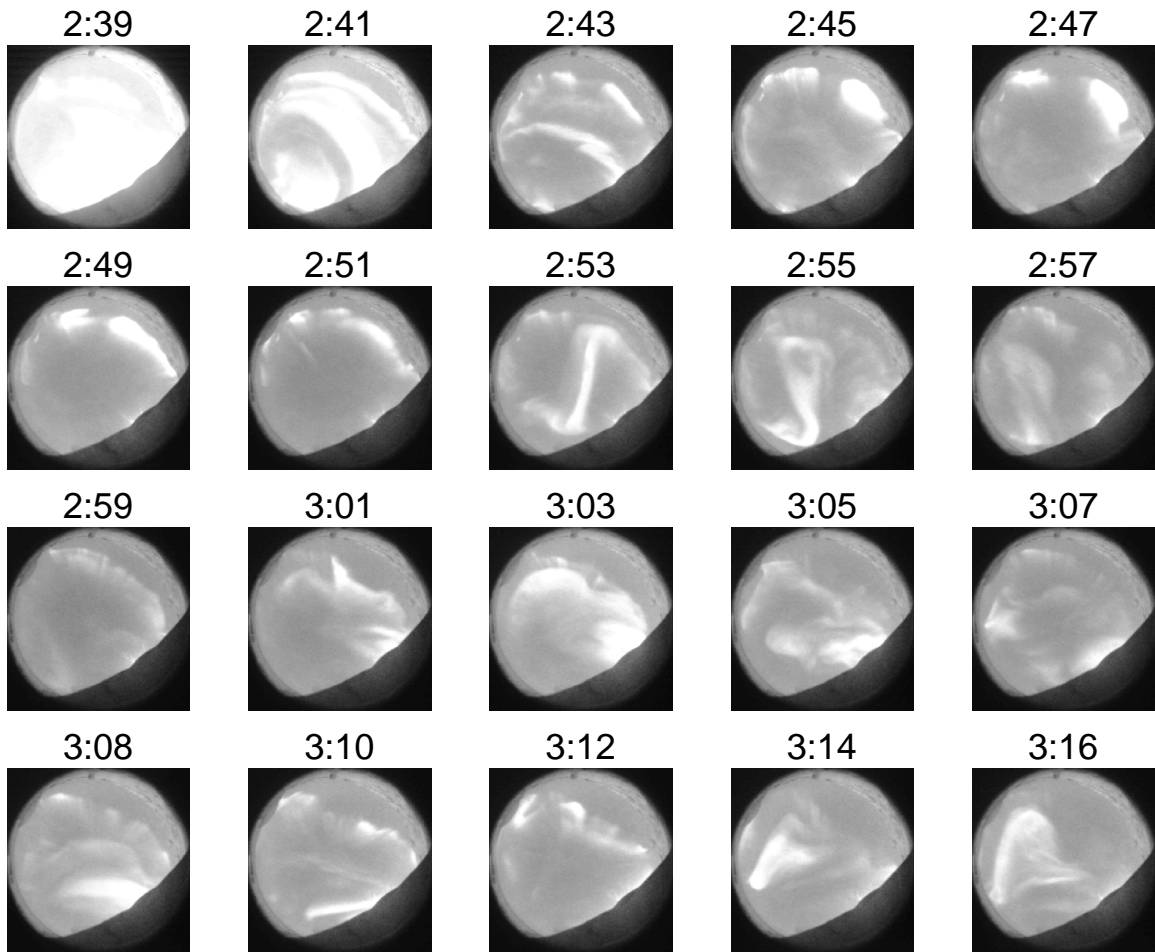


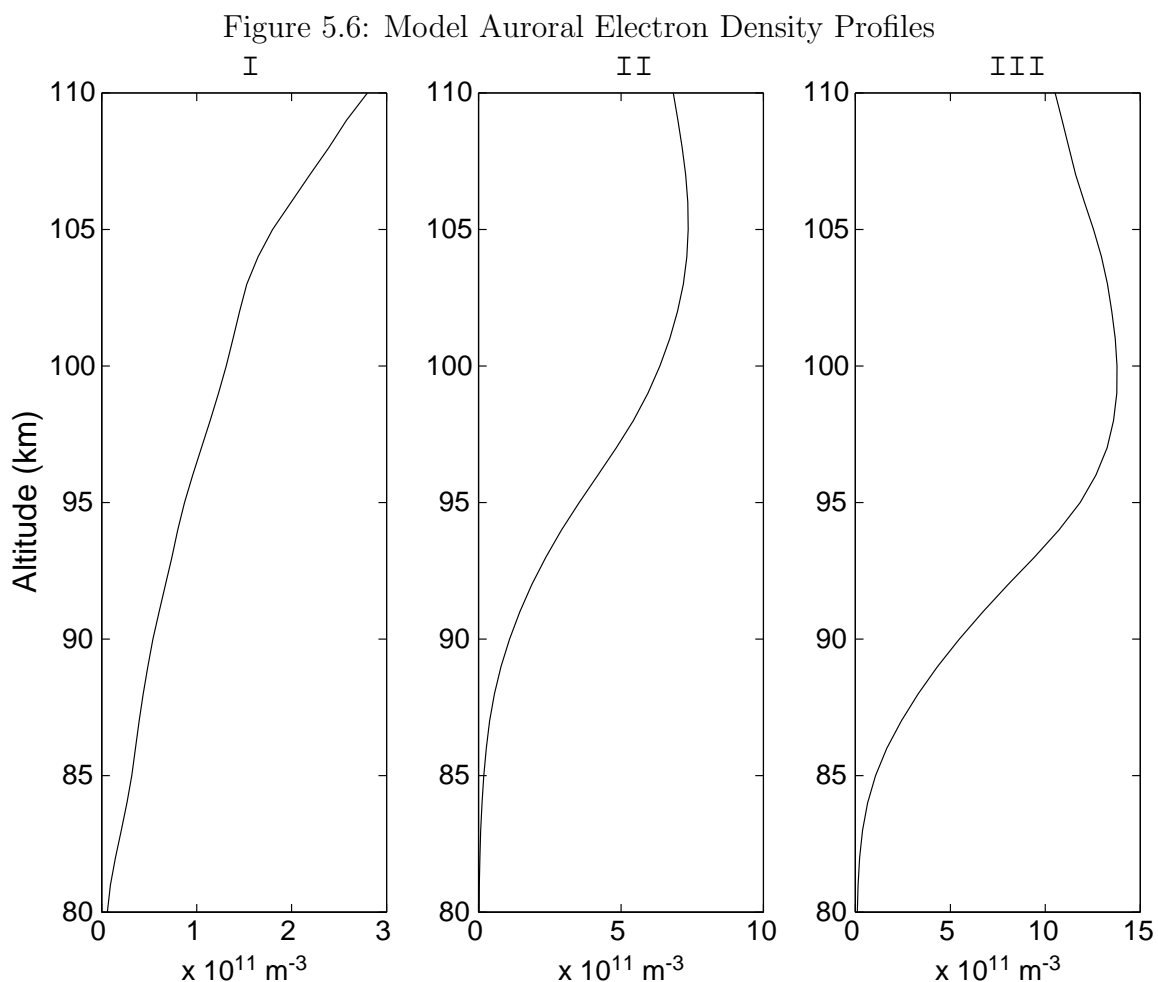
Figure 5.5: All-sky Images at 427.8 nm, 2:39 to 3:16 UT, 11 December 1997



valley and the horizons are at elevation angles of $\sim 10^\circ$. The moon is also visible in several of the frames through 1:46 UT in Figure 5.3. At that time the ‘moon shade’ was rotated to block that bright source from the camera lens. Figure 5.3 shows that aurorae were present near the measurement volume until just after 1:30 UT and that after that time auroral forms quickly receded southward. Figure 5.4 shows that the aurorae remained well south of Sondrestrom until nearly 2:30 UT. This hour-long period that indicates an absence of ionization in Figure 5.2 can thus be interpreted as indeed being without ionization in the general vicinity of the radar and the sodium measurements should thus not reflect any such effects, even with advection.

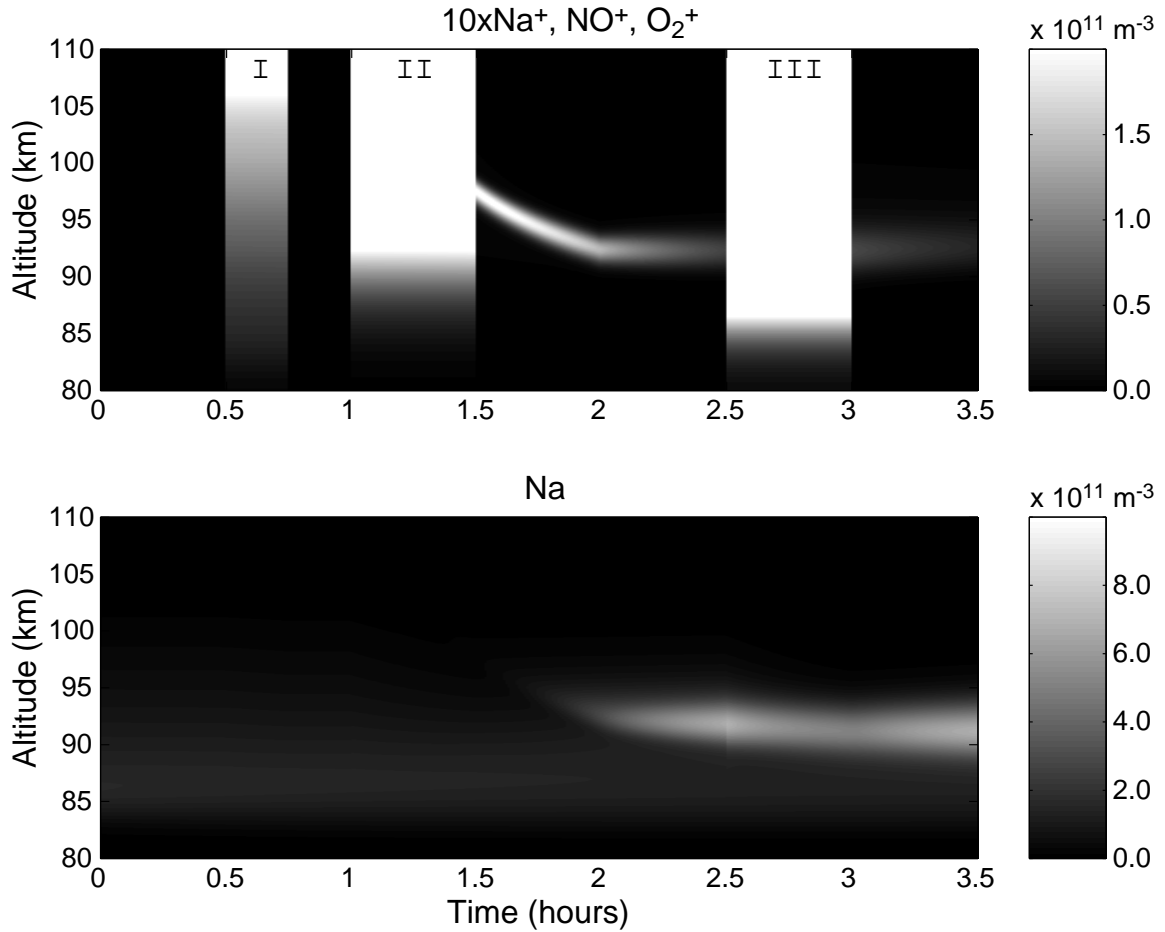
Accurate and definitive modeling of this data set clearly requires a good deal of information that is simply not available. For example, the electric fields associated with the auroral arcs are not known and neither are the E -region neutral wind velocities. The composition of the aurorally enhanced ionization is another important variable and, as indicated in Chapter 3, cannot be easily determined from the information available here. Another important question concerns the fraction of the sporadic- E ionization that is from Na^+ . Each of these parameters can affect the final outcome of the model run. On the other hand, reasonable bounds on the parameters can be set based on previous experimental results. For example, the fraction of the sporadic- E ionization from Na^+ should be relatively small, on the order of 10% or less based on arguments presented in Chapter 2. Likewise, the combination of electric field vector and neutral wind velocity can be constrained to force a sporadic- E layer to descend in a manner that reflects the measured descent. Keeping these constraints in mind, it is useful to attempt constructing a model run which reproduces the behavior of the measurements. Such a construction should indicate whether or not the chemical and dynamical reactions contained in the model *could have been responsible for the measured behavior*. Agreement between the model and measurements will lend some support to these modeled physical and chemical mechanisms.

The coupled dynamics and chemistry model was run with the following conditions. First, it was found that the total Na content prior to 1:30 UT on 11 December 1997 was approximately a factor of two less than that predicted by Figure 3.11 (note that the winter conditions for that figure corresponded to the geophysical conditions on



this date). Due to the uncertainty in, for example, the total deposition rate of Na from meteor ablation, it was not considered a significant deviation to simply scale the initial background profiles by that amount (recall the night-to-night variability in Na from Figure 3.12). Next, total electron density profiles for the times of the aurorae were taken from averages of the actual measurements. Figure 5.6 contains those averaged and smoothed profiles (note that the smoothing was done to prevent noise artifacts from appearing in the model output). Profile I corresponds to approximately 0:30 to 0:45 UT, profile II to 1:00 to 1:30 UT, and profile III to 2:35 to 2:45 UT. The fractional content of NO^+ and O_2^+ for those profiles was chosen, somewhat arbitrarily, to be the low altitude content ratio given by IRI-95: 82.2% NO^+ and 17.8% O_2^+ . The sporadic- E

Figure 5.7: Model of 11 December 1997 Measurements



layer was modeled by inserting a previously formed layer at 102.5 km altitude and at time 1:18 UT. This layer was driven downward by a south-directed 50 mV/m electric field and with no neutral winds. The electric field strength was reduced to 5 mV/m at 2:00 UT to correspond to the stable layer indicated in the measurements. The total content of the sporadic sodium layer was chosen to best match the measurements and *Heinselman et al.*(1998) pointed out that the Na content in the stable sodium layer compared to the electron content of the sporadic-*E* layer matched quite well the expected fractional content of Na^+ in the initial sporadic-*E*. The result of this model run is shown in Figure 5.7. Note that the upper panel displays the sum of the electron density (NO^+ and O_2^+) and 10 times the Na^+ density, in order to make the

sporadic- E layer visible without introducing the more dominant metals such as Fe^+ and Mg^+ . The length of time that the third auroral ionization is applied is extended to 30 minutes to match the measurements. This extension is well beyond the time that the aurorae were present in the data, but this time extension can readily be traded off with the relative NO^+ and O_2^+ concentrations to give essentially the same results (because of the very different charge transfer rates with sodium, as discussed in Chapter 3). In a broad sense, the model results correspond reasonably well to the measurements. The descent of the sporadic- E layer preceded the growth of the sodium layer by approximately the right amount of time. The auroral ionization also led to a reduction of the modeled and measured sporadic sodium. Somewhat disturbingly, however, the modeled sporadic sodium is seen to diffuse *much* more rapidly than the measured layer. This rapid diffusion might partly be ascribed to uncertainties due to advection, but this explanation would require an extremely unlikely constant source for sporadic sodium just up-wind of the measurement volume. A more likely scenario is that this is an indication of the sporadic nature of eddy diffusion. As is discussed in some detail in Appendix A, eddy diffusion is not a simple steady-state phenomenon and it shows significant structure both in time and space. The measurements investigated here appear to suggest that the diffusion present at that time and at the sporadic sodium layer altitudes was purely molecular diffusion. To investigate this possibility, the model was re-run with the eddy diffusion coefficient set to zero. The result of that model run is given in Figure 5.8, and shows a much more compact sporadic sodium layer and one which does not diffuse nearly as rapidly, providing a much better qualitative fit to the data shown in Figure 5.2. To examine the effect more quantitatively, the column content (integrating over altitude) of the measurement can be compared to that from the model, as is done in Figure 5.9. It can clearly be seen from Figure 5.9 that the model, with careful but reasonable choice of the unknown parameters, reproduces the measurements from a quantitative standpoint as well as a qualitative one. As predicted in Chapter 3, the influence of the aurora on the background sodium layer is perhaps measurable but by no means overwhelming. Its influence on the sporadic sodium layer, on the other hand, is easily discerned in the data.

Figure 5.8: Model of 11 December 1997 Measurements, No Eddy Diffusion

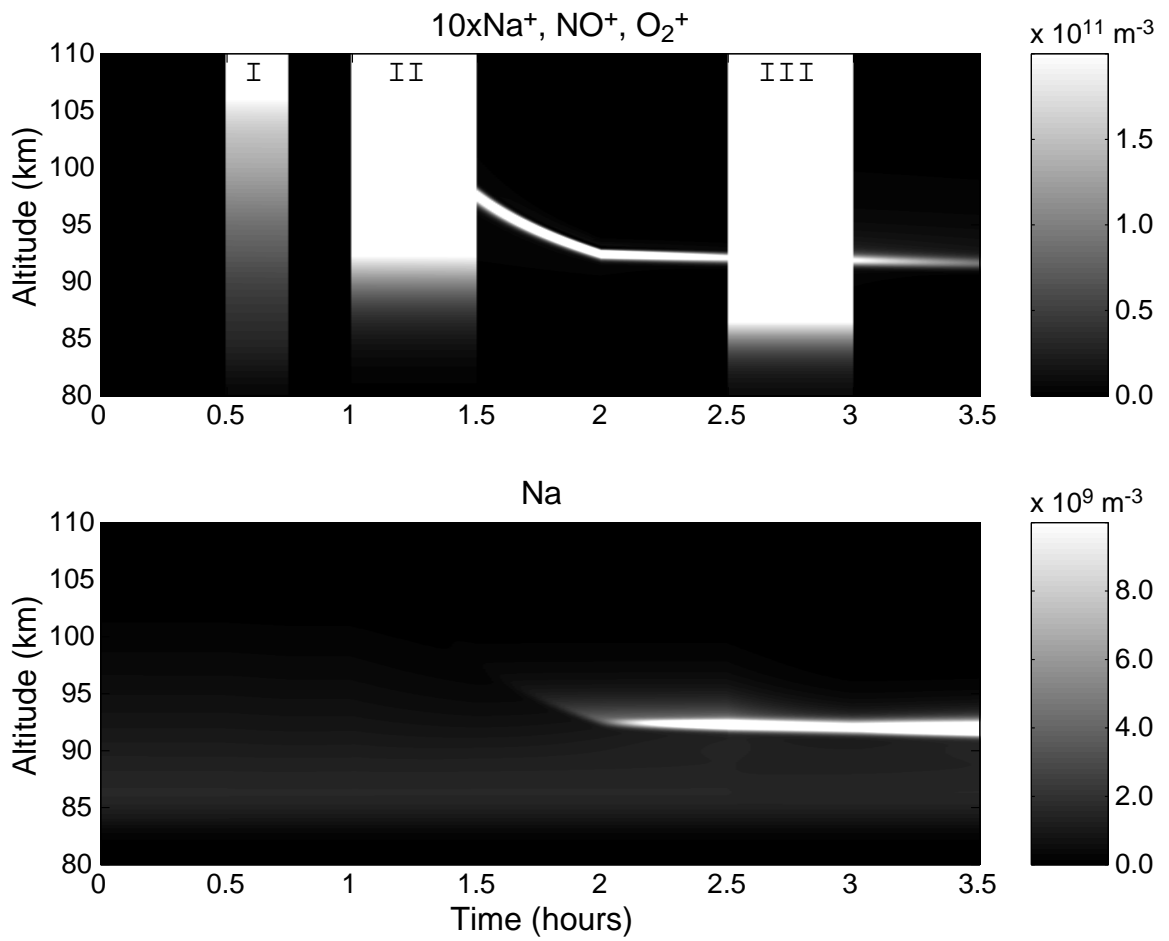


Figure 5.9: Sodium Column Contents, 11 December 1997, Measurements and Model

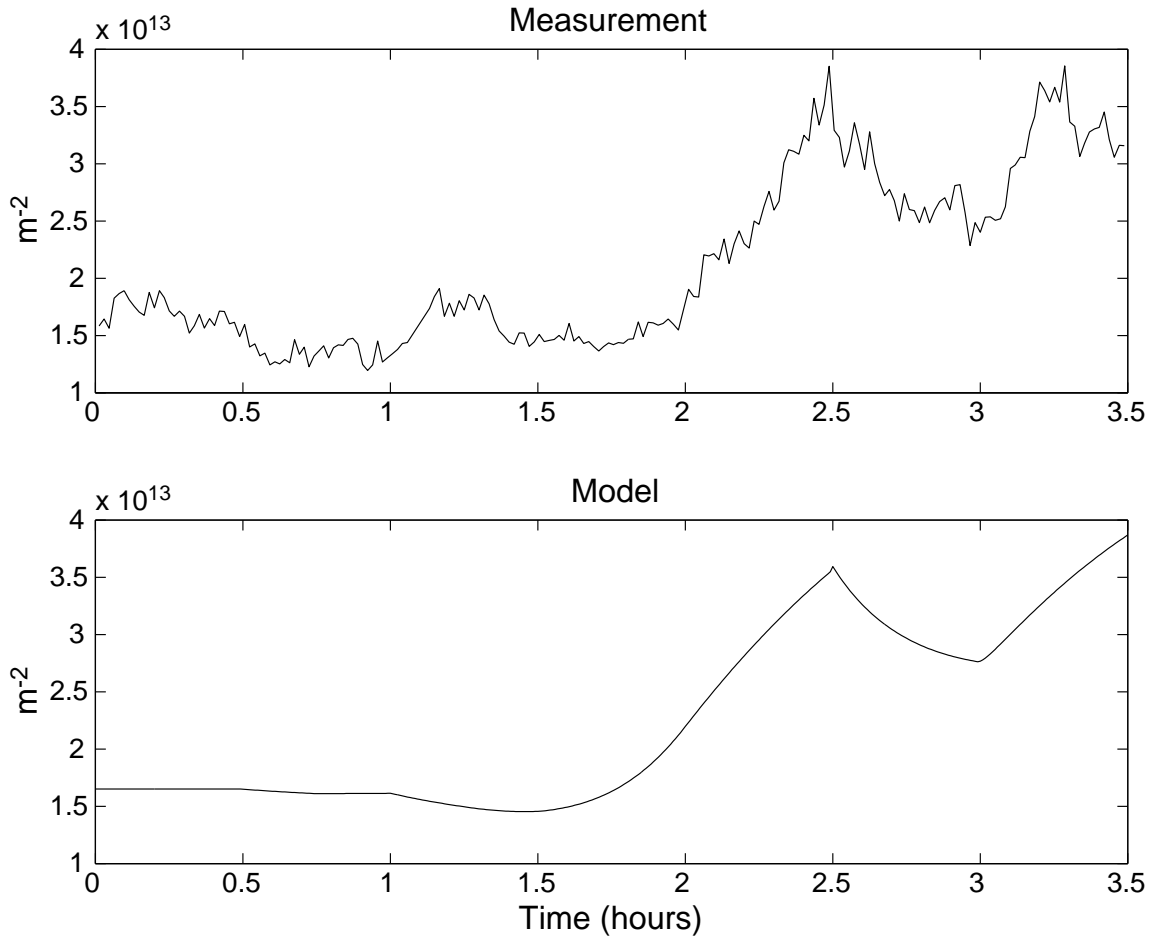
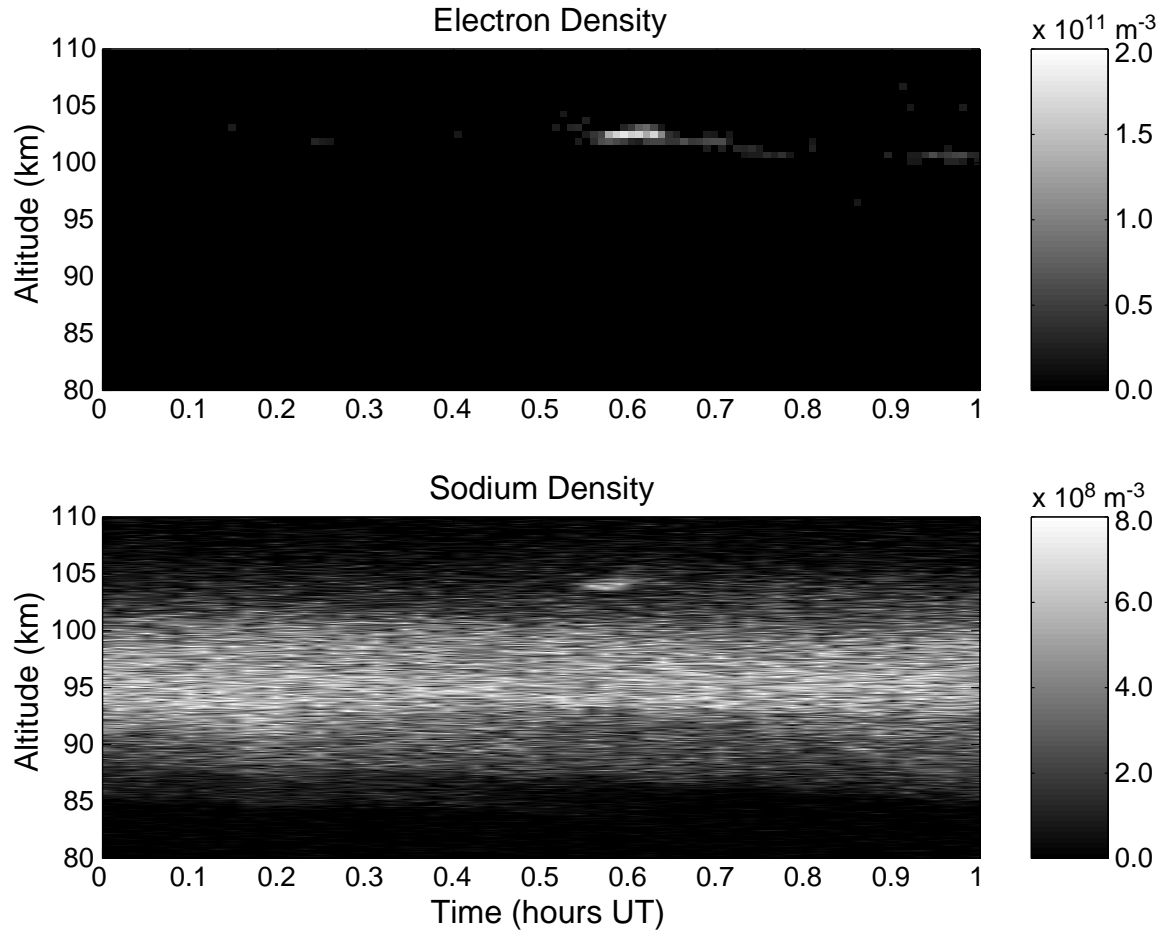


Figure 5.10: High Altitude Sporadic Sodium Layer, 6 February 1998



For the test case just studied, it can be concluded that gas phase chemistry and dynamics alone can explain all of the relevant aspects of the measurements in a time-resolved sense. However, these mechanisms do not explain all aspects of the available measurements. As has been pointed out by, for example, *Kane et al.*(1993) there are instances when the sporadic sodium densities even exceed the total electron densities in sporadic-*E* layers. Similarly, some sporadic sodium layers appear at altitudes well above where the *Cox and Plane*(1998) chemical processes are expected to occur. Figure 5.10, for example, shows the brief occurrence of a weak sporadic sodium layer at nearly 105 km altitude! Many more examples of high altitude sporadic layers have been reported by, for example, *Hansen and von Zahn*(1990). It thus appears

likely that more than one mechanism is at work in the formation of these layers. In any event, once they are formed the results presented in this thesis concerning the influence of auroral ionization on the layer atoms should apply.

5.1 Chapter Summary

A set of measurements of the time evolution of neutral sodium in the presence of auroral ionization is analyzed in detail in this chapter. We find that these measurements are consistent with our model from Chapter 4, except that the eddy diffusion coefficient assumed in that chapter was too large in this instance. This exception is not unexpected because turbulent eddies in the upper atmosphere are known to be quite variable both temporally and spatially.

Chapter 6

Conclusions

Oh, it was wild and weird and wan, and ever in camp o' nights
We would watch and watch the silver dance of the mystic Northern Lights.
And soft they danced from the Polar sky and swept in primrose haze;
And swift they pranced with their silver feet, and pierced with a blinding blaze.
They danced a cotillion in the sky; they were rose and silver shod;
It was not good for the eyes of man—'twas a sight for the eyes of God.

Robert Service

The study presented here describes the influences of aurorally-enhanced ionization on the gas-phase chemistries of iron and sodium in Earth's upper atmosphere. These influences are investigated both via theoretical modeling of the relevant physical and chemical processes and via careful analysis of several sets of measurements of the atmospheric state and dynamics.

Through theoretical modeling of gas-phase iron chemistry, we suggest that the steady-state background iron layer *is not* greatly affected by auroral ionization, largely because the steady-state iron at auroral altitudes is already expected to be in an ionized state. On the other hand, we also show that recently deposited neutral iron, which has not yet been ionized by charge-transfer reactions, *is* significantly affected by aurorae. The same can be said of high altitude (above 90 km) sporadic iron layers — exposure to auroral processes quickly changes the state of that material from Fe to Fe⁺. More specifically, the e-folding time for neutral iron in the presence of 10¹² m⁻³ electron densities is just over 15 minutes. We present a single measurement of

the possible ionization of recently ablated meteoric material.

Modeling of the chemistry of sodium tells a somewhat different story. The slightly higher natural altitude of the steady-state background sodium layer makes it more susceptible than iron to auroral influences. The rate at which auroral ionization affects neutral atomic sodium is also heavily dependent upon the chemical makeup of the ionized species. For aurorae consisting of primarily NO^+ , even a 10^{12} m^{-3} electron density has an e-folding time of nearly an hour. On the other hand, the e-folding time drops to well less than 10 minutes if the O_2^+ concentration makes up the bulk of the ionization.

A model of the formation and dynamics of sporadic ion layers is presented which includes the previously neglected effects of eddy diffusion and auroral ionization. This model is compared with measurements of the time evolution of a sporadic- E layer and it is found to reproduce those measurements quite accurately.

We also present a coupled model with the influences of both sodium chemistry and ion and neutral dynamics. In accordance with previous reports by *Cox and Plane*(1998), this coupled model is shown to be capable of predicting the formation of sporadic neutral sodium layers.

A case study of an aurorally disturbed sporadic sodium layer event is presented in detail, although a number of important parameters are not directly measured and, as a result, *definitive* support for the developed model is not possible. With reasonable values for the unknown parameters, however, it is found that the model reproduces the measurements quite accurately, adding significant credence to the model itself and to the predictions made in earlier sections.

One obvious area for future work is the collection of further examples of these effects and comparison of the measurements with our models. This would help determine whether or not all of the relevant physical and chemical processes are indeed included. Even more desirable would be measurements from additional instrumentation for determining the physical and chemical parameters which must otherwise be estimated. We recommend, for example, that a rocket campaign for *in-situ* measurements of electric fields, $[\text{O}_2^+]/[\text{NO}^+]$ concentration ratios, etc., be mounted in conjunction with incoherent scatter radar and resonant lidar measurements of sporadic- E

and sporadic sodium layers to allow more detailed studies of the relevant physics and chemistry.

Appendix A

Diffusion in the Upper Atmosphere

Big whirls have little whirls which feed on their velocity.
Little whirls have lesser whirls, and so on to viscosity.

Lewis F. Richardson

It should come as no surprise that diffusion processes are central to understanding the limits of layering phenomena in the upper atmosphere. In fact, several *different* types of diffusion come into play during the expansion of trails of ablated meteoric material. We restrict our discussion here to the diffusion of minor constituents in the atmosphere and generally ignore momentum and heat diffusion. Simplified models of diffusive behavior are developed and some of the implications/limitations of these simplifications are pointed out. In particular, many of the derived relations are applicable only to the meteor ablation region of the atmosphere and cannot be used in other altitude regimes. In some cases, the relevant time scales are also critical to understanding the modeling results.

A.1 Molecular Diffusion

Diffusion at the molecular level is well established from both theoretical and experimental grounds — this type of diffusion basically describes the mean relative motion of different constituents due to random thermal motions in the presence of collisions

and in the vicinity of concentration gradients. For the purposes of this thesis, our primary interest is in the diffusion of a minor species in a much more dense background atmosphere. For sodium, for example, the relative concentration is generally less than one part in 10^9 when compared to N_2 . Following the approach described in chapter 15 of *Banks and Kockarts(1973b)*, we start with the following general steady-state (no acceleration) relation for the relative diffusion velocity of gas 1 with respect to gas 2:

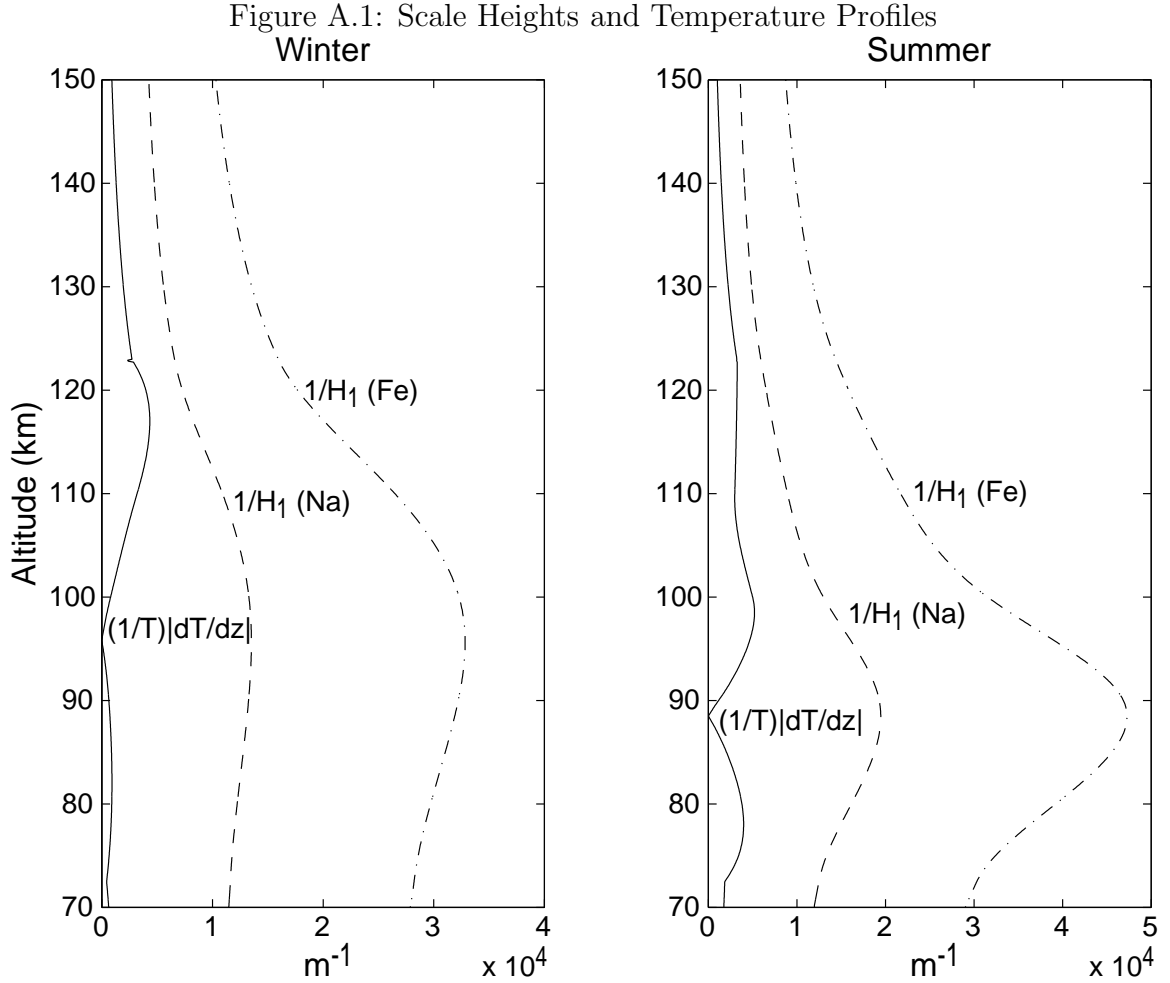
$$\vec{v}_1 - \vec{v}_2 = -D_{12} \left[\frac{n^2}{n_1 n_2} \nabla \left(\frac{n_1}{n} \right) + \frac{m_2 - m_1}{m} \nabla (\ln p) + \alpha_T \nabla (\ln T) \right] \quad (\text{A.1})$$

where D_{12} is the molecular diffusion coefficient of gas 1 in gas 2, \vec{v}_i , n_i , and m_i are the velocity, number density, and mass for gas i , $n = n_1 + n_2$ is the total number density, $m = (n_1 m_1 + n_2 m_2)/(n_1 + n_2)$ is the mean molecular mass, $p = p_1 + p_2$ is the total pressure, α_T is the thermal diffusion factor, and T is the absolute temperature of the gas. For the vertical diffusive motion of a minor species under the assumptions of hydrostatic equilibrium and the ideal gas law, equation (A.1) is simplified to

$$v_z = -D \left[\frac{1}{n_1} \frac{dn_1}{dz} + \frac{1}{H_1} + (1 + \alpha_T) \frac{1}{T} \frac{dT}{dz} \right]. \quad (\text{A.2})$$

where v_z is the relative vertical motion of the minor constituent compared to the background, D is its diffusion coefficient, n_1 is its concentration, $H_1 = k_B T/m_1 g$ is its natural scale height (e-folding distance), k_B is Boltzmann's constant, and g is gravitational acceleration.

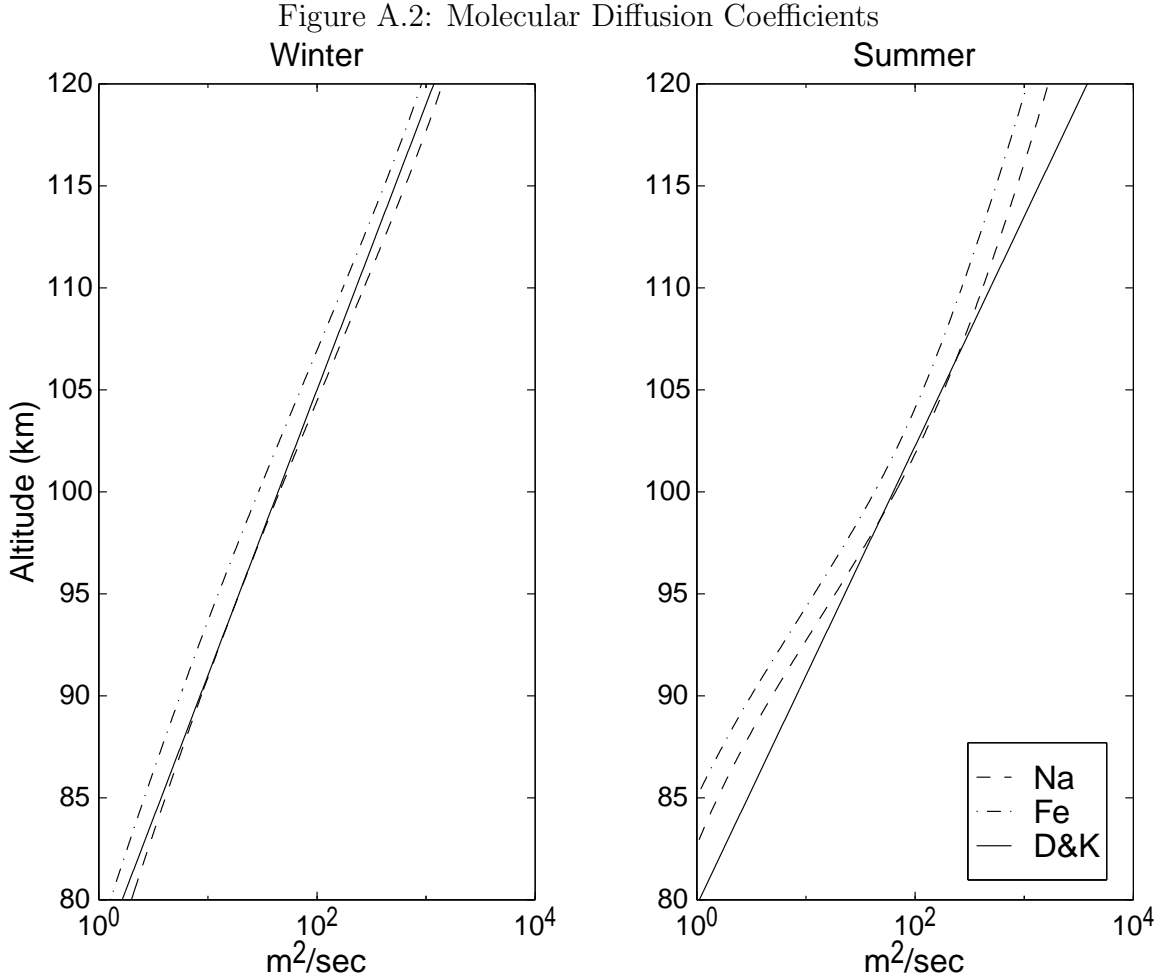
The next level of approximation entails simplifying equation (A.2) by examining the magnitudes of some of the factors. For Ar in N_2 at very low concentrations of Ar, *Banks and Kockarts(1973b)* show $\alpha_T \simeq 0.17$. For Na, whose mass is less than the mean mass of the background gas, α_T is negative while α_T for Fe has a positive value. In any event, we expect α_T to be reasonably small so it can be neglected for these relatively massive metallic constituents. This conclusion is further supported by a comparison of the terms $(1/T)(dT/dz)$ and $1/H_1$ for the altitudes of interest in this study. Some simple calculations of profiles of these two values using model



temperature profiles from MSISE-90 [*Hedin(1991)*] reveal that the scale height term dominates in the 75 km to 140 km altitude region, especially below 110 km (see Figure A.1). Neglecting α_T thus corresponds to neglecting a small perturbation of these secondary temperature gradient effects. We are thus left with the following relation:

$$v_z \simeq -D \left[\frac{1}{n_1} \frac{dn_1}{dz} + \frac{1}{H_1} + \frac{1}{T} \frac{dT}{dz} \right] \quad (\text{A.3})$$

which basically shows that molecular diffusion will tend to drive the scale height of any given constituent toward its natural scale height, H_1 , at a rate given by D and with perturbations from that target state driven by temperature gradients.



The diffusion coefficient, while well determined both theoretically and experimentally for some constituents, has apparently not been specifically measured for the metal species of interest in this work, though *Banks and Kockarts*(1973b) do provide expressions for approximate estimates. In particular, they present the following relation as a function of the constituent masses (converted here to mks units):

$$D_{12} = 6.20 \times 10^6 \left(\frac{1}{m_1} + \frac{1}{m_2} \right)^{1/2} \frac{T^{1/2}}{n}. \quad (\text{A.4})$$

Using MSISE-90, this relation is evaluated for the altitudes of interest in Figure A.2 for both winter and summer conditions at Sondrestrom, Greenland. The diffusion

coefficients presented in *Danilov and Kalgin*(1992) (labelled D&K) are also included in Figure A.2. Note the exponential increase in molecular diffusion with altitude and the relatively small difference between diffusion coefficients for sodium and iron. For much of the work presented in this thesis the profiles of Danilov and Kalgin are used for molecular diffusion of all species. Figure A.2 shows that this approximation is quite good for winter conditions but it may somewhat over-estimate the diffusion coefficient in summer. As shown in Section A.2, this approximation does not significantly affect the overall results because eddy diffusion generally dominates at altitudes below about 100 km, where the neutral (as opposed to ionized) species are most prevalent.

A.2 Eddy Diffusion

Eddy diffusion is a more complicated phenomenon than molecular diffusion because it involves mixing that is driven by turbulent eddies in the background atmosphere. *Banks and Kockarts*(1973b) treat eddy diffusion in a manner similar to molecular diffusion, via a simple Fick's law relation. While we also end up adopting that approach, it is instructive to look at eddy diffusion in greater detail so that the implications of an approach using Fick's law can be appreciated.

It has long been recognized that turbulent motion dominates the atmospheric mixing up to the altitude of the turbopause, around 100 km [e.g. *Brekke*(1997), *Hargreaves*(1992), *Wayne*(1991)]. In this region, referred to as the turbosphere or homosphere, the mixing ratios of the various atmospheric constituents are relatively constant with altitude because the tendency to gravitationally separate different gases is offset by turbulent motion. Above the turbopause, in the heterosphere, various constituents do tend to follow their own individual scale height variations, as discussed in section A.1. The precise nature and occurrence of the turbulent eddies is still not well known due, primarily, to the difficulties involved in making direct measurements of this upper atmospheric region. Nonetheless, various techniques have been utilized to uncover some aspects of the turbulent behavior.

One of the earlier upper atmospheric turbulence measurement techniques involved investigating the scattering characteristics of long duration meteor trails. Work by

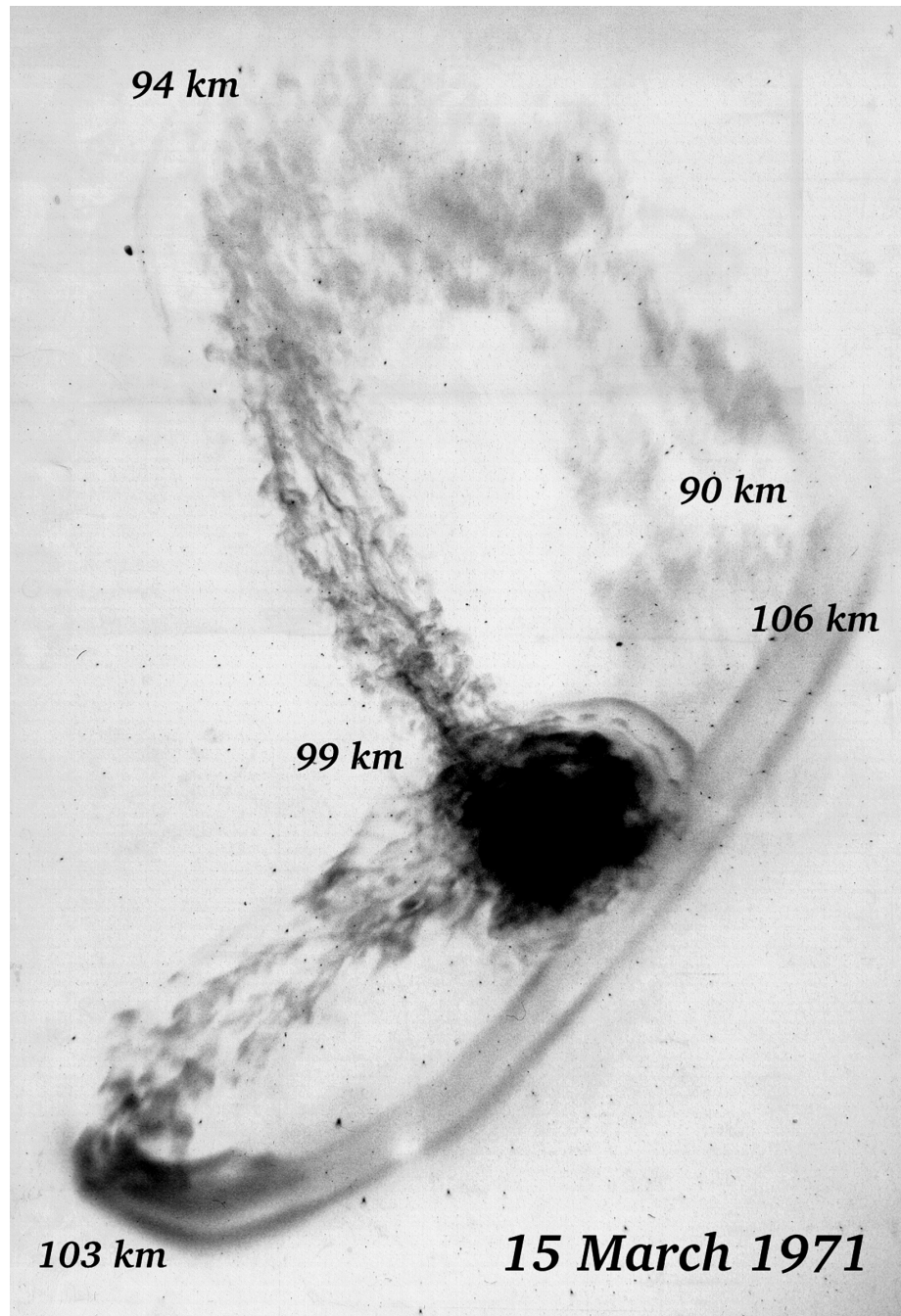
Table A.1: Eddy Diffusion

Time	Diffusion Coefficient
$t < t_2$	D
$t_2 < t < t_1$	wt^2
$t_1 < t$	K

Booker(1956) and *Booker and Cohen*(1956) described the time evolution of that scattering in terms of a size spectrum of eddy turbulence. They basically used the work credited to *Kolmogorov*(1941) in which energy is introduced to the eddy motion at the largest scale sizes, cascades to smaller scale sizes via the process of vortex stretching, and is finally dissipated as heat from the smallest eddies via viscosity (see *Blackadar*(1997) for a brief description of the process). In this process, the eddies start out highly anisotropic at the large end of the spectrum but quickly become essentially isotropic via the energy cascading mechanism. From this starting point, *Booker*(1956) suggested three time regimes over which a meteor trail will experience three different types of diffusive growth. The boundaries of those regimes correspond to the characteristic time constants for the largest (t_1) and smallest (t_2) eddies. After deposition but prior to time t_2 the meteor trail experiences simple molecular diffusion with a constant diffusion coefficient D because it has not yet had time to ‘feel’ the eddy motion. Between times t_2 and t_1 the diffusion coefficient increases as the square of the elapsed time, in Booker’s notation as wt^2 where w is the turbulence power per unit mass. Subsequent to t_1 the diffusion coefficient is now a different constant which Booker called v_1L_1 but which is designated K here, as summarized in Table A.1. One apparent problem with Booker’s analysis is his estimate of the size of the smallest eddies. *Booker*(1956) suggested that at 90 km altitude the eddies could be as small as 1.3 meters — more than an order of magnitude smaller than the eddies measured by sounding rockets (see below). Finally, it is interesting to note that in this early work the effect of turbulence on the meteor trail scattering was referred to as ‘incoherent scattering,’ a term now generally reserved for the incoherent scatter radar technique described in Appendix B, but Booker’s work predated the seminal *Gordon*(1958) paper by several years!

Another method for measuring turbulence entails depositing a chemical or smoke trail in the upper atmosphere with a sounding rocket and observing the trail's temporal evolution photographically from the ground. Earlier rocket launches used sodium as the chemical tracer [e.g. *Rosenberg et al.*(1963b), *Blamont*(1963)], but most recent measurements favor trimethyl aluminum (TMA). The reason for this is that while sodium requires the trail region to be sunlit with an otherwise dark sky as seen from the ground (before sunrise or after sunset), the aluminum in TMA creates a self-luminous trail via reactions with ambient oxygen atoms [*Rosenberg et al.*(1963a)] and can thus be utilized whenever the skies are dark. With ground-based triangulation techniques from multiple site photographs of the trails as well as star fields, TMA is used to measure neutral wind velocities as well as diffusion. Figure A.3 shows an example of a TMA trail as photographed from almost directly below at Hall Beach, Canada [*Heppner and Miller*(1982)]. In the absence of winds, this photograph would have been simply a glowing dot (black in this negative image), but the presence of wind shears with altitude resulted in this backwards B configuration from the perspective of the camera. For the portions of the trail labelled 90 km, 94 km, 99 km, and up to 103 km altitude the trail shows clear signs of turbulent structure. Between 103 km and 106 km, on the other hand, the trail exhibits laminar flow (molecular diffusion). According to *Larsen*(1999), the knot near 99 km appears to be the result of overturning, probably due to a breaking gravity wave. Larsen also indicated that the 'blobby' structure between 90 and 94 km is indicative of nearly isotropic mixing while the 'rope-like' structures from 94 to 103 km suggest a more two-dimensional turbulence. Sequences of such photographs can, of course, be used to infer the temporal evolution of trails. One early TMA experiment, reported by *Rees et al.*(1972), convincingly showed the temporal transition from simple molecular diffusion to eddy-driven diffusion. In contrast to the *Booker and Cohen*(1956) meteor measurements, however, the transition to wt^2 growth first appeared after the much longer time of 32 seconds. *Blamont*(1963) also reported a value for t_2 of approximately 30 seconds, still interpreted as the time constant of the small scale eddies. *Rees et al.*(1972) reported that the smallest eddies measured photographically were on the order of 50 meters in diameter, also in good agreement with earlier reports by *Blamont*(1963) which showed

Figure A.3: TMA Measurement of Winds and Diffusion. This negative image of a TMA trail was photographed from nearly directly below at Hall Beach, Canada [Heppner and Miller(1982)]. The turbopause is evident at ~ 103 km altitude. Photo courtesy of M.F. Larsen.



no turbulent structures smaller than that size. The ~ 50 meter scale size is consistent with a ~ 30 second time constant, so the experimental results and analysis presented by *Booker and Cohen*(1956) for meteor scatter measurements, predicting eddy sizes as small as 1.6 meters, must be viewed with some skepticism. In particular, an analysis by *Bronshten*(1983), p. 233, indicates that meteor trails with durations less than ~ 50 seconds disintegrate mainly because of electron attachment to oxygen molecules, not from eddy diffusion. At the other end of the scale, *Thrane et al.*(1987) indicated that the larger eddies are bounded by buoyancy forces to be typically around 1 km in the mesosphere. Sets of high resolution TMA measurements presented by *Lloyd et al.*(1972) and others revealed another interesting characteristic of the turbulence – that it often occurs in sheet-like structures of limited altitudinal extent interspersed with non-turbulent regions. In a reanalysis of some older data, *Roper*(1996) showed high resolution plots of turbulent diffusion as a function of altitude and related these measurements to breaking atmospheric gravity waves; turbulent structures of less than 1 km in thickness were detected. In addition, Roper reported that neither the thickness nor the altitude of the layers changed with time (over the course of diffusion of individual trails). *Hocking*(1990) adds that turbulence in this region appears to be both temporally and spatially intermittent and that it appears to occur in patches. Temporally, it apparently occurs between 30% and 80% of the time with the lower percentages occurring at lower altitudes.

A less direct but nevertheless very powerful approach to estimating eddy diffusion coefficients entails examination of the extent to which molecular diffusion results in the separation of gases of different masses. As mentioned earlier, eddy diffusion tends to produce a constant mixing ratio for all constituents with altitude and, as such, alters the distribution that would be present in its absence. One way to quantify the effect of eddy diffusion is via the so-called K -theory approach, which basically uses a tensor version of Fick's law to describe the manner in which turbulent eddies affect gradients in minor constituents [*Ebel*(1980)]. A further simplification considers only the vertical component of the diffusion, assuming that the most important eddies are largely isotropic. This leads to the following relation for eddy diffusion velocity, as

presented in *Banks and Kockarts(1973b)*, *von Zahn et al.(1990)*, and elsewhere:

$$v_z = -K \left[\frac{1}{(n_1/n_n)} \frac{d(n_1/n_n)}{dz} \right] = -K \left[\frac{1}{n_1} \frac{dn_1}{dz} - \frac{1}{n_n} \frac{dn_n}{dz} \right] \quad (\text{A.5})$$

which shows that the eddy velocity is driven by the mixing ratio of the minor species n_1 to the background n_n . As expected, the sign of the velocity tends to drive the altitude variation of the mixing ratio toward zero. Imposing ideal gas law constraints yields the following alternate form for this eddy diffusion velocity

$$v_z = -K \left[\frac{1}{n_1} \frac{dn_1}{dz} + \frac{1}{H} + \frac{1}{T} \frac{dT}{dz} \right] \quad (\text{A.6})$$

where $H = k_B T / mg$ is the scale height of the background atmosphere, not the natural scale height of the constituent under consideration. An assumption implicit in this approach of using mixing ratio variations is that the quantity of interest is some ‘average’ diffusion coefficient. The actual atmosphere has a tendency to average over the temporal variations in the turbulent motion that were mentioned in the previous paragraph. The extent of that averaging was discussed by *von Zahn et al.(1990)*, whose analysis indicated that turbulence can, in principle, move the atmosphere to a mixed state very quickly. The return to an unmixed state, by contrast, is quite slow, with a time constant on the order of H^2/D , corresponding to approximately 80 days at 90 km and 4 days at 110 km altitude. Hence, mixing ratio profiles provide quantitative information only on long-term averages of turbulence. Instantaneous measurements of turbulence require the use of other techniques, such as the TMA trails discussed earlier. Thus, the use of altitude profile estimates of K must account for both the source of the profile information and the nature of the application. Calculations of long-term average profiles of meteoric sodium, for example, can more safely rely on K profiles than calculations of estimates of the diffusion of sodium from individual meteor trails can.

While conceptually straightforward, the estimation of eddy diffusion profiles from mixing ratio measurements actually requires a good deal of finesse. The paper by *von Zahn et al.(1990)* discussed an approach to making that estimation based on

rocket-borne mass spectrometer measurements of the ratio of Ar to N₂. Their measurements showed significant variability from launch to launch and, in any event, they suggested that the uncertainties in their estimates of the maximum value of K were on the order of a factor of 2. An analysis by *Danilov and Kalgin*(1992) of a large number of measurements pointed out a number of other obstacles to estimating realistic ‘average’ profiles of K . In particular, they argued that it is important to account for vertical mean transport in the continuity equations for the various constituents. Based on their measurements, *Danilov and Kalgin*(1992) presented profiles of both K and D (molecular diffusion coefficient) for summer and winter conditions and at three different latitudes. Figure 2.3 in Chapter 2 shows their result for the high latitude location (80° N). These profiles are used for most of the work presented in this thesis. Note that the profiles show a number of characteristics of the eddy diffusion. First, the diffusion here is significantly greater in the winter than it is in the summer. This trend resulted directly from the *Danilov and Kalgin*(1992) analysis and it was not well established by previous investigators. Another aspect of note in Figure 2.3 is that the turbopause is more than 10 km higher in the winter than in the summer. Referring back to Figure A.3, these summer and winter turbopause altitude predictions are on either side of that spring-time measurement from 1971.

Appendix B

Incoherent Scatter Radar

The satellite is a natural extension of rockets, which are natural extensions of planes and balloons, which are natural extensions of man's climbing trees and mountains in order to get up higher and thus have a better view.

James Van Allen

The incoherent scatter radar technique had its genesis over 40 years ago when *Gordon(1958)* recognized that Thomson scattering from electrons could be employed for ionospheric studies. He realized that radar technology had advanced to the stage where sufficiently powerful transmitters, large antennas, and sensitive receivers could be brought to bear on the problem of measuring ionospheric electron densities via this type of scattering. The analysis presented by *Gordon(1958)* estimated that the scattered signal would be Doppler broadened in accordance with the thermal speeds of the electrons in the plasma. This extreme broadening requires somewhat greater sensitivity than was available with systems then in existence and, largely based on that analysis, the 305 meter diameter antenna for the Arecibo Observatory was established. Well before the completion of that system, the surprising discovery was made by *Bowles(1958)* that a much more modest system could and did detect Thomson scattering from the ionosphere. The explanation turned out to be the neglected electrostatic coupling between the electrons and ions in the plasma, which results in a spectral width of the return corresponding to the lower thermal speeds of the much more massive ions (with a wealth of additional information about the plasma). This

return is sampled through a more narrow-band system with much more restrictive receive filters and, as a result, much less noise power. A thorough review of the history and technology of incoherent scatter radar (as this technique is now almost universally called) is presented by *Evans(1969)*.

The strength of the incoherent scatter radar technique lies with its ability to measure a wide variety of plasma parameters, due, primarily, to a well developed theory for the impact of plasma characteristics on the shape of the spectra, which is also reviewed by *Evans(1969)*. Another good review is presented in the proceedings from a summer school for the European Incoherent Scatter radar consortium (EISCAT) [*Brekke(1977)*], which consists of a number of chapters that are largely tutorial in nature and include discussions of a number of hardware issues related to the technique. Theories for incoherent scatter were developed, largely in parallel, by a number of investigators using widely different approaches [*Dougherty and Farley(1960)*, *Farley et al.(1961)*, *Dougherty and Farley(1963)*, *Farley(1966)*, *Swartz and Farley(1979)*; *Fejer(1960)*, *Fejer(1961)*; *Salpeter(1960b)*, *Salpeter(1960a)*, *Salpeter(1961)*; *Hagfors(1961)*, *Hagfors and Brockelman(1971)*; *Rosenbluth and Rostoker(1962)*; *Tanenbaum(1968)*]. Both particle and fluid approaches to describing the plasma interactions yield essentially identical predictions and we discuss an intuitive description of one of these approaches in the next section.

B.1 Incoherent Scatter Theory

The characteristics of the Thomson scattering from ionospheric electrons can be derived by considering the superposition of dressed test particles [*Rosenbluth and Rostoker(1962)*]. In such a derivation, a single charged particle is hypothetically placed in a plasma and the characteristics of the plasma are calculated, with superposition of the collective effects of all of the plasma particles yielding the bulk scattering characteristics. While the specifics of the derivation are beyond the scope of this thesis, we gain insight by considering how a single charged particle is neutralized by a sufficiently dense (scale lengths much greater than the plasma Debye length) and collisionless plasma. First, we consider the ion and electron number density variations

for a Maxwellian plasma with a static potential, ϕ , and where $q_e\phi \ll k_B T$:

$$n_j = n_o \exp\left(-\frac{q_e\phi}{k_B T_i}\right) \simeq n_o \left(1 - \frac{q_e\phi}{k_B T_i}\right) \quad (\text{B.1})$$

$$n_e = n_o \exp\left(\frac{q_e\phi}{k_B T_e}\right) \simeq n_o \left(1 + \frac{q_e\phi}{k_B T_e}\right) \quad (\text{B.2})$$

where n_j and n_e are the ion and electron number densities, n_o is the unperturbed ion and electron density, q_e is the magnitude of the charge on an electron, k_B is Boltzmann's constant, and T_i and T_e are the ion and electron temperatures. Next, Poisson's equation can be written as

$$\nabla^2 \phi = -\frac{q_e}{\epsilon_o} (n_j - n_e) = -n_o \frac{q_e^2}{\epsilon_o k_B} \left(\frac{1}{T_i} + \frac{1}{T_e}\right) \phi = \frac{1}{\lambda^2} \phi \quad (\text{B.3})$$

with the following solution:

$$\phi = \frac{q_e}{4\pi\epsilon_o r} \exp\left(-\frac{r}{\lambda}\right). \quad (\text{B.4})$$

This potential corresponds to a variation in the plasma electron density given by the following (keeping in mind that Thomson scattering involves primarily the electrons, due to their greater mobility):

$$\Delta n_e = n_e - n_o \simeq n_o \frac{q_e^2}{4\pi\epsilon_o r} \exp\left(-\frac{r}{\lambda}\right). \quad (\text{B.5})$$

The total number of additional electrons in this cloud around the test charge can be calculated by integrating Δn_e over all space,

$$\iiint_{-\infty}^{+\infty} \Delta n_e dV = \frac{T_i}{T_e + T_i} = \frac{1}{1 + T_r} \quad (\text{B.6})$$

where T_r is the ratio of electron to ion temperatures. A similar relation for the ions is

$$\iiint_{-\infty}^{+\infty} \Delta n_j dV = -\frac{T_i}{T_e + T_i} = -\frac{1}{1 + T_r}. \quad (\text{B.7})$$

For equal ion and electron temperatures (thermal equilibrium), equations (B.6) and (B.7) indicate that the test charge is neutralized by attracting half of an electron and repelling half of an ion. This test charge was assumed stationary at the outset whereas in reality the charges have a distribution of velocities, which results in a characteristic double-humped spectral shape for the incoherent scatter return. The derivation of this shape and its dependencies on the plasma parameters is beyond the scope of this thesis and, in any event, is well described in the listed references.

A second approach to calculating the scattering characteristics of the plasma utilizes a generalized form of the fluctuation-dissipation or Nyquist noise theorem [e.g. *Dougherty and Farley(1960)*, *Renau et al.(1961)*, *Swartz and Farley(1979)*]. This approach calculates the residual thermal fluctuations of the electron density and derives the scattering properties of these fluctuations. Based on this approach, *Buneman(1962)* showed that the following relation is a good approximation to the scattering cross-section for modest temperature ratios ($T_r \lesssim 4$):

$$\sigma = \sigma_e \left[\frac{1}{(1 + k^2 \lambda_D^2)(1 + k^2 \lambda_D^2 + T_r)} + \frac{k^2 \lambda_D^2}{1 + k^2 \lambda_D^2} \right] \quad (\text{B.8})$$

where σ is the per-ion scattering cross-section, σ_e is the Thomson cross-section for a free electron, $k = 2k_0 = 4\pi/\lambda_R$ is the *backscatter* wavenumber for radar wavelength λ_R , and $\lambda_D = \sqrt{\epsilon_0 k_B T_e / q_e^2 n_e}$ is the electron Debye length. Note that in the limit where the radar wavelength, λ_R , is much greater than the Debye length, λ_D , equation (B.8) makes the same prediction as equation (B.6). The two terms of equation (B.8) correspond to very different parts of the incoherent scatter returns. The first term is the power from the ‘ion line’ portion as its spectral shape is dominated by the ion motion, with peaks near the Doppler shifts corresponding to ion acoustic waves traveling toward and away from the observer. The second term corresponds to the

‘plasma line’ return which arises due to scattering from Langmuir waves. In the following paragraphs, we discuss the spectral characteristics of these terms in somewhat greater detail.

The vast majority of incoherent scatter radar measurements deal with the ‘ion line’ portion of the spectrum. This component of the return is spectrally relatively compact, typically spread only a few kilohertz to a few tens of kilohertz around the transmitter frequency. The spectral shape and cross-section used in the data analysis routines for the Sondrestrom Incoherent Scatter Radar [*Kelly(1983)*, *Kelly et al.(1995)*] are derived primarily from the theoretical developments presented in *Dougherty and Farley(1963)* and *Farley(1966)* and described in the review article by *Farley(1971)*. A similar compilation of the relevant equations is also contained in *Turunen(1996)*. This spectral shape is given by the following relation

$$S(\omega) \propto n_e \frac{|y_e|^2 \sum_j p_j \Re \{y_j/\omega_j\} + \left| \sum_j p_j T_r y_j + ik^2 \lambda_D^2 \right|^2 \Re \{y_e/\omega_e\}}{\left| y_e + \sum_j p_j T_r y_j + ik^2 \lambda_D^2 \right|^2} \quad (\text{B.9})$$

where y_e and y_j are the longitudinal components of the electron and ion admittances which describe the dynamic response of the plasma to a sinusoidal driving force and include the effects of thermal motions, $\omega_e = \omega - \vec{k} \cdot \vec{v}_e$, $\omega_j = \omega - \vec{k} \cdot \vec{v}_j$, \vec{v}_e is the electron bulk drift velocity, \vec{v}_j is the bulk velocity for ion species j , p_j is the fraction of the total electron density attributed to ion species j , and $\Re \{ \}$ indicates taking the real part of a complex quantity. *Vickrey(1978)* noted that this relation shows that the return from multiple ion species is not simply the superposition of the returns from the individual species but that the various populations do interact with each other, as is expected in a plasma. The electron admittance function for equation (B.9) is given by

$$y_e = i \frac{1 - \frac{\theta_e - i\psi_e}{\cos \alpha} (1 - \mu_e) Z \left(\frac{-\theta_e + i\psi_e}{\cos \alpha} \right)}{1 + \frac{i\psi_e}{\cos \alpha} (1 - \mu_e) Z \left(\frac{-\theta_e + i\psi_e}{\cos \alpha} \right)} \quad (\text{B.10})$$

where $\theta_e = (m_e/2k_B T_e)^{1/2} (\omega_e/k)$, $\psi_e = (m_e/2k_B T_e)^{1/2} (\nu_{en}/k)$, m_e is the electron

mass, ν_{en} is the electron-neutral collision frequency, α is the angle between \vec{k} and the magnetic field direction, $\mu_e = \sin^2 \alpha / 2\phi_e^2$, $\phi_e = (m_e/2k_B T_e)^{1/2} (\Omega_e/k)$, $\Omega_e = q_e B/m_e$ is the electron gyro frequency, and Z is the plasma dispersion function of *Fried and Conte*(1961). Similarly, the ion admittance function is given by

$$y_j = i \frac{1 - (\theta_j - i\psi_j) Z(-\theta_j + i\psi_j)}{1 + i\psi_j Z(-\theta_j + i\psi_j)} \quad (\text{B.11})$$

where $\theta_j = (m_j/2k_B T_i)^{1/2} (\omega_j/k)$, $\psi_j = (m_j/2k_B T_i)^{1/2} (\nu_{in}/k)$, m_j is the mass of ion species j , and ν_{in} is the ion-neutral collision frequency. The significant complexity and various dependencies illustrated in equations (B.9), (B.10), and (B.11) represent one of the greatest strengths of incoherent scatter radar — the possibility of probing numerous important parameters of the ionospheric plasma. As *Evans*(1969) points out, there are a number of degeneracies which prevent all parameters from being resolved under all conditions, but the technique can nonetheless provide a great deal of important information about the plasma state. In Figure B.1 we show several example spectra calculated from equations (B.9), (B.10), and (B.11). The plasma and neutral parameters are calculated from International Reference Ionosphere (IRI-95) model [*Rawer et al.*(1978), *Bilitza*(1990), *Bilitza*(1998)] and Mass Spectrometer and Incoherent Scatter (MSISE-90) model [*Hedin*(1991)] respectively. The very narrow width of the 100 km spectrum is a result of the high ion-neutral collision frequency at that altitude. At 150 km the spectrum corresponds to a near collision-less situation with the primary ions being NO^+ and O_2^+ . At 200 km the spectral width is greater because the dominant ion species is the less massive O^+ and the ion temperature is also elevated as compared to the lower altitudes. In practice, as is discussed in the next section, instead of measuring power spectral densities it is more straightforward to measure autocorrelation functions (ACFs). Figure B.2 shows the ACFs for the calculations in Figure B.1 — the information content of these two figures is, of course, entirely equivalent as they are simply Fourier transforms of each other.

The second term in equation (B.8) corresponds to the ‘plasma line’ portion of the spectrum. For the case where the radar wavelength is much smaller than the plasma Debye length ($k\lambda_D \gg 1$), this term has a spectral width determined by

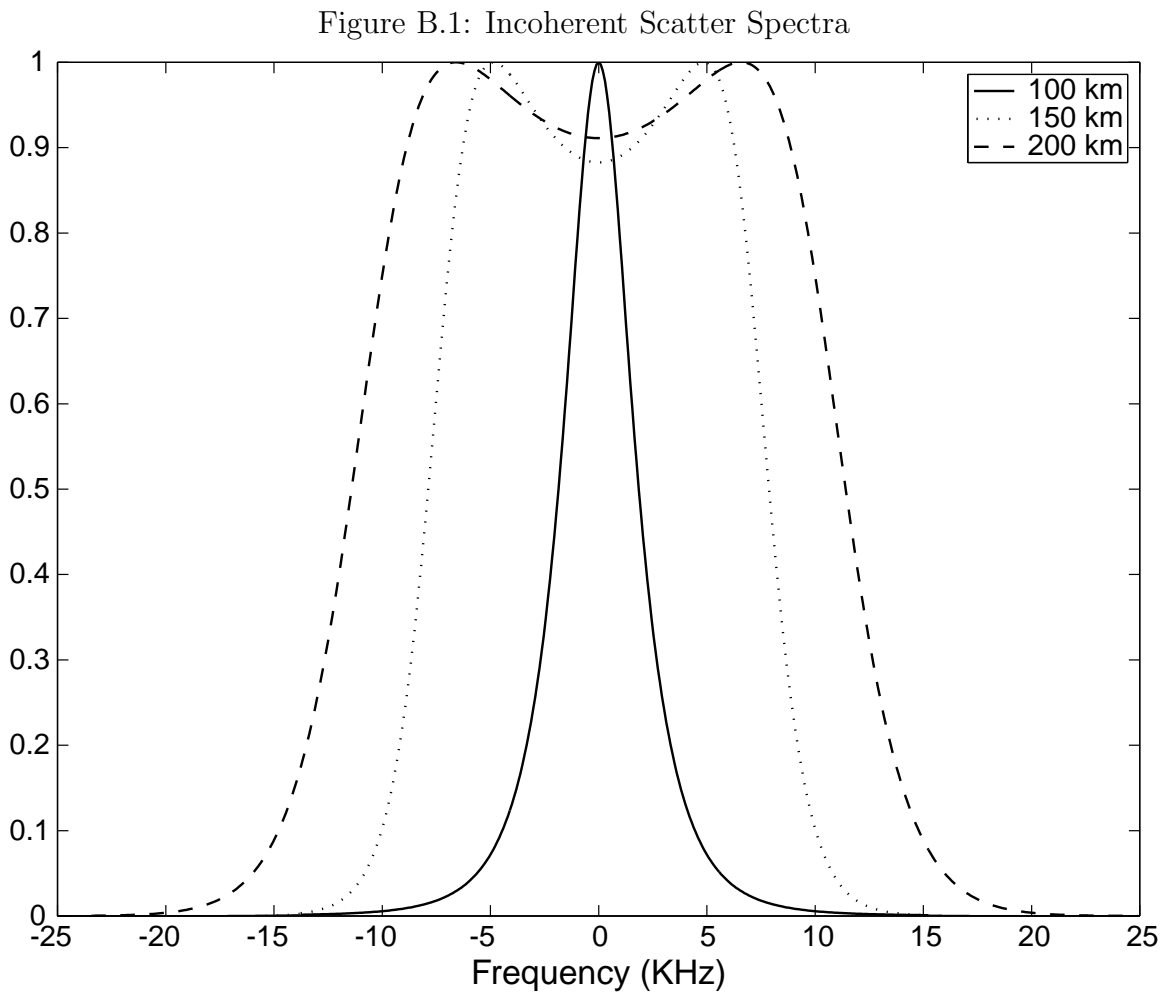
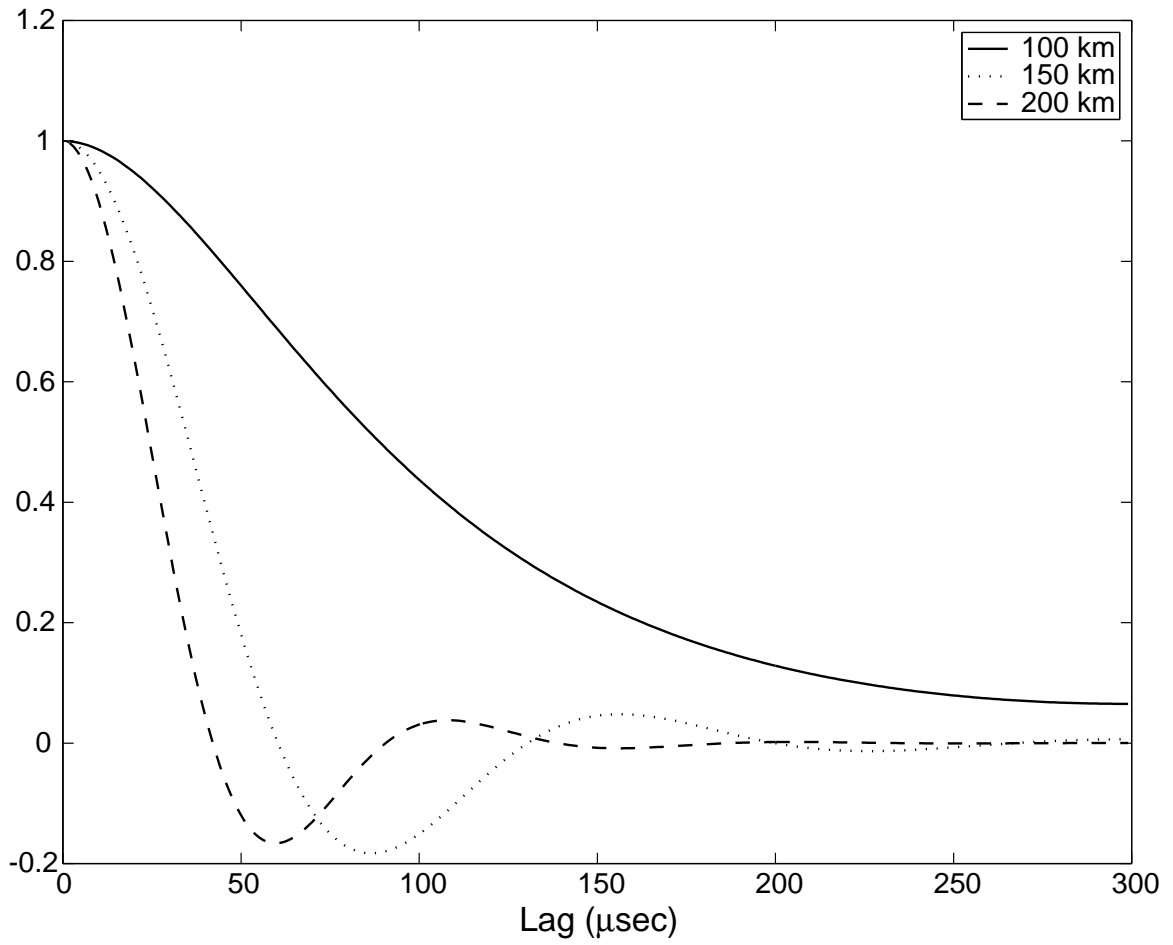


Figure B.2: Incoherent Scatter Autocorrelation Functions



the electron thermal speed, as *Gordon*(1958) predicted. For the case of the radar wavelength much greater than the Debye length, the spectral width is quite narrow but, at the thermal level indicated by equation (B.8), plasma line returns are so weak that they are essentially undetectable by presently operating systems. This is due to the fact that the Langmuir waves that give rise to plasma lines are heavily Landau damped and, as such, their fluctuation spectra are very weak. *Perkins and Salpeter*(1965) showed that they can become detectable, however, in the presence of a suitable excitation source for the waves, such as the energetic electron flux from recently photo-ionized atoms in the daytime *F* region. The required condition is a resonance between these energetic electrons and the Langmuir waves in the medium. *Yngvesson and Perkins*(1968) showed experimentally that a meaningful amount of energy can be transferred into those waves, thus enhancing the scattering from the waves by as much as a factor of ~ 100 . Experimental results [e.g. *Wickwar*(1978), *Valladares et al.*(1988)] and theoretical results [e.g. *Bjørnå et al.*(1982), *Bjørnå and Trulsen*(1986), *Nilsson et al.*(1996)] have shown that plasma lines are also enhanced by aurorally-produced secondary electrons. When enhanced to detectable levels, plasma lines provide additional information about the plasma state because the intrinsic width of *F*-region plasma lines is on the order of only 2 KHz for the $k\lambda_D \ll 1$ case (due to electron-neutral collisions) and the frequencies of the lines are offset to either side of the transmitter frequency by approximately the plasma frequency [*Showen*(1979)]. An approximate relation for this offset is given by

$$f_r^2 = f_{pe}^2 + \frac{3k^2 k_B T_e}{4\pi^2 m_e} \quad (\text{B.12})$$

where f_r is the plasma line frequency offset from the transmitted frequency, $f_{pe} = (1/2\pi)(n_e q_e^2 / m_e \epsilon_0)^{1/2}$ is the electron plasma frequency, k is the wave number of the Bragg scattering (mean of the transmitted and received frequencies) and, as such, is different for the up- and down-shifted plasma lines, and m_e is the electron mass. Note that information about the electron temperature can thus also be derived from the asymmetric shift of the two lines, assuming no bulk electron motion. For more precise calculations of, for example, field-aligned currents from the difference between

drifts of the electrons and ions, *Heinselman and Vickrey*(1992a) showed that a more precise dispersion relation must be employed. They also showed that a good deal of detailed information about the velocity distribution of the enhancing photo-electrons is needed. The strong dependence of the plasma line *frequency* on the electron density is extremely useful for both theoretical as well as practical reasons because this dependence makes it possible, for example, to precisely measure small fluctuations in the local electron density [*Heinselman and Vickrey*(1992b)]. This dependence is also useful for radar system calibration purposes. Estimating electron density from the ion line portion of the return entails measuring the absolute power of the returned signal and, as such, all system gains and losses must be precisely known — a difficult proposition for a large radar. A simple calibration with a plasma line return can readily provide this information, albeit with individual gains/losses lumped together as a single parameter. This utilization of plasma lines is briefly discussed in the next section.

B.2 Radar Techniques

The radar techniques employed for incoherent scatter have a number of unusual characteristics due, of course, to the nature of the ‘targets’ whose characteristics are to be measured. In particular, two features of the scattering medium affect the measurements when compared to more standard search radar techniques: (1) the scatterers fill the antenna beam in the cross-beam direction and (2) the scatterers are randomly distributed spatially, have quasi-random velocities, and effectively overlap in volume (compared with reasonable radar resolutions). As is shown below, the first characteristic affects the radar equation in that the total radar cross-section increases with increasing range — as the beam broadens it includes a larger number of scatterers. The second characteristic affects the spectral measurements because the radar return is essentially a random variable whose instantaneous voltages have little meaning — the only measurements that make sense are power spectral densities and those tend to be spectrally broader than those for many radar applications.

Descriptions of the radar equation for incoherent scatter are found, among other

places, in *Evans*(1969) and *Mathews*(1986). The derivation follows the standard approach found in a variety of books on radar principles [*Skolnik*(1980), *Levanon*(1988)] and assumes that the scattering target is in the far field of an antenna with gain pattern $G(\theta, \phi)$. The power density, F_i at range r from the antenna in a given direction (assuming negligible power loss due to scattering along the path) is given by

$$F_i(\theta, \phi, r) = \frac{P_T L G(\theta, \phi)}{4\pi r^2} \quad (\text{B.13})$$

where P_T is the peak transmitter power and L is the transmit system losses (≤ 1). This power is scattered by the ionospheric electrons and the scattered signal propagates back to the antenna (assuming the backscatter case). The per-electron cross-section σ is given by equation (B.8) where σ_e must be taken as the *radar* cross-section of a free electron, $\sigma_e = 4\pi(r_e \sin \psi)^2 \simeq 9.98 \times 10^{-29} \text{ m}^2$, with r_e being the Thomson electron radius and $\psi = \pi/2$ for backscatter. Note that this cross-section is *not* the same as the Thomson cross-section ($8\pi r_e^2/3$), which gives the total scattered flux. The differential scattering cross-section of the plasma is a function of the electron density at a given position, $n_e(\theta, \phi, r)$, and the differential power density back at the antenna from scatterers at θ, ϕ, r is given by

$$F_s(\theta, \phi, r) = \frac{F_i(\theta, \phi, r) n_e(\theta, \phi, r) \sigma}{4\pi r^2} = \frac{P_T L G(\theta, \phi) n_e(\theta, \phi, r) \sigma}{16\pi^2 r^4}. \quad (\text{B.14})$$

The effects of the collecting aperture of the antenna, $A_e = \lambda^2 G(\theta, \phi)/4\pi$, are included to yield the differential receiver power:

$$dP_r = \frac{P_T L \lambda^2 G^2(\theta, \phi) n_e(\theta, \phi, r) \sigma}{64\pi^3 r^4}. \quad (\text{B.15})$$

Next, we make the assumption that the antenna pattern is narrow enough that the electron density does not vary across the beam, so n_e is effectively a function only of range. For a transmitted pulse of length τ_p in seconds the received signal comes from a range extent of $c\tau_p/2$. Making the further approximation (not always valid) that n_e doesn't change appreciably over that range extent but that it is still a function of

range, we integrate equation (B.15) to yield

$$P_r(r) \approx \frac{P_T L \lambda^2 n_e(r) c \tau_p \sigma}{128 \pi^3 r^2} \iint G^2(\theta, \phi) \sin \theta d\theta d\phi. \quad (\text{B.16})$$

Note that the differential volume is taken as $(c\tau_p/2)r^2 \sin \theta d\theta d\phi$ and that the range extent $c\tau_p/2$ is assumed small. This approximation is not *strictly* valid under all circumstances and analysis software which does not make this assumption is called ‘full-profile analysis’ and this kind of analysis has shown some promise [e.g. *Holt et al.*(1992), *Lehtinen et al.*(1996)] but the computational load tends to be somewhat daunting. The final remaining integral is given its own name, backscatter gain, and is defined as follows

$$G_{BS} = \frac{1}{4\pi} \iint G^2(\theta, \phi) \sin \theta d\theta d\phi. \quad (\text{B.17})$$

This integral can be further simplified for the case of an axially-symmetric parabolic reflector with a 10-dB illumination taper to $G_{BS} = 0.38G(0, 0)$ [*Evans*(1969)]. *Hagen and Baumgartner*(1996) examined this definition closely with the goal of finding an ideal taper and also to consider more general illumination patterns. This exercise is very useful for comparing different systems and for examination of other antenna types (e.g. phased arrays), but for most purposes the on-axis gain can be used along with the relation $G(0, 0) = 4\pi A_e/\lambda^2$, where A_e is the antenna’s effective aperture. Using the on-axis gain, the received power from the ion line is given by the following

$$P_r(r) = \frac{0.38 L c \sigma_e A_e P_T \tau_p}{8\pi} \frac{n_e(r)}{r^2 (1 + k^2 \lambda_D^2)(1 + k^2 \lambda_D^2 + T_r)} \quad (\text{B.18})$$

which is a usual form for the incoherent scatter radar equation. Note that the first set of terms is a constant for any given antenna (except a phased array, for which the backscatter gain/effective aperture changes with off-boresight steering angle) and it is usually lumped into a single ‘system constant.’ The second term depends on the transmitted peak power and pulse width as well as the range to the measurement volume, all of which are controlled system characteristics. The third and final term contains the parameters to be estimated from the received power as well as a pair of confounding parameters, the electron and ion temperatures (in T_r and λ_D). Fortunately these

temperatures are often available either via *a priori* information (e.g. $T_r \approx 1$ below 110 km altitude) or via analysis of the spectral returns. Equation (B.18) shows that at high electron densities the received power is proportional to the electron density. At low electron densities, however, it shows that $P_r \propto n_e^3$. The transition density from a simple linear relationship to an n_e^3 relationship is wavelength-dependent because it is a function of $k\lambda_D$. For the Sondrestrom radar, this dependence effectively limits the lowest detectable electron densities to $\sim 10^{10} \text{ m}^{-3}$. With the system constant terms lumped together, the relationship for estimating the electron density from the received power measurement is:

$$n_e(r) = (1 + k^2\lambda_D^2)(1 + k^2\lambda_D^2 + T_r) \frac{C_s}{P_T\tau_p} r^2 P_r(r) \approx \frac{2C_s}{P_T\tau_p} r^2 P_r(r) = n'_e(r) \quad (\text{B.19})$$

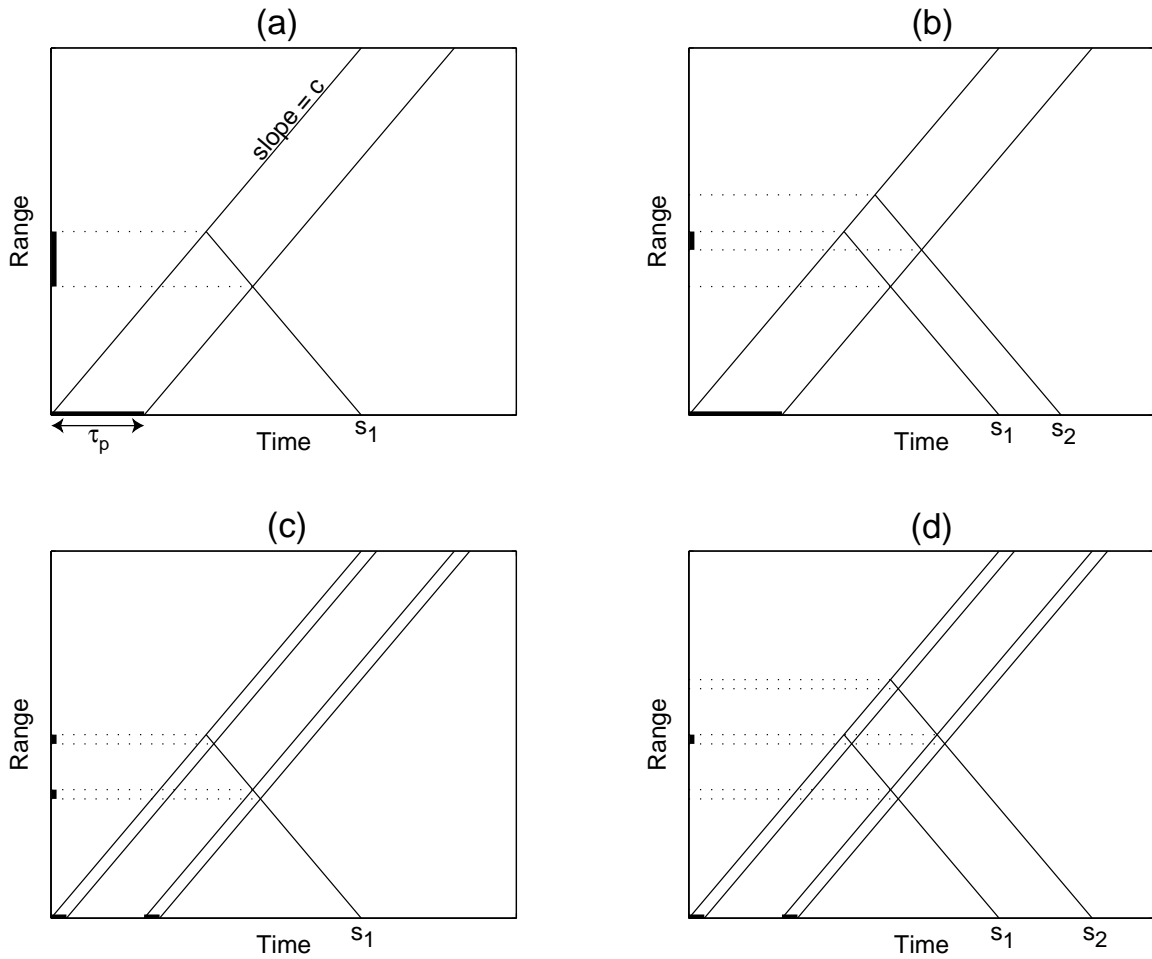
where C_s is the ‘system constant’ and n'_e is the ‘raw density.’ This raw density value assumes that the radar wavelength is much greater than the Debye length and that the electron to ion temperature ratio, T_r , is unity; n'_e is frequently computed as the starting estimate for the electron density after which the effects of T_r and $k\lambda_D$ are accounted for. While C_s can, in principle, be calculated from the parameters shown in equation (B.18), in practice it is estimated via other means because of the difficulties involved with accurately measuring all system losses and A_e , and errors in the factor 0.38 relating backscatter gain to peak antenna gain. This final point is potentially quite significant because the calculation of that factor neglected a number of effects such as aperture blockage due to the feed structures and inaccuracies in the main reflector shape. In any event, C_s is typically estimated by comparing the ion line power measurements with another measure of the electron density. At midlatitude sites it is sufficient to use a co-located ionosonde to match f_oF2 to the incoherent scatter radar-estimated peak F -layer density. At high latitudes, where the ionosphere is much more structured, this technique doesn’t work nearly as well because it is difficult to ensure that the two instruments are measuring the same ionospheric volumes. In this case, a much more thorough method of calibration entails using plasma line frequency offsets to estimate the peak density and calibrating the ion line system constant based on this.

In our previous discussion we considered the power scattered by a simple radio frequency pulse without regard to the spectral measurement or range resolution requirements. As we indicated earlier, the scattered signal is in fact a random variable comprising the scattering from a very large number of randomly distributed electrons. Spectral measurements thus comprise estimating the power spectral density of the return signal as a function of range (altitude), which is typically accomplished in the time domain via estimates of the autocorrelation functions of the returns. In Figure B.3 we show schematically some of the issues involved in this process. Frame (a) of Figure B.3 shows a single pulse of length τ_p propagating outward in range from the transmitter at speed c . At time s_1 the receiver signal is sampled and the contributions to that sample come from a set of ranges indicated by the bold line on the range axis. The length of that bold line is $c\tau_p/2$, indicating that sample s_1 represents an altitude smearing of that amount. Frame (b) shows an autocorrelation lag estimate from the same single pulse. The lag estimate is for delay $(s_2 - s_1)$. Though s_1 and s_2 individually come from ranges smeared over $c\tau_p/2$, the expected value of this lag product has contributions only from the overlapping region. The reason for this is that the signals from different volumes are uncorrelated and they do not contribute to the expected value of the lag product (though they do represent elevated noise levels). Frames (b) and (c) illustrate the same measurements for a pair of closely-spaced pulses. This double-pulse technique for measuring a specific lag product can be extended to multiple pulses (sometimes called multipulse) where the pulse spacings are chosen to eliminate ambiguities [Farley(1972)]. The statistics of the double pulse technique were discussed by Farley(1969) and he showed that the variance of the lag estimate is given approximately by the following proportionality

$$\sigma_{lag}^2 \propto \frac{1}{K} \left(\frac{P_r + P_n}{P_r} \right)^2 \quad (\text{B.20})$$

where K is the number of independent estimates averaged together, P_r is the received power of the scattered signal, and $P_n = k_B T_{sys} B$ is the noise power from a receiver with system temperature T_{sys} and bandwidth B . This result is actually surprising and

Figure B.3: Range-Time Diagrams for Incoherent Scatter Spectral Measurements. Transmit pulses are indicated as bold lines on the time axis of each figure. The RF pulses propagate away from the radar at the speed of light and scattered signals propagate back to the system at the same velocity (indicated by the slopes of the lines). Scattered signals are then sampled at specific times (e.g. s_1) after each transmitted pulse. (a) Power (0-lag) measurement from a single pulse. Note that the return comes from a set of ranges extending $c\tau_p/2$. (b) Lag ($s_2 - s_1$) measurement from a single pulse. The measurement volume corresponds to the overlapping coverage of the two samples. (c) Power measurement from a double pulse. (d) Lag ($s_2 - s_1$) measurement from a double pulse.



comes directly from the noise-like behavior of the scattered signal — for large signal-to-noise ratios (SNRs), equation (B.20) shows that the lag variance is proportional to simply $1/K$ and that doubling the SNR does *not* result in a halving of the lag variance. Thus it generally does not pay to work for SNR (P_r/P_n) much greater than 2 or so — extra signal energy is better spent on generating additional estimates of the lags (increasing K) than on increasing SNR. This realization is the basis for some of the experimental procedures used at the Arecibo Observatory, where the large antenna aperture yields very strong return signals [*Sulzer(1986a)*]. Most other incoherent scatter radars do not ‘suffer’ from this problem and, in fact, P_r/P_n is frequently much less than one and lag statistics are improved via the integration of returns from a very large number of pulses.

A wide array of different techniques have been used to improve both the range resolution and measurement statistics for incoherent scatter radars and, in particular, binary phase coding has been extensively used because of its easy implementation in high power klystron-based systems [*Sulzer(1989)*]. A basis for mathematically understanding these techniques in the context of incoherent scatter has been presented by *Lehtinen(1986)*, *Lehtinen and Huuskonen(1996)*, and references therein, and though this two-dimensional ambiguity function concept is beyond our needs here, the mathematical constructs are by now well established. Two especially interesting techniques which were developed specifically for incoherent scatter (also beyond the present needs) are given in *Sulzer(1986b)* and *Lehtinen and Häggström(1987)* and are called ‘coded long-pulse’ and ‘alternating codes’ respectively. The techniques are mentioned here only because of their importance to incoherent scatter in general. Of greater importance to our work is the utilization of Barker codes to improve range resolution — a topic discussed in most general radar texts [e.g. *Levanon(1988)*, *Skolnik(1990)*] which basically entails encoding the transmitted waveform with a specific sequence of binary phase flips (bauds) and removing those phase flips coherently upon reception. This procedure results, in essence, in a pulse whose characteristics have the average power of the entire coded pulse but the range resolution of a single baud. The problem for incoherent scatter is that the decoding specifically requires a phase-coherent return, a limitation that was investigated by *Gray and Farley(1973)* for the Arecibo

Table B.1: Sondrestrom Radar Parameters

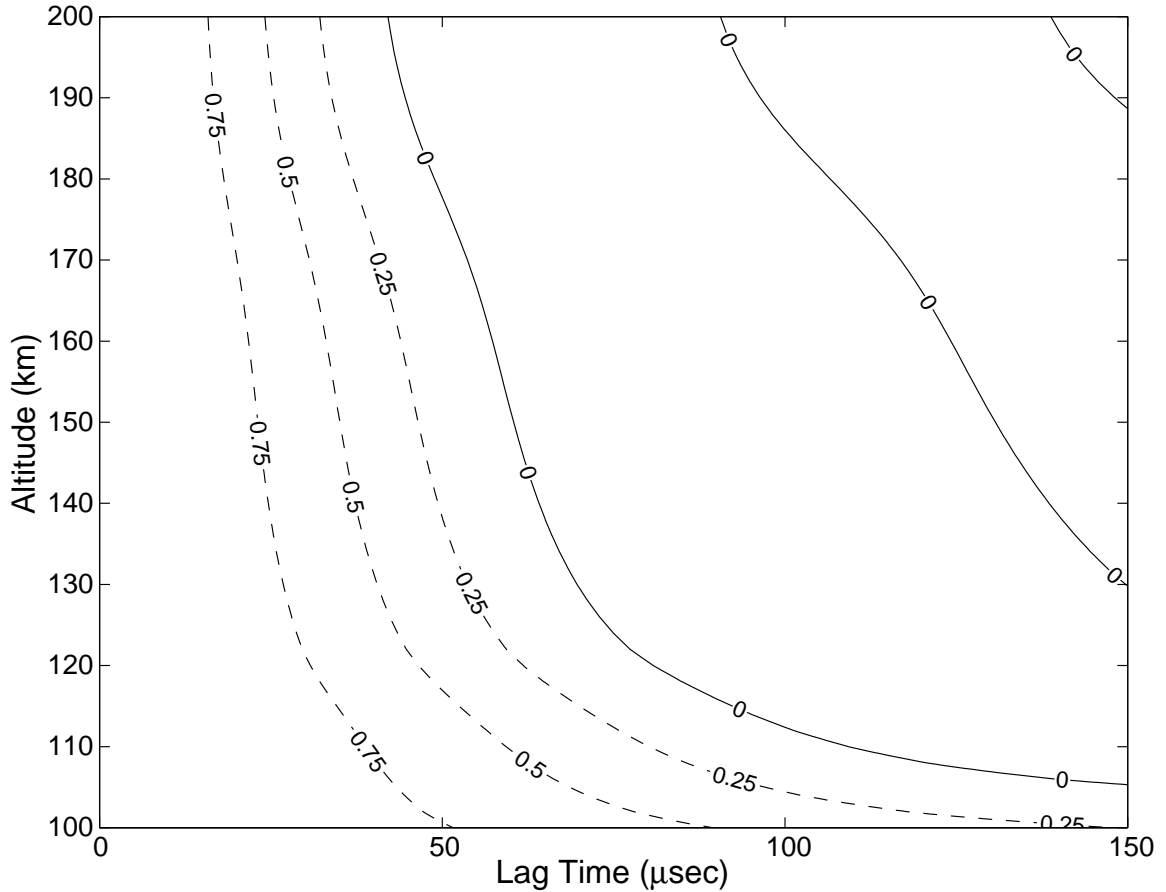
Parameter	Typical Operating Conditions
Transmit Frequency, f_0	1290.0 MHz, 1290.6 MHz
Transmit Peak Power, P_T	3.2 MW
RF Duty Cycle	2.8 %
Antenna Configuration	Cassegrain, Shaped Subreflector
Antenna Diameter	32 m
Antenna Beamwidth	0.5°
Antenna Polarization	circular
System Noise Temperature, T_{sys}	~90 K
Pulse Length, τ_p	2 to 480 μ s
Receiver Bandwidth, B	50 KHz to 1 MHz
System Constant, C_s	1.774×10^{19} s/m ⁵

incoherent scatter radar. In their paper, *Gray and Farley(1973)* established that coherent pulse compression can be used successfully as long as the entire phase-coded pulse length does not exceed the correlation time of the medium being probed and, in particular, that phase codes shorter than the time to the first zero crossing of the autocorrelation function will properly decompress. The first experimental utilization of Barker codes for incoherent scatter was reported by *Ioannidis and Farley(1972)*, and since that time Barker codes have seen wide use for incoherent scatter E -region measurements at a variety of facilities.

B.3 The Sondrestrom Radar

Incoherent scatter radar data for this thesis came from the Sondrestrom Radar near the town of Kangerlussuaq (formerly Søndre Strømfjord), Greenland. This system, which was moved to Greenland from Chatanika, Alaska in 1982, has been described by *Kelly(1983)* and *Kelly et al.(1995)*. The relevant parameters for the radar are given in Table B.1. The station is located at geographic coordinates 66° 59.2' N, 50° 56.8' W and at a magnetic invariant latitude of approximately 74.5° N, which puts it nominally north of the auroral oval at night and at magnetospheric cusp latitudes during the day. Aurora is frequently observed at the station at night, however, when

Figure B.4: Incoherent Scatter Autocorrelation Function Contours, Model Ionosphere



substorms expand northward.

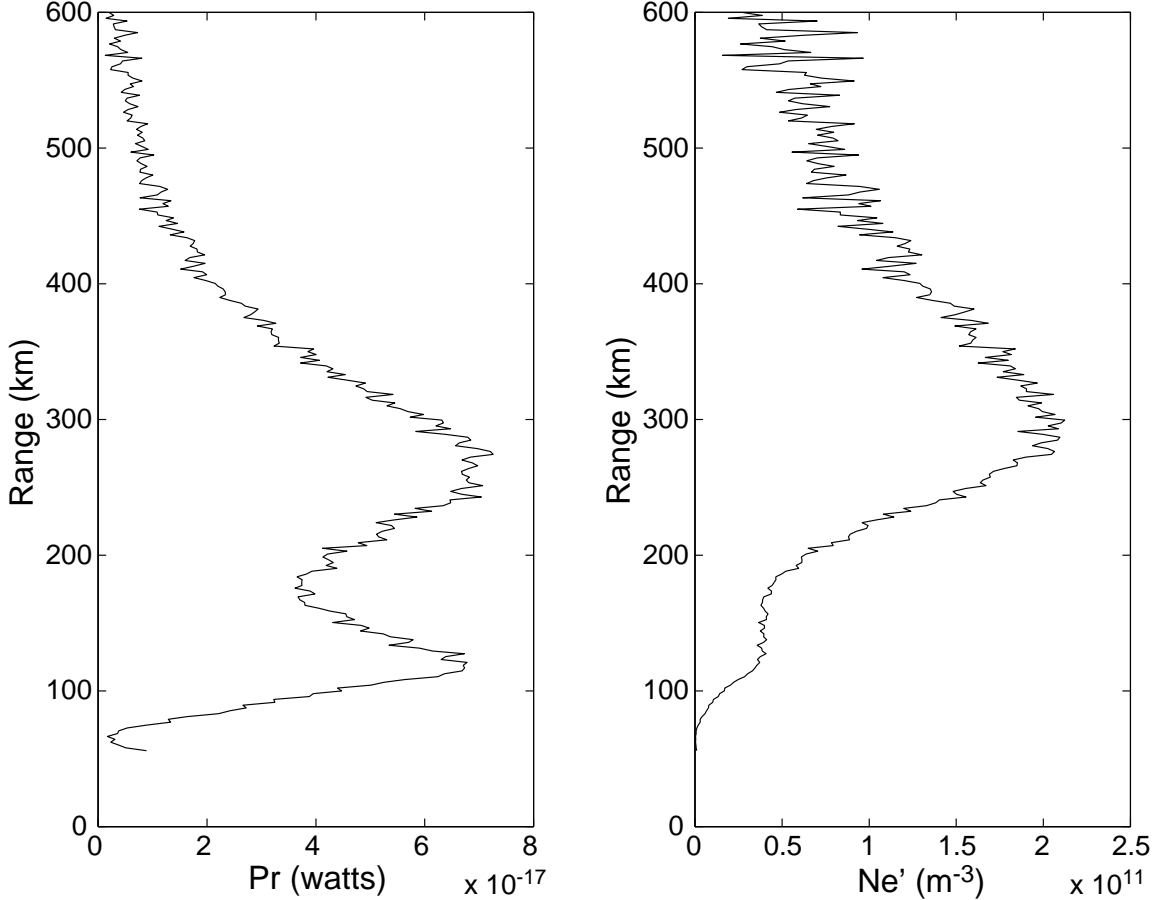
The incoherent scatter radar observations described in this thesis were obtained by developing a new data collection program utilizing an optimized Barker coded pulse. Our first step toward optimizing the code was the determination of the maximum allowable code length for sporadic- E measurements extending up to approximately 150 km altitude. As we show in Figure B.2, the time to the first zero crossing of the autocorrelation function decreases with increasing altitude because the ions become lighter and hotter with altitude. This effect is also shown in Figure B.4, which displays a contour plot of a set of theoretical ACFs that we generated in a manner similar to those shown in Figure B.2. The first zero crossing of the ACF at 150 km altitude occurs at a lag time of approximately 60 μs which, following *Gray*

and Farley(1973), means that the entire coded pulse must be less than this length. Sporadic- E measurements also require range resolutions on the order of 1 km or less if the layers are to be properly resolved so, based on this requirement, we selected a 4 μs baud length for the code. The longest known Barker code is 13 bauds long, yielding a total pulse length of 52 μs , which satisfies both criteria and represents a nearly optimal code for the purposes of measuring power profiles through this region. Actually, the 52 μs value is quite conservative in terms of sporadic- E measurements because the ions present in those layers are primarily the massive Fe^+ , and sometimes Mg^+ , with Fe^+ yielding narrower bandwidths and longer correlation times than those displayed in Figure B.4. On the other hand, measurements of profiles of auroral ionization consisting of O_2^+ and NO^+ are also important to our work and, as such, the 52 μs time is a nearly optimal choice.

In addition to the Barker coded pulses, which occupy most of the available duty cycle, we also intersperse simple uncoded 320 μs pulses to provide ACF estimates for the F region (thus allowing, e.g., electric field measurements) and also to provide E region ACF information under some conditions. As illustrated in Figure B.3, each return sample from the 320 μs pulse has contributions from a set of ranges covering 48 km, which would normally smear together the returns from the entire E region. At times, however, the electron density profiles from the Barker code measurements show essentially no E region densities outside of a thin sporadic- E layer. In these situations, even though the returns from the 320 μs pulses do represent a significant amount of range smearing, this additional information indicates that all of the measured signal in fact comes only from the sporadic- E layer. For this situation, the sporadic- E layer acts like a sampling function to remove the effects of range smearing, and estimates of ion velocity or spectral shape in the layer can be made (albeit without resolving possible variations through the altitude extent of the layer).

A final detail we have not yet discussed is the absolute calibration of the received power. For the Sondrestrom system this calibration is accomplished via the injection, after every transmitter pulse, of a calibrated noise pulse directly into the waveguide prior to the transmit/receive devices and, as such, it reflects most of the important losses in the system. The calibration signal is pulsed on during a time when no

Figure B.5: Sondrestrom Radar Data Example. Integration of 1900 pulses, 320 μs pulse width, 3 MW peak power.



ionospheric returns are expected and estimates are also made of the receiver noise at times adjacent to the calibration pulses. If the calibration pulse injects an effective noise temperature, T_{cal} , and the measured data, noise and calibration powers are designated S_r , S_n and S_c respectively, the received power can be given as follows:

$$P_r(r) = \frac{k_B T_{cal} B}{S_c - S_n} (S_r(r) - S_n). \quad (\text{B.21})$$

Note that the scattered power and calibration noise measurements also include receiver noise, which must be removed to yield parameters proportional to the powers. As an example of data from the Sondrestrom Radar, Figure B.5 displays an inte-

gration of 1900 pulses with each pulse being $320 \mu s$ long and running at a peak transmitter power of 3 MW. Note from that figure that the received power is on the order of 10^{-17} watts, not much considering the transmitter power was 3 MW and the antenna gain is nearly 50 dB!

Appendix C

Sodium Density Lidar

Light brings us news of the Universe.

Sir William Bragg

The discovery and subsequent implementation of practical pulsed laser systems in the early 1960s led naturally to the development of lidar techniques. Analogous to radar, lidar uses time-of-flight and intensity measurements of light from short laser pulses, which are reflected (scattered) from various ‘targets’, to derive the distance to and the scattering characteristics of those targets. Among the earliest of such ‘targets’ was the Moon — a reasonably easy object to locate [*Smullin and Fiocco(1962)*]. The technique was also quickly adopted by atmospheric researchers [e.g. *Fiocco and Smullin(1963)*, *Kent et al.(1967)*, and references therein] for the measurement of atmospheric molecular number densities (Rayleigh scattering) and aerosols (Mie scattering). These early measurements utilized the then newly available ruby laser technology at 694.3 nm wavelength. The discovery of a continuously tuneable narrow-band organic dye laser in 1969 opened up other possibilities, including the tuning of the laser light wavelength to a resonant line of neutral atomic sodium. The first measurements made via this technique were reported by *Bowman et al.(1969)* utilizing resonant excitation of the D_1 line of the sodium D doublet at 589.6 nm. In that paper they noted that the D_2 line would have been preferable as the oscillator strength for D_2 is greater by about a factor of 2, but a suitable interference filter was available to the experimenters only for D_1 . The resonance lidar technique works because the

resonant cross-section of an atom is much greater than its Rayleigh cross-section, with the ratio of these cross-sections being on the order of 10^{14} for sodium [*Bowman et al.*(1969), *Kent and Wright*(1970)], which makes up for the fact that sodium atoms constitute only 1 part in 10^{10} or less in the upper atmosphere [*Hunten*(1967)]. The great strength of the technique is that it allows nearly continuous monitoring of relatively inaccessible regions of the atmosphere (barring, of course, obstacles like intervening clouds and excessive background light), in contrast to the earlier occultation experiments which used sunlight to excite the atoms and a variable shadow height during sunrise and sunset to extract altitude information and for which, as a result, profiles were available only twice each day (see the review by *Hunten*(1967)). Regular and continuous measurements of sodium profiles were first reported by *Sandford and Gibson*(1970) and *Gibson and Sandford*(1971). Though they did not apparently recognize its significance, *Sandford and Gibson*(1970) also reported what may have been the first measurements of a sporadic sodium layer — an increase in Na density by more than a factor of 2 in about one hour at ~ 93 km altitude (the discovery of sporadic Na is usually attributed to *Clemesha et al.*(1978)).

C.1 Sodium Cross-section

Though the resonant lidar technique is conceptually straightforward, accurate interpretation of the measurements requires attention to a number of important details. First there is the question of the lifetime of the excited level of the atom — if this lifetime were greater than a large fraction of a microsecond, it would have significant implications for the range/altitude estimates for the measurements. The absorption for the D_1 line of sodium arises from the transition $3^2S_{1/2} - 3^2P_{1/2}$, so the relevant question is the lifetime of Na $3^2P_{1/2}$. Measurements by *Gaupp et al.*(1982) indicate that this lifetime is 16.4 ns — an insignificant interval for the purposes of resolving altitude in the upper atmosphere. *Gaupp et al.*(1982) also reported earlier measurements for the Na $3^2P_{3/2}$ level which represents the upper level of the D_2 absorption resonance — with values also very near 16 ns. For the purposes of lidar measurements, then, we can regard this absorption and reemission of radiation as a scattering process.

Table C.1: Sodium Absorption Oscillator Strengths

Line	Transition	Wavelength	Oscillator Strength, f
D_1	$3^2S_{1/2} - 3^2P_{1/2}$	589.6 nm	$\frac{1}{3} \times (0.9536 \pm 0.0016)$
D_2	$3^2S_{3/2} - 3^2P_{1/2}$	589.1 nm	$\frac{2}{3} \times (0.9465 \pm 0.0023)$

Next, the total scattering cross-section is considered. *Bowman et al.*(1969) indicated that the integrated cross-section is related to the oscillator strength via the following relation:

$$\int \sigma(\nu) d\nu = -\frac{q_e^2}{4\epsilon_o m_e c} f \quad (\text{C.1})$$

where $\sigma(\nu)$ is the cross-section at frequency ν , q_e is the magnitude of the electron charge, ϵ_o is the permittivity of free space, m_e is the electron mass, c is the speed of light, and f is the oscillator strength of the transition. *Gaupp et al.*(1982) reported the values for the oscillator strength shown in Table C.1, which give the total scattering cross-section without regard to the line shape.

The frequency dependence of the scattering cross-section is also important for accurate interpretation of the lidar returns. The paper by *Fricke and von Zahn*(1985) contains an excellent overview the nature of this relationship for the D_2 line. They pointed out that the line consists, in fact, of 6 hyperfine lines which are Doppler broadened due to the finite temperature of the gas, as summarized in Table C.2. *Fricke and von Zahn*(1985) also point out that the effect of Zeeman splitting on the energy levels (and, thus, wavelengths) is negligible for the magnetic fields present in the sodium layer of the Earth. On the other hand, they show that the effect of Zeeman splitting on the multiplet intensity ratios can be as large as 10% under some circumstances — the magnitude of this effect can be seen in the q_n factors in Table C.2 for Sondrestrom and with regard to equation (C.2). From *Fricke and von*

Table C.2: Sodium D_2 Hyperfine Lines. Wavelengths are referenced to $\lambda_0 = 589.15826$ nm. g_n is the relative multiplet strength. q_n is the B-field and polarization dependent phase function (backscatter) for Sondrestrom. α is the angle between the laser light linear polarization direction and magnetic north.

n	Line	Wavelength Offset	g_n	$q_n(\alpha = 0^\circ)$	$q_n(\alpha = 90^\circ)$	$q_n(\alpha = 45^\circ)$
1	D_{2b} (1-2)	-1.2633×10^{-3} nm	5	1	1	1
2	D_{2b} (1-1)	-1.2234×10^{-3} nm	5	1.0679	1.1	1.0847
3	D_{2b} (1-0)	-1.2051×10^{-3} nm	2	1	1	1
4	D_{2a} (2-3)	$+0.7197 \times 10^{-3}$ nm	14	1.0815	1.1199	1.1017
5	D_{2a} (2-2)	$+0.7879 \times 10^{-3}$ nm	5	1	1	1
6	D_{2a} (2-1)	$+0.8279 \times 10^{-3}$ nm	1	0.9864	0.98	0.9830

Zahn(1985), the equation for the sodium cross-section is given by

$$\sigma(\lambda) = \frac{\pi q_e^2 \lambda_0^2}{m_e c} \frac{f}{\sum_{n=1}^6 g_n} \sqrt{\frac{D}{\pi T}} \sum_{n=1}^6 g_n q_n \exp(-D(\lambda - \lambda_n)^2 / T) \quad (\text{C.2})$$

where $\pi q_e^2 / (m_e c) = \pi r_e c = 2.654002 \times 10^{-6}$ m²/s, $D = c^2 m_e / (2k_B \lambda_0^2) = 357.973 \times 10^{24}$ K/m², T is the atmospheric temperature in K, g_n is the relative multiplet strength, and q_n is the backscatter phase function with correction factors for polarization and the magnetic field. The values for q_n for a linearly polarized, vertically oriented lidar are given by the relations in Table C.3. With this information, then, the shape of the Doppler broadened D_2 line can be computed for a given atmospheric temperature. Figure C.1 shows that line shape for three different temperatures and assuming that the laser polarization is 45° from magnetic north.

Predicting the total per-atom return from the frequency dependent cross-sections requires information about the pulses used to excite the resonances. For Sondrestrom, the dye laser used for measuring sodium has a nominal bandwidth of 1.8 GHz, which corresponds to approximately 2.08×10^{-12} meters – the same order of magnitude as the width of the Doppler-broadened lines in Figure C.1! When the specific laser line shape is known, the ‘effective’ cross-section of the atmospheric sodium can be estimated by integrating the product of that laser line shape and the Doppler-broadened shape which was calculated in the previous paragraph. This approach also assumes

Table C.3: Equations for q_n correction factors for linearly polarized, vertically oriented lidar. I is the inclination of the magnetic field (80.4° for Sondrestrom), B is the magnetic field strength (52.79×10^{-6} T for Sondrestrom), α is the angle between the laser polarization direction and magnetic north. Note that a common factor $3/(3 + 0.137 \times 10^8 B^2)$ has been removed and that the factor $2/3$ is included in the oscillator strength f , not in these equations.

n	q_n
1	$\{5 + 0.2283 \times 10^8 B^2\}/5$
2	$\{5.5 - 3 \sin^2 I \cos^2 I (1 + \cos(2\alpha))$ $+ 0.2867 \times 10^4 \sin I \cos^2 I \sin(2\alpha) B$ $+ \{0.2511 - \cos^2 I [0.0137(1 - \cos(2\alpha))$ $+ 0.1096(1 + \cos(2\alpha)) \sin^2 I]\} \times 10^8 B^2\}/5$
3	$\{2 + 0.0913 \times 10^8 B^2\}/2$
4	$\{15.68 - 10.08 \sin^2 I \cos^2 I (1 + \cos(2\alpha))$ $+ 0.9633 \times 10^4 \sin I \cos^2 I \sin(2\alpha) B$ $+ \{0.7160 - \cos^2 I [0.0460(1 - \cos(2\alpha))$ $+ 0.3682(1 + \cos(2\alpha)) \sin^2 I]\} \times 10^8 B^2\}/14$
5	$\{5 + 0.2283 \times 10^8 B^2\}/5$
6	$\{0.98 + 0.12 \sin^2 I \cos^2 I (1 + \cos(2\alpha))$ $- 0.0115 \times 10^4 \sin I \cos^2 I \sin(2\alpha) B$ $+ \{0.0447 + \cos^2 I [0.0005(1 - \cos(2\alpha))$ $+ 0.0044(1 + \cos(2\alpha)) \sin^2 I]\} \times 10^8 B^2\}/1$

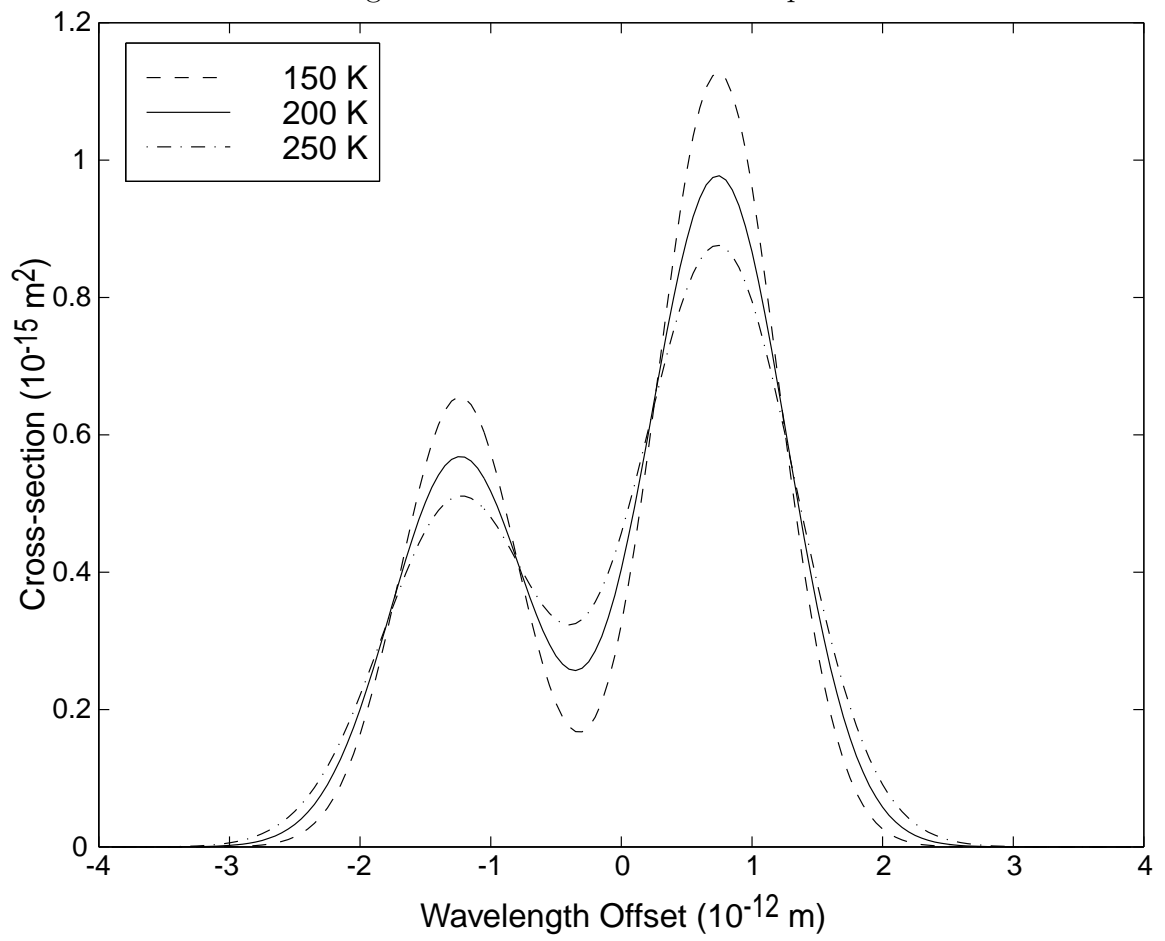
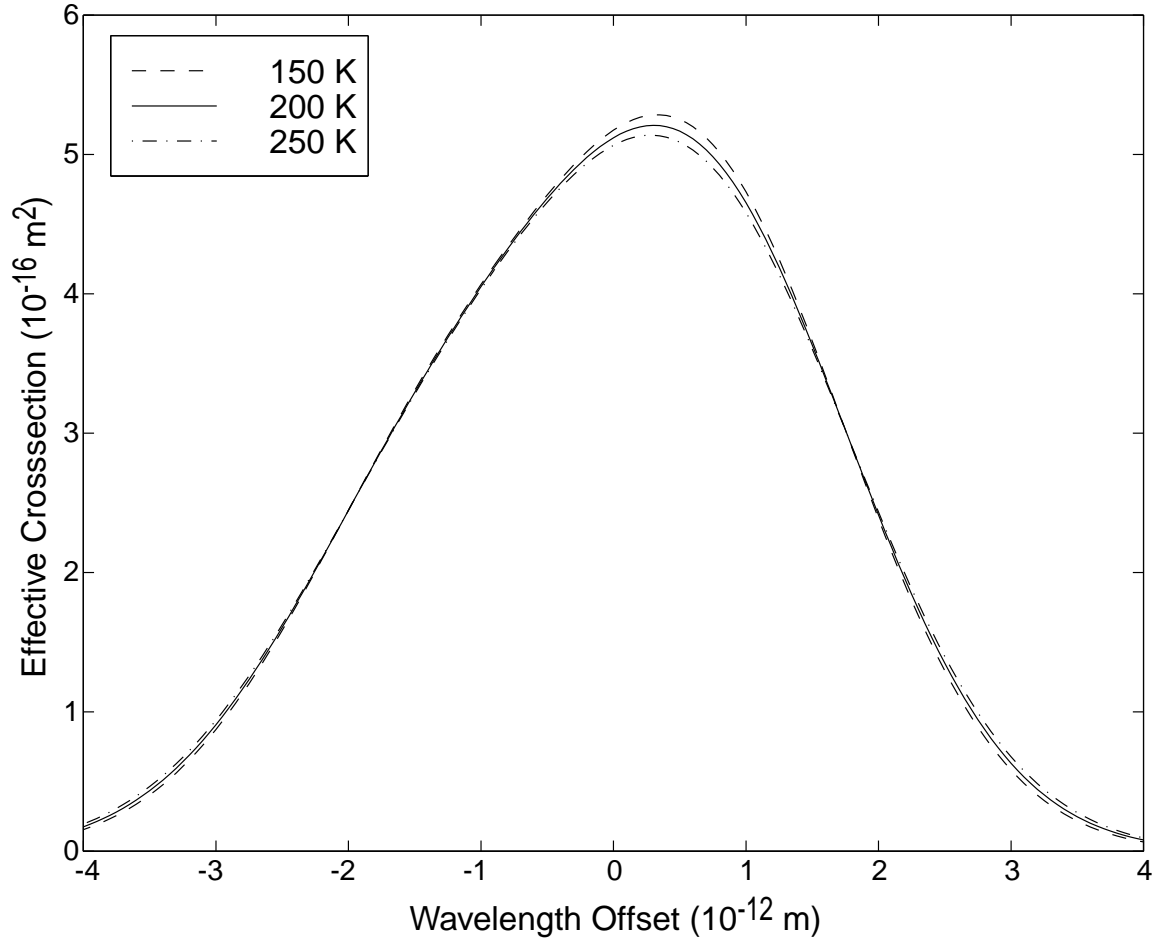
Figure C.1: Sodium D_2 Line Shape

Figure C.2: Sodium D_2 Line Effective Cross-section with a 1.8 GHz laser line width.

(correctly in our case) that the receiver bandwidth is much greater than the line width of the laser and, as such, that it does not affect the received signal. Keeping in mind the fact that the dye laser is wavelength tunable, it is instructive to cross-correlate the two shapes to generate a plot of the ‘effective’ cross-section as a function of the offset between the center wavelength of the laser and that of the sodium line. Assuming a Gaussian line shape for the laser pulse, we show a plot of such an ‘effective’ cross-section in Figure C.2. When the laser is tuned to the peak, the cross-section is not a very strong function of atmospheric temperature and, thus, a single value of the cross-section can safely be used for a wide range of conditions. At 200 K, the ‘effective’ cross-section is approximately 5.21×10^{-16} m 2 .

C.2 Sodium Lidar Technique

One property that distinguishes sodium density lidar techniques from typical radar techniques is the method of calibration. For many radar applications the power ‘on target’ can be estimated with reasonable accuracy by accounting for the effects of transmitter power, antenna gain, and range spreading (r-squared loss). For lidar measurements, however, a confounding factor is the significant loss of power (extinction) due to scattering by aerosols (e.g. thin clouds, dust, smoke) in the troposphere and lower stratosphere. The solution to this problem was pointed out at least as early as *Bowman et al.*(1969) – the vast majority of the troublesome aerosols reside at altitudes well below 30 km, so all measurements made from 30 km and upward contain identical extinction effects. In addition, the molecular number densities are quite well known around this altitude, as are the Rayleigh scattering characteristics, while the atomic sodium densities are vanishingly low so resonant scattering is negligible. Thus we can use photon counting for 30 km altitude as a proxy for the total extinction as well as other system effects such as transmitter power and telescope characteristics! The sodium number density is thus estimated via the following relation from *Fricke and von Zahn*(1985):

$$n_{Na}(r) = n_{Ray}(r_{Ray}) \frac{\sigma_{Ray}}{\sigma_{Na}} \left(\frac{r}{r_{Ray}} \right)^2 \frac{I_{Na}(r)}{I_{Ray}(r_{Ray})} \quad (\text{C.3})$$

where n_{Na} is the sodium number density, r is the range to that density, n_{Ray} is the molecular number density (assumed known) at range r_{Ray} , σ_{Ray} is the per molecule Rayleigh backscatter cross-section, σ_{Na} is the per atom resonant cross-section for sodium, I_{Na} is the received light intensity from sodium altitudes, and I_{Ray} is the measured intensity from the Rayleigh reference altitude ($r_{Ray} \simeq 30$ km). The Rayleigh backscatter cross-section is given by $\sigma_{Ray} = \sigma_{TQRay}(180^\circ)$ where the total cross-section (in m^2) for the homosphere has been presented by *Nicolet*(1984) as

$$\sigma_T = \frac{4.02 \times 10^{-32}}{\lambda^{4.04}} \quad (\text{C.4})$$

for the wavelength region $0.55\mu\text{m} < \lambda < 1\mu\text{m}$ and where λ is given in μm . At the sodium D_2 wavelength this relation yields $\sigma_T = 3.41 \times 10^{-31} \text{ m}^2$. The phase function for pure Rayleigh scattering evaluated for backscatter is $q_{Ray}(180^\circ) = 1.5$ but when the depolarization factor ($\delta \sim 0.03$) is accounted for the modified value becomes $q_{Ray}(180^\circ) = 1.4778$ [*Hansen and Travis(1974)*] (*Penndorf(1957)* found 1.4739), so the resulting backscatter cross-section is given by $\sigma_{Ray} = 5.042 \times 10^{-31} \text{ m}^2$. We should note that one item missing from equation (C.3) is the effect of self-extinction on the sodium measurements. If the sodium number densities become too high, a significant portion of the incident light will be scattered, thus affecting the assumption of simple r-squared loss above 30 km. *Simonich and Clemesha(1983)* showed that this effect is negligible (around 5% or less) for normal column abundances of $5 \times 10^{13} \text{ m}^{-2}$, but that it can become significant under the more rare circumstances of abundances around $2 \times 10^{14} \text{ m}^{-2}$.

C.3 The Sondrestrom Lidar

The sodium lidar data we present in this thesis come from the modified Arclite lidar system at the Sondrestrom Facility near the town of Kangerlussuaq, Greenland. The Rayleigh lidar at that facility has been described by *Thayer et al.(1997)* and recent modifications to the system have added a sodium capability [*Heinselmann et al.(1998)*]. Some specific characteristics of the modified system are given in Table C.4.

A few other details of the lidar measurements we describe in this thesis can best be understood by referring to an example. Figure C.3 shows an hour-long integration of lidar profiles for the morning of 12 September 1998. First, as suggested in the left panel of Figure C.3, the received light intensity is estimated via photon counting with photo-multiplier tubes (PMTs). The time after each laser pulse is split into segments (range bins) of 48 meter length and PMT output pulses are accumulated digitally for each of those bins and integrated over multiple laser pulses. This process yields photon count profiles like those shown in Figure C.3. Below about 15 km the profile shows a curious decrease in the count rate in spite of the fact that the number densities are clearly still increasing exponentially with decreasing altitude. A number

Figure C.3: Lidar data example from 12 September 1998. This represents an hour-long integration of returns at 10 laser pulses per second. The left panel shows the integrated PMT counts. The right panel shows the derived sodium densities.

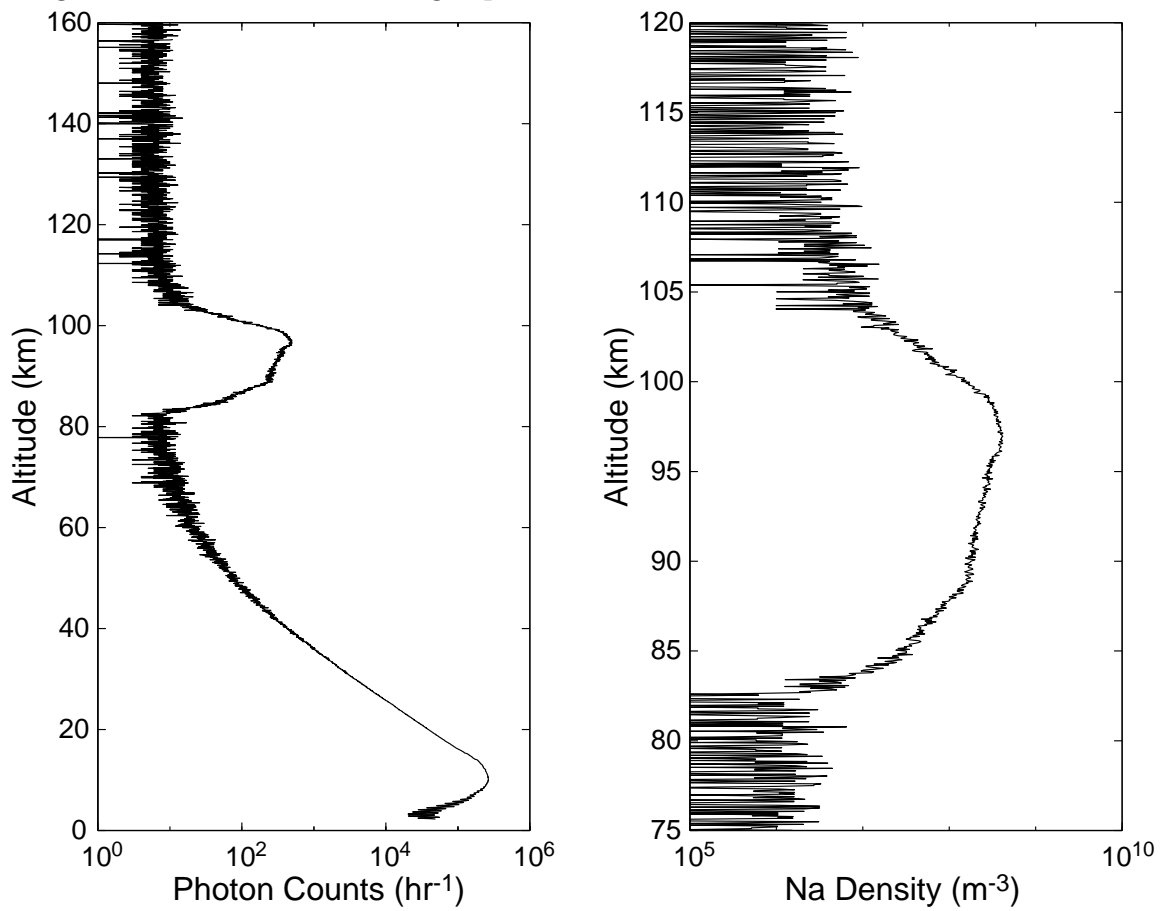


Table C.4: Sondrestrom Lidar Parameters

Parameter	Typical Operating Conditions
Rayleigh Wavelength	532 nm
Rayleigh Pulse Power	560 mJ
Rayleigh Pulse Width	7 ns
Rayleigh Pulse Repetition Frequency	30 pulses/s
Sodium Wavelength	589 nm
Sodium Pulse Power	100 mJ
Sodium Pulse Width	7 ns
Sodium Pulse Repetition Frequency	10 pulses/s
Telescope Diameter	0.92 m
Telescope Configuration	Newtonian
Telescope Field-of-View	0.5 mrad (0.03°)
Number of Receiver Channels	2
Receiver Range Bin Length	192 m

of different factors combine to yield this effect. Firstly, the transmitter and receiver ‘beams’ are not coaxial for the Sondrestrom system but, rather, they intersect above some altitude. Thus, the count rates slowly increase as the common volume grows with altitude (as the cones intersect more and more). Secondly, the PMT output pulses have finite widths and, as a result, when the photon arrival interval is less than that pulse width (when the scattering number densities are too high) photons are simply missed by the counting circuits. In any event, it is reasonably clear that the count rates do represent Rayleigh scattered intensities above 20 km altitude. In this example, the Rayleigh returns drop into the background noise at around 70 km altitude and at higher altitudes (above ~ 120 km) the background levels can be seen to be approximately 10 photons per 48 m bin per hour. Our processing software uses the average count rates between 120 and 140 km to represent that background level. The measured intensity, $I_{meas}(r)$, includes the background intensity, I_{bg} , so the intensity for equation (C.3) must remove that level prior to estimating a sodium density via the simple relation $I_{Na}(r) = I_{meas}(r) - I_{bg}$. The 30 km Rayleigh intensity in our software also uses a set of altitudes, from 28 km to 32 km, in estimating $I_{Ray}(r_{Ray})$. The intensity in this altitude interval is fitted in a least squares sense to a simple function and the 30 km value extracted from the fit. The final missing parameter

from equation (C.3) is the atmospheric number density at 30 km. The MSISE-90 model [*Hedin(1991)*] is used to estimate this value. The result of this calculation for the sample data set is shown in the right-hand panel of Figure C.3.

Appendix D

Ion Flux

I consider that I understand an equation when I can predict the properties of its solutions, without actually solving it.

Paul A. M. Dirac

In this appendix we discuss several issues related to the derivation of the ion flux relation used in Section 4.1. A simplified form of the ion velocity equation is derived first as an aid to understanding the influence of external electric fields on the ion motion in the presence of gradients in the ion-neutral collision frequency. Next, we derived the full ion flux relation that is used in Section 4.1. Finally, we discuss the expressions that are used for estimating ion-neutral collision frequencies in this thesis.

D.1 Simplified Form of Ion Velocity

General cases of the steady-state ion and electron momentum equations are considered in Section 4.1, where we combine and reduce these equations to a form amenable to solution for the ion flux. Before solving the resulting equation in this Appendix, it is instructive to consider a simpler problem and discuss the nature of its solutions in order to put into context the brute-force solution of the more complex situation. Several secondary effects (which can become primary ones under some circumstances) are neglected: the pressure gradient, gravity, neutral winds, and eddy diffusion. Thus our formulation aims to consider the manner in which electric fields alone affect

the motion of ions in the upper atmosphere. Under these approximations, the ion momentum equation of equation (4.6) simplifies to:

$$0 = q_e \left(\vec{E} + \vec{v}_j \times \vec{B} \right) - m_j \nu_{jn} \vec{v}_j \quad (\text{D.1})$$

which can be rearranged to yield:

$$\vec{v}_j = \frac{k_j}{B} \vec{E} + \frac{k_j}{B} \vec{v}_j \times \vec{B} \quad (\text{D.2})$$

where k_j is the ion mobility coefficient, given by

$$k_j = \frac{\Omega_j}{\nu_{jn}} = \frac{q_e B}{m_j \nu_{jn}}, \quad (\text{D.3})$$

Ω_j is the ion gyro frequency, and $B = |\vec{B}|$ is the magnitude of the magnetic field. Next, we utilize the following vector identity:

$$\vec{A} \times (\vec{B} \times \vec{C}) = \vec{B} (\vec{A} \cdot \vec{C}) - \vec{C} (\vec{A} \cdot \vec{B}), \quad (\text{D.4})$$

the use of which allows us to write:

$$\vec{v}_j \times \vec{B} = \frac{k_j}{B} \vec{E} \times \vec{B} + \frac{k_j}{B} (\vec{v}_j \cdot \vec{B}) \vec{B} - k_j B \vec{v}_j. \quad (\text{D.5})$$

Using equation (D.2), we also have:

$$\vec{v}_j \cdot \vec{B} = \frac{k_j}{B} \vec{E} \cdot \vec{B}. \quad (\text{D.6})$$

When considering the effects of an externally applied electric field, the term given in equation (D.6) is zero because \vec{E} and \vec{B} are orthogonal. With some manipulation we derive the following relation which gives the ion velocity vector as a simple function of the electric- and magnetic-fields and the ion-neutral collision frequency:

$$\vec{v}_j = \frac{\Omega_j \nu_{jn}}{\Omega_j^2 + \nu_{jn}^2} \frac{\vec{E}}{B} + \frac{\Omega_j^2}{\Omega_j^2 + \nu_{jn}^2} \frac{\vec{E} \times \vec{B}}{B^2}. \quad (\text{D.7})$$

Inspecting the terms of equation (D.7), it is clear that the altitude-dependent behavior of the ion motion depends on the relationship between the ion gyro frequency and ion-neutral collision frequency as a function of altitude. For the altitude range of interest, the ion gyro frequency is nearly constant while ion-neutral collision frequency varies significantly with altitude, as we show in Section D.3 below. At higher altitudes, where collisions are negligible, the ion motion is in the $\vec{E} \times \vec{B}$ direction with magnitude E/B and at lower altitudes the direction of \vec{v}_j turns toward the direction of \vec{E} and its magnitude is $\Omega_j E / \nu_{jn} B$. The fact that the mean ion velocity *direction* and *magnitude* changes with altitude leads directly to the ion layer formation mechanisms discussed in Chapter 4.

D.2 Ion Flux Derivation

We now derive the coupled ion and electron momentum equation applicable to sporadic ion layer formation in Section 4.1 and equation (4.11) from that section is repeated here for convenience:

$$\begin{aligned}
0 = & -\nabla(n_j k_B T_j) \\
& -\frac{n_j}{n_e} \nabla_{\parallel}(n_e k_B T_e) \\
& + n_j m_j \vec{g} \\
& + n_j q_e \left(\vec{E}_{ext} + \vec{v}_j \times \vec{B} \right) \\
& - n_j m_j \nu_{jn} \left[\vec{v}_j - \vec{u} + K \left(\frac{\nabla n_j}{n_j} - \frac{\nabla n_n}{n_n} \right) \right].
\end{aligned} \tag{D.8}$$

The problem at hand is to solve this equation for the ion flux, $n_j \vec{v}_j$, for inclusion in the continuity equation given by equation (4.5). In practical terms, the relation we wish to derive can be a function of the number density, n_j , which will be integrated in solving equation (4.5), but not a function of the velocity, \vec{v}_j . The anisotropy of equation (D.8), and thus the complexity of its solution, is contained in the cross product term $\vec{v}_j \times \vec{B}$. We begin by rearranging equation (D.8) to separate the velocity

terms and yield the following:

$$\begin{aligned}
m_j \nu_{jn} (n_j \vec{v}_j) + q_e \vec{B} \times (n_j \vec{v}_j) &= -\nabla (n_j k_B T_j) \\
&\quad - \frac{n_j}{n_e} \nabla_{\parallel} (n_e k_B T_e) \\
&\quad + n_j m_j \vec{g} \\
&\quad + n_j q_e \vec{E}_{ext} \\
&\quad + n_j m_j \nu_{jn} \left[\vec{u} - K \left(\frac{\nabla n_j}{n_j} - \frac{\nabla n_n}{n_n} \right) \right].
\end{aligned} \tag{D.9}$$

The analytic solution of equation (D.9) is accomplished with the help of a vector/matrix notation in which the following are defined:

$$\vec{v}_j = \begin{bmatrix} v_x \\ v_y \\ v_z \end{bmatrix}$$

$$\vec{B} = \begin{bmatrix} B_x \\ B_y \\ B_z \end{bmatrix}.$$

With little effort the troublesome cross-product term is written in matrix notation as:

$$\vec{B} \times (n_j \vec{v}_j) = \begin{bmatrix} 0 & -B_z & B_y \\ B_z & 0 & -B_x \\ -B_y & B_x & 0 \end{bmatrix} \cdot (n_j \vec{v}_j). \tag{D.10}$$

The left side of equation (D.9) is thus equivalent to

$$m_j \nu_{jn} (n_j \vec{v}_j) + q_e \vec{B} \times (n_j \vec{v}_j) = \begin{bmatrix} m_j \nu_{jn} & -q_e B_z & q_e B_y \\ q_e B_z & m_j \nu_{jn} & -q_e B_x \\ -q_e B_y & q_e B_x & m_j \nu_{jn} \end{bmatrix} \cdot (n_j \vec{v}_j). \tag{D.11}$$

We now define a matrix \mathbf{A} :

$$\mathbf{A} = \begin{bmatrix} m_j \nu_{jn} & -q_e B_z & q_e B_y \\ q_e B_z & m_j \nu_{jn} & -q_e B_x \\ -q_e B_y & q_e B_x & m_j \nu_{jn} \end{bmatrix}$$

and the solution to equation (D.8) is given by a matrix equation:

$$\begin{aligned} n_j \vec{v}_j = \mathbf{A}^{-1} \cdot & \left\{ -\nabla (n_j k_B T_j) \right. \\ & - \frac{n_j}{n_e} \nabla_{\parallel} (n_e k_B T_e) \\ & + n_j m_j \vec{g} \\ & + n_j q_e \vec{E}_{ext} \\ & \left. + n_j m_j \nu_{jn} \left[\vec{u} - K \left(\frac{\nabla n_j}{n_j} - \frac{\nabla n_n}{n_n} \right) \right] \right\}. \end{aligned} \quad (\text{D.12})$$

The complications introduced by the anisotropy of the cross-product in equation (D.8) have been reduced in equation (D.12) to the evaluation of the matrix inverse \mathbf{A}^{-1} , which has a straightforward analytical solution. An additional subtlety of equation (D.12) arises from the fact that the electron number density, n_e , is not independent of the ion number density, n_j , because bulk charge neutrality constraints require that the electron density be essentially equal to the sum of the various ion densities (assuming singly ionized constituents). We thus split the electron number density into two portions, one associated with the ion species which is modeled, n_j , and one associated with ‘other’ ions, n_{eo} , such as those produced by auroral particle precipitation:

$$n_e = n_j + n_{eo}.$$

In terms of the model, the n_{eo} term is not influenced by the various forcing terms whereas in reality those other ions are affected. This approximation is not a bad one, however, because the dominant ‘other’ ions are those produced by aurorae and by photo-ionization from EUV and, as a result, they consist primarily of NO^+ and O_2^+ which have relatively short lifetimes in this region when compared to metallic ions.

As a result, these ions do not experience the long-term integrated effects that the metal ions respond to.

After some manipulation, the z -component of the flux is given by the following:

$$\begin{aligned}
n_j v_z = & - \left[\left(\frac{k_B T_j}{m_j \nu_{jn}} + K \right) \frac{m_j^2 \nu_{jn}^2 + q_e^2 B_z^2}{m_j^2 \nu_{jn}^2 + q_e^2 B^2} \right] \frac{\partial n_j}{\partial z} \\
& - \left[\frac{k_B T_e}{m_j \nu_{jn}} \frac{B_z^2}{B^2} \frac{n_j}{n_j + n_{eo}} \right] \frac{\partial n_j}{\partial z} \\
& - \left[\frac{k_B}{m_j \nu_{jn}} \left(\frac{\partial T_i}{\partial z} \frac{m_j^2 \nu_{jn}^2 + q_e^2 B_z^2}{m_j^2 \nu_{jn}^2 + q_e^2 B^2} + \frac{\partial T_e}{\partial z} \frac{B_z^2}{B^2} \right) \right] n_j \\
& + \left[K \frac{1}{n_n} \frac{\partial n_n}{\partial z} \frac{m_j^2 \nu_{jn}^2 + q_e^2 B_z^2}{m_j^2 \nu_{jn}^2 + q_e^2 B^2} \right] n_j \\
& - \left[\frac{g}{\nu_{jn}} \frac{m_j^2 \nu_{jn}^2 + q_e^2 B_z^2}{m_j^2 \nu_{jn}^2 + q_e^2 B^2} \right] n_j \\
& + \left[\frac{q_e B_y m_j \nu_{jn} + q_e^2 B_x B_z}{m_j^2 \nu_{jn}^2 + q_e^2 B^2} u_x \right] n_j \\
& - \left[\frac{q_e B_x m_j \nu_{jn} - q_e^2 B_y B_z}{m_j^2 \nu_{jn}^2 + q_e^2 B^2} u_y \right] n_j \\
& + \left[\frac{m_j^2 \nu_{jn}^2 + q_e^2 B_z^2}{m_j^2 \nu_{jn}^2 + q_e^2 B^2} u_z \right] n_j \\
& + \left[\frac{q_e^2 B_y E_{\perp x} - q_e^2 B_x E_{\perp y} + m_j \nu_{jn} q_e E_{\perp z}}{m_j^2 \nu_{jn}^2 + q_e^2 B^2} \right] n_j \\
& - \left[\frac{k_B T_e}{m_j \nu_{jn}} \frac{B_z^2}{B^2} \frac{\partial n_{eo}}{\partial z} \right] \frac{n_j}{n_j + n_{eo}}
\end{aligned} \tag{D.13}$$

which is repeated as equation (4.12) in Section 4.1. In each line of equation (D.13), only the last term changes continuously with time during a model run and all of the other components are held constant for at least some amount of time. The various lines in equation (D.13) are associated with different forcing terms or effects. The first line contains the molecular and eddy diffusion effects for the ions. The second line gives the ambipolar modification due to the electron coupling to the ions (note that if $T_e = T_i$, $n_{eo} = 0$, and B is vertical then this simply doubles the molecular diffusion term from the first line). The third line accounts for temperature gradients

in the diffusion. The fourth line is the eddy diffusion *target*. The fifth line is due to gravity. The sixth through eighth lines are neutral wind forcing terms. The ninth line is the electric field term (note here that all three components of E are assumed to be perpendicular to B and they are all due to external forcing). The tenth and final line is a modification due to the other electrons/ions which are not being modeled (e.g. auroral ionization).

D.3 Collision Frequencies

Many of the processes involved in the formation and dynamics of partially ionized plasmas depend strongly upon the coupling between the ions and electrons that make up the plasma and the more dense neutral atmosphere. Most formulations for the ion-neutral collision frequency (ν_{jn}) calculations found in the literature have their bases in the work of either *Dalgarno(1961)* or *Banks(1966)*. From a simplistic point of view, this collision frequency can be thought of as the rate at which the interacting constituents collide and thus transfer momentum. *Stubbe(1968)*, however, pointed out that ν_{jn} is in reality a fictitious quantity that just happens to have the units of frequency. In his analysis *Stubbe(1968)* also showed that the apparent discrepancies between the developments of *Dalgarno(1961)* and *Banks(1966)* were simply definitional. These definitional differences have resulted in significant errors in, for example, the estimation of height-integrated ionospheric conductivities [*Vickrey et al.(1981)*]. As we indicate in Appendix B, collision frequencies also affect the spectra of incoherent scatter radar returns. *Schlegel et al.(1980)* pointed out that the proper form for the incoherent scatter application is the effective collision frequency in the laboratory frame of reference, as described in *Banks and Kockarts(1973a)*. This is also the proper form for ν_{jn} in the ion momentum equation used in Chapter 4.

In the center-of-mass coordinates, the momentum transfer collision frequency between ions and neutrals is given by

$$\overline{\nu_{jn}} = 2.57 \times 10^{-15} \sqrt{\frac{\alpha_0}{\mu_A}} n_n \quad (\text{D.14})$$

Table D.1: Neutral Gas Polarizabilities

Neutral Gas	α_0 (10^{-24} cm ³)	m_{An} (AMU)
N ₂	1.76	28.0
O ₂	1.59	32.0
O	0.79	16.0

where α_0 is the polarizability of the neutral atom or molecule involved in the collision in units of 10^{-24} cm³ (the collision process is assumed to entail electromagnetic interactions between the ion and the polarized neutral, not direct impact). μ_A is the reduced mass in atomic mass units (AMU) and is given by

$$\mu_A = \frac{m_{Aj}m_{An}}{m_{Aj} + m_{An}} \quad (\text{D.15})$$

where m_{Aj} is the mass of ion j and m_{An} is the mass of the neutral molecule, both given in AMU. The conversion of equation (D.14) to a laboratory frame of reference is given by the following relation:

$$\nu_{jn} = \frac{m_{An}}{m_{Aj} + m_{An}} \overline{\nu}_{jn}. \quad (\text{D.16})$$

Banks and Kockarts(1973a) lists the polarizabilities of various gases and these values for the three dominant gas molecules in the E region are reproduced in Table D.1. The total ion-neutral collision frequency is thus expressed by the following relation:

$$\begin{aligned} \nu_{jn} = & \frac{1.80 \times 10^{-14}}{\sqrt{m_{Aj}(m_{Aj} + 28)}} n_{\text{N}_2} + \\ & \frac{1.83 \times 10^{-14}}{\sqrt{m_{Aj}(m_{Aj} + 32)}} n_{\text{O}_2} + \\ & \frac{9.14 \times 10^{-15}}{\sqrt{m_{Aj}(m_{Aj} + 16)}} n_{\text{O}}. \end{aligned} \quad (\text{D.17})$$

The neutral gas number densities are expressed in m⁻³ in this equation and, for the purposes of modeling, these number densities are estimated using MSISE-90

[*Hedin*(1991)].

Banks and Kockarts(1973a) also give a relation for the electron-neutral collision frequency. Because of the huge mass difference between electrons and neutral atoms/molecules, the center-of-mass and laboratory frames are essentially identical and the collision frequency is given by the following:

$$\begin{aligned} \nu_{en} = & 2.33 \times 10^{-17} (1 - 1.2 \times 10^{-4} T_e) T_e n_{N_2} + \\ & 1.8 \times 10^{-16} (1 + 3.6 \times 10^{-2} \sqrt{T_e}) \sqrt{T_e} n_{O_2} + \\ & 8.2 \times 10^{-16} \sqrt{T_e} n_O. \end{aligned} \quad (D.18)$$

Banks and Kockarts(1973a) note that this expression is highly uncertain but useful for modeling purposes. Simpler expressions are given by a number of authors, including *Kelley*(1989), but they are not significantly different from the expression used here.

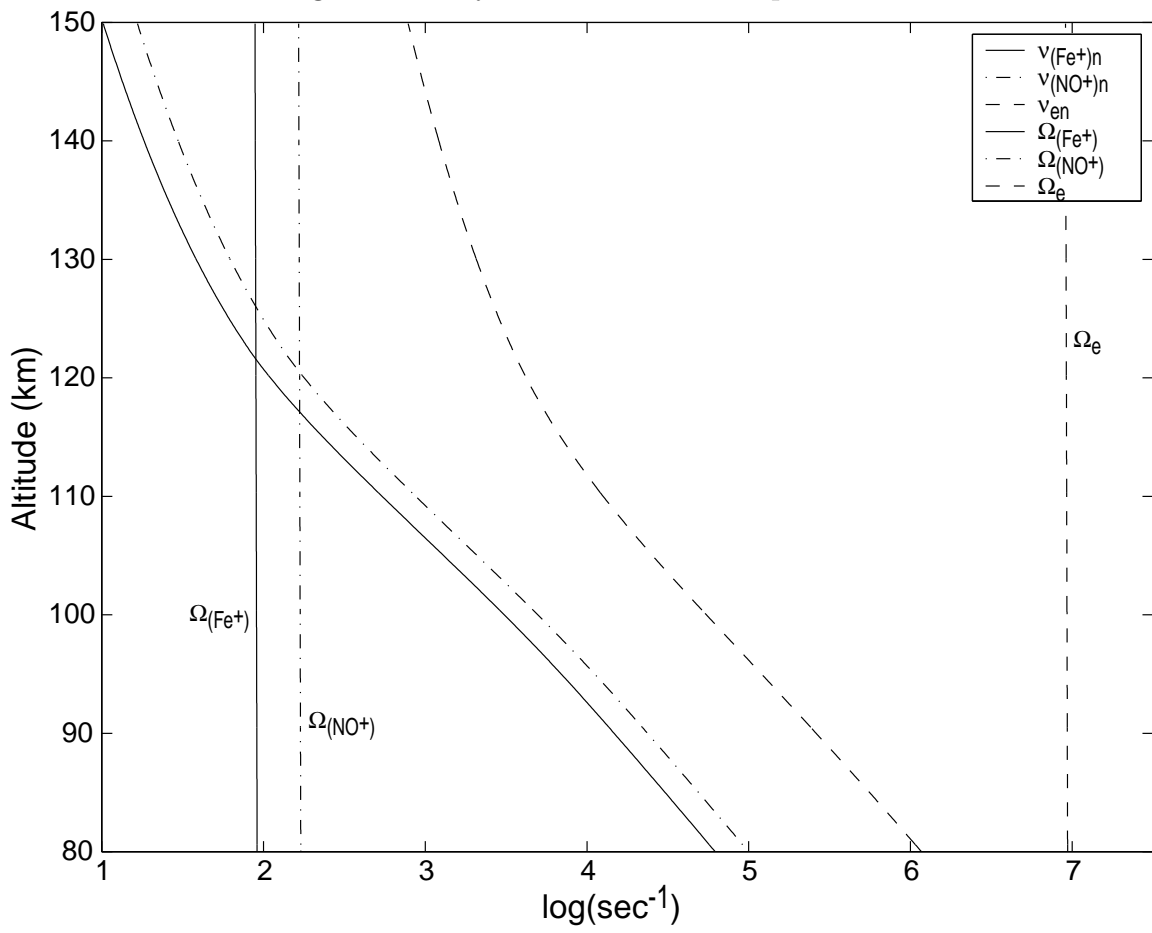
The importance of collisions to ion and electron motion in a plasma varies greatly with altitude in the upper atmosphere. At higher altitudes collisions are relatively unimportant and the plasma particle motion is dominated by gyro-motion about magnetic field lines. At lower altitudes this gyro-motion is significantly disturbed by collisions with neutrals. As a result, we can discuss the importance of collisions with regard to the relative magnitudes of the collision frequencies and the ion and electron gyro frequencies, given by equations (D.19) and (D.20) respectively.

$$\Omega_j = \frac{q_e B}{m_j} \quad (D.19)$$

$$\Omega_e = \frac{q_e B}{m_e} \quad (D.20)$$

The electron gyro-frequency is much greater than that for ions but the important question is how these frequencies compare to the collision frequencies of equations (D.17) and (D.18). The relation between the electron and ion gyro and collision frequencies is illustrated in Figure D.1. For ions, Figure D.1 illustrates the change in collision frequency and gyro-frequency with ion mass and it also shows that the cross-over point from collision-dominated motion to collisionless motion is within the E

Figure D.1: Gyro and Collision Frequencies



region. For electrons, however, even though the electron-neutral collision frequency is much greater than that for ions, the cross-over to collision-dominated behavior is well below the altitudes of interest, due to the much higher gyro-frequency for electrons. In Section 4.1 the electron-neutral collisions are therefore neglected.

Appendix E

Modeling Issues

The process of *calculating* brings about just . . . intuition. Calculation is not an experiment.

Ludwig Wittgenstein

A theory has only the alternatives of being right or wrong. A model has a third possibility: it may be right, but irrelevant.

Manfred Eigen

This appendix discusses a number of issues related to the models used in this thesis.

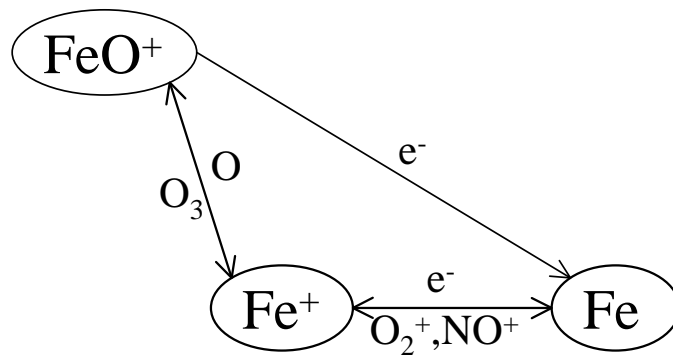
E.1 Chemical Model Example

We illustrate the steps involved in the construction of a chemical model with a simplified example. In this example, we specifically ignore transport and a subset of the iron chemistry model is used, as shown by the set of chemical reactions in Table E.1. The model reactions are illustrated schematically in Figure E.1 and include three Fe-containing constituents: Fe, Fe⁺, and FeO⁺. In our example model, the available Fe atoms are moved between the three constituents by the reactions in Table E.1. Each reaction coefficient corresponds to a rate of change of concentration for the reactants.

Table E.1: Iron Chemistry Example

Reaction	Rate Coefficient
$\text{Fe} + \text{O}_2^+ \rightarrow \text{Fe}^+ + \text{O}_2$	$k_{17} = 1.1 \times 10^{-15} \text{ m}^3/\text{s}$
$\text{Fe} + \text{NO}^+ \rightarrow \text{Fe}^+ + \text{NO}$	$k_{18} = 9.2 \times 10^{-16} \text{ m}^3/\text{s}$
$\text{Fe}^+ + e^- \rightarrow \text{Fe} + h\nu$	$k_{19} = 1.0 \times 10^{-18} \text{ m}^3/\text{s}$
$\text{Fe}^+ + \text{O}_3 \rightarrow \text{FeO}^+ + \text{O}_2$	$k_{20} = 7.0 \times 10^{-16} \text{ m}^3/\text{s}$
$\text{FeO}^+ + \text{O} \rightarrow \text{Fe}^+ + \text{O}_2$	$k_{22} = 1.0 \times 10^{-16} \text{ m}^3/\text{s}$
$\text{FeO}^+ + e^- \rightarrow \text{Fe} + \text{O}$	$k_{23} = 1.0 \times 10^{-13} (200/T)^{1/2} \text{ m}^3/\text{s}$

Figure E.1: Schematic of the Example Iron Chemistry Reactions.



For example, the first reaction basically gives the following two rates:

$$\frac{d}{dt} [\text{Fe}] = -k_{17} [\text{Fe}] [\text{O}_2^+] \quad (\text{E.1})$$

and

$$\frac{d}{dt} [\text{Fe}^+] = k_{17} [\text{Fe}] [\text{O}_2^+] \quad (\text{E.2})$$

where the $[]$ denote concentrations of the various quantities. If we define a state vector \mathbf{X} as

$$\mathbf{X} = \begin{bmatrix} [\text{Fe}] \\ [\text{Fe}^+] \\ [\text{FeO}^+] \end{bmatrix} \quad (\text{E.3})$$

then the reactions in Table E.1 can be written as the vector ordinary differential equation (ODE)

$$\frac{d}{dt} \mathbf{X} = \mathbf{A} \cdot \mathbf{X} \quad (\text{E.4})$$

where the matrix \mathbf{A} is given by the following:

$$\mathbf{A} = \begin{bmatrix} -k_{17} [\text{O}_2^+] - k_{18} [\text{NO}^+] & k_{19} [\text{e}^-] & k_{23} [\text{e}^-] \\ k_{17} [\text{O}_2^+] + k_{18} [\text{NO}^+] & -k_{19} [\text{e}^-] - k_{20} [\text{O}_3] & k_{22} [\text{O}] \\ 0 & k_{20} [\text{O}_3] & -k_{22} [\text{O}] - k_{23} [\text{e}^-] \end{bmatrix}. \quad (\text{E.5})$$

One complicating factor here is that the electron density $[\text{e}^-]$ is related to elements of \mathbf{X} by the assumption of overall charge neutrality in the plasma, i.e.

$$[\text{e}^-] = [\text{O}_2^+] + [\text{NO}^+] + [\text{Fe}^+] + [\text{FeO}^+] \quad (\text{E.6})$$

and equation (E.4) is thus a non-linear ODE so trivial solutions do not exist. Referring back to Table E.1, the rate coefficients for the various reactions are different by several orders of magnitude and even greater differences arise from the concentrations of the reactants, as was shown in Figure 3.2. As a result, this system of equations (and especially those for the full models in Chapter 3) is very stiff. Fortunately, the numerical solution of ODEs has advanced considerably and for the models we

developed in this thesis a commercial stiff ODE solver (built into Matlab[®], from The MathWorks, Inc.) was employed to integrate the equations from a variety of sets of initial conditions.

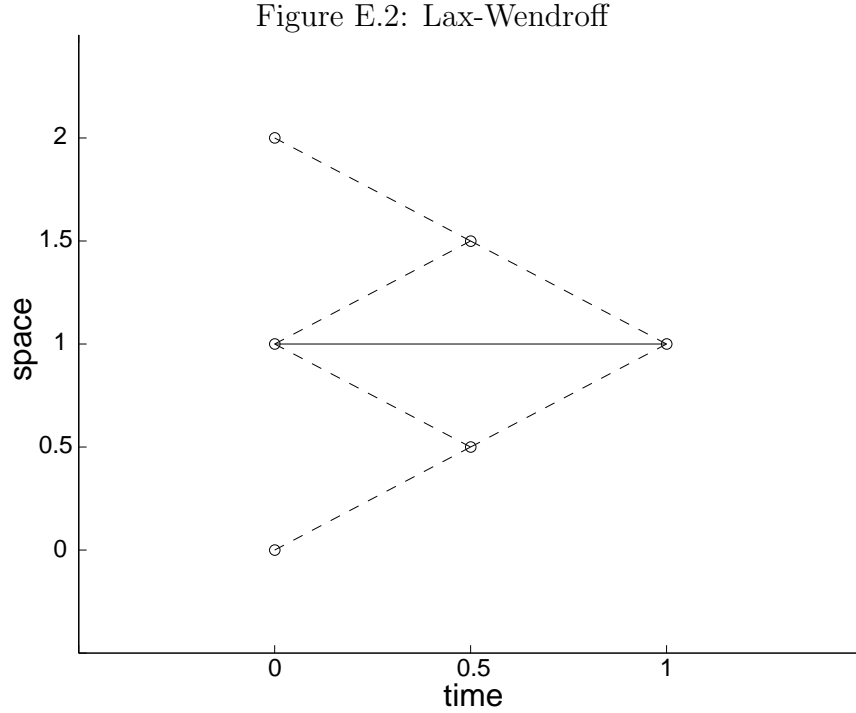
E.2 Ion Dynamics Model

The numerical modeling of equation (4.5) with equation (4.12) from Section 4.1 requires somewhat more effort than the aforementioned chemical models. This is due to the fact that the ion motion equations are PDEs and, as such, spatial derivatives are involved in addition to the temporal ones. Various techniques exist for the numerical solution of such equations [e.g. *Potter(1973)*, *Press et al.(1992)*, *Golub and Ortega(1992)*], though they generally require a good deal of customization for the problem in hand. For pure diffusion problems the *Crank-Nicolson* method is generally considered quite good [*Vesely(1994)*], but the formulation of the difference equations for a more complicated (not purely diffusive) case like the one we consider here is difficult. As a result, we chose to use a modified version of a more general method, the *Lax-Wendroff* scheme [*Potter(1973)*, *Press et al.(1992)*, *Vesely(1994)*] — a solution method applicable to a class known as flux-conservative initial value problems. The prototype equation for these problems is given by

$$\frac{\partial \vec{n}}{\partial t} = -\frac{\partial}{\partial z} \vec{F}(\vec{n}) \quad (\text{E.7})$$

where \vec{F} is the flux which is conserved. For this thesis, equation (E.7) is simply equation (4.5) written in a vector form (solving all altitudes at once) and the flux is given by equation (4.12) and is simply a vector form of $n_j v_z$. Note that one significant difference between the flux-conservative prototype and our situation is that $n_j v_z$ depends both on the density, \vec{n} , and on partial derivatives of that density.

The *Lax-Wendroff* scheme is illustrated diagrammatically in Figure E.2 where an estimate of both n and F is computed at each circle. Starting at time $i_t = 0$ and with initial values for n at all altitudes j_z , the first operation steps forward in time by a half step. This half step uses a simple differencing scheme to estimate the n



values at spatial positions which are also offset by a half step from the initial points. The second operation then uses these intermediate values to calculate fluxes which are used to increment the initial values a full step forward in time. The recursion relations for these two operations can be written as follows:

$$n(i_t + .5, j_z + .5) = \frac{1}{2} [n(i_t, j_z + 1) - n(i_t, j_z)] - \frac{\Delta t}{2\Delta z} [F(n(i_t, j_z + 1)) - F(n(i_t, j_z))] \quad (\text{E.8})$$

and

$$n(i_t + 1, j_z) = n(i_t, j_z) - \frac{\Delta t}{\Delta z} [F(n(i_t + .5, j_z + .5)) - F(n(i_t + .5, j_z - .5))] . \quad (\text{E.9})$$

Note that this scheme is second order accurate in both space and time.

The modifications we made to this scheme were instigated by the fact that the flux

from equation (4.12) is a function of not only n but also $\partial n/\partial z$. The ‘new’ prototype equation is written as follows:

$$\frac{\partial \vec{n}}{\partial t} = -\frac{\partial}{\partial z} \vec{F} \left(\vec{n}, \frac{\partial \vec{n}}{\partial z} \right). \quad (\text{E.10})$$

One approach to solving this equation is to simply estimate the spatial derivative for F by differencing the n values on either side of each point. This tends to decouple the n estimates from the spatial derivative estimates, however, and testing showed that it can lead to significant instabilities. The approach we adopted was estimating F at half grid points in space. This means that the differences for the spatial derivatives are more compact (spatially) but it also forces the n values for the flux calculations to come from averages. In particular, the following recursion formulas are used:

$$n(i_t, j_z + .5) = \frac{1}{2} [n(i_t, j_z) + n(i_t, j_z + 1)], \quad (\text{E.11})$$

$$dndz(i_t, j_z + .5) = \frac{1}{\Delta z} [n(i_t, j_z + 1) - n(i_t, j_z)], \quad (\text{E.12})$$

$$n(i_t + .5, j_z) = n(i_t, j_z) - \frac{\Delta t}{2\Delta z} [F(n(i_t, j_z + .5), dndz(i_t, j_z + .5)) - F(n(i_t, j_z - .5), dndz(i_t, j_z - .5))], \quad (\text{E.13})$$

$$n(i_t + .5, j_z + .5) = \frac{1}{2} [n(i_t + .5, j_z) + n(i_t + .5, j_z + 1)], \quad (\text{E.14})$$

$$dndz(i_t + .5, j_z + .5) = \frac{1}{\Delta z} [n(i_t + .5, j_z + 1) - n(i_t + .5, j_z)], \quad (\text{E.15})$$

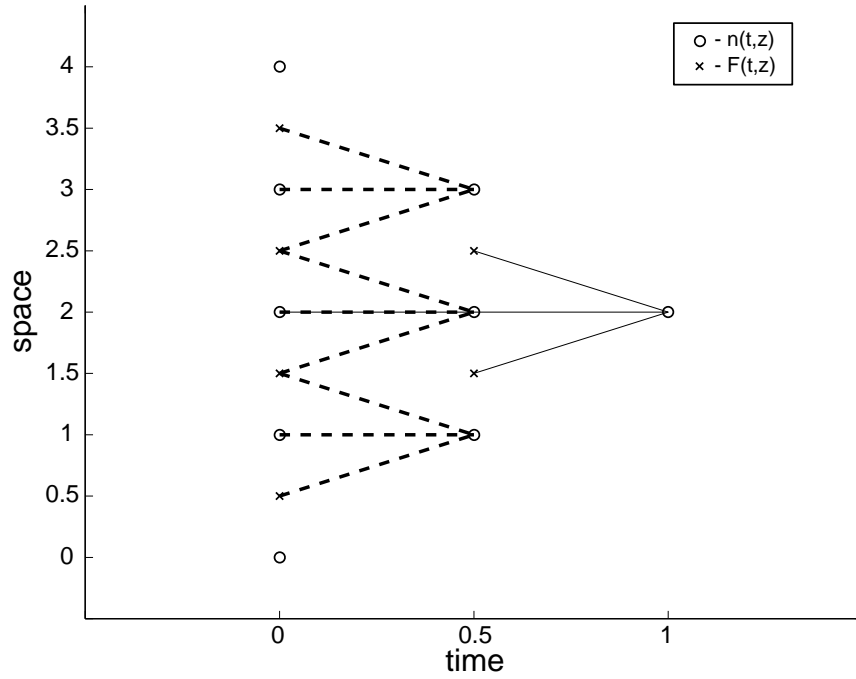
and

$$n(i_t + 1, j_z) = n(i_t, j_z) - \frac{\Delta t}{\Delta z} [F(n(i_t + .5, j_z + .5), dndz(i_t + .5, j_z + .5)) - F(n(i_t + .5, j_z - .5), dndz(i_t + .5, j_z - .5))]. \quad (\text{E.16})$$

We show this schematically in Figure E.3.

The final issue we need to address is the question of boundary conditions. For the model runs presented in this thesis the boundaries were set up to have fixed densities

Figure E.3: Modified Lax-Wendroff



for all constituents. This condition implies that an ion entering one of the end cells is immediately compensated for by the loss of another ion out of the simulation space. We found this to be a satisfactory condition because the boundaries were chosen at large distances from the regions of greatest interest in terms of ion dynamics.

Bibliography

- Abramowitz, E., and I. A. Stegun (eds.), *Handbook of Mathematical Functions*. Dover Publications, Inc., New York, NY, 1965.
- Alpers, M., J. Höffner, and U. von Zahn, Iron atom densities in the polar mesosphere from lidar observations, *Geophys. Res. Lett.*, *17*(12), 2345–2348, 1990.
- Baldwin, B., and Y. Sheaffer, Ablation and breakup of large meteoroids during atmospheric entry, *J. Geophys. Res.*, *76*(19), 4653–4668, 1971.
- Banks, P., Collision frequencies and energy transfer: Ions, *Planet. Space Sci.*, *14*, 1105–1122, 1966.
- Banks, P. M., and G. Kockarts, *Aeronomy, Part A*. Academic Press, Inc., New York, NY, 1973a.
- Banks, P. M., and G. Kockarts, *Aeronomy, Part B*. Academic Press, Inc., New York, NY, 1973b.
- Beatty, T. J., R. L. Collins, C. S. Gardner, C. A. Hostetler, and C. F. Sechrist, Jr., Simultaneous radar and lidar observations of sporadic *E* and Na layers at Arecibo, *Geophys. Res. Lett.*, *16*(9), 1019–1022, 1989.
- Bedey, D. F., The role of electric fields in the occurrence, structure, and drift of thin metallic ion layers in the high-latitude ionosphere, Ph.D. thesis, University of Alaska, Fairbanks, 1996.
- Beer, T., *Atmospheric Waves*. John Wiley & Sons, New York, NY, 1974.

- Behnke, R. A., and J. F. Vickrey, Radar evidence for Fe^+ in a sporadic-*E* layer, *Radio Sci.*, 10(3), 325–327, 1975.
- Bernard, R., Das vorhandensein von natrium in der atmosphäre auf grund von interferometrischen untersuchungen der *D*-linie im abend- und nachthimmellicht, *Zs. f. Phys.*, 110, 291–301, 1938.
- Bernard, R., The identification and the origin of atmospheric sodium, *Astrophys. J.*, 89, 133–135, 1939.
- Bilitza, D., International Reference Ionosphere 1990, Tech. Rep. 90–22, National Space Science Data Center, Greenbelt, Maryland, 1990.
- Bilitza, D., The *E*- and *D*-region in IRI, *Adv. Space Res.*, 21(6), 871–874, 1998.
- Bills, R. E., and C. S. Gardner, Lidar observations of mesospheric Fe and sporadic Fe layers at Urbana, Illinois, *Geophys. Res. Lett.*, 17(2), 143–146, 1990.
- Bjørnå, N., and J. Trulsen, Effect of a power law particle flux on the ionospheric incoherent scattering cross section, *Physica Scripta*, 33, 284–288, 1986.
- Bjørnå, N., O. Havnes, J. O. Jensen, and J. Trulsen, Enhancement of the incoherent scattering plasma lines due to precipitating protons and secondary electrons, *Physica Scripta*, 25, 632–636, 1982.
- Blackadar, A. K., *Turbulence and Diffusion in the Atmosphere*. Springer-Verlag, 1997.
- Blamont, J.-E., Turbulence in atmospheric motions between 90 and 130 km of altitude, *Planet. Space Sci.*, 10, 89–101, 1963.
- Bone, N., *Meteors*. Sky Pub. Corp., Cambridge, Mass., 1993.
- Booker, H. G., Turbulence in the ionosphere with applications to meteor-trails, radio-star scintillation, auroral radar echoes, and other phenomena, *J. Geophys. Res.*, 61(4), 673–705, 1956.

- Booker, H. G., and R. Cohen, A theory of long-duration meteor-echoes based on atmospheric turbulence with experimental confirmation, *J. Geophys. Res.*, *61*(4), 707–733, 1956.
- Bowles, K. L., Observations of vertical incidence scatter from the ionosphere at 41 Mc/sec, *Phys. Rev. Lett.*, *1*(12), 454–455, 1958.
- Bowman, M. R., A. J. Gibson, and M. C. W. Sandford, Atmospheric sodium measured by a tuned laser radar, *Nature*, *221*, 456–457, 1969.
- Brekke, A. (ed.), *Radar Probing of the Auroral Plasma*. Scandinavian University Books, 1977.
- Brekke, A., *Physics of the Upper Polar Atmosphere*. John Wiley & Sons, 1997.
- Bristow, W. A., and B. J. Watkins, Numerical simulation of the formation of thin ionization layers at high latitudes, *Geophys. Res. Lett.*, *18*(3), 404–407, 1991.
- Bristow, W. A., and B. J. Watkins, Incoherent scatter observations of thin ionization layers at Sondrestrom, *J. Atmos. Terr. Phys.*, *55*(6), 873–894, 1993.
- Bronshten, V. A., *Physics of Meteoric Phenomena*. D. Reidel Pub. Co., Dordrecht, Holland, 1983.
- Brown, T. L., The chemistry of metallic elements in the ionosphere and mesosphere, *Chem. Rev.*, *73*(6), 645–667, 1973.
- Buneman, O., Scattering of radiation by the fluctuations in a nonequilibrium plasma, *J. Geophys. Res.*, *67*(5), 2050–2053, 1962.
- Cabannes, J., J. Dufay, and J. Gauzit, Sodium in the upper atmosphere, *Astrophys. J.*, *88*, 164–172, 1938.
- Carter, L. N., J., A comprehensive model of global transport and localized layering of metallic ions in the upper atmosphere, Ph.D. thesis, Boston University, 1995.

- Chamberlain, J. W., *Physics of the Aurora and Airglow*. American Geophysical Union, 1995.
- Chapman, S., Notes on atmospheric sodium, *Astrophys. J.*, *90*, 309–316, 1939.
- Chen, F. F., *Introduction to Plasma Physics and Controlled Fusion, Volume 1: Plasma Physics*. Plenum Press, 1984.
- Clemesha, B. R., Sporadic neutral metal layers in the mesosphere and lower thermosphere, *J. Atmos. Terr. Phys.*, *57*(7), 725–736, 1995.
- Clemesha, B. R., V. W. J. H. Kirchhoff, D. M. Simonich, H. Takahashi, and P. P. Batista, Spaced lidar and nightglow observations of an atmospheric sodium enhancement, *J. Geophys. Res.*, *85*(A7), 3480–3484, 1980.
- Clemesha, B. R., D. M. Simonich, H. Takahashi, S. M. L. Melo, and J. M. C. Plane, Experimental evidence for photochemical control of the atmospheric sodium layer, *J. Geophys. Res.*, *100*(D9), 18,909–18,916, 1995.
- Clemesha, B. R., V. W. J. H. Kirchhoff, D. M. Simonich, and H. Takahashi, Evidence of an extra-terrestrial source for the mesospheric sodium layer, *Geophys. Res. Lett.*, *5*(10), 873–876, 1978.
- Cox, R. M., and J. M. C. Plane, An ion-molecule mechanism for the formation of neutral sporadic Na layers, *J. Geophys. Res.*, *103*(D6), 6349–6359, 1998.
- Cox, R. M., J. M. C. Plane, and J. S. A. Green, A modelling investigation of sudden sodium layers, *Geophys. Res. Lett.*, *20*(24), 2841–2844, 1993.
- Dalgarno, A., Charged particles in the upper atmosphere, *Ann. Geophysicae*, *17*(1), 16–34, 1961.
- Danilov, A. D., Ion chemistry of the lower atmosphere, *J. Atmos. Terr. Phys.*, *56*(9), 1213–1225, 1994.

- Danilov, A. D., and U. A. Kalgin, Seasonal and latitudinal variations of eddy diffusion coefficient in the mesosphere and lower thermosphere, *J. Atmos. Terr. Phys.*, *54*(11/12), 1481–1489, 1992.
- Doolittle, J. H., S. B. Mende, R. M. Robinson, G. R. Swenson, and C. E. Valladares, An observation of ionospheric convection and auroral arc motion, *J. Geophys. Res.*, *95*(A11), 19,123–19,129, 1990.
- Dougherty, J. P., and D. T. Farley, A theory of incoherent scattering of radio waves by a plasma, *Proc. Roy. Soc. A*, *259*, 79–99, 1960.
- Dougherty, J. P., and D. T. Farley, A theory of incoherent scattering of radio waves by a plasma 3. Scattering in a partly ionized gas, *J. Geophys. Res.*, *68*(19), 5473–5486, 1963.
- Ebel, A., Eddy diffusion models for the mesosphere and lower thermosphere, *J. Atmos. Terr. Phys.*, *42*, 617–628, 1980.
- Erickson, J. E., Velocity distribution of sporadic photographic meteors, *J. Geophys. Res.*, *73*(12), 3721–3726, 1968.
- Evans, J. V., Theory and practice of ionosphere study by Thomson scatter radar, *Proc. IEEE*, *57*(4), 496–530, 1969.
- Farley, D. T., A theory of electrostatic fields in a horizontally stratified ionosphere subject to a vertical magnetic field, *J. Geophys. Res.*, *64*(9), 1225–1233, 1959.
- Farley, D. T., A theory of electrostatic fields in the ionosphere at nonpolar geomagnetic latitudes, *J. Geophys. Res.*, *65*(3), 869–877, 1960.
- Farley, D. T., A theory of incoherent scattering of radio waves by a plasma 4. The effect of unequal ion and electron temperatures, *J. Geophys. Res.*, *71*(17), 4091–4098, 1966.
- Farley, D. T., Incoherent scatter correlation function measurements, *Radio Sci.*, *4*(10), 935–953, 1969.

- Farley, D. T., Radio wave scattering from the ionosphere, in *Methods of Experimental Physics*, edited by R. H. Lovberg, and H. R. Griem, vol. 9B, pp. 139–186. Academic Press, 1971.
- Farley, D. T., Multiple-pulse incoherent-scatter correlation function measurements, *Radio Sci.*, 7(6), 661–666, 1972.
- Farley, D. T., J. P. Dougherty, and D. W. Barron, A theory of incoherent scattering of radio waves by a plasma II. Scattering in a magnetic field, *Proc. Roy. Soc. A*, 263, 238–258, 1961.
- Farragher, A. L., J. A. Peden, and W. L. Fite, Charge transfer of N_2^+ , O_2^+ , and NO^+ to sodium atoms at thermal energies, *J. Chem. Phys.*, 50(1), 287–293, 1969.
- Fegley, Jr., B., and A. G. W. Cameron, A vaporization model for iron/silicate fractionation in the Mercury protoplanet, *Earth Planet. Sci. Lett.*, 82, 207–222, 1987.
- Fejer, J. A., Scattering of radio waves by an ionized gas in thermal equilibrium, *Can. J. Phys.*, 38, 1960.
- Fejer, J. A., Scattering of radio waves by an ionized gas in thermal equilibrium in the presence of a uniform magnetic field, *Can. J. Phys.*, 39, 1961.
- Ferguson, E. E., Atmospheric metal ion chemistry, *Radio Sci.*, 7(3), 397–401, 1972.
- Fiocco, G., and L. D. Smullin, Detection of scattering layers in the upper atmosphere (60–140 km) by optical radar, *Nature*, 199(4900), 1275–1276, 1963.
- Foy, R., and A. Labeyrie, Feasibility of adaptive telescope with laser probe, *Astron. Astrophys.*, 152, L29–L31, 1985.
- Franck, J., and C. A. Rieke, Note on the explanation of the D-lines in the spectrum of the night sky, *Astrophys. J.*, 89, 463–464, 1939.
- Fricke, K. H., and U. von Zahn, Mesopause temperatures derived from probing the hyperfine structure of the D_2 resonance line of sodium by lidar, *J. Atmos. Terr. Phys.*, 47(5), 499–512, 1985.

- Fried, B. D., and S. D. Conte, *The Plasma Dispersion Function*. Academic Press, New York, NY, 1961.
- Fugate, R. Q., D. L. Fried, G. A. Ameer, B. R. Boeke, S. L. Browne, P. H. Roberts, R. E. Ruane, G. A. Tyler, and L. M. Wopat, Measurement of atmospheric wavefront distortion using scattered light from a laser guide-star, *Nature*, *353*, 144–146, 1991.
- Gadsden, M., Sodium in the upper atmosphere: meteoric origin, *J. Atmos. Terr. Phys.*, *30*, 151–161, 1968.
- Garcia, R. R., and S. Solomon, A new numerical model of the middle atmosphere 2. Ozone and related species, *J. Geophys. Res.*, *99*(D6), 12,937–12,951, 1994.
- Gardner, C. S., X. Tao, and G. C. Papen, Observations of strong wind shears and temperature enhancements during several sporadic Na layer events above Haleakala, *Geophys. Res. Lett.*, *22*(20), 2809–2812, 1995.
- Gaupp, A., P. Kuske, and H. J. Andrä, Accurate lifetime measurements of the lowest $^2P_{1/2}$ states in neutral lithium and sodium, *Phys. Rev. A*, *26*(6), 3351–3359, 1982.
- Gibson, A. J., and M. C. W. Sandford, The seasonal variation of the night-time sodium layer, *J. Atmos. Terr. Phys.*, *33*, 1675–1684, 1971.
- Goldston, R. J., and P. H. Rutherford, *Introduction to Plasma Physics*. Institute of Physics Publishing, 1995.
- Golub, G. H., and J. M. Ortega, *Scientific Computing and Differential Equations*. Academic Press, Inc., 1992.
- Gordon, W. E., Incoherent scattering of radio waves by free electrons with applications to space exploration by radar, *Proc. IRE*, *46*(11), 1824–1829, 1958.
- Granier, C., J. P. Jégou, and G. Mégie, Resonant lidar detection of Ca and Ca⁺ in the upper atmosphere, *Geophys. Res. Lett.*, *12*(10), 655–658, 1985.

- Gray, R. W., and D. T. Farley, Theory of incoherent-scatter measurements using compressed pulses, *Radio Sci.*, 8(2), 123–131, 1973.
- Grebowsky, J. M., R. A. Goldberg, and W. D. Pesnell, Do meteor showers significantly perturb the ionosphere?, *J. Atmos. Sol.-Terr. Phys.*, 60, 607–615, 1998.
- Hagen, J. B., and H. A. Baumgartner, Backscatter gain of aperture antennas, *Radio Sci.*, 31(4), 693–699, 1996.
- Hagfors, T., Density fluctuations in a plasma in a magnetic field with applications to the ionosphere, *J. Geophys. Res.*, 66(6), 1699–1712, 1961.
- Hagfors, T., and R. A. Brockelman, A theory of collision dominated electron density fluctuations in a plasma with applications to incoherent scatter, *Phys. Fluids*, 14(6), 1143–1151, 1971.
- Hansen, G., and U. von Zahn, Sudden sodium layers in polar latitudes, *J. Atmos. Terr. Phys.*, 52(6–8), 585–608, 1990.
- Hansen, J. E., and L. D. Travis, Light scattering in planetary atmospheres, *Space Sci. Rev.*, 16(4), 527–610, 1974.
- Hargreaves, J. K., *The Solar-Terrestrial Environment*. Cambridge University Press, 1992.
- Hedin, A. E., Extension of the MSIS thermosphere model into the middle and lower atmosphere, *J. Geophys. Res.*, 96(A2), 1159–1172, 1991.
- Hedin, A. E., et al., Empirical wind model for the upper, middle and lower atmosphere, *J. Atmos. Terr. Phys.*, 58(13), 1421–1447, 1996.
- Heide, F., and F. Wlotzka, *Meteorites, Messengers from Space*. Springer-Verlag, Berlin Heidelberg, 1995.
- Heinselmann, C. J., and J. F. Vickrey, On the frequency of Langmuir waves in the ionosphere, *J. Geophys. Res.*, 97(A10), 14,905–14,910, 1992a.

- Heinselman, C. J., and J. F. Vickrey, On the spectral analysis and interpretation of incoherent scatter plasma line echoes, *Radio Sci.*, *27*(2), 221–230, 1992b.
- Heinselman, C. J., J. P. Thayer, and B. J. Watkins, A high-latitude observation of sporadic sodium and sporadic *E*-layer formation, *Geophys. Res. Lett.*, *25*(16), 3059–3062, 1998.
- Helmer, M., and J. M. C. Plane, A study of the reaction $\text{NaO}_2 + \text{O} \rightarrow \text{NaO} + \text{O}_2$: Implications for the chemistry of sodium in the upper atmosphere, *J. Geophys. Res.*, *98*(D12), 23,207–23,222, 1993.
- Helmer, M., J. M. C. Plane, J. Qian, and C. S. Gardner, A model of meteoric iron in the upper atmosphere, *J. Geophys. Res.*, *103*(D9), 10,913–10,925, 1998.
- Heppner, J. P., and M. L. Miller, Thermospheric winds at high latitudes from chemical release observations, *J. Geophys. Res.*, *87*(A3), 1633–1647, 1982.
- Hickey, M. P., and J. M. C. Plane, A chemical-dynamical model of wave-driven sodium fluctuations, *Geophys. Res. Lett.*, *22*(20), 2861–2864, 1995.
- Hines, C. O., *The Upper Atmosphere in Motion*. American Geophysical Union, 1974.
- Hocking, W. K., Turbulence in the region 80–120 km, *Adv. Space Res.*, *10*(12), (12)153–(12)161, 1990.
- Holt, J. M., D. A. Rhoda, D. Tetenbaum, and A. P. van Eyken, Optimal analysis of incoherent scatter radar data, *Radio Sci.*, *27*(3), 435–447, 1992.
- Hughes, D. W., Cosmic dust influx to the Earth, in *Space Research XV*. Akademie Verlag, Berlin, 1975.
- Hughes, D. W., Meteors, in *Cosmic Dust*, edited by J. McDowell. John Wiley and Sons, New York, N.Y., 1978.
- Hunten, D. M., Spectroscopic studies of the twilight airglow, *Space Sci. Rev.*, *6*, 493–573, 1967.

- Hunten, D. M., R. P. Turco, and O. B. Toon, Smoke and dust particles of meteoric origin in the mesosphere and stratosphere, *J. Atmos. Sci.*, *37*, 1342–1357, 1980.
- Huuskonen, A., T. Nygrén, L. Jalonen, N. Bjørnå, T. L. Hansen, A. Brekke, and T. Turunen, Ion composition in sporadic *E* layers measured by the EISCAT UHF radar, *J. Geophys. Res.*, *93*(A12), 14,603–14,610, 1988.
- Ioannidis, G., and D. T. Farley, Incoherent scatter observations at Arecibo using compressed pulses, *Radio Sci.*, *7*, 763–766, 1972.
- Jacobson, M. Z., *Fundamentals of Atmospheric Modeling*. Cambridge University Press, 1999.
- Jones, K. L., Mechanisms for vertical separation of ions in sporadic-*E* layers, *J. Atmos. Terr. Phys.*, *51*(6), 469–476, 1989.
- Jones, R. A., and M. H. Rees, Time dependent studies of the aurora-I. Ion density and composition, *Planet. Space Sci.*, *21*, 537–557, 1973.
- Kane, T. J., and C. S. Gardner, Lidar observations of the meteoric deposition of mesospheric metals, *Science*, *259*, 1297–1300, 1993a.
- Kane, T. J., and C. S. Gardner, Structure and seasonal variability of the nighttime mesospheric Fe layer at midlatitudes, *J. Geophys. Res.*, *98*(D9), 16,875–16,886, 1993b.
- Kane, T. J., C. S. Gardner, Q. Zhou, J. D. Mathews, and C. A. Tepley, Lidar, radar and airglow observations of a prominent sporadic Na/sporadic *E* layer event at Arecibo during AIDA-89, *J. Atmos. Terr. Phys.*, *55*(3), 499–511, 1993.
- Kelley, M. C., *The Earth's Ionosphere, Plasma Physics and Electrodynamics*. Academic Press, Inc., 1989.
- Kelley, M. C., C. Alcalá, and J. Y. N. Cho, Detection of a meteor contrail and meteoric dust in the Earth's upper mesosphere, *J. Atmos. Sol.-Terr. Phys.*, *60*(3), 359–369, 1998.

- Kelly, J. D., Sondrestrom radar – Initial results, *Geophys. Res. Lett.*, *10*, 1112–1115, 1983.
- Kelly, J. D., C. J. Heinselman, J. F. Vickrey, and R. R. Vondrak, Sondrestrom radar and accompanying ground-based instrumentation, *Space Sci. Rev.*, *71*, 797–813, 1995.
- Kent, G. S., and R. W. H. Wright, A review of laser radar measurements of atmospheric properties, *J. Atmos. Terr. Phys.*, *32*, 917–943, 1970.
- Kent, G. S., B. R. Clemesha, and R. W. Wright, High altitude atmospheric scattering of light from a laser beam, *J. Atmos. Terr. Phys.*, *29*, 169–181, 1967.
- Kirkwood, S., Thin ion layers in the high-latitude lower ionosphere, *Adv. Space Res.*, *19*(1), (1)149–(1)158, 1997.
- Kirkwood, S., and U. von Zahn, On the role of auroral electric fields in the formation of low altitude sporadic-*E* and sudden sodium layers, *J. Atmos. Terr. Phys.*, *53*(5), 389–407, 1991.
- Kirkwood, S., and U. von Zahn, Formation mechanisms for low-altitude E_s and their relationship with neutral Fe layers: Results from the METAL campaign, *J. Geophys. Res.*, *98*(A12), 21,549–21,561, 1993.
- Kolmogorov, A. N., The local structure of turbulence in an incompressible fluid for very large Reynolds numbers, *C.R. Acad. Sci. U.R.S.S.*, *30 and 32*, 301–305, 16–18, 1941.
- Kopp, E., On the abundance of metal ions in the lower ionosphere, *J. Geophys. Res.*, *102*(A5), 9667–9674, 1997.
- Larsen, M. F., Personal communication, E-mail about J.P. Heppner TMA trail photograph, 1999.
- Lehtinen, M. S., Statistical theory of incoherent scatter measurements, Ph.D. thesis, University of Helsinki, Finland, 1986.

- Lehtinen, M. S., and I. Häggström, A new modulation principle for incoherent scatter measurements, *Radio Sci.*, *22*(4), 625–634, 1987.
- Lehtinen, M. S., and A. Huuskonen, General incoherent scatter analysis and GUIDAP, *J. Atmos. Terr. Phys.*, *58*(1–4), 435–452, 1996.
- Lehtinen, M. S., A. Huskonen, and J. Pirttilä, First experiences of full-profile analysis with GUIDAP, *Ann. Geophysicae*, *14*, 1487–1495, 1996.
- Levandier, D. J., R. A. Dressler, S. Williams, and E. Murad, A high-temperature guided-ion beam study of $\text{Na} + \text{X}^+$ ($\text{X} = \text{O}_2, \text{NO}, \text{N}_2$) charge-transfer reactions, *J. Chem. Soc., Faraday Trans.*, *93*(16), 2611–2617, 1997.
- Levanon, N., *Radar Principles*. John Wiley & Sons, 1988.
- Lloyd, K. H., C. H. Low, B. J. McAvaney, D. Rees, and R. G. Roper, Thermospheric observations combining chemical seeding and ground-based techniques—I. Winds, turbulence and the parameters of the neutral atmosphere, *Planet. Space Sci.*, *20*, 761–789, 1972.
- Love, S. G., and D. E. Brownlee, Heating and thermal transformation of micrometeoroids entering the Earth's atmosphere, *Icarus*, *89*, 26–43, 1991.
- Love, S. G., and D. E. Brownlee, A direct measurement of the terrestrial mass accretion rate of cosmic dust, *Science*, *262*, 550–553, 1993.
- Mason, B. (ed.), *Handbook of Elemental Abundances in Meteorites*. Gordon and Breach, New York, NY, 1971.
- Mathews, J. D., Incoherent scatter radar probing of the 60–100-km atmosphere and ionosphere, *IEEE Trans. Geosci. Remote Sens.*, *GE-24*(5), 765–776, 1986.
- Mathews, J. D., Sporadic E: Current views and recent progress, *J. Atmos. Sol.-Terr. Phys.*, *60*(4), 413–435, 1998.

- Mathews, J. D., Q. Zhou, C. R. Philbrick, Y. T. Morton, and C. S. Gardner, Observations of ion and sodium layer coupled processes during AIDA, *J. Atmos. Terr. Phys.*, *55*(3), 487–498, 1993.
- McKinley, D. W. R., *Meteor Science and Engineering*. McGraw-Hill, 1961.
- McNeil, W. J., E. Murad, and S. T. Lai, Comprehensive model for the atmospheric sodium layer, *J. Geophys. Res.*, *100*(D8), 16,847–16,855, 1995.
- McNeil, W. J., S. T. Lai, and E. Murad, A model for meteoric magnesium in the ionosphere, *J. Geophys. Res.*, *101*(A3), 5251–5259, 1996.
- McNeil, W. J., S. T. Lai, and E. Murad, Differential ablation of cosmic dust and implications for the relative abundances of atmospheric metals, *J. Geophys. Res.*, *103*(D9), 10,899–10,911, 1998.
- Megie, G., F. Bos, J. E. Blamont, and M. L. Chanin, Simultaneous nighttime lidar measurements of atmospheric sodium and potassium, *Planet. Space Sci.*, *26*, 27–35, 1978.
- Mende, S. B., J. H. Doolittle, R. M. Robinson, R. R. Vondrak, and F. J. Rich, Plasma drifts associated with a system of sun-aligned arcs in the polar cap, *J. Geophys. Res.*, *93*(A1), 256–264, 1988.
- Mendillo, M., J. Semeter, and J. Noto, Finite Element Simulation (FES): A computer modeling technique for studies of chemical modification of the ionosphere, *Adv. Space Res.*, *13*(10), (10)55–(10)64, 1993.
- Muirden, J., *The Amateur Astronomer's Handbook*. Harper and Row, Publishers, New York, N.Y., 3 edn., 1983.
- Murad, E., Problems in the chemistry of metallic species in the *D* and *E* regions, *J. Geophys. Res.*, *83*(A12), 5525–5530, 1978.
- Nath, N., I. S. Mikkelsen, and T. S. Jørgensen, On the formation of high latitude *E_s*-layers, *J. Atmos. Terr. Phys.*, *42*, 841–852, 1980.

- Nicolet, M., On the molecular scattering in the terrestrial atmosphere: An empirical formula for its calculation in the homosphere, *Planet. Space Sci.*, 32(11), 1467–1468, 1984.
- Nilsson, H., S. Kirkwood, J. Liliensten, and M. Galand, Enhanced incoherent scatter plasma lines, *Ann. Geophysicae*, 14, 1462–1472, 1996.
- Norton, O. R., *Rocks from Space*. Mountain Press Pub. Co., Missoula, Montana, 2 edn., 1998.
- Nygrén, T., Vertical plasma transport due to electric fields and neutral winds in the auroral ionosphere, *Adv. Space Res.*, 10(6), (6)297–(6)305, 1990.
- Nygrén, T., L. Jalonen, A. Huuskonen, and T. Turunen, Density profiles of sporadic *E*-layers containing two metal ion species, *J. Atmos. Terr. Phys.*, 46(10), 885–893, 1984a.
- Nygrén, T., L. Jalonen, J. Oksman, and T. Turunen, The role of electric field and neutral wind direction in the formation of sporadic *E*-layers, *J. Atmos. Terr. Phys.*, 46(4), 373–381, 1984b.
- Nygrén, T., B. S. Lanchester, A. Huuskonen, L. Jalonen, T. Turunen, H. Rishbeth, and A. P. van Eyken, Interference of tidal and gravity waves in the ionosphere and an associated sporadic *E*-layer, *J. Atmos. Terr. Phys.*, 52(6-8), 609–623, 1990.
- Öptik, E. J., *Physics of Meteor Flight in the Atmosphere*. Interscience Publishers, Inc., New York, N.Y., 1958.
- Parkinson, M. L., P. L. Dyson, D. P. Monselesan, and R. J. Morris, On the role of electric field direction in the formation of sporadic *E*-layers in the southern polar cap ionosphere, *J. Atmos. Sol.-Terr. Phys.*, 60(4), 471–491, 1998.
- Penndorf, R., Tables of the refractive index for standard air and the Rayleigh scattering coefficient for the spectral region between 0.2 and 20.0 μ and their application to atmospheric optics, *J. Opt. Soc. Am.*, 47(2), 176–182, 1957.

- Perkins, F., and E. E. Salpeter, Enhancement of plasma density fluctuations by non-thermal electrons, *Phys. Rev.*, 139(1A), A55–A62, 1965.
- Plane, J. M. C., The chemistry of meteoric metals in the Earth's upper atmosphere, *Intl. Rev. Phys. Chem.*, 10(1), 55–106, 1991.
- Plane, J. M. C., and M. Helmer, Laboratory studies of the chemistry of meteoric metals, in *Research in Chemical Kinetics*, edited by R. G. Compton, and G. Hancock, vol. 2, pp. 313–367. Elsevier Science B. V., Amsterdam, 1994.
- Plane, J. M. C., and M. Helmer, Laboratory study of the reactions $\text{Mg} + \text{O}_3$ and $\text{MgO} + \text{O}_3$, *Faraday Discuss.*, 100, 411–430, 1995.
- Plane, J. M. C., R. M. Cox, J. Qian, W. M. Pfenninger, G. C. Papen, C. S. Gardner, and P. J. Espy, Mesospheric Na layer at extreme high latitudes in summer, *J. Geophys. Res.*, 103(D6), 6381–6389, 1998.
- Plane, J. M. C., C. S. Gardner, J. Yu, C. Y. She, R. R. Garcia, and H. C. Pumphrey, Mesospheric Na layer at 40°N: Modeling and observations, *J. Geophys. Res.*, 104(D3), 3773–3788, 1999.
- Potter, D., *Computational Physics*. John Wiley & Sons, 1973.
- Press, W. H., S. A. Teukolsky, W. T. Vetterling, and B. P. Flannery, *Numerical Recipes in C*. Cambridge University Press, second edn., 1992.
- Rajasekhar, B., and J. M. C. Plane, An *ab initio* study of dissociative electron attachment to NaHCO_3 and NaCO_3 , and the role of these reactions in the formation of sudden sodium layers, *Geophys. Res. Lett.*, 20(1), 21–24, 1993.
- Rawer, K., D. Bilitza, and S. Ramakrishnan, Goals and status of the International Reference Ionosphere, *Rev. Geophys.*, 16(2), 177–181, 1978.
- Rees, D., R. G. Roper, K. H. Lloyd, and C. H. Low, Determination of the structure of the atmosphere between 90 and 250 km by means of contaminant releases at Woomera, May 1968, *Phil. Trans. R. Soc. Lond. A*, 271(1218), 631–666, 1972.

- Rees, M. H., Auroral ionization and excitation by incident energetic electrons, *Planet. Space Sci.*, *11*, 1209–1218, 1963.
- Rees, M. H., On the interaction of auroral protons with the Earth's atmosphere, *Planet. Space Sci.*, *30*(5), 463–472, 1982.
- Rees, M. H., *Physics and Chemistry of the Upper Atmosphere*. Cambridge University Press, 1989.
- Rees, M. H., and R. A. Jones, Time dependent studies of the aurora—II. Spectroscopic morphology, *Planet. Space Sci.*, *21*, 1213–1235, 1973.
- Renau, J., H. Camnitz, and W. Flood, The spectrum and total intensity of electromagnetic waves scattered from an ionized gas in thermal equilibrium in the presence of a static quasi-uniform magnetic field, *J. Geophys. Res.*, *66*(9), 2703–2732, 1961.
- Roble, R. G., E. C. Ridley, and R. E. Dickinson, On the global mean structure of the thermosphere, *J. Geophys. Res.*, *92*(A8), 8745–8758, 1987.
- Roper, R. G., Rocket vapor trail releases revisited: Turbulence and the scale of gravity waves: Implications for the imaging Doppler interferometry/incoherent scatter radar controversy, *J. Geophys. Res.*, *101*(D3), 7013–7017, 1996.
- Rosenberg, N. W., D. Golomb, and E. Allen, Jr., Chemiluminescence of trimethyl aluminum released into the upper atmosphere, *J. Geophys. Res.*, *68*(20), 5895–5898, 1963a.
- Rosenberg, N. W., D. Golomb, and E. F. Allen, Jr., Chemiluminescence techniques for studying nighttime winds in the upper atmosphere, *J. Geophys. Res.*, *68*(10), 3328–3330, 1963b.
- Rosenbluth, M. N., and N. Rostoker, Scattering of electromagnetic waves by a non-equilibrium plasma, *Phys. Fluids*, *5*(7), 776–788, 1962.

- Rosinski, J., and R. H. Snow, Secondary particulate matter from meteor vapors, *J. Meteor.*, *18*, 736–745, 1961.
- Salpeter, E. E., Electron density fluctuations in a plasma, *Phys. Rev.*, *120*(5), 1528–1535, 1960a.
- Salpeter, E. E., Scattering of radio waves by electrons above the ionosphere, *J. Geophys. Res.*, *65*(6), 1851–1852, 1960b.
- Salpeter, E. E., Effect of the magnetic field in ionospheric backscatter, *J. Geophys. Res.*, *66*(3), 982–984, 1961.
- Sandford, M. C. W., and A. J. Gibson, Laser radar measurements of the atmospheric sodium layer, *J. Atmos. Terr. Phys.*, *32*, 1423–1430, 1970.
- Schlegel, K., H. Kohl, and K. Rinnert, Temperatures and collision frequencies in the polar *E* region measured with the incoherent scatter technique, *J. Geophys. Res.*, *85*, 710–714, 1980.
- Seinfeld, J. H., and S. N. Pandis, *Atmospheric Chemistry and Physics, From Air Pollution to Climate Change*. John Wiley & Sons, Inc., 1998.
- Showen, R. L., The spectral measurement of plasma lines, *Radio Sci.*, *14*(3), 503–508, 1979.
- Simonich, D. M., and B. R. Clemesha, Resonant extinction of lidar returns from alkali metal layers in the upper atmosphere, *Appl. Optics*, *22*(9), 1387–1389, 1983.
- Siskind, D. E., C. A. Barth, and J. M. Russell, III, A climatology of nitric oxide in the mesosphere and thermosphere, *Adv. Space Res.*, *21*(10), 1353–1362, 1998.
- Skolnik, M. I., *Introduction to Radar Systems*. McGraw-Hill, Inc., second edn., 1980.
- Skolnik, M. I., *Radar Handbook*. McGraw-Hill, Inc., second edn., 1990.
- Slattery, J. C., and J. F. Friichtenicht, Ionization probability of iron particles at meteoric velocities, *Astrophys. J.*, *147*(1), 235–244, 1967.

- Slipher, V. M., Emissions in the spectrum of the light of the night sky, *Publ. Astron. Soc. Pacific*, *41*, 262–263, 1929.
- Smullin, L. D., and G. Fiocco, Optical echoes from the Moon, *Nature*, *194*(4835), 1267, 1962.
- Stubbe, P., Frictional forces and collision frequencies between moving ion and neutral gases, *J. Atmos. Terr. Phys.*, *30*, 1965–1985, 1968.
- Sulzer, M. P., A phase modulation technique for a sevenfold statistical improvement in incoherent scatter data-taking, *Radio Sci.*, *21*(4), 737–744, 1986a.
- Sulzer, M. P., A radar technique for high range resolution incoherent scatter auto-correlation function measurements utilizing the full average power of klystron radars, *Radio Sci.*, *21*(6), 1033–1040, 1986b.
- Sulzer, M. P., Recent incoherent scatter techniques, *Adv. Space Res.*, *9*(5), (5)153–(5)162, 1989.
- Swartz, W. E., and D. T. Farley, A theory of incoherent scattering of radio waves by a plasma 5. The use of the Nyquist theorem in general quasi-equilibrium situations, *J. Geophys. Res.*, *84*(A5), 1930–1932, 1979.
- Swider, W., Processes for meteoric elements in the *E*-region, *Planet. Space Sci.*, *17*, 1233–1246, 1969.
- Swider, W., and R. S. Narcisi, Auroral *E*-region: Ion composition and nitric oxide, *Planet. Space Sci.*, *25*, 103–116, 1977.
- Tanenbaum, B. S., Continuum theory of Thomson scattering, *Phys. Rev.*, *171*(1), 215–221, 1968.
- Thayer, J. P., N. B. Nielsen, R. E. Warren, C. J. Heinselman, and J. Sohn, Rayleigh lidar system for middle atmosphere research in the arctic, *Opt. Eng.*, *36*(7), 2045–2061, 1997.

- Thomas, J. A., and E. K. Smith, A survey of the present knowledge of sporadic-*E* ionization, *J. Atmos. Terr. Phys.*, *13*, 295–314, 1959.
- Thomas, R. J., Total mixing ratios, *Planet. Space Sci.*, *22*, 175–177, 1974.
- Thrane, E. V., et al., Small scale structure and turbulence in the mesosphere and lower thermosphere at high latitudes in winter, *J. Atmos. Terr. Phys.*, *49*(7/8), 751–762, 1987.
- Tilgner, C., and U. von Zahn, Average properties of the sodium density distribution as observed at 69°N latitude in winter, *J. Geophys. Res.*, *93*(D7), 8439–8454, 1988.
- Turunen, E., Incoherent scatter radar contributions to high latitude *D*-region aeronomy, *J. Atmos. Terr. Phys.*, *58*(6), 707–725, 1996.
- Turunen, T., T. Nygrén, A. Huuskonen, and L. Jalonen, Incoherent scatter studies of sporadic-*E* using 300 m resolution, *J. Atmos. Terr. Phys.*, *50*(4/5), 277–287, 1988.
- Valladares, C. E., M. C. Kelley, and J. F. Vickrey, Plasma line observations in the auroral oval, *J. Geophys. Res.*, *93*(A3), 1997–2003, 1988.
- Vedder, J. F., 5. Micrometeorites, in *Satellite Environment Handbook*, edited by F. Johnson, pp. 91–100. Stanford University Press, Stanford, CA, 1961.
- Vesely, F. J., *Computational Physics, An Introduction*. Plenum Press, 1994.
- Vickrey, J. F., Incoherent scatter measurements of the motions of H⁺ and O⁺ in the topside ionosphere, Ph.D. thesis, Cornell University, 1978.
- Vickrey, J. F., and M. C. Kelley, The effects of a conducting *E* layer on classical *F* region cross-field plasma diffusion, *J. Geophys. Res.*, *87*(A6), 4461–4468, 1982.
- Vickrey, J. F., R. R. Vondrak, and S. J. Matthews, The diurnal and latitudinal variations of auroral zone ionospheric conductivity, *J. Geophys. Res.*, *86*(A1), 65–75, 1981.

- von Zahn, U., and T. L. Hansen, Sudden neutral sodium layers: a strong link to sporadic *E*, *J. Atmos. Terr. Phys.*, 50(2), 93–104, 1988.
- von Zahn, U., and E. Murad, NaHCO₃: a source of Na atoms for sudden sodium layers?, *Geophys. Res. Lett.*, 17(2), 147–149, 1990.
- von Zahn, U., P. von der Gathen, and G. Hansen, Forced release of sodium from upper atmospheric dust particles, *Geophys. Res. Lett.*, 14(1), 76–79, 1987.
- von Zahn, U., F.-J. Lübken, and C. Pütz, BUGATTI experiments: Mass spectrometric studies of lower thermosphere eddy mixing and turbulence, *J. Geophys. Res.*, 95(D6), 7443–7465, 1990.
- Wallis, D. D., and E. E. Budzinski, Empirical models of height integrated conductivities, *J. Geophys. Res.*, 86(A1), 125–137, 1981.
- Wasson, J. T., and G. W. Kallemeyn, Compositions of chondrites, *Phil. Trans. R. Soc. Lond. A*, 325(1587), 535–544, 1988.
- Wasson, J. T., and F. T. Kyte, Comment on the letter “On the influx of small comets into the Earth’s atmosphere II: Interpretation”, *Geophys. Res. Lett.*, 14(7), 779–780, 1987.
- Wayne, R. P., *Chemistry of Atmospheres*. Clarendon Press, Oxford, second edn., 1991.
- Whitehead, J. D., The formation of the sporadic-*E* layer in temperate zones, *J. Atmos. Terr. Phys.*, 20, 49–58, 1961.
- Whitehead, J. D., Production and prediction of sporadic *E*, *Rev. Geophys. Space Phys.*, 8(1), 65–144, 1970.
- Whitehead, J. D., Recent work on mid-latitude and equatorial sporadic-*E*, *J. Atmos. Terr. Phys.*, 51(5), 401–424, 1989.
- Wickwar, V. B., Plasma lines in the auroral *E* layer, *J. Geophys. Res.*, 83(A11), 1978.

- Yngvesson, K. O., and F. W. Perkins, Radar Thomson scatter studies of photoelectrons in the ionosphere and Landau damping, *J. Geophys. Res.*, *73*(1), 97–110, 1968.
- Young, J. M., C. Y. Johnson, and J. C. Holmes, Positive ion composition of a temperate-latitude sporadic *E* layer as observed during a rocket flight, *J. Geophys. Res.*, *72*(5), 1473–1479, 1967.